

GROWTH AND CHARACTERIZATION OF Te-Se SYSTEM AND SOME TELLURIDES

A. G. KUNJOMANA M.Phil.

**THESIS SUBMITTED
IN PARTIAL FULFILMENT OF THE REQUIREMENTS
FOR THE DEGREE OF
DOCTOR OF PHILOSOPHY**

**SOLID STATE PHYSICS LABORATORY
DEPARTMENT OF PHYSICS
COCHIN UNIVERSITY OF SCIENCE AND TECHNOLOGY
KOCHI - 682 022**

1992

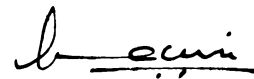
**To my parents and
to my late brother,
I affectionately dedicate this thesis**

CERTIFICATE

Certified that the research work presented in this thesis is based on the original work done by Miss A.G. Kunjomana under my guidance in the Department of Physics, Cochin University of Science and Technology, and has not been included in any other thesis submitted previously for the award of any degree.

Kochi 682022

10 August 1992



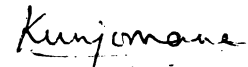
Dr. Elizabeth Mathai
Supervising Teacher

DECLARATION

Certified that the work presented in this thesis is based on the original work done by me under the guidance of Dr. Elizabeth Mathai in the Department of Physics, Cochin University of Science and Technology, and has not been included in any other thesis submitted previously for the award of any degree.

Kochi 682022

10 August 1992



A.G. Kunjomana

PREFACE

Recent developments in semiconductor research and technology over the last decade have led to a renewed interest in the growth of single crystals with better physical perfection and high purity. The major emphasis of these recent investigations has been on the growth of whiskers of a desired length, diameter and crystallographic orientation and with physical properties suitable for device applications. A greater understanding of the structure and properties of single crystals has resulted essentially from the use of a number of sophisticated analytical techniques which give precise information regarding the behaviour of crystals under specific physical conditions.

This thesis presents a study of the growth and characterization of Te-Se system, bismuth telluride (Bi_2Te_3) and indium telluride (In_2Te_3) crystals from vapour phase and melt growth techniques. Tellurium and selenium are VI group chalcogens and share a peculiar hexagonal crystal structure. Within the chains the bonding is covalent but crosslinking the chains it is partially Van der Waals and partially metallic in nature. Bi_2Te_3

is a layered semiconductor of V-VI family which crystallizes in rhombohedral lattice structure with the space group $D_{3d}^5(R\bar{3}m)$ and readily cleaves between the weakly bonded Te layers. In_2Te_3 crystals exist in two forms: a low temperature α -form and a high temperature β -form. The α -modification exists below 550-600°C and possesses a statistically ordered fcc structure with lattice constant $a = 18.486 \text{ \AA}$, and space group $F\bar{4}3m$. In the β -modification, the indium atoms and the vacancies are distributed at random leading to a sphalerite structure with lattice constant $a_0 = 6.158 \text{ \AA}$ and space group $F\bar{4}3m$. These crystals have perfect cleavage along the (111) planes.

Although the general principles of crystal growth can be applied for all materials, the precise method of crystal growth varies from one material to another. The physical vapour deposition (PVD) method is the most versatile of all crystal growth processes for providing crystals with perfection of structure and uniformity of composition. Since not much work has been carried out in the growth of whiskers of Te-Se system, Bi_2Te_3 and In_2Te_3 , it was thought interesting to grow and study whiskers of these materials using the PVD method. Melt

growth technique, namely--the horizontal zone levelling (HZL) method will provide crystals with some degree of control of stoichiometry. Hence this method is also employed for the growth of good single crystals, whose properties are studied after carefully cleaving the crystals at liquid nitrogen temperatures.

The physical properties of solid matter are basically influenced by the existence of lattice defects; as a result the study of crystal defects has assumed a central position in solid state physics and materials science. The study of dislocations in single crystals can yield a great deal of information on the mechanical properties of materials. In order to secure a full understanding of the processes taking place in semiconducting materials, it is important to investigate the microhardness of these materials--the most reliable method of determining the fine structure of crystals, the revelation of micro-inhomogenities in the distribution of impurities, the effect of dislocation density on the mechanical properties of crystals etc. Basically electrical conductivity in single crystals is a defect controlled phenomenon and hence detailed investigation of the electrical properties of these materials is one of the best available methods for the study of defects in them. In the present

thesis a series of detailed studies carried out in Te-Se system, Bi_2Te_3 and In_2Te_3 crystals using surface topographical, dislocation and microindentation analysis as well as electrical measurements are presented.

The thesis opens with twelve chapters which by and large are self-contained with separate introduction and references. In chapter 1 a general introduction to the theories and techniques of crystal growing are given. A brief description is provided to get an understanding of the theoretical aspects of the growth of perfect crystals and that of imperfect crystals. Of the various growth techniques, particular emphasis has been laid upon to describe the importance of vapour growth and melt growth methods since only these methods are of direct interest in the present work.

Chapter 2 is devoted to the description of morphology and growth mechanism of crystals. This section also outlines an account on whiskers, platelets, dendrites and spherulites. The different concepts of hollow whisker growth are also covered in this chapter.

Chapter 3 is intended to provide a brief summary on the different types of defects, geometry of dislocations,

energy associated with dislocations, dislocation reactions, plastic deformation, cleavage of crystals etc. This section also gives a glance at various methods used for the detection of defects in crystals.

Some theoretical and practical aspects of the mechanical properties of crystals are considered in the fourth chapter. Special attention is paid to describe micro-hardness--the most important parameter determining the strength of crystals. The last part introduces some basic ideas of toughness and brittleness of crystals.

Chapter 5 presents the details of the experimental techniques employed in these investigations. This part focus attention on various types of furnaces and other assemblies in connection with the crystal growth system required for the PVD method and HZL method. This is followed by some practical aspects of the ampoules and their pre-treatment involved in the crystal growing. A general review of the techniques such as X-ray diffraction (XRD), electron spectroscopy for chemical analysis (ESCA) and differential scanning calorimetry (DSC) is outlined. A short note is made on the optical microscopic investigations using Scanning electron microscope, Carl Zeiss Jena Epityp-II and Union Versamet-2

metallurgical microscopes. In addition, the details of experimental set up for the study of electrical properties find a place in this part.

In chapter 6, the growth and morphological studies on the as-grown surfaces of $\text{Te}_{1-x}\text{Se}_x$ (where x is the different concentrations of Se as impurity element), Bi_2Te_3 and α - and β -modifications of In_2Te_3 whiskers are described. The whiskers are grown by the PVD method at controlled temperature gradients. Since the source temperatures of Bi_2Te_3 and In_2Te_3 are comparatively high, fused quartz ampoules are used for their growth. The crystals obtained are about 1 to 1.5 cm long with 1 to 2 mm² cross section and are bounded by smooth prism planes. The growth features observed on the prism faces show that these crystals are grown by the layer growth mechanism. Microscopic examinations of these whiskers indicate that they are grown hollow with axial cavities and channels. An explanation is given for the growth mechanism of the hollow nature of crystals on the basis of morphological studies. In addition to straight needles and short well developed prisms, the crystals exhibit different morphologies like platelets, ribbon shaped crystals, twisted growths and kinked whiskers. X-ray diffraction analysis revealed the rhombohedral unit cell dimensions of Bi_2Te_3

whiskers as $a_R = 10.470 \text{ \AA}$ and $\alpha_R = 24^\circ 9' 45''$. The lattice constant of $\alpha\text{-In}_2\text{Te}_3$ whiskers is found to be $a = 18.471 \text{ \AA}$ and that of $\beta\text{-In}_2\text{Te}_3$ whiskers is $a_0 = 6.164 \text{ \AA}$. The composition of constituent elements present in the grown whiskers is analysed using ESCA.

Chapter 7 covers the results of the chemical and thermal etching studies carried out on the whiskers. The dislocation density is determined by using chemical etching. For $\text{Te}_{1-x}\text{Se}_x$ whiskers, the change in the shape and number of etch pits as a function of different additions of Se as impurity to Te are studied. The results indicate that the dissolution directions change with the impurity concentrations. Several etchants have been selected by trial and error to delineate dislocations on the prism faces of Bi_2Te_3 and In_2Te_3 whiskers and the observations are presented here. The morphology of dislocation configurations resulting from thermal etching is also reported.

Chapter 8 is devoted to the details of micro-indentation analysis on the prism faces of grown whiskers. The results obtained are discussed using the existing theoretical models.

Chapter 9 deals with the melt growth of Bi_2Te_3 , and α - and β -modifications of In_2Te_3 crystals by the HZL method. X-ray diffraction profiles to identify the different phases of the grown samples are analysed along with the lattice parameter investigation. DSC analysis is carried out to determine the phase transition temperature of In_2Te_3 samples. Some interesting patterns observed on the cleavage faces relating to the dislocation configurations are presented here.

In chapter 10, a detailed account of the study of dislocations on the cleavage faces of Bi_2Te_3 and In_2Te_3 crystals is given. Particular attention is paid to understand the role of plastic deformation and fracture phenomenon on the cleavage planes. The Frank-Read multiplication mechanism responsible for the movement and multiplication of dislocation during the course of deformation is explained on the basis of observed dislocation spirals and loops in the slip plane, whose shapes are found to be in accordance with the theoretical models. This section also provides an outlook on the nucleation and development of microcracks originated in the slip plane due to the process of cleavage. The mechanism responsible for the crack formation has been suggested.

Chapter 11 is dedicated to the results of indentation studies on the cleavage faces of Bi_2Te_3 and In_2Te_3 samples. Together with an investigation of cracks developed during the indentation process, it elucidates the variation of hardness with applied load. The value of hardness numbers obtained are compared with that of whiskers of these compounds and the strength of crystals are assessed. The contribution of applied stress utilized for the nucleation and propagation of cracks on the indented impression by subjecting various loads are studied to understand the deformation mechanism. The effect of homogeneous generation of dislocations due to high stress and the role of slip mechanism on the mechanical behaviour of these crystals are investigated and are reported here.

The last chapter includes some electrical measurements carried out on the cleavage surfaces of Bi_2Te_3 and In_2Te_3 crystals. The results obtained from these investigations are discussed at some length.

Part of the investigations contained in this thesis has been published in various international journals and presented in national conferences.

LIST OF PUBLICATIONS

1. "Growth and dislocation density of $\text{Te}_{1-x}\text{Se}_x$ whiskers",
J. Cryst. Growth **92** (1988) 666.
2. "Direct observation of Frank-Read sources in stoichiometric bismuth telluride crystals"
J. Mater. Sci. **26** (1991) 6171.
3. "Growth and microindentation analysis of $\alpha\text{-In}_2\text{Te}_3$ whiskers"
Mat. Res. Bull. **26** (1991) 1347.
4. "Growth and microindentation studies of $\beta\text{-In}_2\text{Te}_3$ whiskers"
J. Mater. Sci. Lett. **11** (1992) 613.
5. "Growth and morphology of hollow Bi_2Te_3 whiskers by physical vapour deposition method"
Cryst. Res. Technol. (In Press).
6. "Defect morphology of $\text{Te}_{1-x}\text{Se}_x$ whiskers"
XIX National Seminar on Crystallography, Kottayam (18-20 December 1987).

7. "Growth of Bi_2Te_3 single crystals"
Symposium on Current Trends in Pure and Applied
Physics, Cochin (October 1988).
8. "Growth of In_2Te_3 whiskers"
Solid State Physics Symposium, Bhopal (20-23
December, 1988).
9. "Electrical properties of bismuth telluride crystals"
Solid State Physics Symposium, Varanasi (21-24
December, 1991).
10. "Microhardness studies of $\text{Te}_{1-x}\text{Se}_x$ whiskers"
Solid State Physics Symposium, Varanasi (21-24
December, 1991).
11. "Electrical conductivity of In_2Te_3 crystals"
Solid State Physics Symposium, Varanasi (21-24
December, 1991).
12. "Dissolution kinetics of In_2Te_3 crystals"
Solid State Physics Symposium, Varanasi (21-24
December, 1991).

13. "Observation of stacking faults on the basal plane of Bi_2Te_3 crystals"
(Communicated).
14. "Growth of In_2Te_3 crystals by horizontal zone leveling method"
(Communicated).
15. "Microindentation studies of melt-grown In_2Te_3 crystals"
(Communicated).
16. "Electrical conductivity studies of Bi_2Te_3 crystals"
(Communicated).
17. "Effect of annealing temperatures on the electrical properties of β - In_2Te_3 crystals"
(Communicated).
18. "Dislocation etch studies on In_2Te_3 crystals"
(Communicated).
19. "A study of dislocation etch pits on Bi_2Te_3 whiskers"
(Communicated).

ACKNOWLEDGEMENTS

It is a pleasure for me to express my deep sense of gratitude to Dr. Elizabeth Mathai, Reader, Department of Physics, Cochin University of Science and Technology, for her helpful, understanding and stimulating guidance. I am extremely thankful to her for giving me the necessary advices throughout the course of my research.

I would like to thank Prof.K. Babu Joseph, Head of the Department of Physics, for providing the laboratory and library facilities.

I desire to express particular indebtedness to Dr.B. Pradeep for the many discussions and help which have inspired me much.

I am specially indebted to Mr.P.K. Sarangadharan, for his help and encouragement during my work.

I take this opportunity to express my great appreciation to Dr.R. Navil Kumar for all the help he has rendered to me.

I have been most fortunate to work with Prof.P. Ramasamy, Director, Crystal Growth Centre, Anna University, Madras during my research period. I feel the deepest gratitude to him for all the help he has rendered to me. I am also grateful to Dr.D. Arivuoli, lecturer, Anna University, Madras for the many valuable comments and suggestions.

Grateful acknowledgement is made to the Head, RSIC, IIT, Madras for providing the facilities like ESCA and SEM analysis. Useful discussions and help by Mr.V. Sivanandam, Mrs. Santhi, Dr.Chandramouli and Mr.C. Gopinath, IIT, Madras are sincerely acknowledged.

I would like to thank Dr.P.S. Mukherji, RRL, Trivandrum and Dr.P.K.Joy, Travancore Titanium Products, Trivandrum for helping with the XRD analysis.

I am deeply obliged to Prof.V.N. Sivasankara Pillai, Department of Applied Chemistry for the kind help given to me during this endeavour.

Thanks are also due to the staff of the office of the Department of Physics and USIC for their co-operation and help.

The financial support in the form of JRF and SRF from UGC, New Delhi is gratefully acknowledged.

I appreciate and thank Mr.K.P. Sibiraj and Mr.V.M. Peter for the neat typing and binding of the thesis.

Finally a special word of thanks is due to my family especially to my twin sister Miss A.G. Valyomana who supported me throughout this work and surrounded me with an environment of peace, love and understanding.

A.G. Kunjomana.

CONTENTS

	<u>Page</u>
PREFACE ..	i
LIST OF PUBLICATIONS ..	x
ACKNOWLEDGEMENTS ..	xiii
Chapter 1 GROWTH OF CRYSTALS	
1.1 Introduction ..	1
1.2 Theories of crystal growth ..	1
1.3 Techniques of crystal growth ..	9
1.4 References ..	30
Chapter 2 MORPHOLOGY AND GROWTH MECHANISM OF CRYSTALS	
2.1 Introduction ..	36
2.2 Morphology of crystals ..	37
2.3 Growth mechanism of crystals ..	46
2.4 References ..	48
Chapter 3 DEFECTS IN CRYSTALS	
3.1 Introduction ..	57
3.2 Defects in crystals ..	58
3.3 Etching of crystals ..	77
3.4 Figure captions ..	88
3.5 References ..	89
Chapter 4 MECHANICAL TESTING OF CRYSTALS	
4.1 Introduction ..	95
4.2 Hardness ..	95
4.3 Toughness ..	101
4.4 Brittleness ..	104
4.5 References ..	106

Chapter 5	EXPERIMENTAL TECHNIQUES		
5.1	Introduction	..	112
5.2	Growth techniques	..	112
5.3	X-ray diffraction	..	117
5.4	Electron spectroscopy for chemical analysis	..	118
5.5	Differential scanning calorimetry	..	120
5.6	Optical microscopy	..	121
5.7	Etching studies	..	123
5.8	Microindentation studies	..	123
5.9	Electrical conductivity studies	..	124
5.10	Figure captions	..	126
5.11	References	..	128
Chapter 6	GROWTH AND MORPHOLOGY OF VAPOUR-GROWN Te_{1-x}Se_x, Bi₂Te₃ AND In₂Te₃ CRYSTALS		
6.1	Introduction	..	129
6.2	Experimental	..	134
6.3	Results and discussion	..	136
6.4	Conclusion	..	156
6.5	Figure captions	..	157
6.6	References	..	163
Chapter 7	CHEMICAL AND THERMAL ETCHING STUDIES OF VAPOUR-GROWN Te_{1-x}Se_x, Bi₂Te₃ AND In₂Te₃ CRYSTALS		
7.1	Introduction	..	171
7.2	Experimental	..	174
7.3	Results and discussion	..	175
7.4	Conclusion	..	188
7.5	Figure captions	..	190
7.6	References	..	196

	<u>Page</u>
Chapter 8	
MICROINDENTATION ANALYSIS OF VAPOUR-GROWN	
$\text{Te}_{1-x}\text{Se}_x$, Bi_2Te_3 AND In_2Te_3 CRYSTALS	
8.1 Introduction ..	199
8.2 Experimental ..	200
8.3 Results and discussion ..	201
8.4 Conclusion ..	207
8.5 Figure captions ..	208
8.6 References ..	210
Chapter 9	
GROWTH AND FRACTOGRAPHIC STUDIES OF	
MELT-GROWN Bi_2Te_3 AND In_2Te_3 CRYSTALS	
9.1 Introduction ..	212
9.2 Experimental ..	214
9.3 Results and discussion ..	215
9.4 Conclusion ..	222
9.5 Figure captions ..	223
9.6 References ..	225
Chapter 10	
DISLOCATION STUDIES OF MELT-GROWN	
Bi_2Te_3 AND In_2Te_3 CRYSTALS	
10.1 Introduction ..	228
10.2 Experimental ..	231
10.3 Results and discussion ..	232
10.4 Conclusion ..	255
10.5 Figure captions ..	257
10.6 References ..	266
Chapter 11	
MICROINDENTATION ANALYSIS OF MELT-GROWN	
Bi_2Te_3 AND In_2Te_3 CRYSTALS	
11.1 Introduction ..	269
11.2 Experimental ..	270

	<u>Page</u>
11.3 Results and discussion ..	271
11.4 Conclusion ..	275
11.5 Figure captions ..	277
11.6 References ..	279
Chapter 12 ELECTRICAL CONDUCTIVITY STUDIES OF MELT-GROWN Bi_2Te_3 AND In_2Te_3 CRYSTALS	
12.1 Introduction ..	281
12.2 Mechanism of electrical conduction in semiconductors ..	281
12.3 Experimental ..	285
12.4 Results and discussion ..	286
12.5 Conclusion ..	288
12.6 Figure captions ..	292
12.7 References ..	293

1

GROWTH OF
CRYSTALS

1.1 INTRODUCTION

The study of crystals, which are the most perfectly organized form of solid state, has greatly assisted the understanding of ultimate structure of matter. Recently, because of the demand for large single crystals free from flaws for applications in modern industry, the subject of crystal growth and their characterization has assumed increasing importance both in the academic and technological fields. Several new techniques have been employed to understand the kinetics of the process of growth of crystals and considerable information has been gathered on theoretical grounds.

In this chapter is presented an account of the physical interpretation of growth theories and techniques. The growth of crystals, from vapour and melt is discussed in detail.

1.2 THEORIES OF CRYSTAL GROWTH

Gibbs [1] was the first to realize that the formation of small embryonic clusters with some critical size is a prerequisite for a macroscopic phase transformation to take place. He compared the conditions governing

the growth of water droplets to growth of crystals and defined the equilibrium form as that possessing minimum total surface free energy for a given volume. If the volume free energy per unit volume is considered as constant throughout a crystal bounded by n faces, this criterion can be expressed as $\sum_{i=1}^n \sigma_i \cdot F_i$ is a minimum where σ_i is the surface free energy per unit area of the i^{th} face of area F_i .

The thermodynamic treatments of nucleation suggested by Gibbs were later generalized by various authors. Curie [2] calculated the shapes and end forms of crystals in equilibrium with solution or vapour consistent with the idea of Gibb's criterion. The theory given by Wulff [3] implies that on a crystal, the velocities of growth of different faces in the directions of normals are proportional to the appropriate specific surface free energies. Bravais [4] suggested that the velocities of the growth of the different faces of a crystal would depend upon the density of lattice points in various planes i.e., on reticular density. This Bravais theorem was further extended by Donnay and Harker [5]. After the Gibbs and Curie theories, Soehncke [6] introduced the idea of surface energies by postulating that the faces which possess the

greatest reticular densities are those with minimum surface energies and hence have minimum velocities of growth. A descriptive amount of the development of the various growth theories is given by Buckley [7].

The theories of crystal growth can be classified into two parts by considering the theory of the growth of perfect crystals and that of imperfect crystals.

1.2.1 Growth of Perfect Crystals

Kossel [8], Stranski [9] and Volmer [10] have put forward an atomic theory to explain the growth of perfect crystals. To illustrate the KSV model, consider a cubic crystal made up of small cubes representing unit cells. Each cube is attracted equally by all its six neighbours and only the nearest neighbours attract one another. The surface of a perfect cubic crystal at the absolute zero of temperature appear as flat and smooth on a molecular layer partially covered by another layer. As the temperature is raised, the atoms or molecules may leave the step end face (as well as the surface layer) because of thermal motion and shift either into the environment or onto the surface, into one of the surface sites with a different number of bonds with the lattice. While some molecules are getting

vapourized, other molecules from the vapour phase reach the crystal surface and are adsorbed there. On reaching the equilibrium stage, the step ceases to be straight and acquires a certain number of vacant sites, adsorbed atoms and kinks and becomes rough. Atoms get absorbed on the crystal faces and they migrate towards a step and moves along it to a kink position to get incorporated or re-evaporated. To commence growth, saturation is to be increased. Now more and more atoms get absorbed and they get deposited on the step kinks. As a result the step advances with a certain velocity and later disappears after completing the surface. Further growth requires a step which in turn requires an additional energy.

(i) Adsorption layer

When a crystal is surrounded by a vapour with pressure P , then $P/\sqrt{2\pi mkT}$ particles of mass m impinge on unit surface per unit time. Majority of the particles are absorbed on the surface and form an adsorption layer. The migration distance x_s of the adsorbed molecule is given by the Einstein's formula

$$x_s^2 = D_s \tau_s \quad (1.1)$$

where D_s is the diffusion coefficient and τ_s the mean life time on the surface. In the Kossel-Stranski model

$$x_s \sim a \exp(3 \phi / 2kT) \quad (1.2)$$

where ϕ is the nearest neighbour interaction.

(ii) Advance of Steps

The mode of advance of the steps can be analyzed on the basis of BCF theory [11]. A step advances by the process of incorporating more and more adsorbed molecules at kink sites at high supersaturation.

The supersaturation in the vapour is,

$$\sigma = \alpha - 1 ; \quad \alpha = P/P_0 \quad (1.3)$$

where P is the actual vapour pressure, and P_0 the equilibrium value. Similarly the supersaturation σ_s of adsorbed atoms is defined by,

$$\sigma_s = \alpha_s - 1 ; \quad \alpha_s = n_s/n_{s0} \quad (1.4)$$

where n_{s0} is the equilibrium concentration of adatoms on the surface.

The rate of advance 'v' of a straight step is given as,

$$V = 2 \sigma x_s \nu \exp(-W/KT) \quad (1.5)$$

where ν is a frequency factor and W , the evaporation energy. The rate of advance is then proportional to the supersaturation as well as to the migration distance of adsorbed atoms.

(iii) Surface Nucleation

On perfect crystal faces steps could be excited by thermodynamic fluctuations. Once the step has covered along the whole surface further growth is possible only by the initiation of a new island monolayer or twodimensional nucleus, which requires an additional energy. The excess free energy F for the formation of such a layer is given by,

$$g(r) = -kT \ln \alpha \pi r^2 / a^2 + \gamma 2\pi r / a \quad (1.6)$$

γ being the edge free energy per molecule. The rate of nucleation I per unit area per unit time may be written as,

$$I = \nu N_0 \exp (-g_c / kT) \quad (1.7)$$

where N_0 is the number of lattice sites per unit area and ν is the number of molecules arriving per unit time towards the critical nucleus. This thermodynamical derivation can be substantiated by the kinematic approach of Becker and Doring [12] and Frank [13].

According to the surface nucleation theory, the probability of the formation of nuclei is negligible below a supersaturation of 25-50 per cent. However, real crystals are frequently observed growing at supersaturation of 1% or lower. This led to the conclusion that the growth of crystals at low supersaturations could only be explained by the fact that real crystals are not perfect.

1.2.2 Growth of Imperfect Crystals

Burton, Cabrera and Frank [11] have developed the theory of growth of real crystals by taking into account the presence of dislocations. Recognizing that crystals are not perfect, Frank [14] proposed the best known mechanism for reproducing surface steps. He pointed out that the intersection of screw dislocations with the growing surface generates continuous train of ledges which allows continuous growth with large number of kinks. Therefore the barrier of surface nucleation can be prevented. When the atoms are adsorbed on the crystal surface, they diffuse to the step and finally to the kinks where they are adsorbed for the building up of the crystal and the step advances. Since the step provided by the emergence of a screw dislocation terminates at the dislocation point, further growth takes

place only by the rotation of step around the dislocation point. At a particular supersaturation, each point on a straight step will advance with the same speed and developed into the formation of spiral patterns on the crystal surface. A ledge which forms a portion of the spiral and has a radius of curvature ρ , will advance with a velocity v_ρ given by,

$$v_\rho = v_\infty (1 - \rho_c/\rho) \quad (1.8)$$

where v_∞ is the rate of advance of a straight step and ρ_c is the critical radius of curvature.

Let $\theta(r)$ represents the rotating spiral in polar coordinates (r, θ) . The radius of curvature at a point r will be,

$$\rho = (1 + r^2 \theta'^2)^{3/2} / (2r\theta' + r^2 \theta'' + r\theta''') \quad (1.9)$$

where θ' and θ'' are the derivatives of $\theta(r)$.

The normal velocity at the point r is,

$$v(r) = \omega r (1 + r^2 \theta'^2)^{-1/2} \quad (1.10)$$

ω^* being the angular velocity of the whole spiral and is given by,

$$\omega^* = v_{\infty} / 2 r_c \quad (1.11)$$

The spacing between the successive arms of the spiral will be constant and is given by,

$$dr = 4 \pi r_c \quad (1.12)$$

Following the suggestion of Frank [14] that screw dislocations account for crystal growth at supersaturations too low for growth by two dimensional nucleation, several workers observed growth spirals [15-16].

1.3 TECHNIQUES OF CRYSTAL GROWTH

The growth methods for obtaining single crystals may be classified into three categories. Vapour growth, melt growth and solution growth depending on the phase transitions involved in the crystal growth process. The choice of a concrete growing method depends on the material to be obtained and requirements of growth kinetics (rate of growth), size, shape, purity and economics. This section deals with the technological aspects of the different growth methods currently employed.

1.3.1 Growth from the Vapour Phase

Crystallization from the vapour phase is widely used for growing bulk crystals, epitaxial films, thin coatings, filamentary and platelet crystals. Vapour growth is attractive because of its versatility in producing crystals with high purity, uniformity of composition and perfection of structure. Furthermore, the low growth rate typical of these methods proves an advantage in growing multilayer structures for applications in semiconductor technology. The various transport mechanisms of vapour species are treated in [17].

1.3.1.1 The Driving Force of Vapour Growth

The driving force for condensation can be expressed in terms of supersaturation. At equilibrium, the pressure P_{∞} in equilibrium with bulk solid or liquid phase can be written as,

$$P_{\infty} = A \exp \frac{-\Delta H_{SV}}{kT} = A' \exp \frac{-\Delta H_{LV}}{kT} \quad (1.13)$$

where A , A' are constant and ΔH_{SV} , ΔH_{LV} are the latent heats of condensation from the solid and liquid phases, respectively.

A solid or liquid phase exposed to the pressure P_∞ will neither grow nor evaporate, since these are equilibrium conditions in which the vapour phase is saturated with respect to the condensed phase. A pressure P_a from an external source is supersaturated with respect to the solid phase at temperature T_b which has an equilibrium pressure P_b . The ratio $P_a/P_b = \mathcal{L}$ is the saturation ratio. At T_b , the solid is in equilibrium with vapour with pressure P_b and has the same chemical potential. The driving force for condensation is the free energy difference per atom G_v between vapour at pressure P_a and P_b ,

$$G_v = kT_b \int_{P_a}^{P_b} \frac{dp}{P} = -kT_b \ln \frac{P_a}{P_b} = -kT_b \ln \mathcal{L} \quad (1.14)$$

The incidence pressure P_a must derive from solid or liquid at a higher temperature than T_b . Using equation (1.13).

$$\mathcal{L} = \frac{P_a}{P_b} = \exp\left[\Delta H_{SV} \left(\frac{1}{kT_b} - \frac{1}{kT_a}\right)\right] \quad (1.15)$$

$$G_v = -\Delta H_{SV} \left(\frac{T_a - T_b}{T_a}\right) \quad (1.16)$$

1.3.1.2 Methods of Vapour Growth

The methods of crystallization from the vapour phase can be distinguished into two principal groups: In one, the methods are based on purely physical condensation and in the other, a chemical reaction is involved which produces the crystallizing substance. A common feature of all these methods is the need to deliver material from some localized source. The location of the starting material is called the source zone and the site at which it is deposited, the crystallization zone.

(a) Physical Vapour Deposition (PVD)

The feature common to this group of methods is that the substance is delivered to the growing crystal in the form of its own vapour, which consists of atoms and molecules as well as association of them. The PVD method of growth is applicable to materials which have appreciable vapour pressure at the concerned growth temperature. In this method, a sealed ampoule containing the crystallizing substance is placed in the temperature gradient. The charge material is placed in the hotter part of the ampoule. Owing to the temperature dependence of the equilibrium vapour pressure, a concentration gradient is

established in the ampoule, the concentration being higher in the hotter part. Under the effect of this gradient, the substance is transported to the colder end (crystallization zone) where the vapour is supersaturated and therefore can be condensed. This method is also called closed ampoule method, the details of which are described in the literature [17,18]. Thus single crystals can be grown where the substance is converted directly from solid to vapour and back again to solid under vacuum conditions in the ampoule. Molecular Beam method [19,20], and Cathode sputtering [21] are also be considered as physical transport or deposition methods. These methods are mainly useful for the production of epitaxial films of germanium, silicon, $A^{II}B^{VI}$, $A^{IV}B^{IV}$ and $A^{III}B^V$ compounds both on substrates of the same substance and on foreign substrates. The pvd technique has been used to grow ZnSe [22,23] and CdS crystals [24].

A most sophisticated version of the closed ampoule method was used by Kaldis [25] to grow oxides and sulphides of the rare earths. Another variation of this method was developed on the basis of the travelling heater technique. This is Piper and Polich [26] method. In this technique, the charge is placed in one end of the silica tube and

slowly pulled through a furnace whose temperature profile has a single peak. The capsule is initially opened at the end where crystal is to grow so that gaseous contamination produced during the early part of the experiment could escape. A cooled stopper is then inserted and the capsule is sealed by material going over the opening. This approach removes volatile impurities if they diffuse rapidly out of the source material and has been used to grow some of the large crystals of the II-VI compounds in particular.

(b) Chemical Vapour Deposition (CVD)

The feature common to this group of methods is that they involve a chemical reaction. This reaction serves not only to supply material for crystallization but also has an active influence on the crystallization process. These methods are used for crystallizing compounds [27-31].

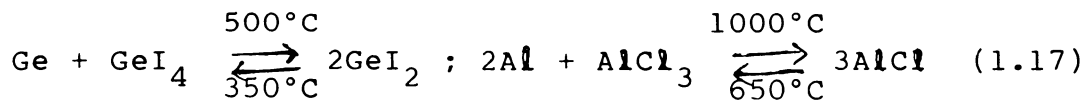
(i) Chemical Transport Method

The crystallizing substance interacts in solid or liquid form with another substance in the source zone and transforms into gaseous compounds. These are then

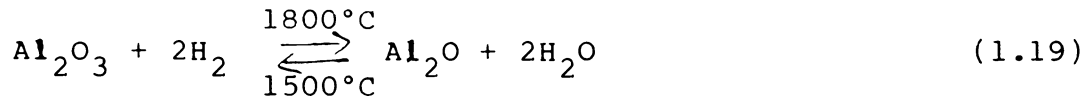
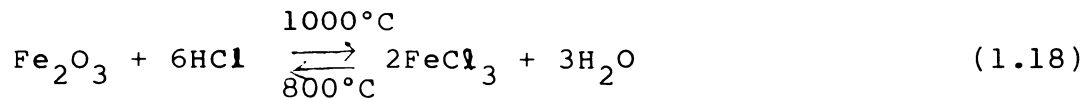
transported to a zone with a different temperature and decomposing by the reverse reaction, they release the nutrient [32].

Below are some typical examples of the transport reactions used in crystal growing,

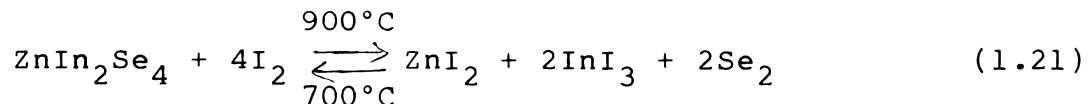
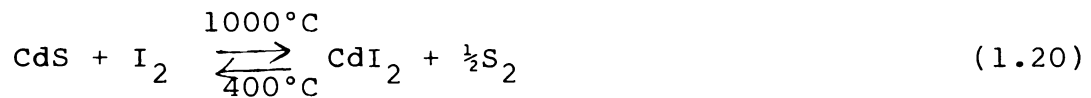
- (1) Transport of elements by means of the disproportionation reaction:



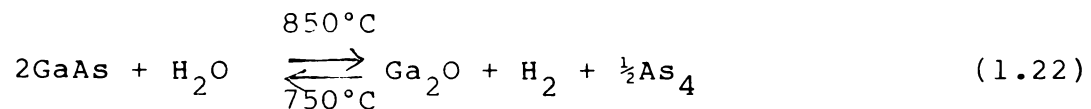
- (2) Transport of oxides by hydrogen chloride or hydrogen:



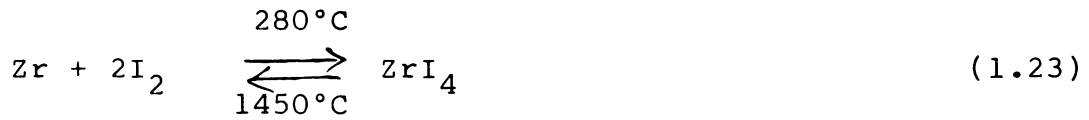
- (3) Transport of chalcogenides by iodine:



- (4) Transport in water vapours:



(5) Iodide transport to obtain pure metals:

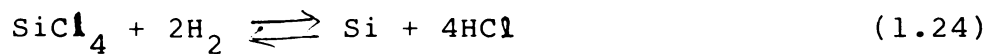


(ii) Vapour Decomposition Method

A volatile compound is introduced into the crystallization zone. Under the effect of a gaseous reducing agent and/or a high temperature or other factors, it decomposes, releasing the crystallizing substance.

The two principal methods are reduction and thermal decomposition (pyrolysis) of compounds.

A typical example of reduction process is the growing of silicon films by reduction of silicon tetrachloride with hydrogen [33,34].



A typical example of thermal decomposition method is the silane method of growing silicon films [35,36].



(iii) Vapour-Phase Synthesis Method

The crystallizing substance is formed as a result of a reaction between the gaseous components directly in the crystallization zone. Vapour-phase synthesis method is used to obtain crystals of silicon carbide and $A^{III}B^V$ compounds.

1.3.2 Growth from the Melt

Melt growth is a field of crystal growth which relates to solids which can be melted and crystallised. All materials can be grown in single crystal form from the melt provided they melt congruently, they do not decompose before melting and they do not undergo a phase transformation between the melting point and room temperature. By these methods, metals, elemental and compound semiconductors, oxides, halides, high melting point refractories etc. are grown. The main advantage of this kind of crystallization is that it permits highest growth rates and allow the achievement of structurally perfect and composition controlled single crystals, such as to meet the stringent required for electronic materials.

1.3.2.1 The Driving Force of Melt Growth

The crystallization of a melt is a first order phase change from liquid to solid involving the liberation

of latent heat. The driving force of a melt growth process can be expressed as $\Delta G_{SL} = \Delta H_{SL} - T \Delta S_{SL}$, where ΔG_{SL} is the free-energy change between the two phases, ΔH_{SL} and ΔS_{SL} are the corresponding enthalpy and entropy changes and T is the temperature.

At equilibrium, $\Delta G_{SL} = 0$

or,

$$\Delta S_{SL} = \frac{\Delta H_{SL}}{T_M} \quad (1.26)$$

where T_M is the equilibrium melting point for a non (but near to) equilibrium process, in which the melt is undercooled at a temperature T below the melting temperature T_M ,

$$\Delta G_{SL} = \Delta H_{SL} \frac{T_M - T}{T_M} = \Delta H_{SL} \left(\frac{\Delta T}{T_M} \right) \quad (1.27)$$

$\frac{\Delta T}{T_M}$ is the relative undercooling and it gives the effective driving force of the crystallization process. The driving force can also be expressed in terms of supersaturation σ . At T_M , both solid and liquid phases are in equilibrium with the saturated vapour P_M ,

$$P_M = A \exp \frac{-\Delta H_{SV}}{kT_M} = A' \exp \frac{-\Delta H_{LV}}{kT_M} \quad (1.28)$$

If the melt is undercooled at $T < T_M$, the vapour pressures at T for the two phases will be,

$$P_L = A' \exp \frac{-\Delta H_{LV}}{kT} \quad (1.29)$$

$$P_S = A \exp \frac{-\Delta H_{SV}}{kT} \quad (1.30)$$

substituting for A'/A from equation (1.28) and putting $\Delta H_{SV} - \Delta H_{LV} = \Delta H_{SL}$ the latent heat of fusion giving,

$$\sigma = \frac{P_L}{P_S} - 1 = \exp \left[\Delta H_{SL} \left(\frac{1}{kT} - \frac{1}{kT_M} \right) \right] - 1 \quad (1.31)$$

where $P_L/P_S = \alpha$ is the saturation ratio.

The free energy change between the two phases is expressed as,

$$\Delta G_{SL} = -kT \ln \alpha = -\Delta H_{SL} \left(\frac{T_M - T}{T_M} \right) \quad (1.32)$$

A more rigorous evaluation of free energy in solidification from the melt has been given by Jones and Chadwick [37].

1.3.2.2 Interface Kinetics

Melting or freezing is taking place at an interface. The process depends on atom motion, and so the

rate of motion of the interface $\frac{d\lambda}{dt}$ depends among other factors, on the mobility of atoms in the liquids.

Assuming the atom motion at the interface to be a simply activated process, the rate at which atoms join the crystal can be written as [38],

$$R_F = R_F^{\circ} \exp(-\Delta G^*/KT) \quad (1.33)$$

where ΔG^* is the activation energy for liquid diffusion of a growth unit.

Similarly the rate at which atoms leave the crystal is,

$$R_M = R_M^{\circ} \exp[-(\Delta G^* + \Delta H_{SL})/KT] \quad (1.34)$$

where the term $(\Delta G^* + \Delta H_{SL})$ represents the activation energy for melting.

At equilibrium $R_M = R_F$ or

$$R_M^{\circ}/R_f^{\circ} = \exp\left(\frac{\Delta H_{SL}}{kT_M}\right) \quad (1.35)$$

By comparison with equation (1.26),

$$\frac{\Delta H_{SL}}{T_M} = \Delta S_{SL} = k \ln \left[\frac{R_M^{\circ}}{R_F^{\circ}} \right] \quad (1.36)$$

The net growth rate is given by,

$$v = R_F - R_M = R_M^{\circ} \exp\left(\frac{-\Delta G^*}{kT}\right) \left[\frac{R_F^{\circ}}{R_M^{\circ}} - \exp\left(\frac{-\Delta H_{SL}}{kT}\right) \right] \quad (1.37)$$

$$= R_M^{\circ} \exp\left(\frac{-\Delta G^*}{kT}\right) \exp\left(\frac{-\Delta H_{SL}}{kT_M}\right) \left[1 - \exp\left(\frac{-\Delta H_{SL} \Delta T}{kT_M T}\right) \right] \quad (1.38)$$

For small $\Delta T/T_M$, and replacing $R_M^{\circ} = a \nu$ the inter-atomic distance times the vibration frequency in the solid,

$$v = a \nu \exp\left(\frac{-\Delta G^*}{kT}\right) \exp\left(\frac{-\Delta H_{SL}}{kT_M}\right) \left(\frac{\Delta H_{SL} \Delta T}{kT_M T} \right) \quad (1.39)$$

This formulation assumed implicitly that all sites at the crystal liquid interface are equivalent and are active growth sites. This is not true in general. In more realistic cases, only a fraction of interface sites are available for growth unit attachment, which can be accounted for by multiplying equation (1.39) by suitable factors. Thus when screw dislocation mechanism are dominant, so that the growth sites are on the edge of the spiral, the factor will be,

$$f = \alpha_1 \frac{\Delta H_{SL}}{\gamma_L} \frac{\Delta T}{T_M} \quad (1.40)$$

where γ_L is ledge free energy, and α_1 is geometric constant. From equations (1.39) and (1.40) one gets $V \propto (\Delta T)^2$ for small undercooling. For surface nucleation growth, classical two-dimensional nucleation theory leads to a factor

$$f = \alpha_2 \exp(-T^*/\Delta T) \quad (1.41)$$

$$\text{where } T^* = \frac{\alpha_2 \gamma_L^2 T_M}{kT \Delta H_{SL}} \quad (1.42)$$

Combining equations (1.39) and (1.41) one gets an expression predicting small growth rates until $\Delta T \sim T^*$, and V increases very rapidly with increasing undercooling.

1.3.2.3 Methods of Melt Growth

The methods of growing single crystals from the melt are divided into two groups: Methods with a large melt volume (Normal freezing methods) and that with a small melt volume (zone melting methods). The most striking example of the influence of the melt volume on the quality of the growing crystal is the distinct difference between

the impurity distribution along the length of grown crystals by these two methods.

(a) Normal Freezing

Unidirectional crystallization is one of the methods used with a large melt volume. A cylindrical container holding the melt moves into the cool region of the furnace, so that a crystal nucleating at the cooler end of the container gradually increases in size until it occupies the whole container. Controlled solidification of the first nucleus is promoted by removing the latent heat generated by the solidification process by conduction into the solid rather than into the liquid. In unidirectional crystallization the amount of impurity in the middle portion of the crystal remains constant and therefore this method is preferred for the impurity activation of crystals. The distribution of impurities is given by the normal freeze equation,

$$C_s = k_o C_o (1 - g)^{k_o - 1} \quad (1.42)$$

where C_s is the concentration of the impurity (solute) in the crystal, k_o its distribution coefficient and C_o its initial concentration in the charge and g is the fraction

of the melt solidified. The essential feature of normal freezing methods is the steady motion of a freezing solid-liquid interface along an ingot which is mounted either horizontally or vertically.

(i) Horizontal Normal Freezing

Horizontal NF methods are commonly referred to as the horizontal Bridgman or Chalmer's technique. The charge is contained in a boat which is placed within a horizontal furnace tube which can be filled with the required ambient gas (or evacuated). A muffle furnace is placed around the tube and serves to melt the charge. Directional solidification is obtained by slowly withdrawing the boat from within the furnace (or moving the furnace away from the boat). This method is used for growing large crystals of corundum, GaAs, yttrium aluminium garnet etc.

(ii) Vertical Bridgman-Stockbarger Method

In this method, the compound is melted by raising the temperature above the melting point in a vertically mounted crucible inside a vertical furnace. The crucible is then slowly, lowered with respect to the temperature profile, so that the melt could be frozen from the tip and

one crystal remains which increases in size until it fully occupies the cross section of the container.

This method is not commonly used to obtain metallic, organic and a number of dielectric single crystals such as oxides, fluorides, sulphides and halides. Single crystals of sapphire (Al_2O_3) can be grown by this method. Crystals of Te doped GaSb [39] and SnSe_2 [40] were grown by this method. Materials which expand on solidification cannot be grown by this method.

(iii) Czochralski Method

For growth of crystals using this method the charge material is melted in a crucible. A pull rod with a chuck containing a seed crystal at its lower end is positioned above the crucible. The seed crystal is dipped into the melt whose temperature is adjusted until a meniscus can be supported by the seed crystal. The pull rod is then slowly lifted and rotated and by carefully adjusting the power supplied to the crucible, a crystal of the desired diameter can be produced.

Czochralski method has gained wide recognition particularly in growing single crystals of silicon [41] and other materials [42-44].

(iv) Kyropoulos Method

In the Kyropoulos method, crystal growth is achieved by gradually reducing the melt temperature with the aid of a special cooler. Either spontaneous nucleation or crystallization on a seed is possible. This method is used in growing crystals of fluorides, chlorides etc. and single crystals of corundum.

(v) Verneuil Method

In this method, a small amount of material is melted on top of a ceramic pedestal by means of an oxy-hydrogen flame. Crystallization occurs by the withdrawal (and simultaneous rotation) of the pedestal from the hot zone. This method is used for the growth of single crystals of ruby, sapphire, aluminium-magnesium spinel (MgAl_2O_4), rutile (TiO_2), yttrium oxide (Y_2O_3) etc.

(b) Zone Melting

Zone melting is conducted with a small melt volume. It is the generic name of a family of methods for purifying elements and compounds and for preparing materials of desired composition [45]. In these methods, a short liquid region or zone travels slowly through a

relatively long charge or ingot of solid. As the zone travels, it redistributes impurities along the charge. The final distribution depends on the impurity distribution in the starting charge, on the distribution coefficient k of an impurity between the liquid and solid of the charge material and on the size, number and travel direction of the zones. The distribution of impurities is of the form,

$$C_s = C_o \{ 1 - (1-k_o) \exp (-k_o x/L) \} \quad (1.43)$$

where L is the zone length parallel to the direction of zone motion. The detailed theoretical treatments of the distribution of impurities is discussed in [46].

(i) Zoning in a Container

For attaining a sharp zone boundary and a short zone, it is necessary to have a container with a good lateral heat transfer and a poor longitudinal heat transfer. So the walls of the container must be as thin as possible. The cross-section of the container is designed in such a way that the charge has a minimum surface contact with the container. The longitudinal shape of the charge and container is determined by the total length of the ingot. Radial, helical and spiral models have been

described by Pfann [47]. The molten zone should preferably have a constant length, a stable solid-liquid interface and a well defined thermal gradient. For materials having low thermal conductivities, the zone width tends to vary. This has been overcome by slowly rotating the container about its axis. Sahoo et al. [48] have grown $\text{Hg}_{1-x}\text{Cd}_x\text{Te}$ ($x=0.2$) crystal ingots by zone melting. They have designed the ampoule to a special shape to have a stable hot zone configuration and temperature profile of the furnace was programmed during the zone melting to maintain the zone length nearly constant.

(ii) Zone Refining without Containers

The zone melting method can also be carried out with the ingot in the vertical direction. In this technique by Keck and Golay [49], a molten zone is maintained between a vertically mounted seed crystal and a charge rod by surface tension forces. This technique doesn't require a crucible, the melt is in contact only with its own solid. This is used for the production of oxygen-free silicon single crystals and for single crystals of refractory metals.

1.3.3 Growth from Solution

Single crystals of materials which melt incongruently, decompose before melting or undergo a phase transformation between the melting point and room temperature are grown from solution. Advantage of solution growth is that it requires lower temperatures and can lead to a lower density of lattice defects. In this method, a saturated solution is prepared in a suitable solvent and crystallization is initiated by slow cooling of the solution or slow evaporation of the solvent. The classification of methods employed for solution growth is given by Bardsley [50]. Large and perfect crystals of industrially important crystals like potassium dihydrogen phosphate [51] and diglycine sulphate [52] are grown by this method.

1.4 REFERENCES

- [1] J.W.Gibbs, *Collected Works*, (Longman's Green and Co., London 1878), p.325.
- [2] P.Curie, *Bull. Soc. Franc. Miner.*, 8 (1885) 145.
- [3] G.Wulff and *Z.Kristallogr*, 34 (1901) 449.
- [4] A.Bravais and *A.Etudes, Crystallographiques*, (Gauthier Villars, Paris, 1866).
- [5] J.D.Donnay and D.Harker, *Amer. Min.* 22 (1937) 446.
- [6] L.Soehncke, *Entwicklung einer theorie d. krystallstruktur*, (Leipzig, 1879).
- [7] H.E.Buckley, *Crystal Growth* (Wiley, New York, 1958).
- [8] W.Kossel, *Nachr. Ges. Wiss. Gottingen. Math. Physik.* K1 11A (1927) 135.
- [9] I.N.Stranski, *Z. Phys. Chem.* 136 (1928) 259.
- [10] M.Volmer, *Kinetic der phasenbildung* (Steinkopff Dresden and Leipzig, 1939).

- [11] W.K.Burton, N.Cabrera and F.C.Frank, Phil. Trans. Roy. Soc. A243 (1951) 299.
- [12] R.Becker and W.Doring, Ann. Phys. 24 (1937) 719.
- [13] F.C.Frank, J. Cryst. Growth, 13/14 (1972) 154.
- [14] F.C.Frank, Disc. Faraday Soc. 5 (1949) 48.
- [15] A.R.Verma, Crystal Growth and Dislocations (Butterworths, London, 1953).
- [16] S.Amelinckx, Solid State Physics, Supplement, Vol.6 (Academic Press, 1964).
- [17] M.M.Faktor and I.Garrett, Growth of crystals from the vapour (Chapman and Hall, London, 1974).
- [18] C.H.L.Goodman, Crystal Growth, Theory and Techniques, Vol.1 (Plenum Press, London, 1974).
- [19] L.Holland, Vacuum deposition of thin films, (Chapman and Hall, London, 1956).

- [20] P.Archibald, E.Parent, Solid State Technol. 19 (1976) 32.
- [21] L.I.Maissel, Physics of thin films, Vol.3, eds. G.Hass and R.E.Thun (Academic Press, New York, 1966) p.61.
- [22] E.E.Anderson, H.Y.Cheng and M.J.Edgell, Optical Materials: Processing and Science, Symposium, San Diego, USA, 1989.
- [23] H.Y.Cheng and E.E.Anderson, J. Cryst. Growth, 96 (1989) 756.
- [24] C.H.Su, S.L.Lehoczky and F.R.Szofran, J. Cryst. Growth, 101 (1990) 221.
- [25] E.Kaldis and R.Widmer, J. Phys. Chem. Solids. 26 (1965) 1697.
- [26] W.W.Piper and S.J.Polich, J. Appl. Phys. 32 (1961) 1278.
- [27] F.P.Banmgartner, M.L.Sterner and E.Bucher, J. Electron. Mater. 19 (1990) 777.

- [28] R.M.Biefield and G.A.Hebner, *Appl. Phys. Lett.* **57** (1990) 1563.
- [29] K.Balakrishnan, B.Vengatesan, N.Kanniah and P.Ramasamy, *Cryst. Res. Technol.* **25** (1990) 633.
- [30] C.Kloc, M.C.Lux-Steiner, M.Keil, J.R.Baumann, G.Doll and E.Bucher, *J. Cryst. Growth.* **106** (1990) 635.
- [31] O.Bertrand, N.Floquet and D.Jacquot, *J. Cryst. Growth.* **96** (1989) 708.
- [32] J.Mercier, *J. Cryst. Growth*, **56** (1982) 235.
- [33] H.C.Theuerer, *J. Electro Chem. Soc.* **108** (1961) 649.
- [34] J.Bloem and L.J.Gilling, *Current Topicsⁱⁿ Mat. Sci.*, Vol.1 (North-Holland, Amsterdam, 1978) p.147.
- [35] D.C.Gupta, *Solid State Technol.*, **14** (1978) 33.
- [36] M.L.Hammond, *Solid State Technol.*, **21** (1978) 68.
- [37] D.R.H.Jones and G.A.Chadwick, *Philog. Mag.* **24** (1971) 995.

- [38] K.A.Jackson and B.Chalmers, *Can. J. Phys.* 34 (1956) 473.
- [39] U.N.Roy and S.Basu, *Indian J. Phys. A.* 63A (1989) 467.
- [40] V.P.Bhatt, K.Gireesan and G.R.Pandya, *J. Cryst. Growth.* 96 (1989) 649.
- [41] W.Zulehner, *Proceedings of the Sixth International Symposium on Silicon Materials Science and Technology. Semiconductor Silicon, 1990, Canada.*
- [42] M.Gospodinov and P.Sveshtarov, *Cryst. Res. Technol.* 25 (1990) K58.
- [43] A.Valcic, S.Nikolic and T.Valick, *Inf. Midem,* 19 (1989) 3.
- [44] S.K.Khanna and K.G.Rajan, *Bull Mater. Sci.* 8 (1986) 467.
- [45] W.G.Pfann, in *Crystal Growth and Characterization*, eds., R.Ueda and J.B.Mullin, (North-Holland Pub. Co., New York, 1975) p.53.

- [46] B.R.Pamplin, *Crystal Growth*, (Pergamon Press, New York, 1975).
- [47] W.G.Pfann, *Zone Melting*, (Wiley, New York, 1966).
- [48] D.Sahoo, R.Prasad, R.V.Srikantaiah and B.Ghosh, in: *Current Trends in Crystal Growth and Characterization*, ed. K.Byrappa (M.I.T. Associates Pvt. Ltd., Bangalore, 1991).
- [49] P.H.Keck and M.J.Golay, *Phys. Rev.* **89** (1953) 1297.
- [50] W.Bardsley, D.T.J.Hurle and J.B.Mullin, *Crystal Growth: A Tutorial Approach* (North-Holland Pub. Co., New York, 1979).
- [51] K.Orban, G.Partay, A.Lukacs, L.Vannay and J.Sarkozi, *Cryst. Res. Technol.* **24** (1989) 591.
- [52] G.R.Pandya and D.D.Vyas, *Cyrst. Res. Technol.* **21** (1986) 183.

2

MORPHOLOGY AND GROWTH
MECHANISM OF CRYSTALS

2.1 INTRODUCTION

Crystals exhibit a wide range of morphologies. The macroscopic form and structure exhibited by a crystal is its morphology. Surface morphology is not only an indicator of internal crystal perfection, but also it provides the link between this perfection and growth conditions. For a long time it is known from experiments that every crystal has a number of characteristic flat surfaces which extend parallel to themselves during growth. Besides this, a crystal possesses planes with a more or less clearly expressed stepped nature, while there are also planes which generally exist for a short duration, and are rounded. It has long been known that the interplanar angles of a crystal remains the same irrespective of the habit. The characteristic growth form of a crystal is the polyhedron in which the various planes are demarcated by edges. If the growth of such a polyhedral crystal is studied at constant external conditions, then it is found that after a particular time the crystal acquires a final form which remains unchanged with further growth. Such forms are called stationary or stable growth forms.

In this chapter, a brief description of morphology and growth mechanism of crystals is given. This section also outlines an account on whiskers, platelets, dendrites and spherulites.

2.2 MORPHOLOGY OF CRYSTALS

The classical treatment for the problem regarding the precise derivation of the crystal form made by Gibbs [1] is purely phenomenological. Gibbs and Curie defined the equilibrium form as that possessing minimum total surface energy for a given volume. The second approach developed by Stranski and Kaishev [2] is atomistic as it considers material exchange across the crystal/ambient phase interface on a microscope scale. According to this approach, the mechanism by which the equilibrium form of a crystal with its surroundings is maintained can be understood when the elementary evaporation and condensation processes on the crystal surface are considered. If the crystal structure and the interatomic distances are known, the equilibrium forms of large crystal can be deduced. The equilibrium form for a simple cubic lattice is cubic, which is the same result that found from the Gibbs-Wulff theorem.

The growth of crystals involves the formation of strong bonds between the crystalline units. The deposition of a growth unit at a kink site is more probable than at other positions, because at kink positions the unit is more strongly bonded to the crystal than at other sites. Hence the crystal is bounded by units that are parallel to the directions in which there is an uninterrupted chain of strong bonds between the building units. Such a chain is called a periodic bond chain (PBC) [3]. Layer growth is possible only when there exists strong bonds between PBCs. If the PBCs are not bonded, layer growth does not occur because the probability of deposition of a PBC is the same everywhere. For the Kossel crystal three types of faces can be visualized, namely (a) flat faces (F faces) containing two PBC vectors in a layer d_{hkl} , (b) stepped faces (S faces) containing only one PBC vector in a layer d_{hkl} and (c) kinked faces (K faces) containing no PBC in a layer d_{hkl} . The three types of faces have different growth mechanisms. F faces grow by a layer growth mechanism, are therefore slowly growing and hence are important faces. S faces grow by one-dimensional nucleation. K faces do not require nucleation and hence grow fast and are normally absent on crystal surfaces. The different nature of bonding

that exist in the various faces of a crystal thus promotes or prevents growth to give the crystal, the observed morphology.

Several authors have investigated the morphology of crystals grown from various methods [4-15]. Van der Voort[4] has studied the morphology of crystals grown from aqueous solutions. Wang et al. [5] have observed the surface morphology of Pb, Bi, Sr, Ca, Cu, O high T_c superconducting crystals grown by slow cooling method. The morphology of ADP and KDP crystals was studied by Rashkovich and Shekunov [6]. Kauda et al. [7] have reported the morphology of synthetic diamonds grown from Na_2CO_3 solution. Saito et al. [8] have observed the growth steps on the surface of the NaCl crystals by TEM with the aid of a decoration replica method. The study of surface morphology of vapour grown HgI_2 platelets was done by Szurgot and Laskowski [9]. Trumbore and Haar [10] have reported the morphological features of NbSe_3 and Nb_2Se_9 crystals. The morphology of melt grown bismuth germanate crystals has been investigated by Smet et al. [11]. Sangwal [12] has discussed the micromorphology of as-grown surfaces of single crystals. The growth features like elementary spirals,

macrospirals, hillocks of dislocations and non-dislocation origin, interlacing and slip patterns, macrosteps, inclusions, block structures, growth striations and impurity striations are described. The morphology of SnTe and PbTe crystals grown from the gas phase has been reported by Varshava et al. [13]. Banan et al. [14] grew single crystals of pure and doped TGS crystals and studied the morphology. Tomizuka et al. [15] have grown CuCl and CuBr crystals from the vapour phase and observed the morphological patterns.

2.2.1 The Kinetic Generation of Crystal Forms

(a) Whiskers

Whiskers have negligible dimensions compared to their length and hence are usually considered as filaments or fibres. Whiskers can be grown by the solid-solid transformation [16], from vapour [17], from solution [18] or by electromigration [19]. However, it is difficult to control the diameter and length of these crystals. The properties of whiskers have found to differ substantially from comparable bulk materials of the same composition, in particular with respect to their crystallization kinetics, defect structure and their mechanical behaviour. The interest in

whiskers has been aroused by many reasons. One of the particular features of interest is their fast growth along a basic crystallographic direction.

Again the morphological phenomenon of whisker growth is connected with the phenomenon of high mechanical strength. The unique properties of these near one dimensional crystals offer intriguing possibilities for a variety of optical, electronic and magnetic devices. The interest in the growth of whiskers is also related to the growth of small diameter crystals because for some applications small crystals are better than larger ones. These include their solidification behaviour, surface morphology and crystal defects. The morphology of whiskers has been found to depend upon the material, growth method and growth conditions. Nabarro and Jackson [20] have described different morphologies like straight whiskers, kinked whiskers, ribbon like squeeze whiskers, spiral whiskers and other complex forms grown from various elements and compounds. Many theories have been proposed to explain the growth of whiskers under a great variety of conditions. The earliest theory of whisker growth is that of Peach [21]. The process of whisker growth consists of the diffusion of vacancies along the cores of dislocations from the surface.

Frank [22] and Eshelby [23] have explained the growth of whiskers from the base assuming the presence of a hump on the surface of the substrate with a constraining collar at the base of a whisker. The dislocation model of Frank consists of a spiral dislocation at the base of the whisker with one end meeting the free surface and the other running as a screw into the main mass of the whisker. On the basis of direct observation of helical dislocations and the theories on the spiral prismatic dislocations, Amelinckx et al. [24] have developed a model for whisker growth. Theories were also developed for the whiskers growing at the tip. According to the theory of Frank [25], Sears [26] postulated that whiskers contain a screw dislocation emerging at the growing tip. Such an axial dislocation provides a preferred growth site and accounts for the unidirectional growth. The various observations of dislocation loops, spirals and helices show that the dislocation model is acceptable. However, the dislocation model for whisker growth is not concerned with impurities. The modification of growth by impurities provides possible mechanisms for producing whisker like profiles. Several authors have investigated the whisker growth of various substances [27-47].

The growth of dislocation free whiskers was also observed in various materials. In this case the axial dislocation is not essential. Wagner and Ellis [48] have put forward a new mechanism known as the vapour-liquid-solid (VLS) mechanism. Its main feature is that a liquid phase, in the form of a droplet of an alloy of the material is situated between the vapour and the growing crystal. The surface of the liquid alloy has a large accommodation coefficient and is therefore a preferred site for deposition. Silicon crystals were grown by this mechanism. The diameter of a whisker growing from the VLS mechanism depends on the diameter of the drop and therefore this mechanism can serve as a basis for controlled growth of whiskers. The V-L-S mechanism has been found to be operative in the case of several materials [49-52].

Different growth methods were employed to produce hollow whiskers by many authors and different interpretations have been suggested to explain the hollow morphology. Rectangular hollow needles of NbO_2 were grown by Cohen [53] using electrodeposition method from molten fluorides. Webb and Bertalone [54] have reported the growth of hollow CsCl whiskers. The growth of hollow KCl whiskers was reported by Yoshida [55]. Natarajan et al. [56] have investigated the

hollow morphology of solution grown triglycine sulphate-phosphate crystals. They have explained the formation of hollow crystals as due to the variation in diffusion of solute towards the edge and centre of the crystal. Maeda et al. [57] confined to the point that the growth mechanism of hollow crystals is a helicoidal growth from the place of the screw dislocation through a lamellar-like growth. Simov et al. [58] have made observations of hollow CdTe crystals with a scanning electron microscope. The morphology of hollow ZnS single crystals has been investigated by Lendvay and Kovacs [59]. Arivuoli et al. [60] have grown hollow SbSeBr crystals from vapour and reported that these whiskers join with the original needle on its lateral surfaces by two dimensional nucleation.

(b) Platelets

Vapour grown whiskers are often accompanied by plate-like or two dimensional crystals. In the case of platelets, growth is inhibited in one direction, whereas in whiskers, it is inhibited in two directions. Many investigators have noted a genetic relation between these crystalline forms [61,62]. Platelet growth results from the crystal structure of the material. There are compounds such as the chalcogenides of group III (GaS, GaSe etc.) and

dichalcogenides of group IV (SnS_2 , ZrSe_2 , TiTe_2 etc.) which have layer structures. Strong covalent bonds exist within the layers whereas weak van der Waals bonds exist between the layers. Accordingly these compounds tend to crystallize in platelet form. The formation of platelets depends on the crystallization conditions: temperature, supersaturation, impurities etc.

(c) Dendrites

For a great number of lattices, growth from vapour can occur easily without the need of source of steps. Any layered structure, for example, the hexagonal metals Zinc and Cadmium will grow under certain circumstances as very thin plates normal to the c-axis. The growing surfaces probably prism planes in the case of hexagonal metals appear to behave as nonsingular surfaces and as such do not seem to require source of steps for their growth. This type of growth is dendrite growth [63]. George and Premachandran [64] have reported the dendrite growth of phthalic anhydride crystals.

(d) Spherulites

Spherulites are spherically symmetric crystalline aggregates and are observed in minerals, polymers and other materials [20]. This macroscopic spherical symmetry is in

violation with the uniform packing of microscopic units. They radiate from a nucleus with the substructure of needles with small angle branchings to fill the area created by the outwardly increasing volume.

2.3 GROWTH MECHANISM OF CRYSTALS

The growth of a crystal results from the addition of new atoms, molecules or more complex aggregates. As indicated in chapter 1, thermal fluctuations ensure a certain density of kinks on steps and surfaces. On atomically smooth surfaces, kinks are possible because of the individual vacancies in the surface layer and at steps having a length of several interatomic distances, these steps making up the boundaries of vacancies or adatom micro-aggregates. The filling of vacancies and their aggregates in the surface layer leads to their disappearance. Adatom aggregates are built up by two dimensional nucleation. The growth of atomically smooth surfaces is called layer growth and requires the nucleation of new steps, for further growth of the crystal. The most comprehensive information on the kinetics and processes of layer growth is obtained by observing this growth directly in a microscope, but it is much simpler and hence more common to study the surface morphology of grown crystals.

A brief review on crystal growth mechanisms and kinetics has been given by Glicksman and Selleck [65]. Haldenwang [66] proposed a generalised model of crystal growth kinetics. The growth mechanism of lithium tetraborate crystals was explained by Robertson and Young [67]. Arivuoli et al. [68] have grown bismuth seleniodide single crystals from the vapour revealing a layer growth mechanism. Desai and Patel [69] have done microtopographic investigations of ferroelectric magnesium hydrogen phosphate single crystals and studied the growth mechanism involved. The morphological considerations on the growth mechanism of ZnO crystals were given by Kitano et al. [70]. The mechanism of growth of metallic copper whiskers has been discussed by Jha and Grievsen [71]. Kishan Rao and Prasad [72] have done a topographic study on anthracene crystals. Desai and Hanchinal [73] have grown single crystals of ammonium hydrogen tartrate. It was suggested that two dimensional nucleation, spreading and piling up of growth layers were mainly responsible for the growth of these crystals.

2.4 REFERENCES

- [1] J.W.Gibbs, Collected Works, (Longman's Green and Co. 1878) p.325.

- [2] I.N.Stranski and R.Kaischew, Z.Physik. Chem. 26B (1934) 100.

- [3] P.Hartman, Crystal Growth: An Introduction, (North Holland, 1973) p.367.

- [4] E.Van der Voort, J. Cryst. Growth 110 (1991) 662.

- [5] Y.Wang, P.Bennema, L.W.M.Schreurs, J.Wnuk and P.Van der Linden, Appl. Phys. A, Solids Surf. A52 (1991) 348.

- [6] L.N.Rashkovich and B.Yu Shekunov, J. Cryst. Growth, 100 (1990) 133.

- [7] H.Kauda, M.Akaishi and S.Yamaoka, J. Cryst. Growth, 106 (1990) 471.

- [8] Y.Saito, C.Kaito, K.Fujita and S.Maeda, J. Electron Microsc. 39 (1990) 11.

- [9] M.Szurgot and J.Laskowski, *Cryst. Res. Technol.* 25 (1990) 753.
- [10] F.A.Trumbore and L.W.ter Haar, *Chem. Mater.* 1 (1989) 490.
- [11] F.Smet, P.Bennema, J.P.V.d.Eerden and W.J.P.V.Enckevort, *J. Cryst. Growth* 97 (1989) 430.
- [12] K.Sangwal, *Prog. Cryst. Growth. Charact.* 19 (1989) 189.
- [13] S.S.Varshava, S.N.Bekesha, I.V.Kurilo and L.N.Pelekh, *Inorg. Mater.* 23 (1987) 1286.
- [14] M.Banon, A.K.Batra and R.B.Lal, *J. Mater. Sci. Lett.* 8 (1989) 1348.
- [15] A.Tomizuka, H.Iwanaga and N.Shibata, *J. Cryst. Growth*, 91 (1988) 27.
- [16] K.Nakahigashi and Y.Shimomura, *J. Cryst. Growth.* 28 (1975) 367.

- [17] I.Yamai and H.Saito, *J. Cryst. Growth*, 45 (1978) 511.
- [18] N.Zelinger, J. Flicstein and A.Zangvil, *J. Cryst. Growth*. 42 (1977) 253.
- [19] Y.Smooha and Y.Komem, *J. Cryst. Growth* 38 (1977) 149.
- [20] F.R.Nabarro and P.J.Jackson, in: *Growth and Perfection of Crystals*, Eds. R.H.Doremus, B.W.Roberts and D.Turnbull,(Wiley, New York, 1958).
- [21] M.O.Peach, *J. Appl. Phys.* 23 (1952) 1401.
- [22] F.C.Frank, *Philos. Mag.* 44 (1953) 854.
- [23] J.D.Eshelby, *Phys. Rev.* 91 (1953) 755.
- [24] S.Amelinckx, W.Botinck, W.Dekeyser and F.Seitz, *Philos. Mag.* 8 (1957) 355.
- [25] F.C.Frank, *Disc. Farad. Soc.* 5 (1949) 48.
- [26] G.W.Sears, *Acta. Metall.* 3 (1955) 361.

- [27] K.R.Karasek, S.A.Bradley, J.T.Donner, H.C.Yeh and J.L.Schienle, *J. Mater. Sci.* 26 (1991) 103.
- [28] I.Matsubara, T.Ogura, H.Tanigawa, H.Yamashita, M.Kinoshita and T.Kawai, *J. Cryst. Growth.* 110 (1991) 973.
- [29] K.Okada, H.Mutoh, N.Otsuka and T.Yano, *J. Mater. Sci. Lett.* 10 (1991) 588.
- [30] A.A.Shchetinin, O.D.Kozenkov, A.V.Gilyarovikii and E.E.Popova, *Inorg. Mater.* 25 (1989) 1045.
- [31] S.U.Goldenberg and O.D.Khlebnikov, *Sov. Phys. Solid State*, 32 (1990) 720.
- [32] Y.Fujiki, M.Watanabe, Y.Onoda, S.Yoshikado and T.Ohachi, *Nippon Seramikkusu Kyokai, Gakujutsu Ronbunshi*, 98 (1990) 1169.
- [33] V.F.Banar, D.V.Gitsu, I.Zasavitskii and G.V.Flusov, *Sov. J. Quantum Electron* 19 (1989) 441.
- [34] S.Oishi and M.Hirao, *J. Mater. Sci. Lett.* 8 (1989) 1397.

- [35] J.Homeny, L.J.Neergaard, K.R.Karasek, J.T.Donner and S.A.Bradley, *J. Am. Ceram. Soc.* 73 (1990) 102.
- [36] M.Fujii, H.Iwanaga and N.Shibata, *J. Cryst. Growth*, 99 (1990) 179.
- [37] S.Komatsu and Y.Moriyoshi, *J. Cryst. Growth*, 102 (1990) 899.
- [38] Y.Yan, J.Chen, L.Wang, Qi Li, D.Feng, Li Cao and C.Yao, *Mater. Lett.* 8 (1989) 305.
- [39] H.Iwanaga, A.Tomizuka, N.Shibata, T.Matsumoto, H.Katsuki and M.Egashira, *J. Cryst. Growth*, 83 (1987) 602.
- [40] S.Mansour and R.Scholz, *Mater. Lett.* 9 (1990) 511.
- [41] W.Guo, X.G.Ning, J.Zhu and H.Q.Ye, *J. Cryst. Growth* 106 (1990) 400.
- [42] H.Iwanaga, M.Egashira, K.Suzuki, M.Ichihara and S.Takeuchi, *J. Mater. Sci. Lett.* 8 (1989) 1179.

- [43] S.Oishi and M.Hirao, *J. Mater. Sci. Lett.* **8** (1989) 1397.
- [44] J.B.Li, G.Peng, S.R.Chen, Z.G.Chen and J.G.Wu, *J. Am. Ceram. Soc.* **73** (1990) 919.
- [45] H.Iwanaga, T.Iwasaki, S.Motojima and S.Takeuchi, *J. Mater. Sci. Lett.* **9** (1990) 731.
- [46] W.Guo, X.G.Ning, J.Zhu and H.Q.Ye, *J. Cryst. Growth* **106** (1990) 400.
- [47] H.Schachner, G.Horlville and P.Fontaine, *Colloq. Phys.* (1989) 219.
- [48] R.S.Wagner and W.C.Ellis, *Trans. Met. Soc. AIME*, **233** (1965) 1053.
- [49] Y.C.Zhou, X.Chang, J.Zhou and F.Xia, *Mater. Lett.* **10** (1990) 288.
- [50] R.Ganesh, D.Arivuoli and P.Ramasamy, *Cryst. Res. Technol.* **26** (1991) K60.

- [51] R.de Jong, R.A.Mc Cauley and P.Tambuysen, J. Am. Ceram. Soc. 70 (1987) 338.
- [52] S.Motojima, M.Hasegawa and T.Hattori, J. Cryst. Growth 87 (1988) 311.
- [53] U.Cohen, J. Cryst. Growth, 46 (1979) 147.
- [54] W.W.Webb and N.O.Bertalone, J. Appl. Phys. 31 (1960) 207.
- [55] K.Yoshida, Japan J. Appl. Phys. 3 (1964) 565.
- [56] V.Natarajan, C.Subramanian and P.Ramaswamy, J. Mater. Sci. Letts. 7 (1988) 511.
- [57] M.Maeda, F.Goto and K.Miyata, Japan J. Appl. Phys. 3 (1964) 426.
- [58] S.B.Simov, P.R.Kamadjev M.M.Gospodinov and V.F.Gantcheva, J.Cryst. Growth, 26 (1974) 294.
- [59] E.Lendvay and P.Kovacs, J. Cryst. Growth 7 (1970) 61.

- [60] D. Arivuoli, F.D. Gnanam and P.Ramasamy, J. Mater. Sci. Letts. 6 (1987) 249.
- [61] J. Chikawa and T. Nakayama, J. Appl. Phys. 35 (1964) 2493.
- [62] G.H. Diersen and T. Gabor, J. Cryst. Growth 16 (1972) 99.
- [63] J.J. Gilman, The Art and Science of Growing Crystals, (John Wiley, New York, 1963).
- [64] J. George and S.K. Premachandran, J. Cryst. Growth 41 (1977) 325.
- [65] M.E. Glicksman and M.E. Selleck, Mater. Res. Soc. (1987) 433.
- [66] P. Haldenwang, J. Cryst. Growth 96 (1989) 652.
- [67] D.S. Robertson and I.M. Young, J. Mater. Sci. 17 (1982) 1729.

- [68] D.Arivuoli, F.D.Gnanam and P.Ramasamy, J. Mater. Sci. 22 (1987) 981.
- [69] C.C.Desai and K.N.Patel, Cryst. Res. Technol. 24 (1984) 681.
- [70] M.Kitano, T.Hamabe, S.Maeda and T.Okabe, J. Cryst. Growth 108 (1991) 277.
- [71] A.Jha and P.Grieveson, J. Mater. Sci. 25 (1990) 2299.
- [72] K.Kishan Rao and P.B.V.Prasad, Cryst. Res. Technol. 24 (1989) K139.
- [73] C.C.Desai and A.N.Hanchinal, Cryst. Res. Technol. 22 (1987) 803.

3

DEFECTS IN
CRYSTALS

3.1 INTRODUCTION

Knowledge of the nature and distribution of defects in crystals is necessary because they (1) have deleterious effects on the performance of electronic devices, (2) affect plasticity and crystal strength, electronic and ionic conductivity and diffusion properties and (3) play an important role in crystal growth. Defects in a real crystal may be divided into chemical impurities and lattice defects. Lattice defects are point defects (Interstitials, vacancies, substitutions and antisites) line defects (dislocations), surface defects (grain boundaries, twin boundaries, stacking faults etc.) and volume defects (inclusions, precipitates and point-defect clusters).

The concept of dislocations has led to a more complete understanding of the physical behaviour of crystals and their properties and has provided a guiding principle for producing crystals of increasing perfection. The dislocation, as its name implies, is a geometrical fault or disturbance in the otherwise regular packing of the atoms. Since the amount of plastic deformation and the consequent generation of dislocations have a very significant effect on the semiconducting properties, it is

helpful to have an understanding of the basic types of dislocation and their movement, interaction and generation in the crystal. Etching is one of the widely used techniques to reveal dislocations in crystals. Although etching was first applied to dislocations, its domain has expanded to various other fields in defect studies.

The aim of this chapter is to provide a brief summary on the different types of defects in crystals. The various methods for the observation of dislocations are also presented.

3.2 DEFECTS IN CRYSTALS

3.2.1 Point Defects

All the atoms in a perfect lattice are at specific atomic sites. In a pure metal, two types of point defects are possible, namely a vacant atomic site or vacancy and an interstitial atom. The vacancy has been formed by the removal of an atom from an atomic site and the interstitial by the introduction of an atom into a non-lattice site. Intrinsic point defects are introduced into crystals by virtue of temperature for at all temperatures above 0 K, there is a thermodynamically stable concentration. The change in free energy ΔF associated with the introduction of n vacancies or interstitials in the lattice is,

$$\Delta F = nE_f - T\Delta S \quad (3.1)$$

where E_f is the energy of formation of one defect and ΔS is the change in entropy of the crystal. The equilibrium fraction of defects corresponding to a condition of minimum free energy is given by,

$$n_{eq} = n_t \exp\left(\frac{-E_f}{kT}\right) \quad (3.2)$$

where n_t is the total number of atomic sites and k is Boltzmann's constant. The rate at which a point defect moves from site to site in the lattice is proportional to $\exp(-E_m/kT)$, where E_m is the defect migration energy and is typically $\sim 0.1-1.0$ eV.

Impurity atoms in a crystal can be considered as extrinsic point defects and they play a very important role in the physical and mechanical properties of whole materials. Impurity atoms can take up two different types of site: (a) substitutional, in which an atom of the parent lattice lying in a lattice site is replaced by the impurity atom, and (b) interstitial in which the impurity atom is a non-lattice site. All the point defects mentioned produce a local distortion in the perfect lattice. The amount of distortion and hence the amount of additional energy in the

lattice due to the defects depends on the amount of space between the atoms in the lattice and the size of the atoms introduced. Additional effects are important when the removal or addition of atoms changes the local electric charge in the lattice. Vacancies can occur either (a) in pairs of opposite sign, forming divacancies known as Schottky defects or (b) in association with interstitials, Frenkel defects.

3.2.2 Grain Boundaries

Crystalline solids usually consist of a large number of randomly oriented grains separated by grain boundaries. Each grain is a single crystal and contains defects. When the misorientation between the grains is small, the boundary consists of an array of dislocations and is called a low angle boundary. However, when the misorientation is large, the atomic arrangement at the boundary is more complicated and varies significantly with the angle of misorientation. The geometry of two misoriented grains result in an array of edge dislocations. The relation between the misorientation θ and the spacing between individual dislocations D is,

$$D = \frac{b}{\theta} \quad (3.3)$$

where b is the magnitude of the burgers vector of the dislocations.

From the known elastic stress field around a dislocation, the grain boundary energy E per unit area varies with the orientation difference is given by the formula,

$$E = E_0 \theta [A - \ln \theta] \quad (3.4)$$

where E_0 and E are independent of θ . The parameter E_0 depends only on the elastic distortion and the parameter A depends on the non-elastic core energy of the dislocation. Equation (3.4) is the only energy relation that follows directly from the properties of a known array of dislocations without any additional assumptions which could be altered to fit the experimental results.

The relationship between the structure and strength of grain boundaries in Silicon bicrystals with $\langle 111 \rangle$ twist misorientations was determined by Sato et al. [1]. Frost [2] has developed a model to explain the grain boundary structure in Ni_3Al . The atomic structure of grain

boundaries in semiconductors was studied by Bourret and Bacmann [3] by electron microscopic observations.

3.2.3 Twin Boundaries

Deformation twinning is a process in which a region of a crystal undergoes a homogeneous shear that produces the original crystal structure in a new orientation. In the simplest cases, this results in the atoms of the original crystal (parent) and those of the product crystal (twin) being mirror image of each other by reflection in composition plane. The process differs from slip in which there is no rotation of the lattice. Deformation twinning can be induced by plastic deformation and is particularly important in body-centred cubic and close-packed hexagonal metals and many non-metallic crystals. When a growing twin meets a flat surface it will produce a well-defined tilt, and this can readily be detected in an optical microscope.

3.2.4 Stacking Faults

A stacking fault is a planar defect and it is a local region in the crystal where the regular sequence has been interrupted. Stacking faults are not expected in planes with ABABAB ... sequences in body centered or face-

centered cubic lattices because there is not alternative site for an A layer resting on a B layer. However, for ABCABC ... or ABABAB ... stacking of the close-packed planes in close-packed structures there are two possible positions of one layer resting on another.

A stacking fault ending within the crystal is always bordered by a partial dislocation. Along a partial dislocation, nearest neighbour relations are violated, the maximum misfit energy per atom is higher than for a fault and lower than for a total dislocation. Since a stacking fault has to lie in one plane, the partial dislocation must also lie in that plane. A partial dislocation whose Burgers vector lies in the plane of the fault is called a Shockley partial. The Shockley partial is one of the three types of partial dislocations associated with plane faults in fcc. The other two are Frank partial dislocations. A partial whose Burgers vector is not parallel to the fault is a Frank partial dislocation. There are two kinds of Frank partials in fcc; they differ in the sign of the Burgers vector $\pm n$. A negative Frank partial is formed when a part of a plane has been removed. If the inserted plane ends inside the crystal, its boundary is a positive Frank partial.

3.2.5 Volume Defects

Crystal defects such as precipitates, voids and bubbles can occur under certain circumstances and have important effects on the properties of crystalline solids.

3.2.6 Dislocations

(a) Geometry of Dislocations

Dislocations may be considered to have, in general, two components, an edge component and a screw component. Fig.3.1 represents the geometry of an edge dislocation. The pure edge dislocation may be thought of as the edge of an extra half plane of atoms inserted in the crystal. The terminal atoms of the half plane have fewer nearest neighbours than the rest of atoms and are positioned along the dislocation line. Edge dislocations are called positive when the extra plane of atoms is above the slip plane and negative when it is below.

A screw dislocation can be visualized as being produced by taking a sharp cut part away through the crystal and shearing it one inter-atomic spacing parallel to the cut (Fig.3.2). The important feature of this operation is that it transforms successive atomic planes into a single spiral surface, all along the line of

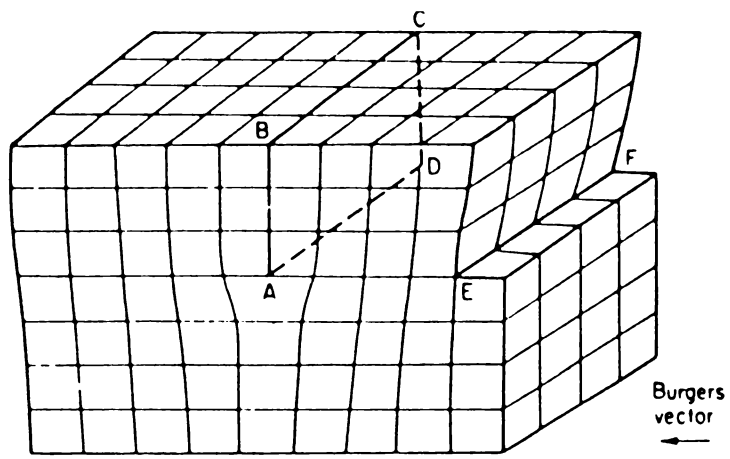


Fig. 3.1

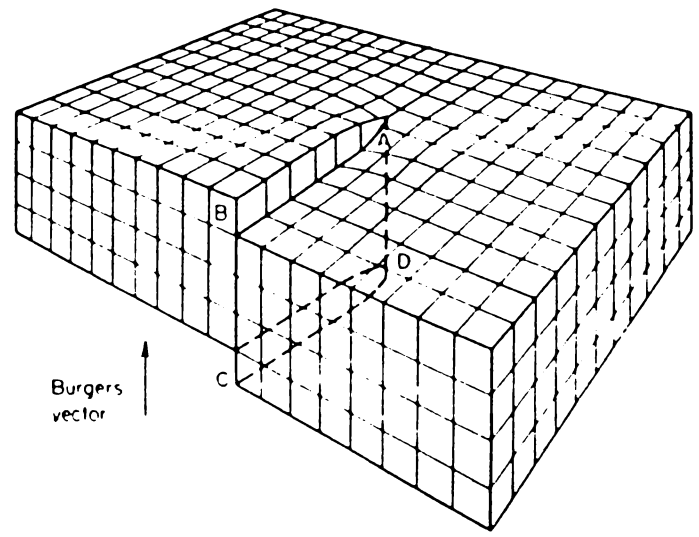


Fig. 3.2

distortion without a specific slip plane. Screw dislocation can have either right handed or left handed pitch; dislocations of the same pitch repel each other, whereas those of opposite pitch attract each other.

An excellent account of the theoretical and experimental study of dislocations has been given by Cottrell [4], Read [5], Friedel [6], Hull [7], Kovacs and Zsoldes [8] and Nabarro [9]. Takeuchi [10] has described the fundamental aspects of dislocations, such as the elastic strain field, self energy, line tension and line mass.

(b) Burgers Vector and Burgers Circuit

A Burgers circuit is any atom-to-atom path taken in a crystal containing dislocations which forms a closed loop. In the presence of a dislocation, the path of the line corresponding to the circuit does not form a closed loop. The vector required to complete the circuit is called the Burgers vector. The Burger vector of an edge dislocation is normal to the line of the dislocation and that of a screw dislocation is parallel to the line of the dislocation. Dislocation lines can end at the surface of a

crystal and at grain boundaries, but never inside a crystal. Thus dislocations must either form closed loops or branch into other dislocations.

(c) Energy Associated with Dislocations

To estimate the energy of a crystal, consider a cylindrical crystal of length l and radius r with a screw dislocation of burger vector b along its axis [4]. The strain energy density or work per unit volume is,

$$U = \frac{1}{2} G \epsilon^2 \quad (3.5)$$

where G is the shear modulus and ϵ the deformation.

Substituting $\epsilon = b/(2\pi r)$

$$u = \frac{1}{2} G (b/2\pi r)^2 \quad (3.6)$$

Since for a section of a cylinder of thickness δr the unit volume is equal to $2\pi r l \delta r$, the complete deformation energy per unit length for a screw dislocation is given by,

$$E_{\text{disl}}(\text{screw}) = l \int_{r_0}^r u 2\pi r l dr = \frac{Gb^2}{4\pi} \ln \frac{r}{r_0} \quad (3.7)$$

where r_0 is the radius of the central core. Similarly for edge dislocation, it is shown that,

$$E_{\text{disl}}(\text{Edge}) = \frac{Gb^2}{4\pi(1-\nu)} \ln \frac{r}{r_0} \quad (3.8)$$

where ν is Poisson's ratio.

(d) Dislocation reactions

A dislocation can interact with one another to form a single dislocation. Such interactions of dislocations are called dislocation reactions. This unification does not take place along the whole length of the dislocation line but may result in nodes. The Franks law of conservation of Burgers vectors states that the sum of Burgers vectors flowing into the node is equal to the sum of Burgers vectors flowing out of the node. Taking an approximation that the energy per unit length of the dislocation line is directly proportional to the square of the Burgers vector, the criterion for the combination of two dislocations may be written as,

$$b_1^2 + b_2^2 > b_3^2 \quad (3.9)$$

where b_1 and b_2 are the Burgers vectors of the two dislocations combining to form a dislocation of strength

b_3 . Similarly a dislocation of Burgers vector b_1 may dissociate into two dislocations, b_2 and b_3 if,

$$b_1^2 > b_2^2 + b_3^2 \quad (3.10)$$

(e) Plastic Deformation

The plastic deformation in a crystal occurs by the atomic planes sliding over each other. The displacement takes place along specific planes called slip planes and specific directions called slip directions. The slip plane is normally the plane with the highest density of atoms and the direction of slip is the direction in the slip plane in which the atoms are most closely spaced. A slip plane and slip direction in the plane constitutes a slip system. Slip results in the formation of steps on the surface of the system.

The shearing force required to move the top row of atoms across the bottom row in a crystal is given by a sinusoidal relation as,

$$\tau = \frac{Gb}{2\pi a} \sin 2\pi x/b \quad (3.11)$$

where τ is the applied shear stress, G is the shear modulus, b the spacing between atoms in the direction of

the shear stress, a the spacing of the rows of atoms and x is the shear translation of the two rows away from the low-energy equilibrium position. The maximum value of τ is called the theoretical critical shear stress, which is given by,

$$\tau_{th} = \frac{b}{a} \frac{G}{2\pi} \quad (3.12)$$

The edge dislocations and screw dislocations present in the crystal can move under low stresses and will cause slip resulting in traces with a step height equal to the Burgers vector. Kirpichnikova et al. [11] have investigated the plastic deformation of crystals of $(CH_3)_2NH_2Al(SO_4)_2 \cdot 6H_2O$. The study on plastic deformation of zinc single crystals was carried out by Zagoruiko and Soldatov [12].

(f) Movement of Dislocations

There are two types of dislocation movement, glide or conservative motion in which the dislocation moves in the surface which contains both its line and Burgers vector and climb or non-conservative motion in which the dislocation moves out of the glide surface normal to the Burgers vector. Glide of many dislocations results in slip in crystalline solids.

Screw dislocations tend to move from one type of planes to another. This process is known as cross-slip. When the Burgers vector is not in the plane of the loop, the slip surface defined by the dislocation line and its Burgers vector is a cylindrical surface. The dislocation is called prismatic dislocation.

The glide force F on a unit length of dislocation is defined as the work done when unit length of dislocation moves unit distance,

$$F = \tau b \quad (3.13)$$

The stress τ is the shear stress in the glide plane resolved in the direction of b and the glide force F acts normal to the dislocation at every point along its length.

(g) Multiplication of Dislocations

Crystals subjected to deformation often acquire an increasing number of dislocations. The very large number of dislocations necessary to explain the plastic deformation must be generated from sources within the crystal. A possible mechanism for the continuous generation of dislocations in the course of their movement was first

proposed by Frank and Read [13] and this has been the basis of all later ideas. According to this mechanism, dislocations are generated as a result of the movement of the edge segment of the dislocation fixed at one or two ends. Such a fixed dislocation is called a Frank-Read source.

When the slip surface is sharply bent, the sharp bend in the dislocation permits the dislocation to produce a very large amount of slip on a single slip plane. This slip mechanism called the Frank-Read mechanism explains that, in typical crystals, slip is not homogeneous, but is concentrated on a relatively few active slip planes which slip by many atomic spacings [5]. The following part describes how Frank-Read mechanism can produce new closed loops of dislocation. The basic mechanism for the formation of dislocation loop requires a section of dislocation that lies in a slip plane and leaves that plane at a point in the interior of the crystal.

Multiplication of dislocations by means of a Frank-Read source is demonstrated in Fig.3.3. The source consists of section DD' of the dislocation line which is fixed at both ends. The plane of the figure corresponds to the slip plane. The applied shear stress τ produces a

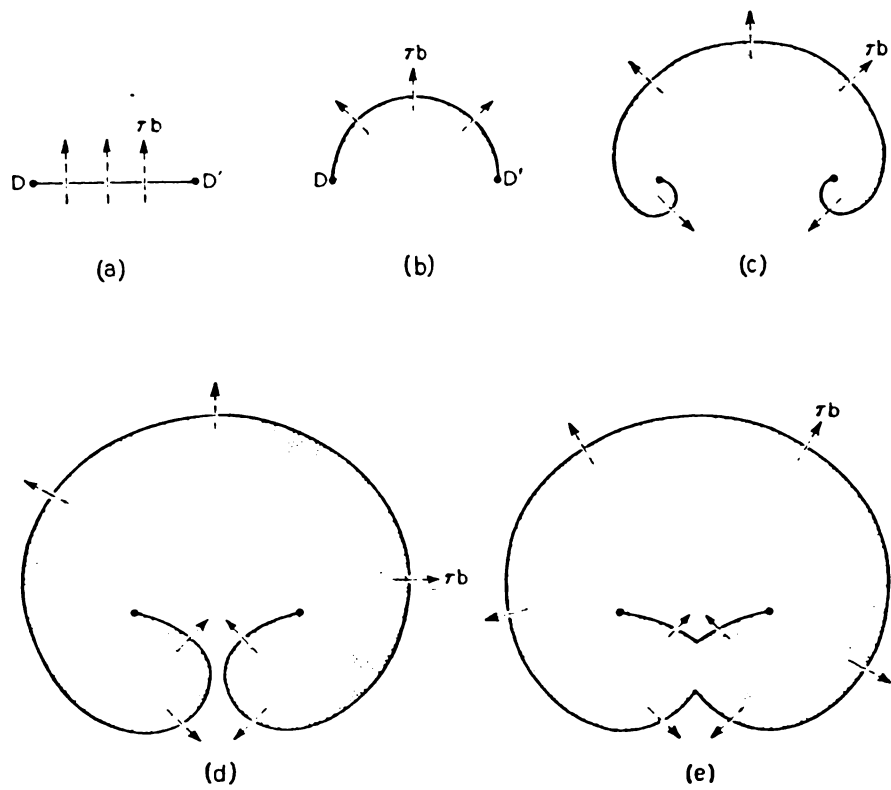


Fig. 3.3

normal force on the dislocation and tends to make it bow out. The radius of curvature R depends on the stress according to the equation,

$$\tau_0 = T/bR \quad (3.14)$$

where T is the line tension of the dislocation segment and is defined as the increase in energy per unit increase in the length of a dislocation line,

$$T = \alpha gb^2 \quad (3.15)$$

substituting for T in eq.(3.14), the expression for the stress required to bend a dislocation to a radius R is,

$$\tau_0 = \frac{\alpha Gb}{R} \quad (3.16)$$

Thus as τ increases, R decreases and the line bows out until the minimum value of R is reached at the position illustrated in Fig.3.3(b). Here R equals $L/2$ where L is the length of DD' and with $\alpha = 0.5$, the stress is,

$$T_{\max} = Gb/L \quad (3.17)$$

If the stress is raised about this critical value corresponding to the semicircular form, then the dislocation

becomes statistically unstable and expands indefinitely. The subsequent events are shown in Fig.3.3(c)-(e). In the final stage, the two parts of slipped area annihilate on meeting. The result is a large closed loop of dislocation, which continues to expand and repeats the same process all over again. Dash [14] observed Frank-Read sources in silicon crystals using decoration technique. Frank-Read sources were also found experimentally in potassium chloride, stainless steel and cadmium [15].

When one end of the dislocation segment is anchored in the interior of the crystal while the other end emerges at the surface, a Frank-Read spiral is formed. Fig.3.4 shows seven successive stages in the development of a spiral, whose operation involves the same principle as that of the Frank-Read source.

(h) Cleavage

Fracture (cleaving) is accompanied by the formation of two free surfaces which requires considerable energy expenditure. Therefore, it cannot be produced instantly over a large surface. It must propagate from one point to another under the form of a crack starting from an initial localized nucleus. Cleaving can be regarded as a

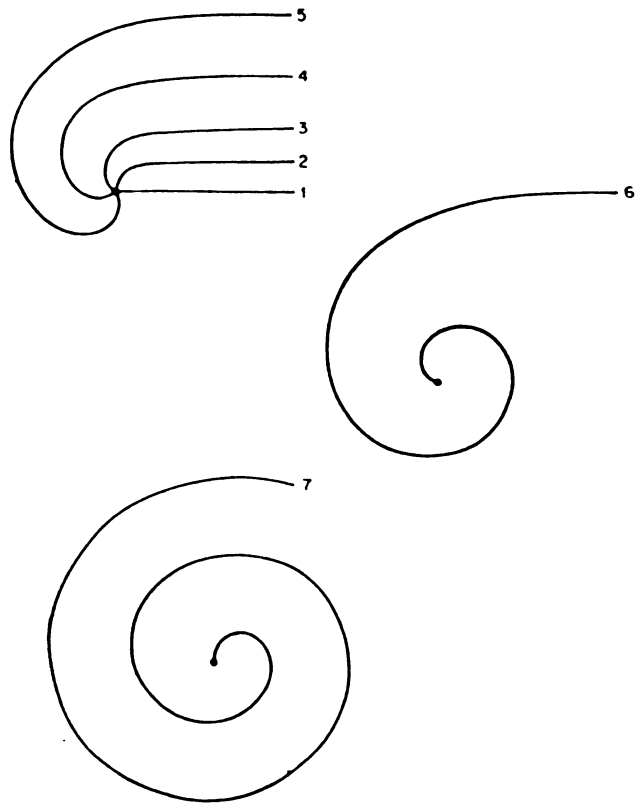


Fig. 3.4

process as a result of which crack edge move apart to an approximately, interatomic distance. The crack dislocations are obviously piled up at the tip of the crack in a way analogous to slipping dislocations piled up in a slip line or twinning dislocations in a twin lamella. Thus the cleavage process can be described satisfactorily in terms of dislocations. The cleavage planes are characterized by the minimum cohesion in the direction perpendicular to them and are seem to be well defined and close packed crystallographic planes. Cleavage probably prefers these planes because they have a definite smaller surface energy. The analysis of fracture surfaces has been carried out by several authors [16-18]. The cleavage steps often converge to form river patterns. It is interesting to note that the rivers run in the direction the crack propogates. A quantitative analysis of river formation for slowly moving cracks was given by Friedel [6].

The specific energy of the surface formed on cleaving is equal to

$$2\gamma \sim Gb/5 \quad (3.18)$$

where G is the shear modulus.

Moving apart of the edges of a nucleus crack requires a tensile stress,

$$\sigma \sim 2\gamma/b = G/5 \quad (3.19)$$

This is a very high stress which exceeds even the theoretical ultimate shear strength ($G/10$). The substantial role of the crack size was first pointed out by Griffith [19]. He considered stress σ_m at the ends of a flat ellipsoidal crack of diameter L in the field of tensile stress σ perpendicular to the crack. This stress is equal to,

$$\sigma_m = \sigma \sqrt{L/r} \quad (3.20)$$

where r is the distance to the end of the crack beyond its limits. If L is not too small then at a distance of the order of several interatomic distances from the end of the crack, σ_m may be about 100 times higher than the applied stress and thus reach the theoretical value of the strength. Then the crack will grow.

The critical size of a crack capable of widening at a given stress is expressed as,

$$L = \frac{2\gamma G}{\alpha(1-\nu)\sigma^2} \quad (3.21)$$

where α is a numerical factor of order unity. This equation gives the Griffith criterion for crack propagation.

Plastic strain may not only accompany fracture but also cause crack nucleation if the deformation of crystals is non-uniform. There are a variety of mechanisms of crack formation in plastic deformation. Dislocation pile-ups and twin intersections are the major sources for crack formation.

(i) Observation of Dislocation

A wide range of techniques has been used to study the distribution, arrangement and density of dislocations and to determine their properties. Amelinckx [20] has reviewed the methods of direct observations of dislocations. The techniques can be divided into five main groups: (1) surface methods in which the point of emergence of a dislocation at the surface of a crystal is revealed. (2) Decoration methods in which dislocations in bulk specimens transparent to light are decorated with precipitate particles to show up their position (3) Transmission electron microscopy, in which the dislocations are studied at very high magnification in specimens 0.1 to

4.0 μm thick. (4) X-ray diffraction in which local differences in the scattering of X-rays are used to show up the dislocations. (5) Field ion microscopy, which reveals the position of individual atoms. Of the various methods, etching is the simplest method for the detection and characterization of crystal defects such as grain boundaries, slip lines, dislocations, stacking faults and vacancies. A brief discussion of this method is given in the next section.

3.3 ETCHING OF CRYSTALS

Although a number of general principles have been formulated over the years, etching techniques are still based on a qualitative and empirical basis. The first direct proof of the applicability of etching to reveal dislocations was given by Gevers et al. [21] and Horn [22]. Etch pits located at the centres of spirals are attributed to screw dislocations and those located elsewhere are attributed to edge dislocations.

The method of etching consists in immersing the crystal in a suitable medium which may be a pure liquid, a solution or a gas. Small pits nucleate and grow at the emergence points of dislocations. Dislocation etchants are

different for specific crystals and there is no rule to find out the dislocation etchant for a specific crystal. There are different methods of etching. They are chemical etching, thermal etching, solution etching, preferential oxidation, electrolytic etching, cathodic sputtering and hydrothermal etching [23].

3.3.1 Chemical Etching

The usefulness of the chemical etching technique lies in the formation of visible, sharp, contrasting etchpits at dislocation sites. Different theories of dissolution exist in the literature which may be used to explain the etching phenomenon. Nucleation of etchpits at dislocations has been attributed to the elastic strain associated with the dislocations which causes a decrease in the activation energy for nucleation [24]. Though the elastic strain is known to promote localised etching [25], the role of it in the formation of etch pits at dislocation sites is questionable. The screw dislocations have shear stress fields which vanishes at the surface except at the core, whereas strain energy associated with an edge dislocation is retained at the surface and extends to a considerable distance beyond the core.

It has been proposed that the dislocation core energy is primarily responsible for the formation of etchpits [26]. Some of the arguments are: (a) It is difficult to reveal dislocations in metals than in covalent or ionic crystals; the core energy of dislocations in metals is less than in other types of materials while the elastic strain energy associated with dislocations is about the same in all materials. (b) The stress fields of dislocations close to each other tend to cancel out particularly when dislocations form a tilt boundary; thus isolated dislocations should etch faster than those close together if their elastic energies affected significantly the etching process. However, all dislocations in a given crystal etch at approximately the same rates. (c) In compounds with zinc blende structure the positive and negative dislocations etch differently although their strain fields are identical. Sangwal [23] has provided a comprehensive account of the different types of theories.

When a dissolution nucleus forms on the surface, there occurs a change in the free energy $\Delta G_p = \Delta G_s + \Delta G_v$, where ΔG_s is the change in surface energy and ΔG_v the change in the volume energy. Analogous to the free energy change involved in the formation of a two-dimensional

growth nucleus, the change in the free energy corresponding to the formation of a circular etch pit of height h and radius r may be given by,

$$\Delta G_p = \Delta G_s + \Delta G_v = 2\pi rh\gamma - \frac{\pi r^2 h \Delta\mu}{\Omega} \quad (3.22)$$

where γ is the edge free energy and Ω the volume occupied by each atom. The critical radius of the nucleus of an etch pit at particular thermodynamic conditions is stable.

(a) Reliability of Etchants

Etch pits can be formed by point defect clusters, precipitates (or impurity inclusions), surface damage, foreign particles etc. Etch pits which are not associated with dislocations usually do not reappear after repeated polishing and etching, as they are caused by shallow defects. Etch pits due to shallow dislocation loops disappear in pairs. Etch pits associated with individual dislocations on the other hand, reappear upon repeated polishing and etching, since the dislocations cannot terminate within the crystal. When cleavage is possible, the etch pit patterns should appear as mirror images on the cleaved surfaces. If crystals can be obtained in thin plates, a one-to-one correspondence of etch pits on opposite sides can be a proof for the reliability of an etchant.

Some etchants are capable of distinguishing between edge and screw dislocations [24]. The delineation of dislocations at grain boundaries and the ability to reveal fresh dislocations produced by scratching [27] or indentation [28] can also be taken as evidence that the etchant is capable of delineating the dislocations.

There are a number of useful tabulations in the literature of etchants and conditions for the formation of dislocation etch pits [23].

(b) Factors Affecting Etchpit Morphology

The factors of importance to chemical etching can be distinguished into those predominantly affecting the overall (macroscopic) rate of etching and into those affecting primarily the microscopic nature of etching i.e., the resulting microstructure of the surface.

In preferential etchants, the morphology of dislocation etch pits depends on orientation structure and on the angle at which the dislocation line intersects the surface. If the dislocation moves from its pit position during etching, as in the case of shallow dislocation half-

loops, or as a result of applied stress, then the bottom of the pit becomes flat and upon continued non-preferential etching, the pit is eliminated. The successful formation of an etchpit is influenced by the etching rates along the dislocation line, parallel to the surface and perpendicular to the surface. Depending upon the relative values of the etching rate, the morphology of pits will change. The morphology of etch pits depends strongly on the crystal structure [29].

Semiconductor surfaces, like all surfaces are susceptible to mechanical damage. Mechanical means of surface preparation, such as cutting, abrading, or even metallographic polishing lead to a damaged (cold-worked) surface layer, whose depth depends on the hardness of the material, the type and size of abrasive, the temperature and applied pressure. A ground surface differs from a polished surface in that the former has many shallow, piled-up dislocation loops, some misorientation and increased surface roughness. Etchpits may be formed by the dislocation and the geometry imposed by these may be propagated in changed form, well below the depth of the original defects.

A mechanically damaged surface etches more rapidly than an undamaged one [30-34]. The greater etch rate on the damaged surface has been attributed to the combined effect of increased surface area and dislocation density. The depth of the surface damage has been determined successfully in semiconductors by a number of methods, based on the increase in etching rate, the broadening of X-ray lines, the increase in recombination velocity of excess holes and electrons and the increase in surface electrical conductivity resulting from cold work. The effect of surface damage on the microstructure persists even after the damaged layer has been removed.

Impurities play significant part in controlling the etching behaviour. Both these impurities associated with the dislocations in the crystal and those present in the etchants will affect the etch pit formation. In the dissolution process, the presence of impurities in the etchant presumably reduces the flow of steps across the surface in a manner exactly analogous to the reverse of growth process, where it has been observed that certain poisons in the solution still impede the rate of crystal growth. The impurity will probably be adsorbed at the steps and more particularly at the kinks in them, and

therefore it will tend to protect them from chemical attack. The overall rate of dissolution of the crystal is thereby decreased and higher undersaturations can be maintained. Under such conditions, the tendency to form etch pits is increased. Gatos and Lavine [35] reported that the etch rate of B{111} surfaces of InSb is reduced by the addition of stearic acid and n-butylamine to oxidising etchants, but the much lower rate of A{111} surfaces remains practically unaffected.

The morphology is also influenced by the nature of dislocations and their relative orientations with the surface. Gilman et al. [36] have reported an etchant for LiF to distinguish between edge and screw dislocations. The relative orientation of dislocation with the surface affects the symmetry of pits. The dislocation if perpendicular to the surface will produce symmetrical pits while any deviation from it produce asymmetry [20]. If the dislocations are parallel

or almost parallel to the surface, etch grooves or pits elongated in the direction of dislocation will result [37]. Combined with other direct dislocation observation techniques such as electron microscopy, X-ray topography, decoration etc., etching has been successfully used for defect studies. Several authors have used chemical etching technique to study dislocations. Poria and Shah [38] have reported the reactivity at dislocations in bismuth using the etchants containing trifluoroacetic acid and trichloroacetic acid. Wermke et al. [39] observed low and high angle boundaries and lamellar twins on CdTe and (Cd, Zn)Te single crystal ingots using etching technique. The dislocations in InP have been revealed by Nishikawa et al. [40] using the solution containing HBr and C_2H_5OH . The etch pit study of different crystallographic faces of L-arginine phosphate (LAP) single crystals has been done by Rao et al. [41]. Charles and Gnanam [42] have carried out the dislocation studies of solution grown $NaSbF_4$ and $Na_3Sb_4F_{15}$ single crystals by chemical etching. The geometry of growth dislocations present in potassium bichromate crystals grown from aqueous solution has been reported by Szurgot [43]. Peter et al. [44] have reported the etch features in bismuth germanate single crystals. The structural imperfections of CdTe crystals grown from the vapour phase has been reported by Klinkova et al. [45].

3.3.2 Thermal Etching

When a crystal is heated at high temperature, evaporation of the surface in a manner reverse to growth takes place and frequently etch pits are formed. Thermal etch pits on arsenic [46] and antimony [47] were correlated with dislocations by chemical etching and by matching evaporated cleavage surfaces. A one-to-one correspondence of thermal etch pits with dislocations has also been reported in some works [48,49] but has not been found in others [50]. In some cases the thermal etch pits are formed at impurity-contaminated dislocations [49] or at impurity aggregates [50].

An interesting feature of thermal etch pits is that at low temperatures they ^{are} crystallographically oriented, but at temperatures close to the melting point of the crystals they are circular in morphology. The circular pits, like crystallographically oriented etch pits, are always terraced in the form of concentric rings originating from a source, but in some cases evaporation spirals are observed on the surface [51].

The mechanism of chemical-etch pit formation is also applicable for thermal etch pits. However, there is a

basic difference in thermal and chemical etch-pit formation. In thermal etching, transport of the evaporated material is only away from the surface. Thus thermal etching can, at the maximum, be controlled by the volume diffusion of the evaporated material when evaporation is carried out in some gaseous atmosphere.

3.4 FIGURE CAPTIONS

Fig.3.1: An edge dislocation in a simple cubic lattice.

Fig.3.2: A screw dislocation in a simple cubic lattice.

Fig.3.3: Diagrammatic representation of the dislocation movement in the Frank-Read source.

Fig.3.4: Seven successive stages in the development of a spiral. The plane of the figure is the slip plane.

3.5 REFERENCES

- [1] K.Sato, H.Miyazaki, Y.Ikuhara, H.Kurishita and H.Yoshinaga, Mater. Trans. JIM. 31(1990) 865.
- [2] H.J.Frost, Acta Metall. 36 (1988) 2199.
- [3] A.Bourret and J.J.Bacmann, Rev. Phys. Appl. 22 (1987) 563.
- [4] A.H.Cottrell, Dislocations and Plastic Flow in Crystals (Oxford University Press, Oxford, 1953).
- [5] W.T.Read, Dislocations in Crystals (Wiely, New York, 1953).
- [6] J.Friedel, Dislocations (Pergamon Press, London, 1964).
- [7] D.Hull and D.J.Bacon, Introduction to Dislocations (Pergamon Press, New York, 1984).
- [8] I.Kovacs and L.Zsoldos, Dislocations and Plastic Deformation (Pergamon Press, New York, 1973).
- [9] F.R.N.Nabarro, Dislocations in Solids (North Holland Pub. Co., New York, 1979).

- [10] S.Takeuchi, Solid State Phys. 25 (1990) 821.
- [11] L.F.Kirpichnikova, V.I.Mozgovoi, A.A.Urusovskaya and L.A.Shuvalov, Sov. Phys. Crystallogr, 35 (1990) 548.
- [12] L.N.Zagoruiko and V.P.Soldatov, Fiz. Met. Metalloved, 10 (1990) 199.
- [13] F.C.Frank and W.T.Read Jr., Phys. Rev. 79 (1950) 722.
- [14] W.C.Dash in "Dislocations and Mechanical Properties of Crystals", ed. J.Fisher (Wiley, New York, 1957) p.57.
- [15] L.A.Shuvalov, Modern Crystallography IV (Springer Verlag, Heidelberg, 1988).
- [16] P.Panfilov, A.Yermakov and G.Baturin, J. Mater. Sci. Lett. 9 (1990) 1162.
- [17] Z.Huang and M.Yao, Scr. Metall. 23 (1989) 1335.
- [18] J.Y.Lee and K.N.Subramanian, J. Mater. Sci. 18 (1983) 1765.

- [19] A.A.Griffith, *Trans. Roy. Soc.* **A221** (1920) 163.
- [20] S.Amelinckx, *Direct Observation of Dislocations*, Vol.6, Eds. F.Seitz and D.Turnbull (Academic Press, New York, 1964).
- [21] R.Gevers, S.Amelinckx and W.Dekeyser, *Naturwissenschaften* **39** (1952) 448.
- [22] F.H.Horn, *Philos. Mag.* **43** (1952) 1210.
- [23] K.Sangwal, *Etching of Crystals, Theory, Experiment and Application* (North Holland, New York, 1987).
- [24] N. Cabrera in "The Surface Chemistry of Metals and Semiconductors", ed. H.C. Gatos (John Wiley, 1960), p.71.
- [25] V.A. Phillips, in: "Modern Metallographic Techniques and their Applications, (Wiley-Interscience, 1971).
- [26] J.J. Gilman, in: *The Surface Chemistry of Metals and Semiconductors*, ed. H.C.Gatos (Wiley, 1960).
- [27] H. Nishikawa, *Japan J. Appl. Phys.* **12** (1973) 1647.

- [28] A.R. Patel and A. Venkateswara Rao, *J. Cryst. Growth* **47** (1979) 213.
- [29] A. Koma, E. Takimoto and S.Tanaka, *Phys. Stat. Solidi* **40** (1970) 239.
- [30] P.R. Camp, *J. Electrochem. Soc.* **102** (1955) 586.
- [31] T.M. Buck, in: *The Surface Chemistry of Metals and Semiconductors*, ed. H.C.Gatos (Wiley, New York), p.107.
- [32] H.C. Gatos, M.C. Lavine and E.P. Warekois, *J. Electrochem. Soc.* **198** (1961) 645.
- [33] B. Tuck and A.J. Baker, *J. Mater. Sci.* **8** (1973) 1559.
- [34] K. Sangwal and S.K. Arora, *J. Phys. D.* **12** (1979) 645.
- [35] H.C. Gatos and M.C. Lavine, *J. Appl. Phys.* **31** (1960) 743.

- [36] J.J. Gilman, W.G. Johnston and G.W. Sears, *J. Appl. Phys.* **29** (1958) 747.
- [37] W.C. Dash, *J. Appl. Phys.* **29** (1958) 705.
- [38] K.C. Poria and B.S. Shah, *Indian J. Phys. A.*, **65A** (1991) 252.
- [39] B. Wermke, M. Muhlberg, A. Engel and P. Rodolph, *Cryst. Res. Technol.* **24** (1989) 365.
- [40] H. Nishikawa, T. Soga, T. Jimbo, N. Mikuriya and M. Umeno, *Jpn. J. Appl. Phys. I. Regul. Pap. Short Notes*, **28** (1989) 941.
- [41] S.M. Rao, A.K. Batra, C. Rao and R.B. Lal, *J. Cryst. Growth* **106** (1990) 481.
- [42] J.B. Charles and F.D. Gnanam, *Cryst. Res. Technol.* **25** (1990) 1063.
- [43] M. Szurgot, *Cryst. Res. Technol.* **25** (1990) 285.
- [44] A. Peter, K. Polgar, L. Contreras and E. Dieguez, *Cryst. Res. Technol.* **24** (1989) 613.

- [45] L.A. Klinkova, N.I. Ganovich and O.S. Kolesnikova,
Inorg. Mater. **24** (1988) 1084.
- [46] G.M. Rosenblatt, P.K. Lee and M.B. Dowell, J. Chem.
Phys. **45** (1966) 3454.
- [47] G.M. Rosenblatt, J. Phys. Chem. **71** (1967) 1327.
- [48] H. Bethge, Phys. Stat. Solidi. **2** (1962) 775.
- [49] A.R. Patel and S.K. Arora, J. Phys. D. **7** (1974) 2301.
- [50] C.C. Desai, J.L. Rai and V. John, Surf. Technol.
14 (1981) 225.
- [51] A.R. Patel and R.M. Chaudhari, Jpn. J. Appl. Phys.
7 (1968) 363.

4.1 INTRODUCTION

The mechanical properties of crystals are evaluated by mechanical testing which reveals certain mechanical characteristics. The fastest and simplest type of mechanical testing is hardness measurement. The rapid evaluation of the ability of materials to undergo plastic strain can be made by measuring hardness. This is mainly achieved by indentation. Various other mechanical characteristics of the materials such as toughness, brittleness etc. have specific correlation with hardness [1]. Hence the study of hardness provides an important tool in securing a clear understanding of the mechanical behaviour of crystals.

The description of hardness, toughness and brittleness of crystals forms this chapter.

4.2 HARDNESS

The hardness is a measure of the resistance to deformation or damage of a material. It depends not only on the material studied, but also on the measuring conditions. The hardness measured by the indentation method is usually called microhardness because the hardness in this method is evaluated within a limited region. The results of a

microhardness measurement essentially depend on the face under test, the choice of the load applied to the indenter, the choice of loading time and exposure to the load, the correct patterns of impression on the test specimen, the method for preparing the specimens for investigation etc.

A considerable literature exists on the hardness measurements of several materials [2-10]. Although the mechanism of deformation during indentation is not clearly understood, hardness testing provides useful information regarding the mechanical behaviour of brittle solids. Plendl and Gielisse [11] have correlated the hardness of several crystals with the lattice energy. Microhardness studies on some III-V and II-VI compound semiconductors have been made by Nagabhooshanam and Haribabu [12]. They have compared the results with other properties of crystals such as melting point, ionicity etc. The microhardness study of SnTe and PbTe crystals was investigated by Varshava et al. [13]. Banar et al. [14] showed that an increase in the pressure of inert gas in the process of preparation of filamentary crystals of the PbTe leads to an increase in microhardness. The microhardness of TiN whiskers has been investigated by Wokulski [15]. Kurilo et al. [16] have studied the dependence of microhardness of CdTe crystals on

the indentation depth reduced to constant deformation rate. Investigations on the hardness properties of alloys and eutectic systems were carried out by many authors. Crocker et al. [17] have explained the microhardness in PbTe and related alloys. Krokha et al. [18] have investigated the hardness of aluminium alloys. The microhardness of $\text{Cd}_x\text{Hg}_{1-x}\text{Te}$ ternary alloys has been measured by Sharma et al. [19] at room temperature as a function of composition. Time dependence of the hardness of two phase alloys like In-Bi, Pb-Sn, Bi-Sn was studied by Leonov et al. [20]. Roslov et al. [21] have studied the microhardness of single crystals of solid solutions of Bi-Sb system. Zemskov et al. [22] found that in Bi-Sb alloy crystals with an Sb content 3 at % the microhardness was governed only by the Sb concentration in Bi and not depending on the growth rate.

Microhardness studies were also extended on organic materials. Joshi and Shah [23] have discussed the results of hardness number of anthracene, phenanthrene and benzoic acid single crystals in terms of the geometrical packing of molecules in the crystals. In addition to the investigations of room temperature hardness the knowledge of high temperature hardness (hot hardness) is also of considerable interest. The creep behaviour of SiC crystals at high

temperature was investigated by Hirai et al. [24] by hardness measurement at high temperatures. Kumashiro et al. [25] have studied the mechanical behaviour of TiC single crystals by the measurement of microhardness upto 1500°C. They have determined the activation energy for creep from the temperature dependence of the relaxation behaviour of indentation.

4.2.1 Methods of Hardness Measurement

There are several types of hardness measurements: static and dynamic indentation, scratching, measuring the height of rebound of a penetrator dropped on the test piece etc. In static indentation, the hardness of the material depends on the resistance to plastic strain. The application of the elastic rebound method permits better evaluation of the elastic properties of the material. The results of hardness measurement by the scratching method depend on the tendency of the material towards fracture. The scratching hardness is measured by two methods namely Mohs hardness and Martens hardness. The Mohs hardness is determined by the ability of the body to be scratched by a harder body or to scratch a softer one. Hardness is measured in Mohs scale, in which ten standard minerals are arranged in the order of their ability to be scratched. The measure of Martens



hardness is the width of the scratch made by a standard diamond cutter (pyramid, cone). In dynamic hardness measurements, the indenter is dropped on the specimen surface. The energy of impact is the measure of hardness.

The classes of hardness are named after the inventors of different types of indenter.

(a) Brinell Hardness

T
549.32/33
K1111

Brinell Hardness (H_B) is determined by the impression left by a steel ball. Here the microhardness is equal to the load applied divided by the surface area of the impression obtained, in which the diameter is measured after the load is removed.

$$H_B = \frac{2P}{\pi D (D - \sqrt{D^2 - d^2})} \quad (4.1)$$

where P is the applied load in Kg, D the diameter of the ball in mm and d is the diameter of the indentation in mm.

(b) Meyer Hardness

The Meyer hardness (H_M) is measured as the ratio of the load and the projected area of indentation.

$$H_M = P/\pi r^2 \quad (4.2)$$

where P is the applied load in kg, r the radius of indentation. For a cold-worked material, the M_H is essentially constant and independent of the load.

(c) Vickers Hardness

Vickers hardness (H_V) is determined by pressing down a standard-sized pyramid and calculated as the standard load divided by the lateral surface of the pyramidal impression obtained. Here the base diagonal is determined after the load is removed. The indenter used is a diamond pyramid with a square base and an apex angle of 136° between the opposite faces. When using such a pyramid, the microhardness is calculated by the formula,

$$H_V = 1.8544P/d^2 \quad (4.3)$$

where p is the load applied to the indenter (kg) and d is the impression diagonal (mm).

(d) Knoop Hardness

A Knoop indenter is a diamond ground to a pyramidal form which produces a diamond shaped indentation with the long and short diagonals in the approximate ratio of 7:1.

Knoop hardness (H_K) is the applied load divided by the uncovered projected area of indentation.

$$H_K = P/L^2C \quad (4.4)$$

where P is the applied load (Kg), L is the length of longer diagonal (mm) and C is a constant of the indenter.

(e) Rockwell Hardness

The test utilizes the depth of indentation under constant load as a measure of hardness. A dead load is first applied to seat the specimen and then the major load for indentation is applied. The depth of indentation is automatically recorded on a dial gauge in terms of arbitrary hardness numbers.

4.3 TOUGHNESS

Toughness denotes the resistance to fracture of a material. Among a large number of methods available for toughness [26-29], the indentation method is the best suited for brittle materials with low toughness value. This is due to the simplicity and rapidity with which toughness can be evaluated using small samples. Toughness is an important

parameter for characterising the fracture process initiated by microcracks. During indentation, cracks are initiated around the indented impression and these cracks propagate on subsequent loading. The shaping of brittle materials by drilling, grinding, cutting and abrasion, the damage and erosion of surface etc., are all closely related to the manner of initiation and propagation of microcracks. According to Griffith [30], the crack is assumed to initiate at some dominant flaw in the specimen surface and then propagate into a characteristic cone in accordance with the requirements of an energy balance condition. Hagan [31] and Lawn and Marshall [32] have proposed models to predict the critical load and flaw size conditions which should prevail at the threshold of crack initiation. Several parameters have become available for specifying resistance to crack growth after the development of Griffith-Irwin fracture mechanics. Of these, fracture toughness has gained the widest acceptance as a material quantity in design. The evaluation of toughness is of attracting interest for many researchers [33-41].

Several investigators have used indentation techniques to study glide, deformation anisotropy, cracks etc. in various crystals. The study of cracks in melt grown cadmium iodide crystals has been reported by Chaudhari et al. [42]. Charles and Gnanam [43] observed crack patterns on NaSbF_4 and NaSb_2F_7 single crystals using a Leitz Wetzler microhardness tester. Lawn and Marshall [44] suggested that the dimensions of cracks are directly proportional to the size of the indentation mark or the diagonal length. The initiation of radial cracks were observed by Desai and Ramana [45] on their lead hydrogen phosphate single crystals. In garnet crystals, fracture starts with radial cracking from the corners of the indented impression followed by well developed lateral cracks [46].

The formula for crack propogating under loading conditions determined by the analysis of the deformation fracture mechanics of the indentation process can be represented under equilibrium conditions as,

$$P/l^{3/2} = \beta_0 K_c ; \text{ for } l \geq d/2 \quad (4.5)$$

where P is the applied load, l is the crack length, β_0 is the indenter constant, which is equal to 7 for Vickers indenter [1], K_c is the toughness and d is the diagonal length of the indentation mark.

4.4 BRITTLENESS

Brittleness is said to measure the relative susceptibility of a material to two competing mechanical responses, deformation and fracture [1]. This is an important property as far as the mechanical behaviour of material is considered. A number of useful parameters have been devised for quantifying both deformation and fracture properties separately. But little effort has been made to combine such parameters into a common description. The crack model proposed by Rice and Thomson [47] represents the most important attempts in this direction. Another basic idea stems from realization that a suitable indentation pattern can provide simultaneous information on deformation and fracture properties of a given material [48,49]. Lawn and Marshall [1] have proposed the ratio of hardness to toughness as an index of brittleness.

A definite physical significance is attached to this factor in the indentation problem [27,32,50]. The brittleness can be estimated by indentation from the load causing cracks near the impression. An arbitrary scale of estimating the brittleness of refractory compounds [51] is given in Table 4.1.

Table 4.1: Arbitrary scale for estimating the brittleness number of refractory compounds.

Brittleness No.	Character of the impressions
0	No visible cracks or chipping
1	One small crack
2	One crack not coinciding with the continuation of the diagonal of the impression. Two cracks in adjacent corners of the impression.
3	Two cracks in opposite corners of the impression
4.	More than three cracks. One or two chips at the sides of the impression
5	Shape of the impression broken up.

4.5 REFERENCES

- [1] B.R.Lawn and D.B.Marshall, *J. Am. Ceram. Soc.* **62** (1979) 347.
- [2] K.N.Reddy and T.S.P.L.N. Prasad, *Phys. Stat. Solidi A*, **123** (1991) K105.
- [3] C.Ascheron, H.Neumann and G.Kuhn, *Cryst. Res. Technol.* **26** (1991) 213.
- [4] T.T.Rao and D.B.Sirdeshmukh, *Cryst. Res. Technol.* **26** (1991) K53.
- [5] G.Constantinidis, R.D.Tomlinson and H.Neumann, *Philos. Mag. Lett.* **57** (1988) 91.
- [6] C.C.Jiang, T.Goto and T.Hirai, *J. Less-Common Met.* **163** (1990) 339.
- [7] S.W.Lee, J.H.Ahn, S.Danyluk and A.G.Elliot, *J. Appl. Phys.* **68** (1990) 4276.
- [8] O.V.Aliksandrov, I.N.Zelinkman and K.V.Kiseleva, *Sov. Phys.-Lebedev Inst. Rep.* (1985) 46.

- [9] S.M.Dharmaprakash and P.Mohan Rao, *Cryst. Res. & Technol.* 21 (1986) 1567.
- [10] C.Ascheron, H.Neumann, G.Dlubek and R.Krause, *J. Mater. Sci. Lett.* 5 (1986) 891.
- [11] J.N.Plendl and P.J.Gielisse, *Phys. Rev.* 125 (1962) 828.
- [12] M.Nagabhooshanam and V.Haribabu, *Cryst. Res. Technol.* 20 (1985) 1399.
- [13] S.S.Varshava, S.N.Bekesha, I.V.Kurilo and L.N.Pelekh, *Lenin Inorg. Mater.* 23 (1987) 1143.
- [14] V.F.Banar, F.G.Donika, M.P.Dyntu and D.F.Miglei, *Sov. Phys. Crystallogr.* 30 (1985) 603.
- [15] Z.Wokulski, *Phys. Stat. Solidi* 120 (1990) 175.
- [16] I.V.Kurilo, V.P.Alekhin, S.I.Bulychev and S.P.Pavlishin, *Inorg. Mater.* 20 (1984) 182.
- [17] A.J.Crocker and M.Wilson, *J. Mater. Sci.* 13 (1978) 833.

- [18] V.A.Krokha, M.Z.Ermankov, V.K.Kudryashov and O.B.Levleva, *Met. Sci. Heat Treat.*, 32 (1990) 144.
- [19] B.B.Sharma, S.K.Mehta and V.V.Agashe, *Phys. Stat. Solidi.*, 60 (1980) K105.
- [20] V.N.Leonov and A.V.Bryukhanov, *Phys. Chem. Mater. Treat.* 21 (1987) 301.
- [21] S.A.Roslov, A.D.Belaya and V.S.Zemskov, *Inorg. Mater.* 11 (1975) 1131.
- [22] V.S.Zemskov, V.V.Rozhdestvenskaya and N.N.Lukash, *Inorg. Mater.* 12 (1976) 970.
- [23] M.J.Joshi and B.S.Shah, *Cryst. Res. Technol.* 19 (1984) 1107.
- [24] T.Hirai and K.Niihara, *J. Mater. Sci.* 14 (1979) 2253.
- [25] Y.Kumashiro, A.Itoh, T.Kinoshita and M.Sobajima, *J.Mater. Sci.* 12 (1977) 595.
- [26] A.G.Evans, *Fracture Mechanics of Ceramics, Vol.I*, Plenum Press, New York (1974).

- [27] A.G.Evans and E.A.Charles, J. Amer. Ceram. Soc. 59 (1976) 371.
- [28] B.R.Lawn and E.R.Fuller, J. Mater. Sci. 10 (1975) 2016.
- [29] J.J.Petrovic, L.A.Jacobson, P.K.Talty and A.K.Vasudevan, J. Amer. Ceram. Soc. 58 (1975) 113.
- [30] A.A.Griffith, Phil. Trans. Roy. Soc. Lond. 221 (1920) 163.
- [31] H.T.Hagan, J. Mater. Sci. 14 (1979) 2975.
- [32] B.R.Lawn and A.G.Evans, J. Mater. Sci. 12 (1977) 2195.
- [33] J.Echigoya, Y.Takabayashi and H.Suto, J. Mater. Sci. Lett. 5 (1986) 153.
- [34] M.Ashizuka and R.C.Bradt, J. Mater. Sci. Lett. 1 (1982) 314.
- [35] J.L.Henshall and C.A.Brookes, J. Mater. Sci. Lett. 4 (1985) 783.

- [36] P.Lemaitre, J. Mater. Sci. Lett. 7 (1988) 895.
- [37] K.Hayashi, S.Tsujimoto, Y.Okamoto and T.Nishikawa, J. Soc. Mater. Sci. Jpn., 40 (1991) 405.
- [38] N.Narita, K.Higashida, T.Torii and S.Miyaki, Mater. Trans. Jim. 30 (1989) 895.
- [39] H.Kobayashi, Y.Arai, T.Araki and T.Oku, J. Soc. Mater. Sci. Jpn., 39 (1990) 1076.
- [40] G.Baran, M.Degrange, C.Roques-Carmes and D.Wehebi, J. Mater. Sci. 25 (1990) 4211.
- [41] B.Wermke and M.Petzold, Cryst. Res. Technol. 25 (1990) K121.
- [42] S.K.Chaudhary, A.Gaur and G.c.Trigunayat, Cryst. Res. Technol. 25 (1990) K87.
- [43] J.B.Charles and F.D.Gnanam, Cryst. Res. Technol. 25 (1990) 1451.
- [44] B.R.Lawn and D.B.Marshall, in: Fracture Mechanics of Ceramics eds. R.C.Bradt, D.P.H.Hasselman and F.C.Lange (Plenum Press, New York) p.205.

- [45] C.C.Desai and M.S.V.Ramana, J. Mater. Sci. 23 (1988) 617.
- [46] M.P.Horvath, J. Mater. Sci. 19 (1984) 1159.
- [47] J.R.Rice and R.Thomson, Philos. Mag. 29 (1974) 73.
- [48] R.W.Douglas, J. Soc. Glass Technol. 42 (1958) 145.
- [49] K.Peter, Glastechn. Ber. 37 (1964) 333.
- [50] A.G.Evans and T.R.Wilshaw, Acta Metall. 24 (1976) 939.
- [51] V.M.Glazov and V.N.Vigdorovich, Microhardness of metals and semiconductors, (Consultants Bureau, New York, 1971).

5

EXPERIMENTAL
TECHNIQUES



Fig. 5.1

5.1 INTRODUCTION

Various techniques employed in the investigations presented in the thesis are described in brief in this chapter. The physical vapour deposition (PVD) method and horizontal zone levelling (HZL) method used for the growth of $\text{Te}_{1-x}\text{Se}_x$, Bi_2Te_3 and In_2Te_3 crystals are briefly outlined. To determine the structure and lattice constant of the grown crystals, X-ray diffraction method was used. Electron Spectroscopy for Chemical Analysis (ESCA) was employed to identify the elements present in the samples and Differential Scanning Calorimetric (DSC) method was employed to determine the phase transition temperature of In_2Te_3 samples. The details of microscopes used for the study of crystal surfaces are presented. In this chapter, a brief account of chemical and thermal etching techniques for the dislocation studies is included. The last part of this chapter also gives a short note on the experimental set up used for the microindentation analysis and electrical measurements of the crystals.

5.2 GROWTH TECHNIQUES

5.2.1 Vacuum Sealing of Ampoules

The ampoules were cleaned thoroughly by washing first with cleaning solutions and then ultrasonically

with doubly distilled water and acetone and finally dried. For sealing of the ampoule containing the reactants, an adaptor with provision for connecting the neoprene tube to the ampoule and a penning gauge head for pressure measurement was used and was fixed to the base plate of a vacuum coating unit. This system is shown in Fig.5.1. The ampoule was connected to the vacuum system and evacuated to a pressure of 10^{-5} Torr. The lower end of the ampoule was kept in a freezing mixture to avoid the sublimation of materials during fusing. After attaining the final pressure, the ampoule was sealed at the constriction.

5.2.2 Preparation of homogeneous charge of $\text{Te}_{1-x}\text{Se}_x$, Bi_2Te_3 and In_2Te_3

The starting materials of $\text{Te}_{1-x}\text{Se}_x$, Bi_2Te_3 and In_2Te_3 were prepared from elements of tellurium (99.999%), selenium (99.999%), bismuth (99.999%) and indium (99.999%). These materials were supplied by Nuclear Fuel Complex, Hyderabad, India. For preparing alloys of $\text{Te}_{1-x}\text{Se}_x$, the materials were vacuum sealed in precleaned glass ampoule of length 10 cm and diameter 10 mm. In the case of Bi_2Te_3 and In_2Te_3 , quartz ampoules of length 10 cm and diameter 12 mm were used for filling the reactant materials. In

order to mix the materials properly, a constant temperature (Muffle furnace) was used. The photograph of the furnace is shown in Fig.5.2. The furnace can attain a maximum temperature of 1000°C. It has an attached temperature controlling assembly which is capable of controlling the temperature of the furnace to an accuracy of $\pm 2^\circ\text{C}$. The ampoule was inserted in the furnace and slowly heated to avoid the cracking of the ampoule. Very slow heating results in good homogenization and better composition of the samples. After mixing, the melt was cooled slowly by slow reduction of the current through the furnace. An arrangement is attached to the furnace to rock the ampoule at intervals for proper mixing.

5.2.3 Vapour growth of $\text{Te}_{1-x}\text{Se}_x$, Bi_2Te_3 and In_2Te_3 crystals

The growth of $\text{Te}_{1-x}\text{Se}_x$, Bi_2Te_3 and In_2Te_3 whiskers was carried out by the physical vapour deposition (PVD) method. For growth, a horizontal linear gradient furnace with two zones was used. The experimental set up is shown in Fig.5.3. The core of the furnace consists of a ceramic tube of about 50 cm length and 4 cm inner diameter. The source and growth zones of the furnace are two ceramic tubes with regularly spaced inner grooves for the heater

windings (Kanthal Al wire). The furnace tube and the heater assemblies were insulated using thick asbestos winding and were covered using a MS outer jacket. A maximum temperature of 1000°C was achieved by giving about 4 amps of current to the furnace.

The $\text{Te}_{1-x}\text{Se}_x$ crystals were grown in pyrex glass ampoules whereas Bi_2Te_3 and In_2Te_3 crystals were grown in quartz ampoules. One end of the ampoule was closed and the other end was uniformly constricted to allow for sample introduction and easy sealing. Two round dimples were made on the ampoules in order to increase the degree of mixing of the vapours. In physical transport methods of crystal growth, transporting of the reactants from the hot zone to the cold zone is taking place at a low pressure in the ampoule. The sealed ampoule was placed in the furnace and was subjected to reverse transport so that the traces of materials at the growth zone would be removed. For the growth process, the source zone was maintained at higher temperature and the growth zone at a lower temperature. The temperature of both zones was controlled to an accuracy of $\pm 1^\circ\text{C}$ using two independent temperature controllers. After the growth of crystals, the ampoule was removed carefully from the furnace. Good crystals were obtained in the form of whiskers with well developed prism faces.

5.2.4 Melt growth of Bi_2Te_3 and In_2Te_3 crystals

The crystal growth set up for Bi_2Te_3 and In_2Te_3 crystals by horizontal zone levelling (HZL) method is shown in Fig.5.4. It consists of a fabricated furnace which could be raised to a temperature of 1000°C . The length of the furnace tube is about 106 cm. Kanthal Al wire was used for the heater windings. The length of the kanthal heating element was so chosen that 250 volts AC could be applied to the coils without the coils getting damaged. For insulation, the heating zone was covered by asbestos windings. Since kanthal at high temperatures is liable to be reactive with asbestos, the leads were taken out after enclosing them with beads of porcelain. The two ends of the tube can be closed tight by rubber stoppers. The temperature profile along the axis of the furnace was carefully determined using a chromel alumel thermocouple. For growing crystals, the ampoule containing the homogeneous charge was placed in the furnace. The charge end was kept at higher temperature while the sealed end was kept at lower temperature. Good stoichiometric crystals of Bi_2Te_3 and In_2Te_3 were obtained and were cleaved to get optically plane surface for their characterisation.

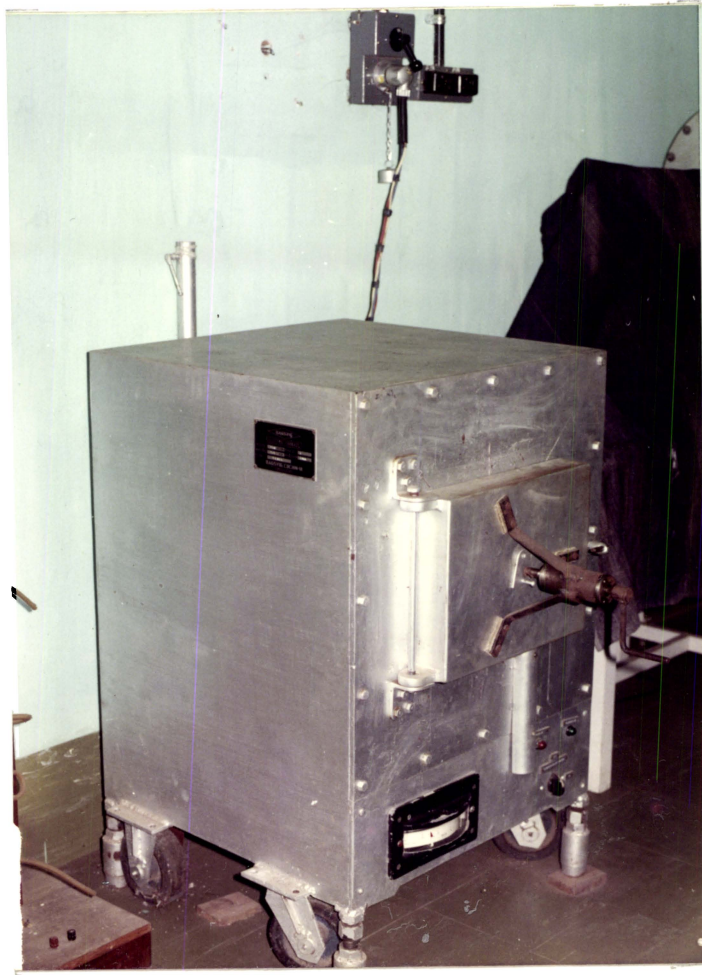


Fig. 5.2

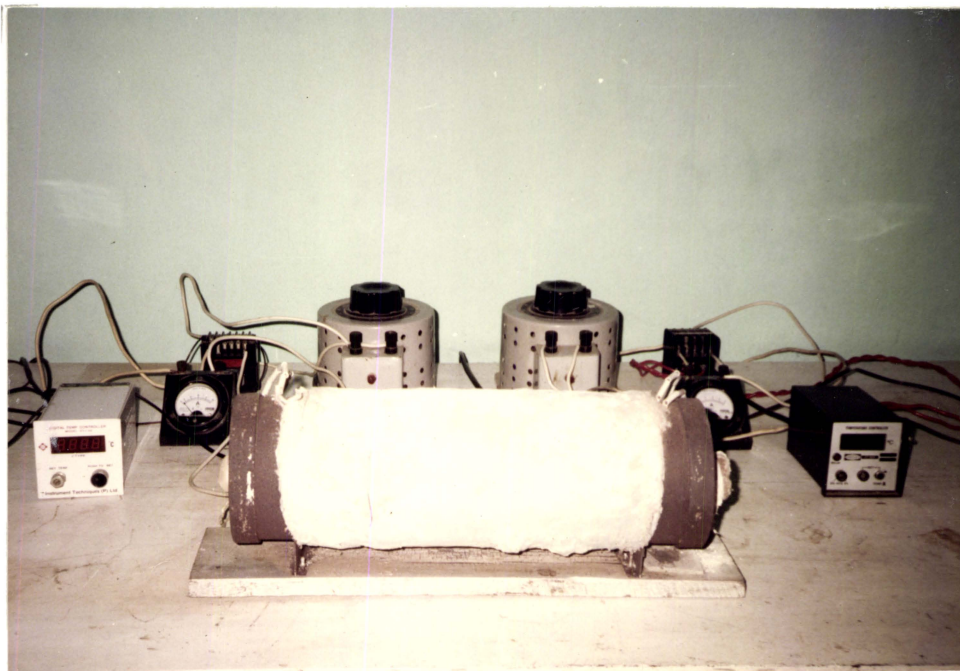


Fig. 5.3

5.3 X-RAY DIFFRACTION (XRD)

X-ray diffraction study was used to identify the compound and its structure. According to Bragg's law

$$2d \sin \Theta = n\lambda \quad (5.1)$$

where d is the lattice spacing, Θ the incident angle of X-ray beam, n is an integer and λ the wavelength of the incident radiation.

In the powder method, the crystal to be examined is reduced to a very fine powder and placed in a beam of monochromatic X-rays. Each particle of the powder is a tiny crystal oriented at random with respect to the incident beam. In X-ray diffractometers, the X-ray source, the specimen and the detector are so arranged to obey the Bragg's law. When λ the wavelength is known the interplanar distance ' d ' of the crystal can be determined.

A Philips PW 1710/00 X-ray unit was used for these studies. Filtered $\text{CuK}\alpha$ radiation was employed as the X-ray source. The accelerating potential applied to the X-ray tube was ~ 40 kV and the tube current ~ 15 mA.

The intensity of the diffracted radiation against 2θ was recorded by a recorder running in synchronization with the goniometer. The lattice parameters of the crystals can be determined by indexing the powder patterns [1].

5.4 ELECTRON SPECTROSCOPY FOR CHEMICAL ANALYSIS (ESCA)

X-ray photoelectron spectroscopy is a powerful new analytical technique currently experiencing widespread use. The technique is commonly called ESCA for electron spectroscopy for chemical analysis [2].

When an X-ray or electron beam of precisely known energy impinges on the samples, inner shell electrons are ejected and the energy of the ejected electrons is measured. This is the phenomenon on which ESCA is based. In order to eject an electron beam from a K-orbital, the energy of the radiation falling on it must be greater than the energy required to displace it. The energy of the escaping electron is designated as E_k (This proposes that the electron comes from the K shell). The binding energy of this electron is given by the equation,

$$E_b = h\nu - (E_k + C) \quad (5.2)$$

where E_b is the binding energy of electron, $h\nu$ is the energy of the photon, E_k is the kinetic energy of the escaping electron and C is an instrumental constant.

At a given energy of the incident photons, the photoelectron spectrum of a material reflects the various occupied electronic levels and bands in the material. Because the energies of the various electronic levels are usually different for different materials, photoelectron spectra are characteristic of the material. If E_b is measured, it is possible to deduce information about the chemical composition of the specimen atoms in the molecule. Since E_b the original binding energy of the emitted electron depends on the energy of the electronic orbit and the element from which electron is emitted, it can be used to identify the elements involved. The quantity of the electrons is proportional to the concentration of the material. Changes in the chemical composition of the atom causes changes in E_b . Since the electrons ejected in ESCA technique are necessarily of low energies, the smaller energy differences can be easily measured, the electrons cannot escape from any significant depth in the sample. The phenomenon is therefore confined to atoms on the

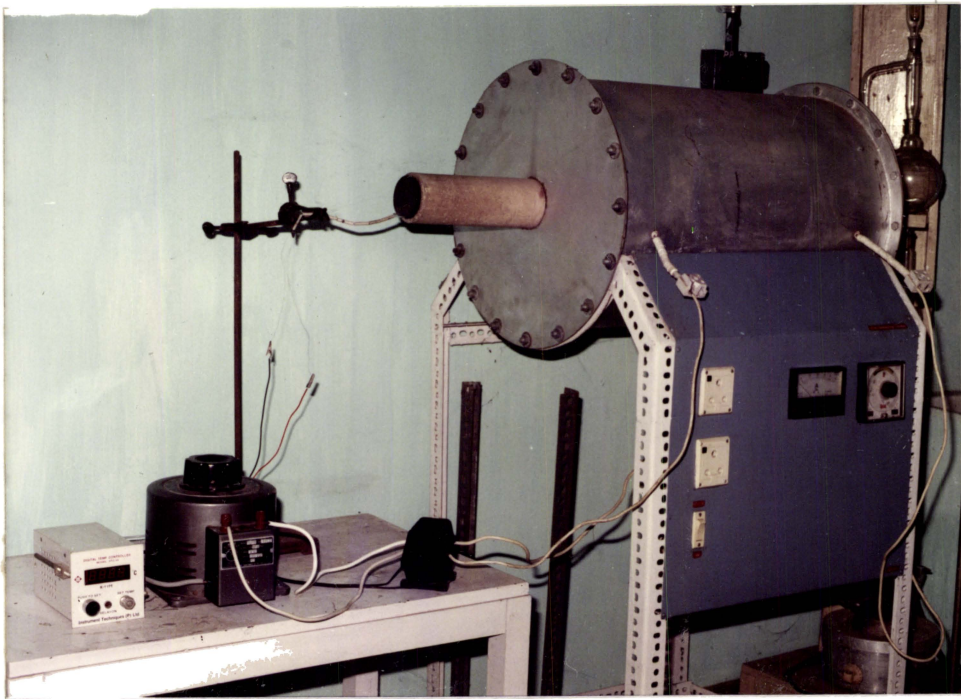


Fig. 5.4

surface of the sample and provides a method of surface analysis.

The ESCALAB MK II spectrometer (VG Scientific Ltd. UK) with $MgK\alpha$ ($h\nu = 1253.6$ eV) radiation as the source was used for the analysis.

5.5 DIFFERENTIAL SCANNING CALORIMETRY (DSC)

Thermal analysis continues to be one of the fastest growing instrumental techniques for the study of a material and differential scanning calorimetry (DSC) is one of the advanced techniques in the field of thermal analysis. Thermal analysis using DSC has been successfully employed to study the equilibrium between the different phases in complexes, the thermodynamic properties, crystallization energies, microstructural evolution in alloys, phase transitions, effect of temperature rise on structural change, heat capacity, enthalpy etc. Basically the DSC technique allows the determination of the time derivative of the heat content per unit mass of the sample, $\dot{H}(t) = dH/dt$ as a function of time t for a given heating rate, $\dot{T} = dT/dt$ and a given temperature, $T(t)$. The DSC traces of crystals were obtained using a Perkin Elmer Delta Series Differential Scanning Calorimeter (model DSC-7).

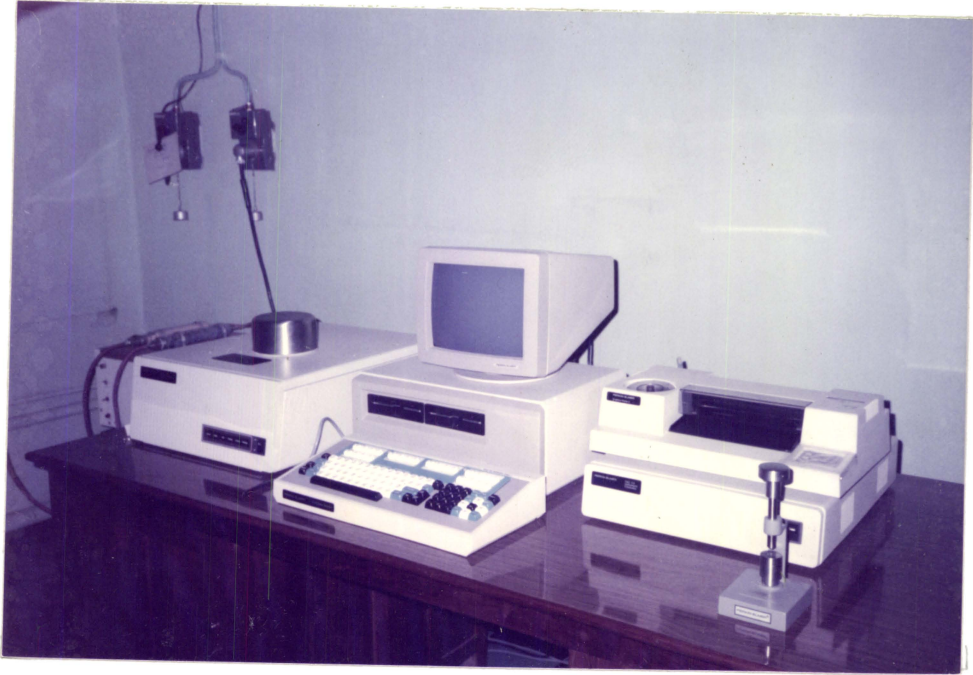


Fig. 5.5

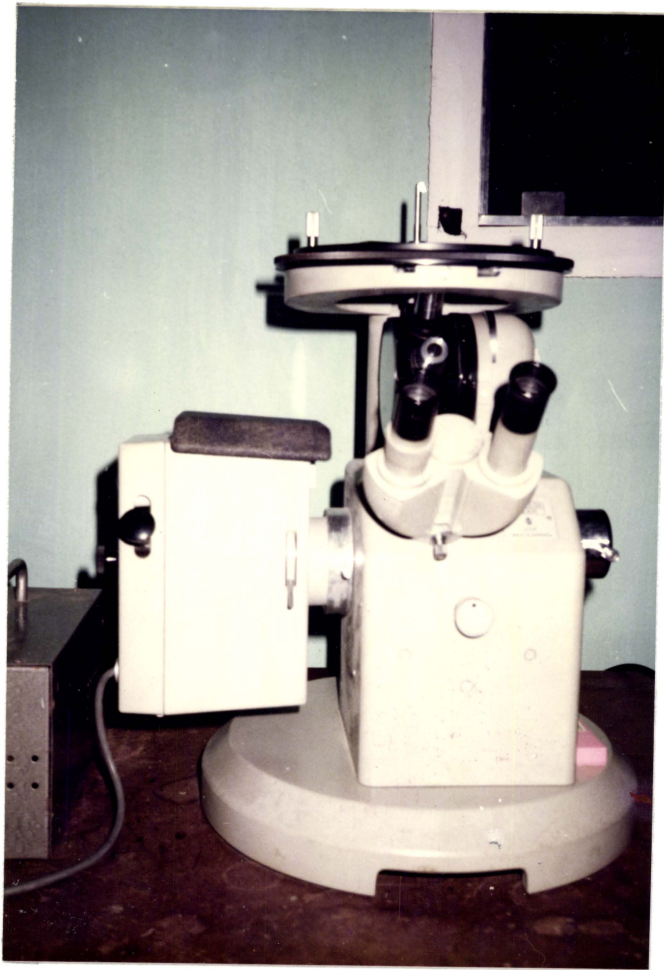


Fig. 5.6

The photograph of the instrument is shown in Fig.5.5. The spectrum was recorded with a scanning rate of 5°C/min. The distinct variation in the heat flow of the samples was studied and the phase transition temperature has been determined.

5.6 OPTICAL MICROSCOPY

Optical microscopy is one of the best suited methods for observing crystal surfaces. The information about the mechanism of crystal growth can be obtained from the observation of growth patterns. Crystals with good plane faces were used for the morphological studies.

A Carl-Zeiss Jena Epityp II metallurgical microscope (Fig.5.6) was employed for the optical studies of crystal surfaces. This microscope carries a binocular vision system. The microphotographs of the crystal surfaces were taken with the help of a photographic attachment of the microscope.

The inverted metallurgical type Union Versamet-2 microscope (Fig.5.7) was also used for the microtopographical studies. This microscope consists of two different system for the optical examination of crystals

viz. Transmission system and reflection system. The illuminating system can be shifted from reflecting to transmitting modes. For change over between reflected light illumination (24 V, 150 W, halogen) and transmitted light illumination (12 V, 50 W, halogen), a light source changeover switch was used. The reflection mode was used in the present case as the crystals used for the study were opaque. The microscope possesses a built-in photo mechanism for large size and 35 mm film. The photographic lenses for 35 mm photographs and large size photographs are on a rotating turret. The magnification of each lens can be seen through a display window. Lenses can be changed by turning the outer knurled ring until the magnification required appears in the display window. The unit also carries one pair of 10 X eye pieces. For photography, the image can be focussed on the projection screen.

In both the above microscopes, the specimen to be studied is placed on a movable stage above the objective lens. The stage can be moved in circular and crosswire directions. Focussing is done by raising and lowering the stage by rack and pinion arrangement and by fine movement.

Microscopic study of the crystal surfaces was also carried out by means of a scanning electron microscope (Cambridge Steroscan S-180).

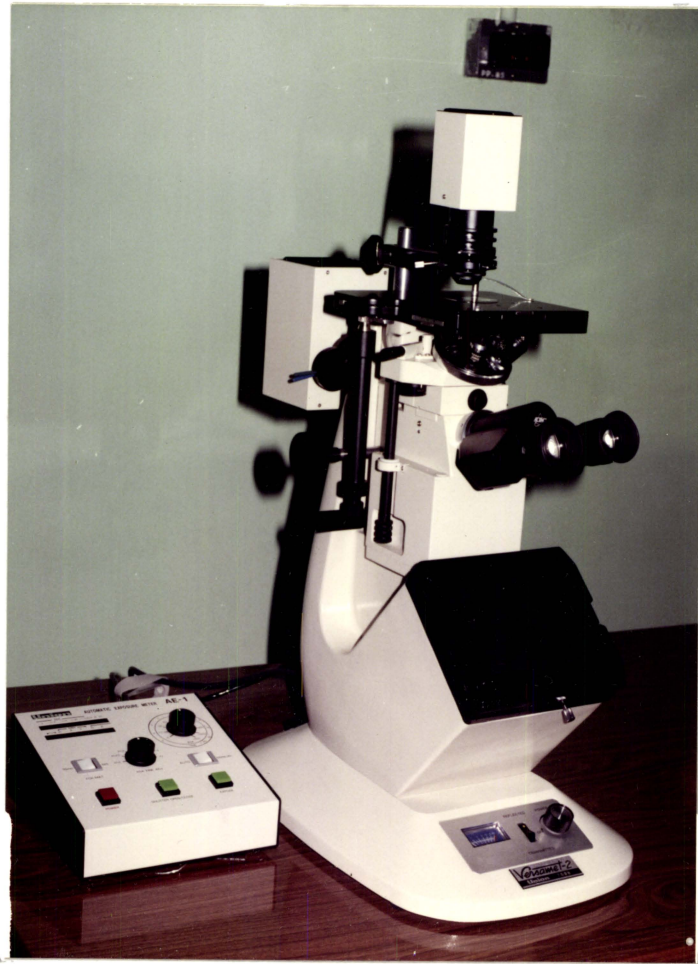


Fig. 5.7

5.7 ETCHING STUDIES

During the present investigations on dislocations, chemical and thermal etching techniques were employed. As-grown crystals and cleaved crystals were used for etching studies. Chemical etching was performed by immersing the crystals in different etchants and the etched surfaces were studied under optical microscopes.

Thermal etching was carried out in a high vacuum system using a diffusion pump in conjunction with a rotary pump. A vacuum of the order of 10^{-5} Torr was achieved using this system. The etching was carried out under different temperatures and pressures. The temperature was measured by a chromel alumel thermocouple and the pressure was measured using a penning ionisation gauge. Fig.5.8 shows the photograph of the vacuum system.

5.8 MICROINDENTATION STUDIES

Microindentation analysis was carried out using a Hanemann Microhardness Tester (model D32) which can be attached to the Carl-Zeiss Jena Epityp II metallurgical microscope. The experimental set up is shown in Fig.5.9. The diamond pyramid is polished in the shape of a quadrangular Vickers pyramid--whose sides have a slope of 22° ,

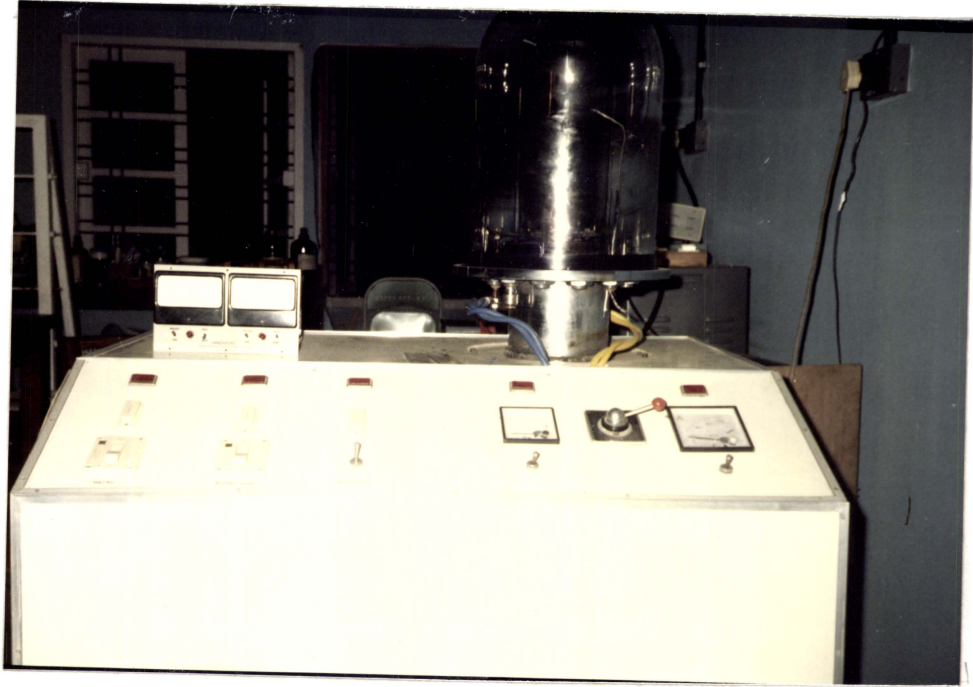


Fig. 5.8

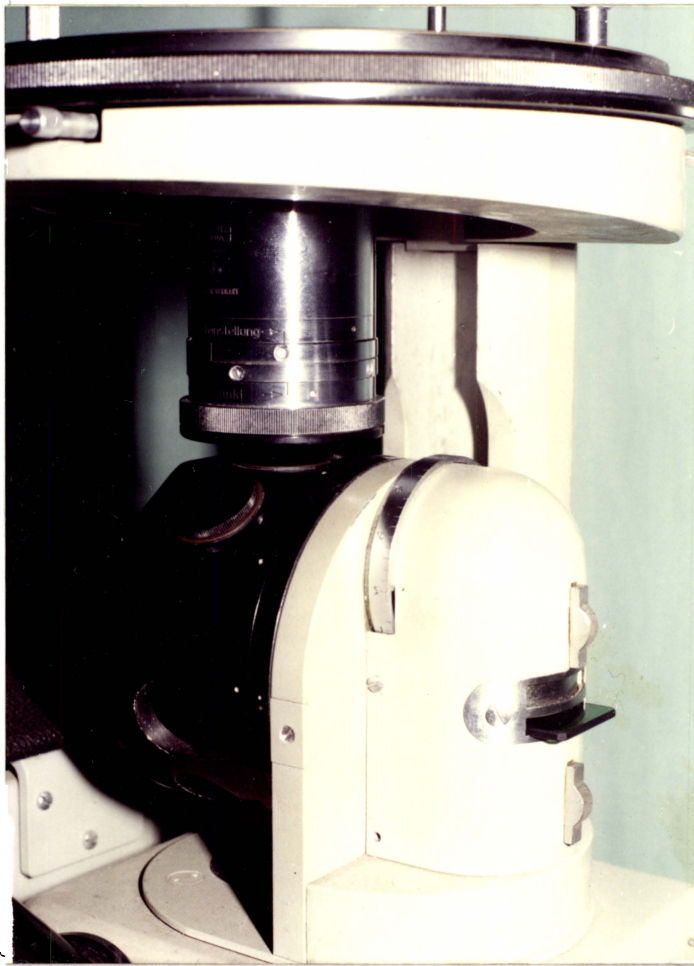


Fig. 5.9

the rest of the diamond being shaped as a short bar whose diameter is so small that it can be mounted in a centered hole drilled into the front lens. This leaves a sufficiently large annular portion of the front lens free for illumination and image formation. The hardness tester is also provided with an optical device to indicate the testing load. The objective with the diamond is suspended from two disc springs. Any load applied to the diamond causes the suspension to activate the optical system, which indicates the load observable through the eyepiece. The eyepiece micrometer has two reticles (one stationary and one sliding), each of which has a right angle ruled on it. The two markings can be used to measure the diagonal length of the indentation mark. Using this technique, hardness, toughness and brittleness of the crystals can be evaluated.

5.9 ELECTRICAL CONDUCTIVITY STUDIES

Fig.5.10 shows the schematic diagram of the metallic chamber used for the study of electrical conductivity of crystals. The electrometer was connected in series with the power supply and the crystal and the electrical circuit for the measurement is shown in Fig.5.11.

Electrical contacts to the crystals were made by coating the surfaces with the silver paint. Sample was

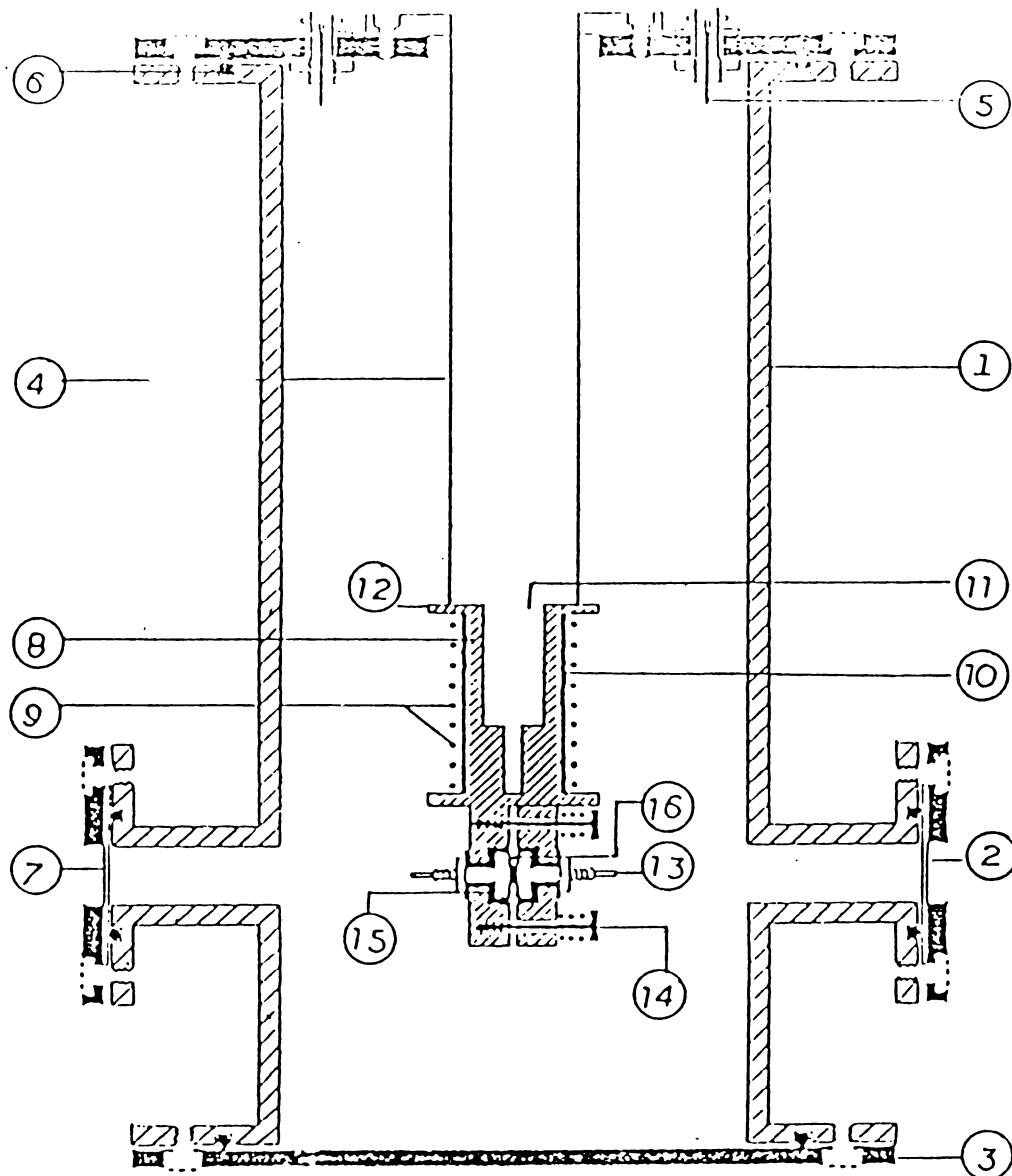


Fig. 5.10

- | | |
|--------------------|----------------------------|
| 1. MS CHAMBER | 8. COPPER COLD FINGER |
| 2. GLASS WINDOW | 9. HEATER WINDINGS |
| 3. MS FLANGE | 10. MICA INSULATION |
| 4. SS PIPE | 11. LN ₂ CAVITY |
| 5. BNC | 12. SAMPLE HOLDER |
| 6. NEOPRINE O-RING | 13. COPPER ELECTRODES |
| 7. TO VACUUM PUMP | 14. SPRING LOADED SCREWS |
| | 15. TEFLON INSULATION |
| | 16. THERMOCOUPLE |

placed in the metallic chamber and a steady voltage of ~ 9 V was applied by a battery. Current was measured using an electrometer. The power to the heater was provided from a stabilized voltage source. Sample temperature was measured using a Chromel-Alumel thermocouple kept in contact with the sample surface. The conductivity can be evaluated with the known values of the magnitude of the current, area, thickness of the sample and the applied voltage. A photograph of the experimental set up is shown in Fig.5.12.

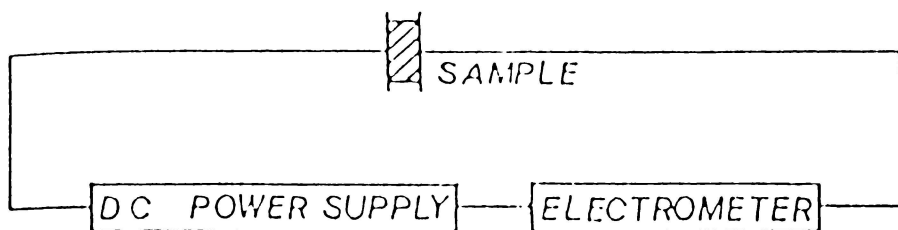


Fig. 5.11



Fig. 5.12

5.10 FIGURE CAPTIONS

Fig.5.1: Vacuum system for fusing the ampoule.

Fig.5.2: Constant temperature furnace.

Fig.5.3: Experimental set up for the growth of crystals by PVD method.

Fig.5.4: Experimental set up for the growth of crystals by HZL method.

Fig.5.5: Perkin-Elmer Delta Series Differential Scanning Calorimeter.

Fig.5.6: Carl Zeiss Jena Epityp II microscope.

Fig.5.7: Union Versamet-2 microscope.

Fig.5.8: Vacuum system for thermal etching.

Fig.5.9: Experimental set up for microindentation analysis.

Fig.5.10: Schematic diagram of the metallic chamber for the measurement of electrical conductivity.

Fig.5.11: Schematic diagram of the measurement of electrical conductivity.

Fig.5.12: Experimental set up for the measurement of electrical conductivity.

5.11 REFERENCES

- [1] B.D.Cullity, Elements of X-ray Diffraction (Addison-Wesley Pub. Co., USA, 1959)

- [2] W.E.Swartz, Jr., in: Instrumentation in Analytical Chemistry, Vol.2, ed. S.A.Borman (American Chemical Society, USA, 1982).

GROWTH AND MORPHOLOGY OF VAPOUR-GROWN
 $\text{Te}_{1-x}\text{Se}_x$, Bi_2Te_3 AND In_2Te_3 CRYSTALS

6.1 INTRODUCTION

Owing to the potential applications of tellurium, selenium and $\text{Te}_{1-x}\text{Se}_x$ alloy crystals in various devices, a widespread interest has evolved in studying their properties. Tellurium and selenium are VI group chalcogens and share a peculiar hexagonal crystal structure. Within the chains the bonding is covalent, but cross-linking the chains it is partially van der Waals and partially metallic in nature [1]. Consequently, the physical properties are anisotropic.

Keezer et al. [2] have investigated the crystal growth from the liquid and vapour phases over the full range of the Se-Te system. Shih and Champness [3] have reported the growth of Se-Te mixed crystals using the Czochralski method. Also Quang et al. [4] have grown monocrystalline Te-rich $\text{Se}_x\text{Te}_{1-x}$ alloys using the Czochralski method. Shiosaki and Kawabata [5] have used a Te seeding Bridgman method to grow $\text{Se}_x\text{Te}_{1-x}$ single crystals containing 70 to 100 at % Se at growth rates of 0.2 to 1.5 mm/h. Using the Bridgman method and a zone levelling technique, single crystals over the whole range of composition were obtained by Beyer et al. [6]. Bhatt and Trivedi [7] have grown $\text{Se}_{90}\text{-Te}_{10}$ crystals from the melt by

the Bridgman technique using thallium as an impurity. Vapour growth of hollow $\text{Se}_{90}\text{-Te}_{10}$ whisker crystals using a vertical gradient furnace and their morphological studies have been carried out by Bhatt et al. [8,9].

Bismuth telluride is a narrow-gap semiconductor ($E_g = 0.16$ eV) belonging to V-VI family and finds application in thermoelectric devices [10,11]. Crystallographic data for this compound were originally published by Lange [12] who described the structure as rhombohedral with the space group $D_{3d}^5(\bar{R}3m)$. Later, from the measurements on annealed powder samples of the stoichiometric compound, Francombe [13] obtained accurate values of structure-cell parameters, i.e.,

$$a_R = 10.473 \text{ \AA}, \quad \alpha_R = 24^\circ 9' 32''$$

The atoms of the Bi_2Te_3 structure are arranged in layers which are stacked in the rhombohedral [111] direction in cubic close-packing. It can schematically be described by the layer sequence,

...|Te-Bi-Te-Bi-Te|Te-Bi-Te-Bi-Te|Te-Bi-Te-Bi-Te|...

It is seen that tellurium occurs in two different positions, namely $\text{Te}^{(1)}$ and $\text{Te}^{(2)}$ sites. $\text{Te}^{(1)}$ represents the atom sites limiting the five layered lamellae and $\text{Te}^{(2)}$ the sites in the centre of these lamellae.

A striking feature of Bi_2Te_3 crystals is the ease with which they can be cleaved along the basal (0001) planes (referred to hexagonal axes). It has been reported by Drabble and Goodman [14] that the bonding between Bi-Te layers is predominantly covalent and partially ionic in character, while that between Te-Te layers is of the van der Waals kind and that cleavage occurs between the weakly bonded Te layers. Because of the inherent chain type structure these crystals mainly grow as needles.

The growth of Bi_2Te_3 crystals by melt methods was carried out by a number of authors [15-23]. Arivuoli et al. [24] have reported the growth of single crystals of V-VI group compounds from vapour. They obtained platelets and needle crystals of Sb_2Te_3 and As_2Te_3 . But the growth conditions for Bi_2Te_3 needles have not been reported.

Indium telluride belongs to III-VI group compounds. It is receiving increasing attention due to their important optical [25], thermoelectric [26] and

photoelectric properties [27] and their possible applications in switching and memory devices [28]. The structure determination for indium telluride crystals was performed by Zaslavskii et al. [29-30]. They have found that In_2Te_3 exists in two modifications: a low temperature α -form and a high temperature β -form. The α -modification exists below 550-600°C and possesses a statistically ordered fcc structure with lattice constant $a = 18.486 \text{ \AA}$. The space group of this modification is $F\bar{4}3m$ [30]. In the β -modification, the indium atoms and the vacancies are distributed at random leading to a sphalerite structure with lattice constant $a_0 = 6.158 \text{ \AA}$ and space group $F\bar{4}3m$. Most of the physical properties of this compound have been carried out on samples prepared by melt growth techniques [31-34]. Verkelis [35] has grown β -modification of In_2Te_3 crystals by the chemical gas-transport method and obtained needle shaped crystals bounded by (111) planes. Not much work has been reported on the growth and characterization of In_2Te_3 crystals.

6.1.1 Hollow Crystals

Growth of crystal whiskers has been of scientific interest for several hundred years, because their strength approaches the theoretical strength of perfect crystals.

The academic interest in whiskers has been centered around the different growth mechanisms responsible for the growth of whiskers. Investigations into the morphology of the growth surface suggest important conclusions about the growth mechanism. Moreover, hollow crystals find importance for the fabrication of certain devices using electrodes attached to the inner and outer surfaces with favourable geometrical arrangement [36]. As a consequence, extensive studies have been reported on the morphology and growth mechanism of whiskers grown from various substances [37-41]. Hollow crystals of II-VI compounds have been studied by many authors [42-44]. Hollow crystals in V-VI family like As_2Te_3 and Sb_2S_3 - Sb_2Se_3 system were also reported [45,46]. However, very little information is available in the literature on the observation of hollow needles of Bi_2Te_3 and In_2Te_3 . Hence, in view of the research interest to understand the mechanism responsible for the growth of hollow whiskers, an attempt has been made to grow and examine whiskers of $\text{Te}_{1-x}\text{Se}_x$ at compositions $x = 0$ to 10 at % Se, Bi_2Te_3 and In_2Te_3 by physical vapour deposition (PVD) method. Morphological studies of these whiskers have been done and are reported here. The presence of constituent elements in the grown whiskers was analysed using ESCA.

X-ray analysis has also been made to determine the structure and lattice constant.

6.2 EXPERIMENTAL

For the synthesis of $\text{Te}_{1-x}\text{Se}_x$ alloy containing 0 to 10 at % Se, Bi_2Te_3 and In_2Te_3 , high purity elements (99.999%) of tellurium, selenium, bismuth and indium were used. A constant temperature furnace described in chapter 5 was used for mixing the melt of respective samples.

In order to prepare homogeneous alloys of $\text{Te}_{1-x}\text{Se}_x$, appropriate quantities of the materials were vacuum sealed at a pressure of 10^{-5} Torr in thoroughly cleaned pyrex glass ampoules of length 10 cm and diameter 10 mm. The sealed ampoule was kept in the furnace at 500°C for about 24 h. The melt was stirred mechanically for proper mixing of the constituents and it was slowly cooled to the room temperature.

In the case of Bi_2Te_3 and In_2Te_3 , the materials were vacuum sealed in quartz ampoules of length 10 cm and diameter 12 mm. For Bi_2Te_3 , the furnace temperature was raised to 700°C for 24 h and the ampoule was periodically

rotated for homogenization. In the case of In_2Te_3 , the temperature was slowly increased upto 750°C to avoid breaking of the ampoules. The melt was held at this temperature for 48 h and kept for proper mixing of the components. For preparing $\alpha\text{-In}_2\text{Te}_3$, the melt was allowed to cool slowly to room temperature at a rate of 10°C/h , whereas for $\beta\text{-In}_2\text{Te}_3$, the melt was slowly cooled to 480°C and then quenched to ice temperature. Identification of the compounds was made using a philips 1710/00 X-ray powder diffractometer with $\text{CuK}\alpha$ radiation as the X-ray source. The powder diffractogram of the samples revealed that Bi_2Te_3 and α and β -forms of In_2Te_3 had been formed.

About 10 g of the charge thus obtained was used to grow whisker crystals using the PVD method. The charge was sealed in pre-cleaned ampoules at a pressure of 10^{-5} Torr. Growth experiments were carried out in a two zone horizontal gradient furnace which is described in chapter 5. Before starting growth, the growth zone was cleaned by subjecting the ampoules to reverse transport, so that any trace of materials at the growth end of the ampoule would be removed. For growth of $\text{Te}_{1-x}\text{Se}_x$ crystals, ampoules of pyrex glass having 19 cm length and 18 mm outer diameter were used. The source temperature was maintained

at 500°C and the growth temperature was varied from 250 to 300°C. Quartz ampoules of length 19 cm and diameter 15 mm were used for growing Bi_2Te_3 crystals. The temperature of source and growth zones was changed to different values and kept constant during growth to an accuracy of $\pm 1^\circ\text{C}$. The deposition time was around 72 hours. For α and β - In_2Te_3 crystals, quartz ampoules of length 19 cm and diameter 10 mm were used. The temperature difference between the two zones was varied from 80°C to 100°C and kept controlled for about 120 h for the growth of α - In_2Te_3 crystals. In the case of β - In_2Te_3 crystals, the growth zone temperature was kept at 450°C. The growth time was around 140 h. The crystals obtained were in the form of hollow whiskers bounded by smooth prism faces. The as-grown surfaces of the crystals were observed in reflection using Carl-Zeiss Epityp II and Union Versamet-2 metallographic microscopes. XPS analysis was carried out using an ESCALAB MK II spectrometer (VG Scientific Ltd., UK). The experiment was performed using a $\text{MgK}\alpha$ ($h\nu = 1253.6$ eV) source.

6.3 RESULTS AND DISCUSSION

6.3.1 $\text{Te}_{1-x}\text{Se}_x$ Whiskers

The effect of source temperature and growth temperature was studied for the successful growth of

crystals. When the source temperature was kept at 500°C and growth temperature at 250°C, thick needle type crystals were obtained (Fig.6.1) after a growth time of about 100 h. Fig.6.2 shows the whiskers formed when the source temperature was maintained at 500°C and the growth temperature at 300°C. The growth time was about 72 h. The crystals obtained were about 1 cm long with 1 to 2 mm² cross section. Further increase in growth time resulted in no significant change of length, but only the thickness was found to be increased. The XPS survey scans of Te_{0.99}Se_{0.01} and Te_{0.95}Se_{0.05} whiskers are depicted in Figs.6.3(a) and 6.3(b) respectively. Both tellurium and selenium peaks are clearly visible. As shown in these figures, the Te 3d levels are sharp.

It has been observed that whiskers with small concentrations of Se grow along the c-axis and are bounded by (10 $\bar{1}$ 0) prisms planes. The whiskers obtained were hollow with three or four well developed prism faces [47]. Most of the crystals were deposited on the wall of the ampoule between the two dimples. The SEM photograph of a typical whisker is depicted in Fig.6.4(a). Figs.6.4(b) and 6.4(c) show the higher magnification of the tip and prism face of this whisker, where the hollow morphology can be clearly seen.

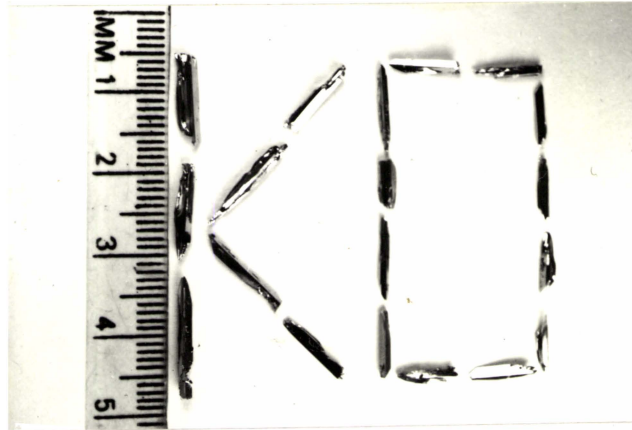


Fig. 6.1

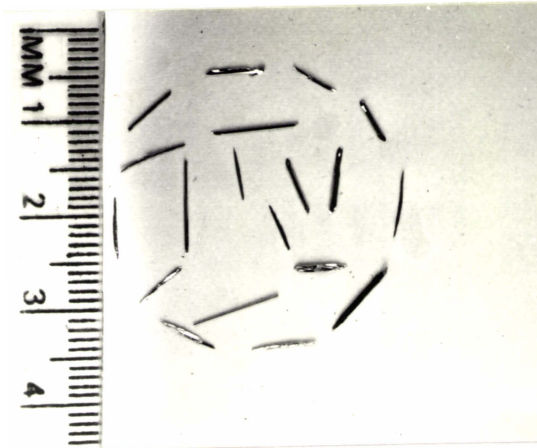


Fig. 6.2

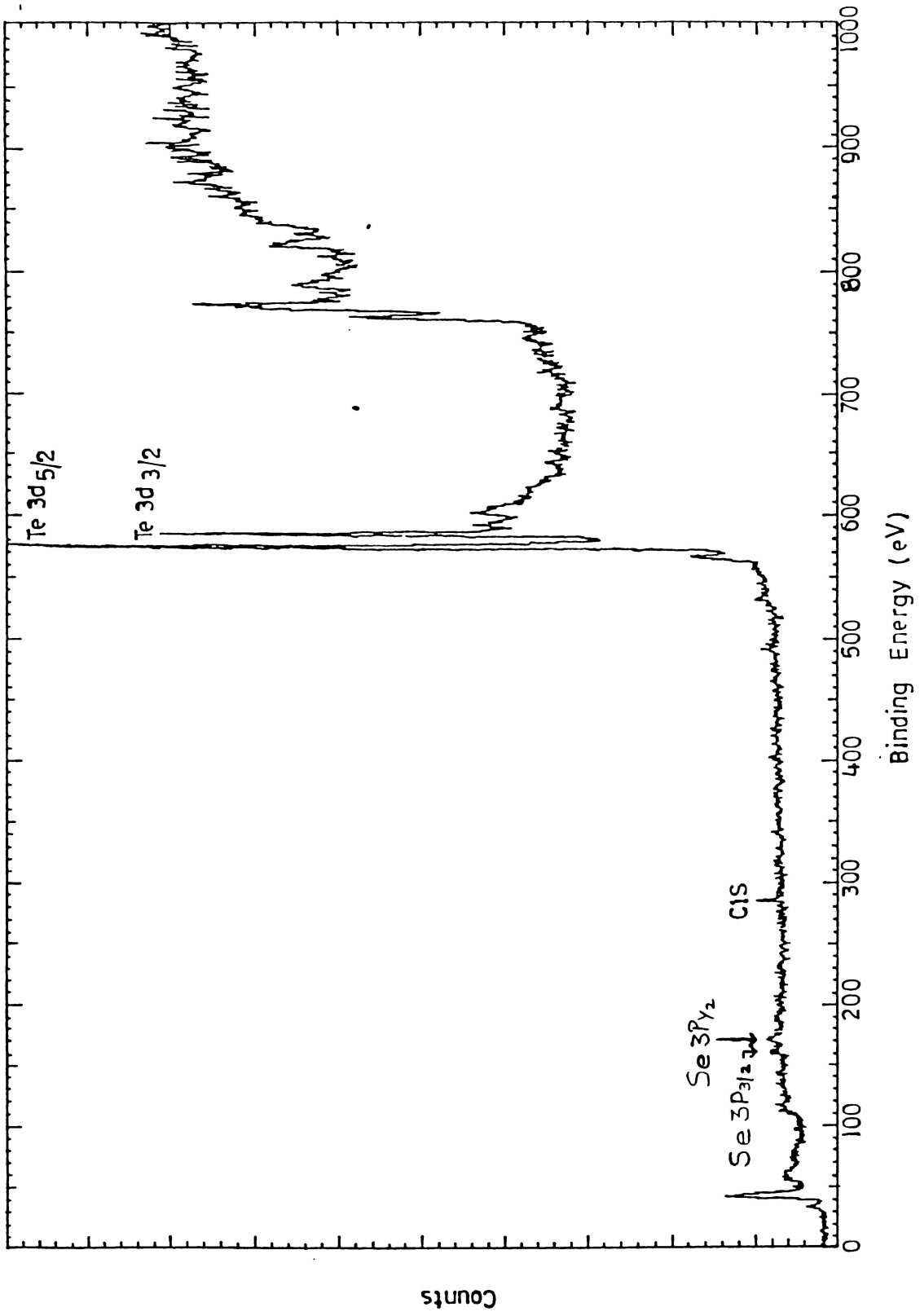


Fig. 6.3(a)

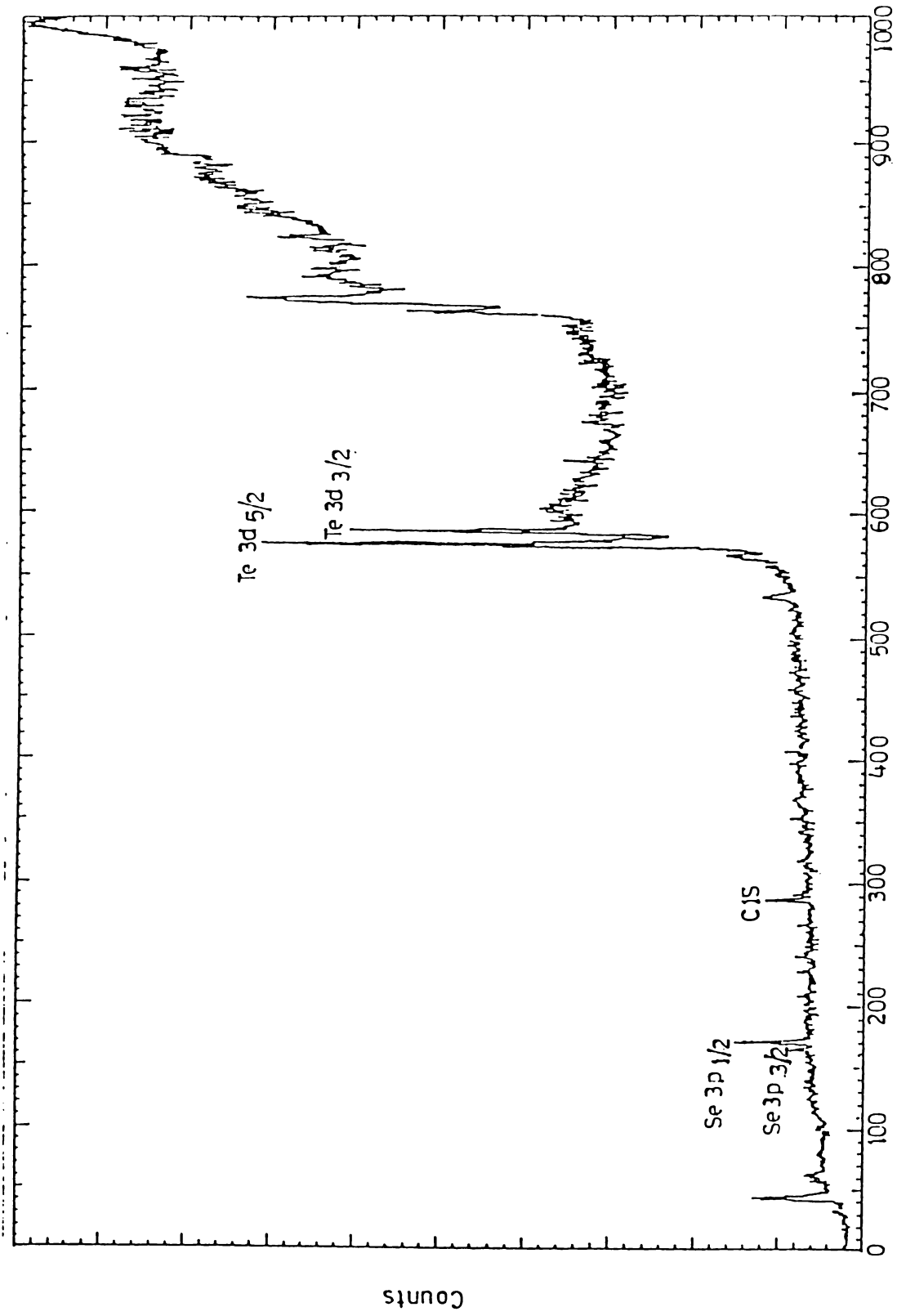


Fig. 6.3(b)

Many interesting observations have been found on the whiskers grown for various concentrations of Se during the present investigations. The outer surfaces of the grown hollow whiskers are usually smooth and the inner surfaces are stepped. Characteristic step like growth layers on the inner side of the prism face of a $\text{Te}_{0.98}\text{Se}_{0.02}$ whisker are shown in Fig.6.5. Fig.6.6 indicates the numerous striations on the inner surface of the prism plane of a $\text{Te}_{0.97}\text{Se}_{0.03}$ whisker. The growth features are lying parallel to the c-axis. The sides of the whiskers are further developed by the layer mechanism.

On examining the upper flat surface of the whiskers, it has been observed that a cavity is spreading from one edge of the whiskers. This is shown in Figs.6.7 and 6.8. This leads to the conclusion that the whiskers are grown from the tip. Fig.6.9 shows a hollow $\text{Te}_{0.97}\text{Se}_{0.03}$ whisker with a small whisker lying on its prism face. The irregularities in the growth conditions are responsible for this. When the growing surface is not perfectly planar, small spurs may form on the surface and join together with some mismatch, due to some local super-cooling or irregularity in growth rate. Observations on the prism faces of some whiskers showed growth of short

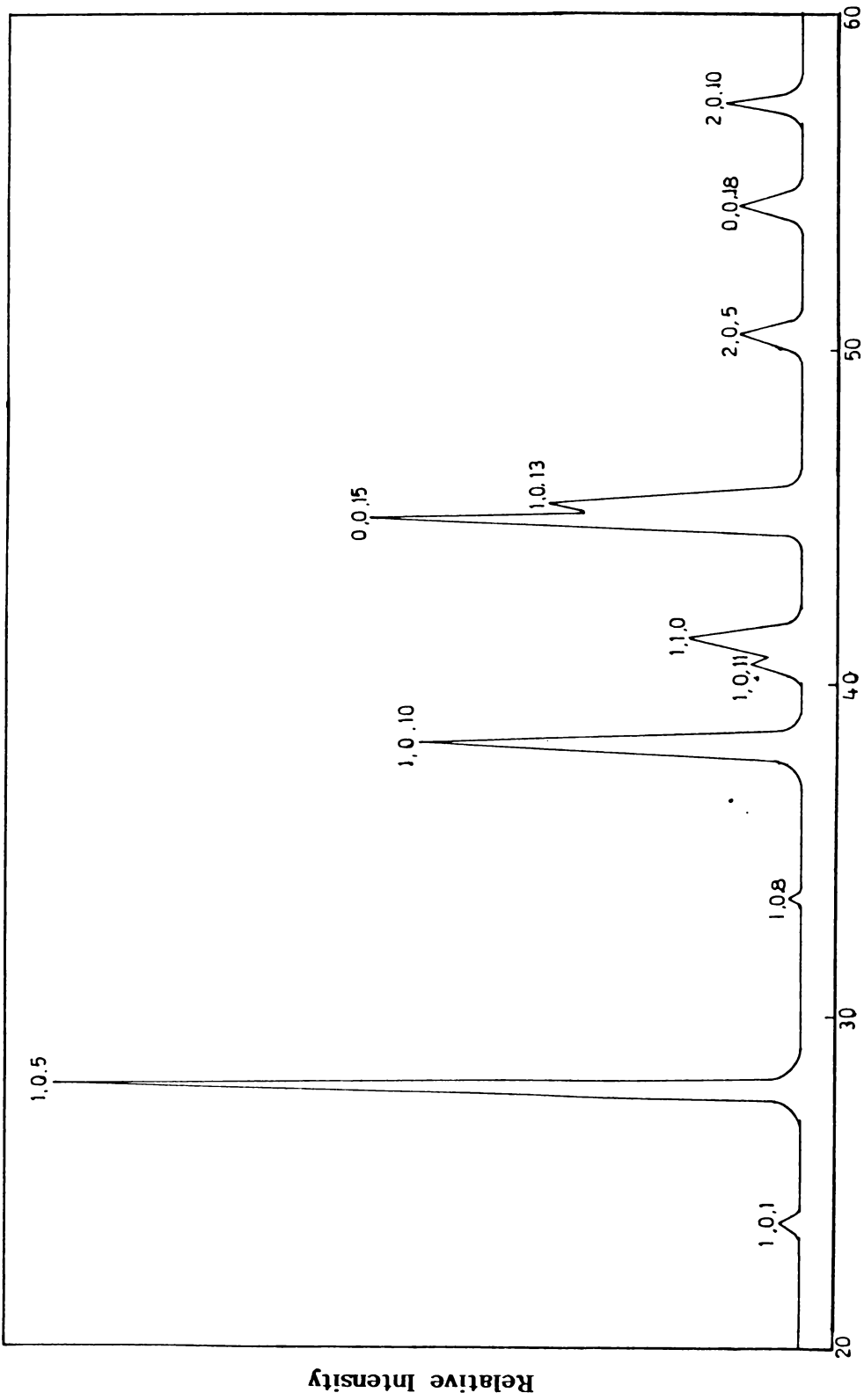
side whiskers (Fig.6.10). Some of the whiskers also showed rough surfaces due to insufficient material supply or due to temperature fluctuations. Fig.6.11 shows such a surface of a $\text{Te}_{0.90}\text{Se}_{0.10}$ whisker.

6.3.2 Bi_2Te_3 Whiskers

Most of the crystals grow as needles when the growth zone temperature was kept at 20°C less than the melting point of the compound [48]. A single source may produce thick hollow needles of about 10 mm long as shown in Fig.6.12.

Fig.6.13 shows the X-ray diffraction profile of Bi_2Te_3 whiskers. The calculated d-values are presented in Table 6.1. The rhombohedral unit cell dimensions calculated from the X-ray powder analysis are found to be $a_R = 10.470 \text{ \AA}$ and $\alpha_R = 24^\circ 9' 45''$. The values agreed well with that reported in the literature [13]. Surface composition of Bi_2Te_3 whiskers was analysed using ESCA and the XPS spectrum is shown in Fig.6.14.

Fig.6.15 shows the prism face of a well developed crystal. When the prism faces were not developed, axial cavities extending parallel to the c-axis were observed.



2θ (Deg.)

Fig. 6.13

Table 6.1 X-ray powder data for bismuth telluride crystal

hkl*	Standard Pattern		Grown Crystal	
	d (Å)	I/I ₀	d (Å)	I/I ₀
1,0,1	3.780	8	3.769	7
1,0,5	3.220	100	3.218	100
1,0,8	2.694	5	2.692	6
1,0,10	2.378	55	2.376	54
1,0,11	2.237	11	2.232	11
1,1,0	2.191	35	2.191	19
0,0,15	2.032	40	2.029	60
1,0,13	1.995	6	1.998	36
2,0,5	1.810	20	1.810	13
0,0,18	1.694	5	1.692	13
2,0,10	1.610	16	1.609	14

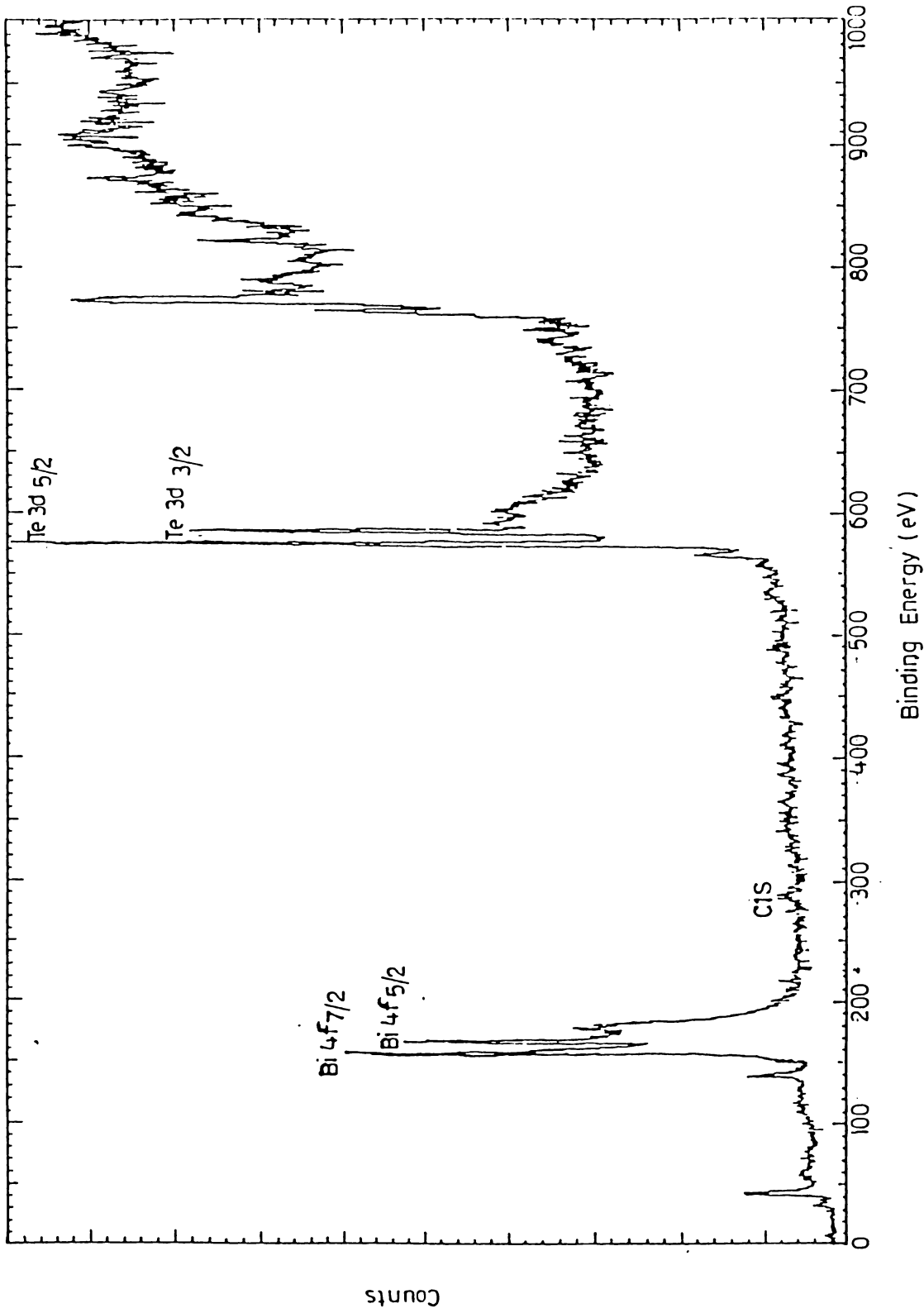


Fig. 6.14

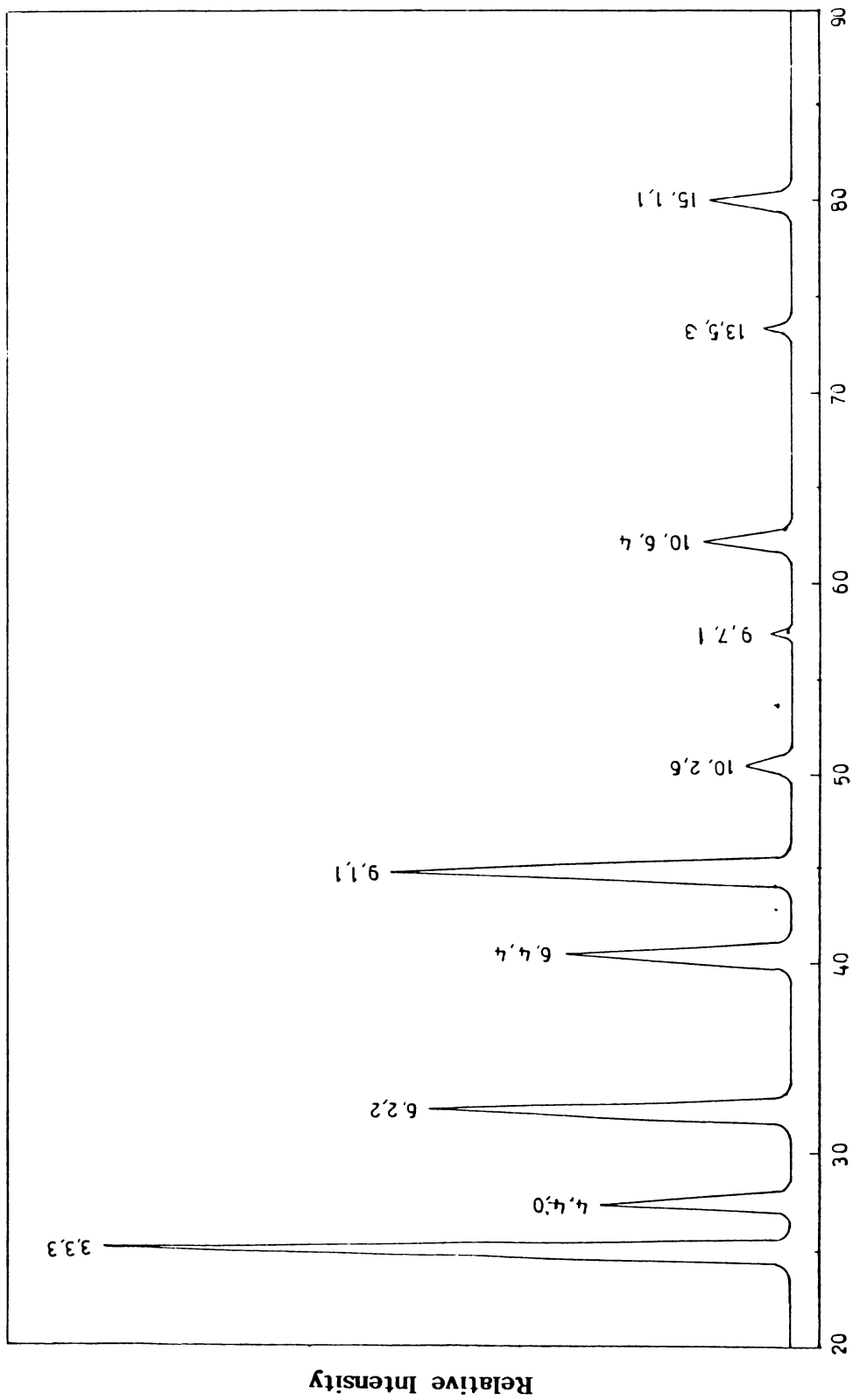
The presence of axial channels indicative of hollow growth are shown in Fig.6.16. Fig.6.17 reveals clearly the hollow nature of a Bi_2Te_3 whisker. The hollow crystals with partially developed prism faces had been used to study the growth features inside the prism faces. Fig.6.18 shows growth layers on the prism face of a whisker. Here layers of different thicknesses are advancing in the direction of c-axis. This is due to the consecutive deposition of layers by tangential motion of steps. Microscopic observation on the inner surface of whiskers showed growth striations parallel to the c-direction (Fig.6.19) which are forming the walls of whiskers. Growth layers propagating from the cavities near the edge of a whisker is shown in Fig.6.20. From this figure, it is seen that thick steps are more near the cavities and become thinner as they approach the base end of the whisker.

Bismuth telluride crystals exhibit different forms due to the anisotropy of supersaturation in the growth region. In some cases it is found that two independent whiskers meeting at a point and still continued their growth forming an X-shape and a Y-shape (Fig.6.21). This suggests that even though the tip of a growing whisker met another whisker, the growth continued further. A large

number of microcrystals were also found overgrowing on some whiskers (Fig.6.22). The overgrowth may be developed during the later stage of growth. Another interesting observation revealed the formation of irregular twisted growth of these whiskers. A more characteristic defect is a sharp kink in the axis of a whisker. Fig.6.23 shows a kinked whisker, the growth kink has an angle of about 30° . This type of growth kinks were observed by Baker [49], who measured the angles between the kink segments in zinc whiskers and suggested that they are the possible angles between the orthohexagonal axes of a single crystal. The kinking phenomenon reflects a fluctuation during growth at the site of the origin of the whisker, that is, in the nucleating grain.

6.3.3 α - In_2Te_3 Whiskers

Hollow crystals of α - In_2Te_3 were obtained after 120 h [50]. Fig.6.24 illustrates some typical needle shaped crystals grown during the present study. A few platelets were also observed. In Fig.6.25 the as-grown faces of the crystals are depicted. The X-ray diffraction pattern of these crystals is shown in Fig.6.26. The calculated d values were critically compared with standard d values given by Mamadev et al. [34] and are listed in



2θ (Deg.)

Fig. 6.26

Table 6.2. From this, it is fairly clear that the present crystals correspond to the α -modification of In_2Te_3 . This fact is also confirmed by the determination of lattice constant, which is found to be $a = 18.471 \text{ \AA}$. The chemical composition of In_2Te_3 crystals has been examined using ESCA (Fig.6.27).

The prism faces of whiskers showed many characteristic growth patterns. Fig.6.28 shows the channel formation observed on the side of a whisker. On some of the needle surfaces, layer growth fronts were also formed (Fig.6.29). In Figs.6.30(a) and 6.30(b), growth steps propagating from the tip of whiskers can be seen. From these observations, it can be inferred that the growth of whiskers is accelerated from the tip. A hollow cavity spreading from one edge of the whisker is depicted in Fig.6.31. Fig.6.32 shows the deposition of microcrystallites on the wall of the tube. As seen the hollow cavities are present on all the surfaces.

6.3.4 β - In_2Te_3 Whiskers

Fig.6.33 shows the X-ray diffraction pattern for β - In_2Te_3 whiskers. The results of indexing this pattern are listed in Table 6.3, which is found to be quite

Table 6.2 X-ray Powder Data for α -In₂Te₃ Crystal

Bragg angle, θ (deg.)	Calculated, d (\AA)	Reported [34], d (\AA)	I/I ₀	hkl
12.54	3.550	3.552	100	3,3,3
13.67	3.260	3.264	30	4,4,0
16.12	2.775	2.772	55	6,2,2
20.17	2.235	2.232	35	6,4,4
22.36	2.026	2.024	60	9,1,1
25.22	1.809	1.808	10	10,2,6
28.55	1.613	1.611	7	9,7,1
31.04	1.495	1.493	16	10,6,4
36.63	1.292	1.293	8	13,5,3
38.99	1.225	1.226	15	15,1,1

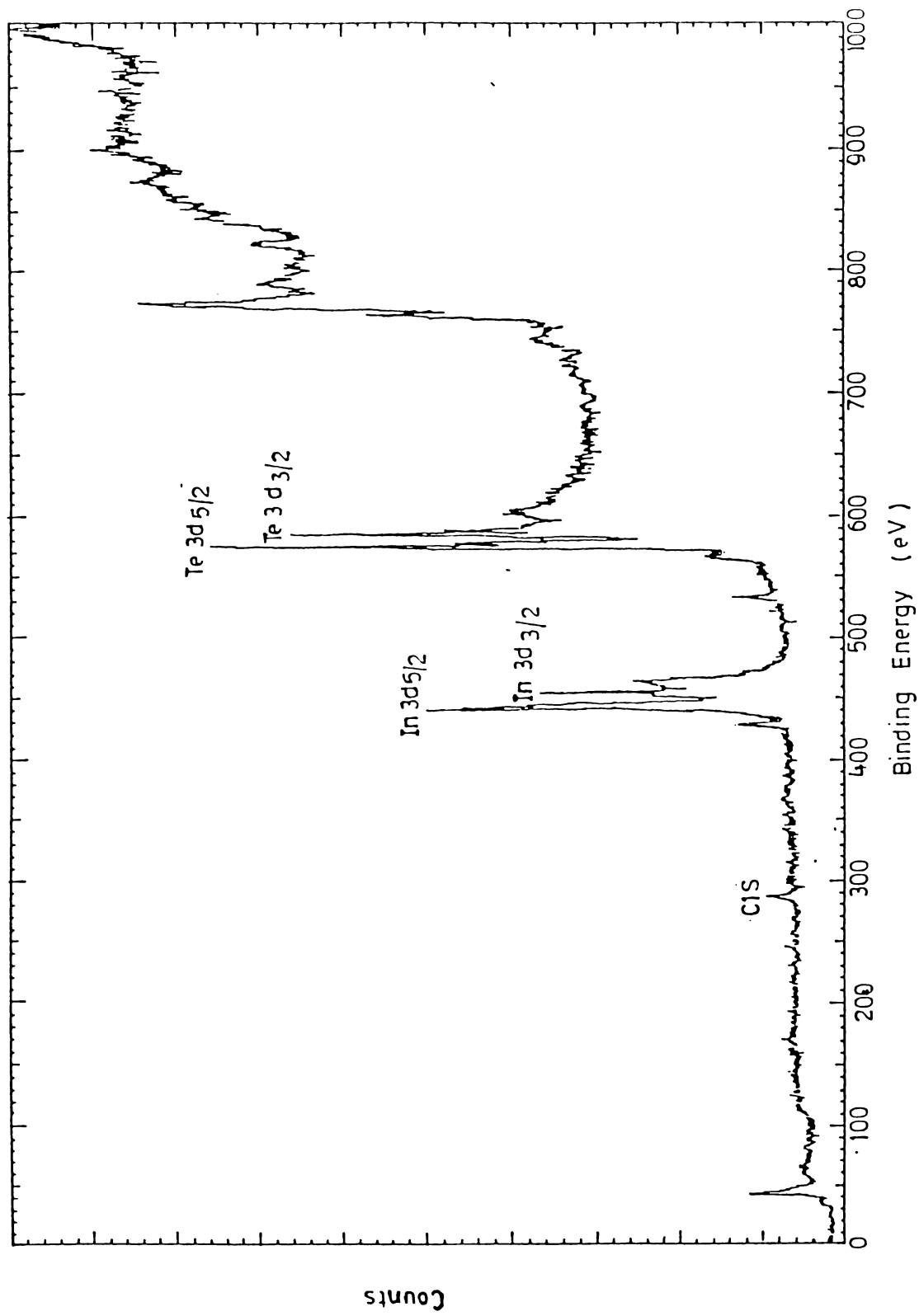


Fig. 6.27

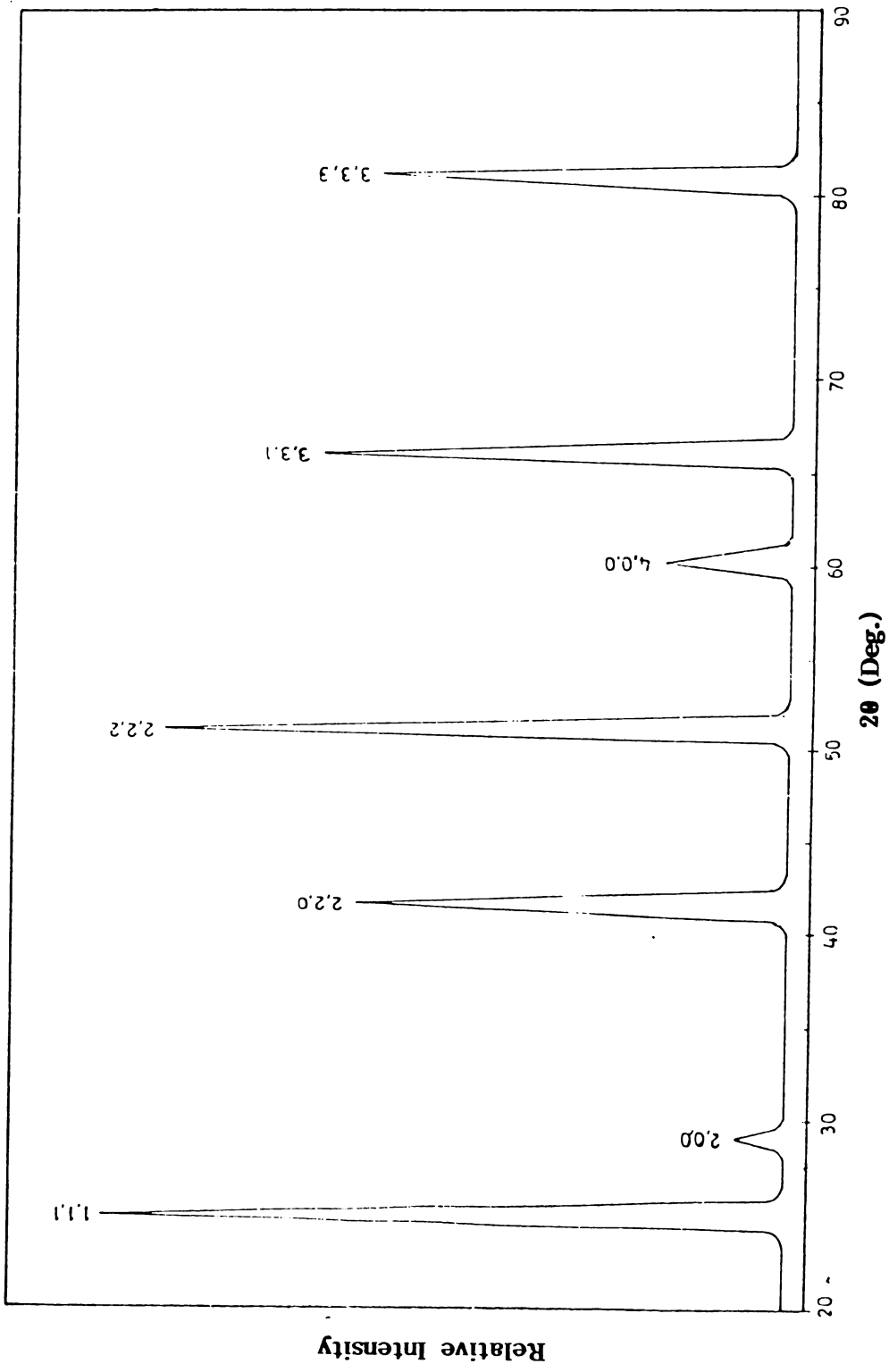


Fig. 6.33

Table 6.3 X-ray powder data for β -In₂Te₃ crystal

Bragg angle, θ (deg.)	Calculated, d (Å)	Reported [35], d (Å)	I/I ₀	hkl
12.51	3.558	3.548	100	1,1,1
14.57	3.064	3.069	10	2,0,0
20.71	2.179	2.178	65	2,2,0
25.68	1.778	1.779	92	2,2,2
30.07	1.538	1.539	21	4,0,0
33.00	1.415	1.415	70	3,3,1
40.56	1.185	1.186	62	3,3,3

consistent and reproducible with that reported in [35]. The value of lattice constant is found to be $a_0 = 6.164 \text{ \AA}$.

Fig.6.34 depicts needle type whiskers deposited on the wall of the tube. In this case also, almost all the whiskers were grown hollow [51]. $\beta\text{-In}_2\text{Te}_3$ crystals are also interesting from the point of their surface features. Growth patterns indicative of layer growth were observed on the prism face of whiskers (Figs.6.35(a) and 6.35(b)). Fig.6.36 shows the propagation of steps from the tip of a crystal. In most cases, the inner surfaces of the crystals were covered with numerous striations and ridges as shown in Fig.6.37. In Fig.6.38, an irregular shaped needle clearly depicting the hollow nature can be seen: the hollow cavity is wider at the upper edge of the needle and tapers along the prism face. A smooth well developed crystal is shown in Fig.6.39. In some whiskers, the tips were kinked as shown in Fig.6.40.

6.3.5 Growth Mechanism of Crystals

There are different growth mechanisms responsible for the growth of whiskers. Some theories of whisker growth require the presence of a screw dislocation lying along the axis of the whisker. When a crystal grows by the

addition of atoms or molecules along a step provided by screw dislocation, the step will wind itself into a helicoid. Hence the surfaces of crystals grown by screw dislocation mechanism are often covered with growth spirals or other distinctive features relating to screw dislocation [52]. But in the present case, no such observations are found, which indicates that screw dislocation mechanism is not active in the growth of $\text{Te}_{1-x}\text{Se}_x$, Bi_2Te_3 and α and β - In_2Te_3 whiskers.

Another mechanism responsible for the growth of whiskers is vapour-liquid-solid (VLS) mechanism. If the growth of crystal is taking place by this mechanism, a small globule is usually revealed at the tip of whiskers. The observation on the tip part of the grown whiskers has not found any globule formation. This also suggests that in the present case, the whiskers are not grown due to VLS mechanism.

Layer-by-layer growth of atomically smooth surface is an important mechanism by which the crystalline lattice is built. In layer-by-layer growth, the kinks are concentrated at steps only. Elementary steps are separated by atomically smooth areas. The growth of stepped surface

is further achieved only by the motion of existing steps, and the formation of fresh nuclei. As mentioned earlier, a number of whiskers grown in the present work have shown characteristic growth patterns lying parallel to the c-axis. The growth features of $\text{Te}_{1-x}\text{Se}_x$ whiskers indicative of layer growth are seen in Figs.6.5 and 6.6. In the case of Bi_2Te_3 whiskers, growth layers spreading on the prism faces were observed (Figs.6.18, 6.19 and 6.20). From these figures, it is seen that the step height of the layers is decreasing during their tangential motion. Growth steps forming the walls of whiskers are visible in Fig.6.19. Layer growth fronts were also observed on the prism faces of $\alpha\text{-In}_2\text{Te}_3$ (Figs.6.28, 6.29, 6.30(a) and 6.30(b)) and $\beta\text{-In}_2\text{Te}_3$ whiskers (Figs.6.35(a), 6.35(b), 6.36 and 6.37). From all these observations, it is clear that the whiskers grown in the present case grow by spreading of layers on their prism faces due to layer growth mechanism. The source of growth steps is provided by two-dimensional nucleation, which determines the growth rate of whiskers. The observations on layer growth are similar to those reported for BiSeI [53].

During the present investigation, the formation of hollow crystals has been observed in all cases. For

$\text{Te}_{1-x}\text{Se}_x$ crystals, hollow cavities are observed from the tip (Fig.6.7) indicating that the crystals are growing from the tip. The theory developed for whiskers growing at the tip parallels to that of bulk crystals. If the axis of whisker growth is the direction of high density and if the faces that bind the whiskers are low energy surfaces, the nucleation on the tip will be easier compared to the other faces. Once a layer is completed on the whisker tip, subsequent growth will be favoured only by having additional energy. At higher supersaturations, the nucleation rates at apexes and edges are the highest due to the enhanced heat transfer and supersaturation. This mode of growth results in hollow regions with steps inside.

For Bi_2Te_3 whiskers, axial channels due to hollow growth were observed. When the prism faces surrounding the axial cavities (Fig.6.16) have started to grow, the tendency of these faces to grow in any direction other than the c-direction slows down and the crystal increases in length. After growth along the c-direction for a considerable length, it stops growing in the c-direction also. At this stage, the periphery of the cavity in the edge (Fig.6.20) becomes the preferential growth site and starts growing from the edge.

In the case of α - In_2Te_3 whiskers, hollow cavities are formed on all the surfaces (Fig.6.32). It is due to the fact that when the vapour from the source arrives in the colder portion of the tube during growth it condenses and forms extremely minute microdrops on the wall. At the instance of solidification, a very minute hollow cavity is created on the top surface of the crystallite. The process of filling the cavities forms the sides of whisker. This give rise to the formation of hollow nature on the inner prism faces. The edge of hollow β - In_2Te_3 whiskers also showed cavities (Fig.6.38). Since the formation of two-dimensional nucleation at the edges is more than at the centre of the face, the layers from the edges of the growing faces move towards the centre.

6.3.6 Observation of Stacking Faults on the Basal Plane of Bi_2Te_3 Crystals

Stacking faults and the associated partial dislocations have been observed by several workers. The first direct observation of prismatic loops in aluminium was made by Hirsch et al. [54]. Eikum and Thomas [55] have reported the formation of diamond-shaped prismatic loops in quenched fcc metals. Ning and Ye [56] have observed intrinsic stacking faults closed by two shockley partial dislocations

in the (111) plane of SiC by high resolution electron microscopy. Tendeloo et al. [57] have observed Frank type sessile dislocations in $\text{YBa}_2\text{Cu}_3\text{O}_7$. The nucleation of dislocation loops from vacancies has been studied by Jackson [58]. The formation of dislocation loops is also pronounced in crystals with layer type structures. The weak binding between layers can result in stacking faults of low energy and hence unit dislocations are usually widely dissociated into partial dislocations [59]. Grigoriadis and Stoemenos [60] have observed dislocation configurations due to stacking faults in silicon ditelluride single crystals. Delavignette and Amelinckx [61] observed large hexagonal loops on the cleavage plane of Sb_2Te_3 crystals slowly grown from the melt. Their observations indicated that these are prismatic loops resulting from deviations of the stoichiometric composition. But the observation of stacking faults on the basal (0001) planes of Bi_2Te_3 crystals grown from vapour phase has not been investigated so far.

The temperature difference between the source zone and growth zone (ΔT) was found to have a strong effect on the growth of crystals. At low values of ΔT , the growth was slow and resulted in whiskers of stoichiometric composition whose morphological studies have already been

described in section 6.3.2. But at large values of ΔT , the whisker crystals were found to be developed with all their six sides. As a result, short hexagonal prisms (Fig.6.41) having pyramidal tips were formed. During the growth, stacking faults were created on the basal planes of all crystals bordered by partial dislocations as a consequence of condensation of excess vacancies. Since the bonds are weakest and diffusion is easiest between two $\text{Te}^{(1)}$ layers, vacancy loops will preferentially nucleate in the basal plane. Due to the preferential occupation of the Te layers by vacancies during slow cooling, the crystals become enriched with these point defects and resulted into the formation of non-stoichiometric crystals. Similar results were reported by Delavignette and Amelinckx [61] on the cleavage plane of melt grown Sb_2Te_3 crystals, who explained the reason for their occurrence on the basis of deviations from stoichiometry. To support this point of view, they examined cleavage planes of melt grown Bi_2Te_3 crystals which are nearer to stoichiometry but couldn't observe any dislocation loops. In the present work also, such type of prismatic loops were not observed on the cleavage plane of stoichiometric Bi_2Te_3 crystals grown by horizontal zone levelling method. From these facts, it is clear that the loops were formed due to the deviations from stoichiometric

composition of the crystals [62]. Tendeloo et al. [57] also concluded that non-stoichiometry can be accommodated by means of Frank type sessile dislocations.

Fig.6.42(a) shows the hexagonal cross section of another crystal, showing the precipitation of Te vacancies in the form of prismatic loops. The angle between the adjacent sides of the hexagonal cross section being about 120° . The vacancies formed migrate to the dislocations in their vicinity and become absorbed due to the fact that the stress field of the dislocations exert an attraction on the point defects [63]. In the present case, the region of attraction is mainly on the central part of the basal plane. As a consequence of elastic interaction between vacancies and dislocations, the centre of a prismatic loop is the preferred site for nucleation of a new prismatic loop [64] which may lead to the formation of pairs of loops. The higher magnification of the central part of Fig.6.42(a) is shown in Fig.6.42(b), which reveals the formation of concentric pairs of circular prismatic loops. The loops are formed due to Frank partial dislocations and are sessile, since they cannot move by glide. In order to confirm whether the loops are formed by condensation of Te vacancies, the crystals were etched in the etchant 10 mg I_2

+ 7 ml H_2SO_4 + 10 ml CH_3OH at an elevated temperature 100°C for 2 min. All the prismatic loops vanished and closed hexagonal loops exhibiting the hexagonal symmetry of the basal plane were observed. Fig.6.42(c) is the etched face of the crystal shown in Fig.6.42(a) showing such features.

Since the basal plane of Bi_2Te_3 is a glide plane, nucleation of glissile dislocations due to shockley partials were also observed on some basal planes along with Frank partials (Fig.6.43(a)). Since the patterns are not clearly visible at lower magnification, they are observed under higher magnifications. Fig.6.43(b) depicts the full view of sessile loops and glissile dislocations on the basal plane shown in Fig.6.43(a). The splitting of the total dislocation lying in the basal plane into an extended dislocation consisting of a pair of Shockley partials connected by a strip of fault is also visible in the figure. It is interesting to note that all the dislocation lines are parallel to the adjacent sides of the hexagonal plane. The higher magnification of the regions marked A, B and C in Fig.6.43(b) is shown in Figs.6.43(c), 6.43(d) and 6.43(e) respectively. In Fig.6.43(c) concentric pairs of perfect hexagonal loops can be seen. The change in shape

of the loops observed in Figs.6.42(b) and Fig.6.43(c) may be attributed to the change in cooling rates of the crystals. The interaction between sessile loops and glissile dislocations is also seen in Fig.6.43(c). Various interactions among several types of dislocations in zinc have been described in detail by Fourdeux et al. [65]. They observed loops of sessile dislocations formed by condensation of point defects and partial glissile dislocations by electron transmission microscopy and by X-ray diffraction microscopy. The reaction of three dislocations intersecting one another to form nodes is also observed. Fig.6.43(d) depicts a typical node created by the interaction of extended dislocations. In Fig.6.43(e) the interaction of parallel dislocation segments forming steps and kinks are shown. Fig.6.44(a) represents the basal plane (shown in Fig.6.43(a)) after etching in 10 mg I_2 +7 ml H_2SO_4 + 10 ml CH_3OH solution at 100°C for 2 min. In this case also, the prismatic loops disappeared. On comparing Figs.6.43(a) and 6.44(a), it is seen that the contrast of the dislocation lines was considerably increased after etching. Moreover, rows of etch pits and etch grooves were formed along the dislocation segments (Figs.6.44(b), 6.44(c) and 6.44(d)). Fig.6.44(d) is the higher magnification of the region marked D in Fig.6.43(b) after etching.

From these observations it is evident that all the lines formed in the basal planes are associated with dislocations. The region marked E in Fig.6.43(b) after etching is shown in Fig.6.44(e). The creation of a pair of kinks in the straight dislocation segment is clearly revealed.

6.4 CONCLUSION

Hollow whiskers of $\text{Te}_{1-x}\text{Se}_x$, Bi_2Te_3 and α and β - In_2Te_3 have been grown by PVD method. The growth features observed on the prism faces indicate that layer growth mechanism is responsible for the growth of whiskers. A possible explanation is given to account for the hollow nature of crystals considering the two dimensional nucleation.

Concentric pairs of prismatic loops are observed on the basal plane of short hexagonal prisms of Bi_2Te_3 , due to the deviations from stoichiometric composition resulting from the condensation of Te vacancies. Interactions between sessile loops and glissile dislocations are observed.

6.5 FIGURE CAPTIONS

Fig.6.1: Needle type crystals of $\text{Te}_{1-x}\text{Se}_x$.

Fig.6.2: Whiskers of $\text{Te}_{1-x}\text{Se}_x$.

Fig.6.3(a): X-ray photoelectron spectrum of $\text{Te}_{0.99}\text{Se}_{0.01}$ whisker.

Fig.6.3(b): X-ray photoelectron spectrum, of $\text{Te}_{0.95}\text{Se}_{0.05}$ whisker.

Fig.6.4(a): SEM photograph of a $\text{Te}_{0.99}\text{Se}_{0.01}$ whisker.

Fig.6.4(b): SEM photograph showing the tip of whisker in Fig.6.4(a).

Fig.6.4(b): SEM photograph showing the prism face of whisker in Fig.6.4(a).

Fig.6.5: Step-like growth features on the prism face of a $\text{Te}_{0.98}\text{Se}_{0.02}$ whisker.

Fig.6.6 Parallel striations on the inner prism face of a $\text{Te}_{0.97}\text{Se}_{0.03}$ whisker

- Fig.6.7 Formation of a cavity from the tip of a $\text{Te}_{0.96}\text{Se}_{0.04}$ whisker.
- Fig.6.8 Formation of a cavity from the tip of a $\text{Te}_{0.94}\text{Se}_{0.06}$ whisker.
- Fig.6.9 A hollow $\text{Te}_{0.97}\text{Se}_{0.03}$ whisker with a small whisker lying on it.
- Fig.6.10 Growth of short side whiskers on a $\text{Te}_{0.92}\text{Se}_{0.08}$ whisker.
- Fig.6.11 Rough surface of a $\text{Te}_{0.90}\text{Se}_{0.10}$ whisker.
- Fig.6.12 Needle crystals of Bi_2Te_3 .
- Fig.6.13 X-ray diffraction profile of Bi_2Te_3 whisker.
- Fig.6.14 X-ray photoelectron spectrum of Bi_2Te_3 whisker.
- Fig.6.15 Prism face of a Bi_2Te_3 whisker.
- Fig.6.16 Channel formation on an incomplete prism face of a Bi_2Te_3 whisker.

- Fig.6.17 A hollow Bi_2Te_3 whisker.
- Fig.6.18 Growth layers on the prism face of a Bi_2Te_3 whisker.
- Fig.6.19 Growth striations on the inner surface a Bi_2Te_3 whisker.
- Fig.6.20 Propagation of growth layers from the edge of a Bi_2Te_3 whisker.
- Fig.6.21 Whiskers of Bi_2Te_3 meeting together to form an X-shape and Y-shape.
- Fig.6.22 Surface of a Bi_2Te_3 whisker showing overgrowth of microcrystals.
- Fig.6.23 A kinked Bi_2Te_3 whisker having 30° growth kink.
- Fig.6.24 Needle crystals of $\alpha\text{-In}_2\text{Te}_3$.
- Fig.6.25 As-grown faces of $\alpha\text{-In}_2\text{Te}_3$ crystals.
- Fig.6.26 X-ray diffraction profile of $\alpha\text{-In}_2\text{Te}_3$ whisker.

- Fig.6.27 X-ray photoelectron spectrum of In_2Te_3 crystals.
- Fig.6.28 Channel formation on the prism face of a $\alpha\text{-In}_2\text{Te}_3$ whisker.
- Fig.6.29 Growth patterns on the prism face of a $\alpha\text{-In}_2\text{Te}_3$ whisker.
- Figs 6.30(a) Growth steps propagating from and the tip of and 6.30(b) $\alpha\text{-In}_2\text{Te}_3$ whiskers.
- Fig.6.31 $\alpha\text{-In}_2\text{Te}_3$ needle showing hollow cavities in the tip.
- Fig.6.32 Hollow structure on the surface of microcrystallites of $\alpha\text{-In}_2\text{Te}_3$.
- Fig.6.33 X-ray diffraction profile of $\beta\text{-In}_2\text{Te}_3$ whisker.
- Fig.6.34 Needle type whiskers of $\beta\text{-In}_2\text{Te}_3$ deposited on the wall of the tube.
- Figs 6.35(a) Growth layers on the prism face of $\beta\text{-In}_2\text{Te}_3$ and 6.35(b) whiskers.

Fig.6.36 Propagation of steps from the tip of a β - In_2Te_3 whisker.

Fig.6.37 Striations and ridges on the inner prism face of a β - In_2Te_3 whisker.

Fig.6.38 A hollow β - In_2Te_3 needle.

Fig.6.39 A well developed β - In_2Te_3 crystal.

Fig.6.40 A kinked β - In_2Te_3 whisker.

Fig.6.41 SEM photograph of a short hexagonal prism of Bi_2Te_3 whisker.

Fig.6.42(a) Hexagonal cross section of a Bi_2Te_3 crystal.

Fig.6.42(b) Cricular prismatic loops on the basal plane shown in Fig.6.42(a).

Fig.6.42(c) The basal plane shown in Fig.6.42(a) after etching.

Fig.6.43(a) Another basal plane of a Bi_2Te_3 crystal.

Fig.6.43(b) Formation of sessile loops and glissile dislocations on the basal plane shown in 6.43(a) [Marker, 1 div. = 10 μ m]

Fig.6.43(c) Higher magnification of the region A shown in Fig.6.43(b) [Marker, 1 div. = 1 μ m]

Fig.6.43(d) Higher magnification of the region B shown in Fig.6.43(b).

Fig.6.43(e) Higher magnification of the region C shown in Fig.6.43(b).

Fig.6.44(a) Basal plane of Bi₂Te₃ crystal shown in Fig.6.43(a) after etching.

Fig.6.44(b) Photograph showing the regions in Figs.6.43(d) and 6.44(c) and 6.43(e) after etching.

Fig.6.44(d) Higher magnification of the region marked D in Fig.6.43(b) after etching.

Fig.6.44(e) Higher magnification of the region marked E in Fig.6.43(b) after etching.

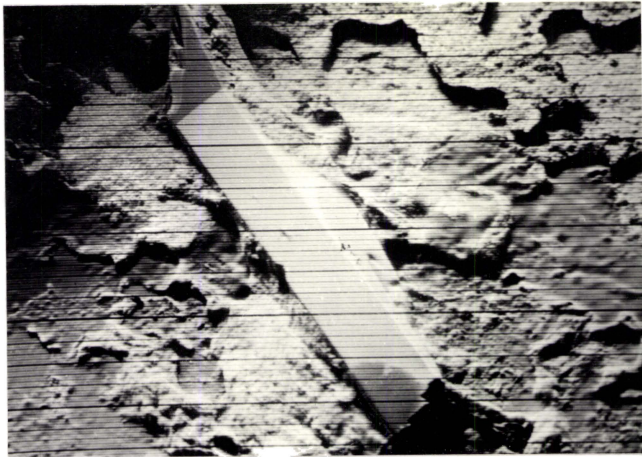


Fig. 6.4(a)

(x 50)



Fig. 6.4(b)

(x 240)

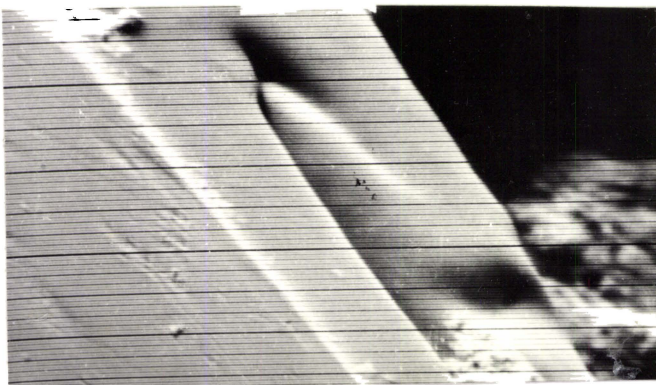


Fig. 6.4(c)

(x 350)

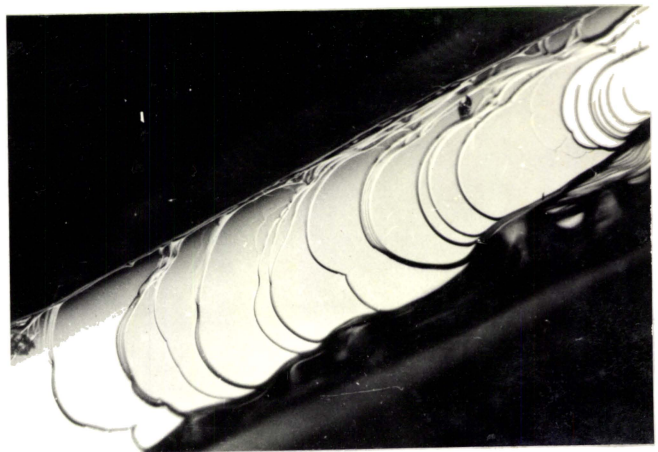


Fig. 6.5

(x 80)

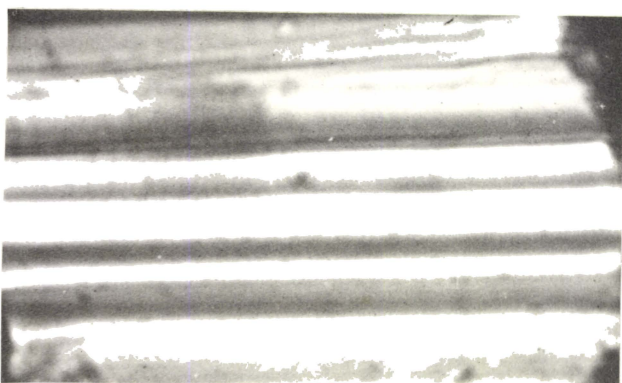


Fig. 6.6

(x150)

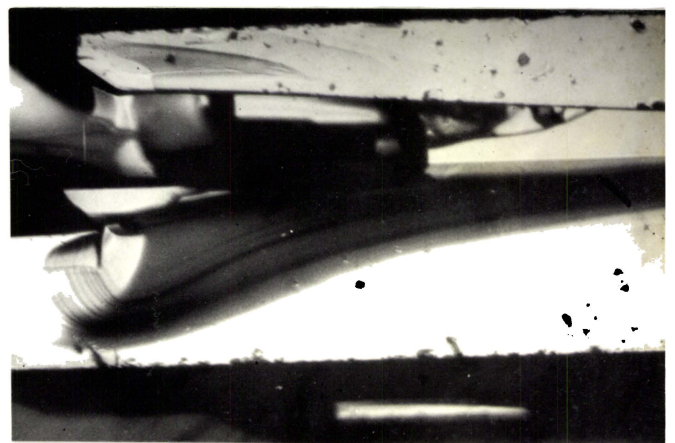


Fig. 6.7

(x100)

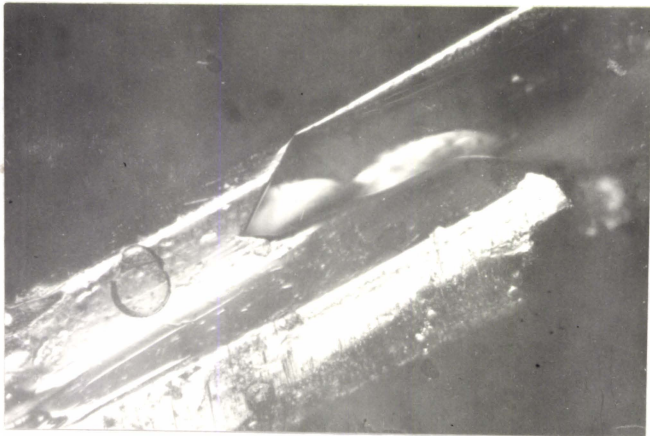


Fig. 6.8

(x80)

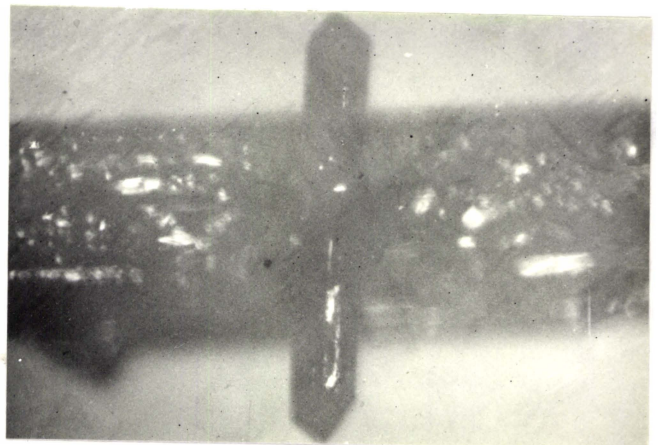


Fig. 6.9

(x80)

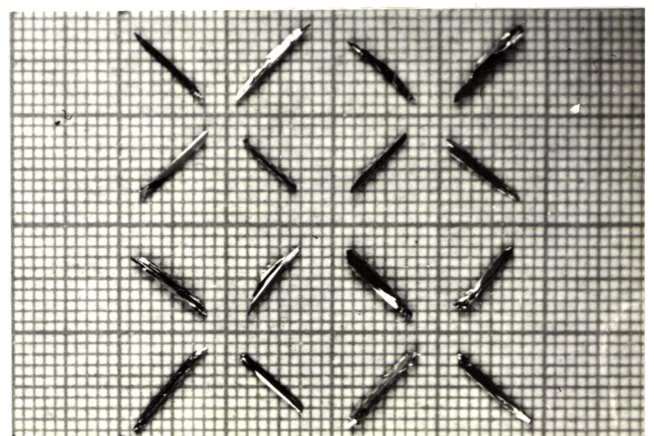


Fig. 6.10

(x 50)



Fig. 6.11



(x240) Fig. 6.12

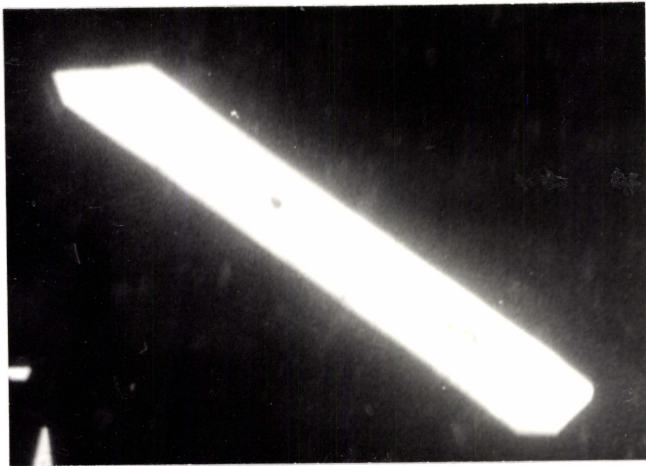


Fig. 6.15

(x33)

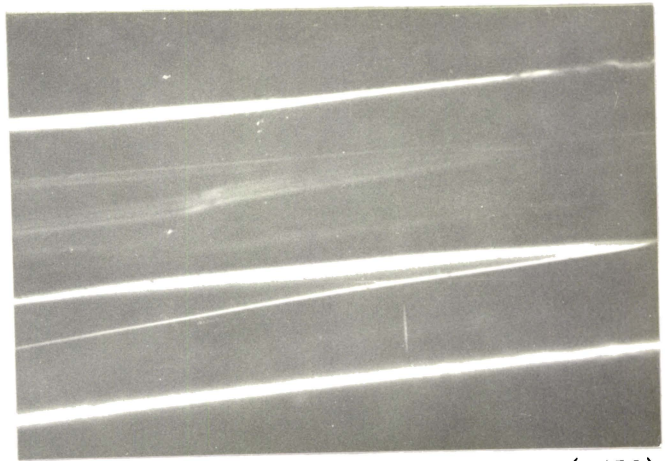


Fig. 6.16

(x150)

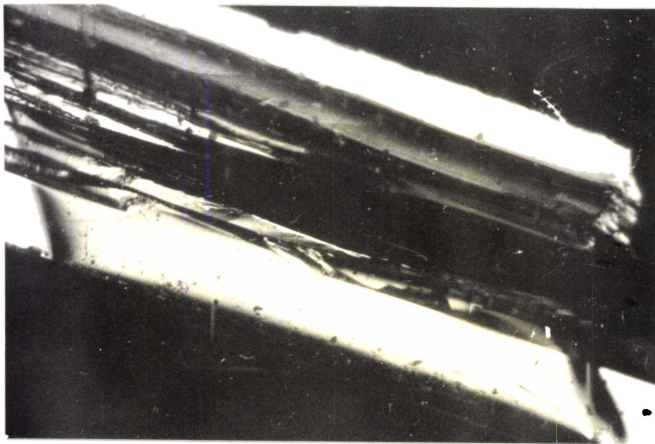


Fig. 6.17

(x100)



Fig. 6.18

(x150)

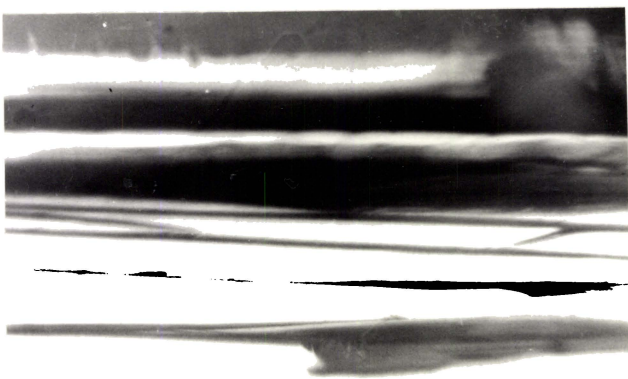
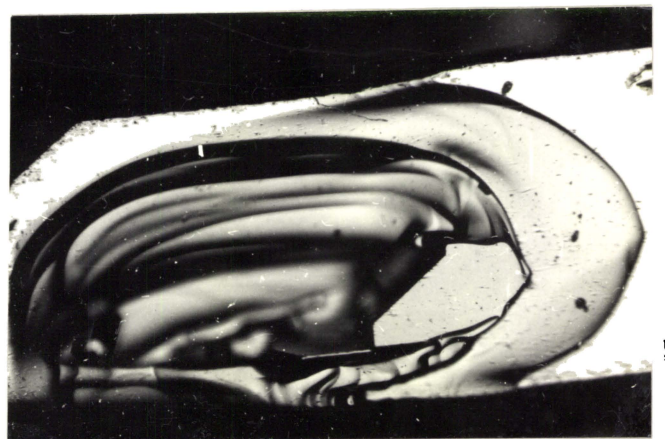


Fig. 6.19



(x100) Fig. 6.20

(x100)

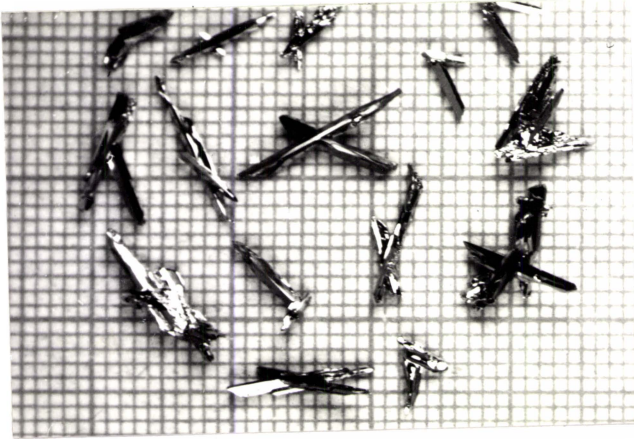


Fig. 6.21

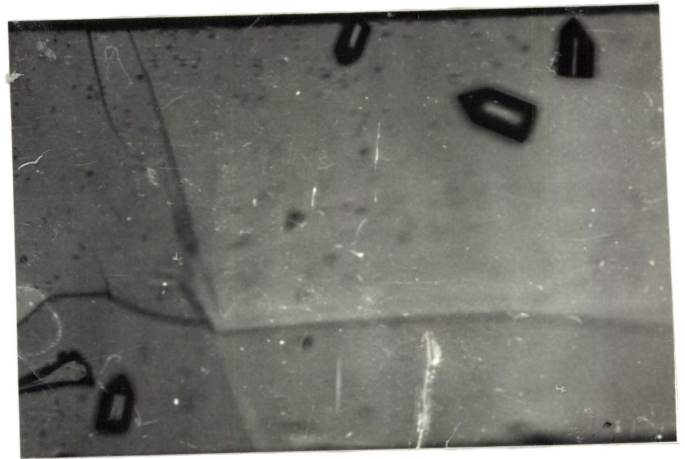


Fig.6.22

(x 80)



Fig. 6.23

(x 33)

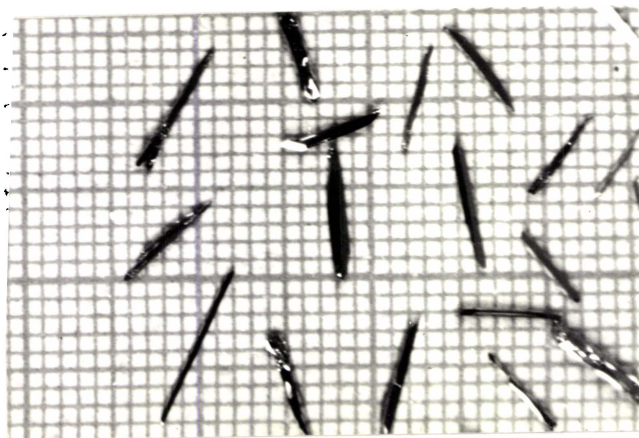


Fig. 6.24

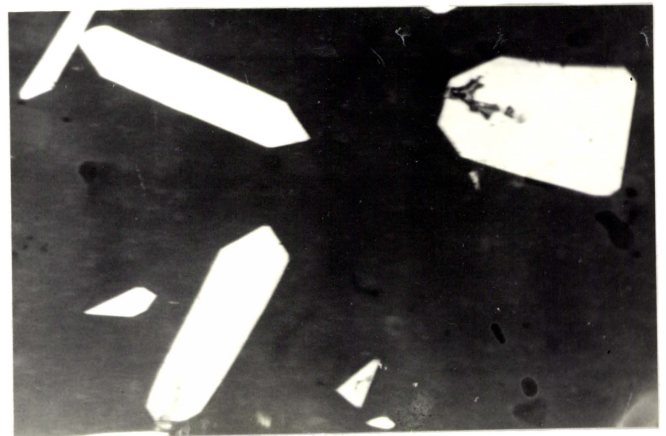


Fig. 6.25

(x125)

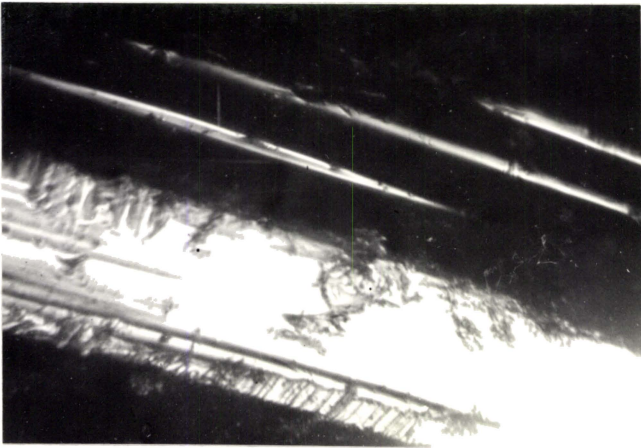


Fig. 6.28

(x150)

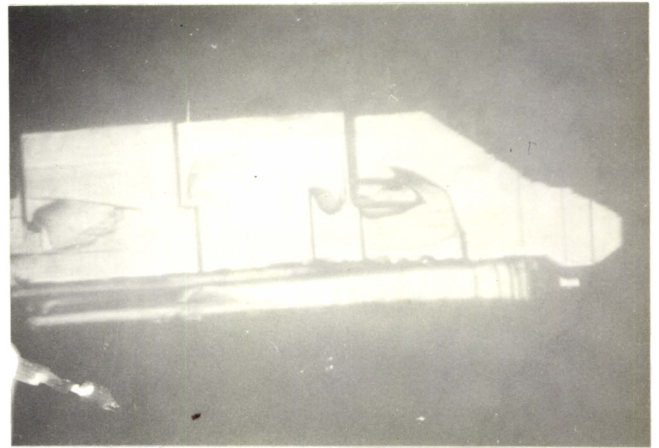


Fig. 6.29

(x 80)



Fig. 6.30(a)

(x80)

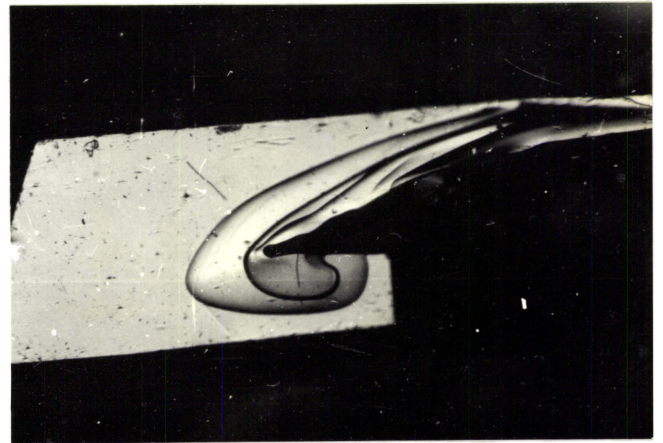


Fig. 6.30(b)

(x 80)

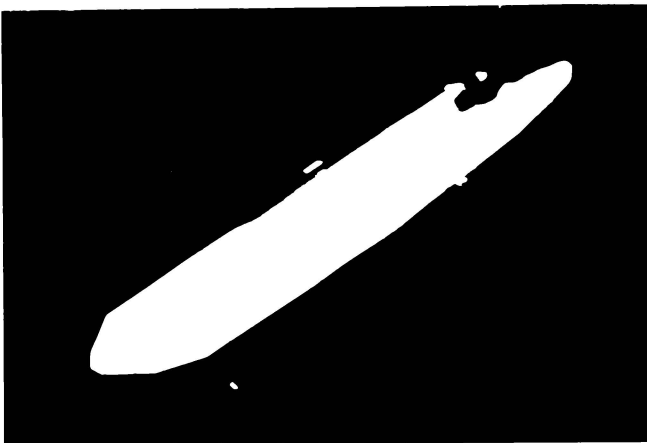


Fig. 6.31

(x80)



Fig. 6.32

(x 33)



Fig. 6.34

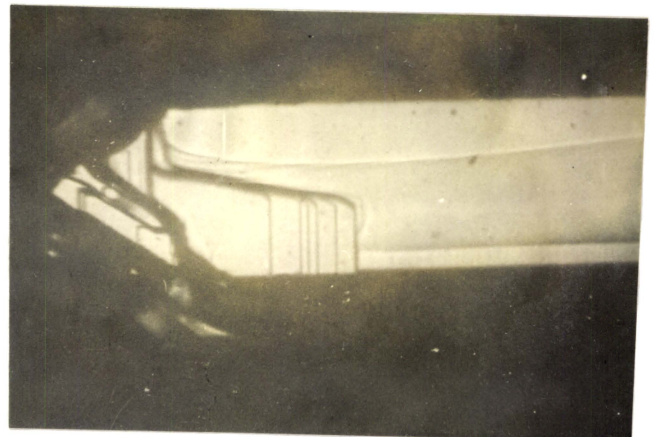


Fig. 6.35(a) (x100)

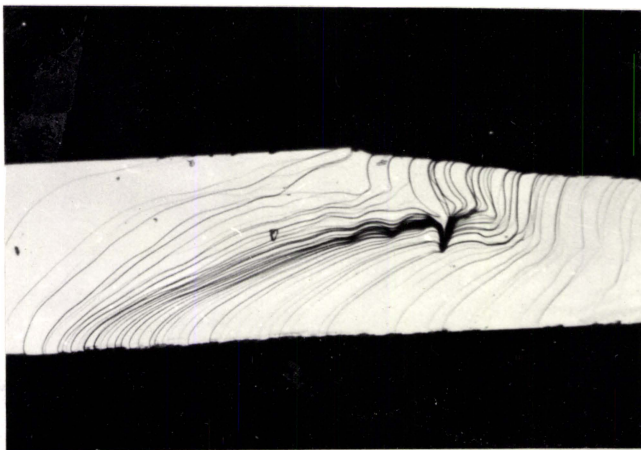


Fig. 6.35(b)

(x80)

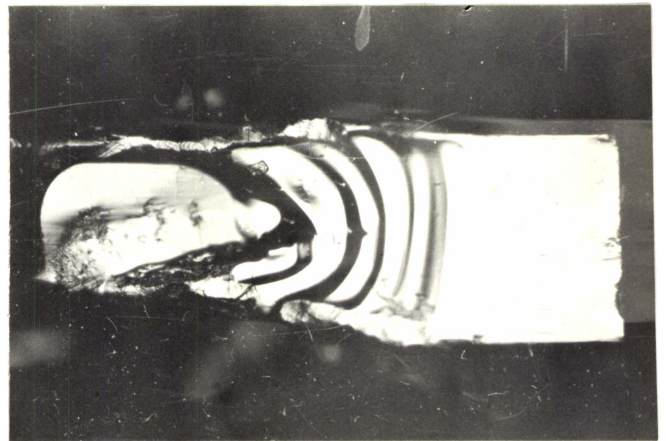


Fig. 6.36

(x 80)

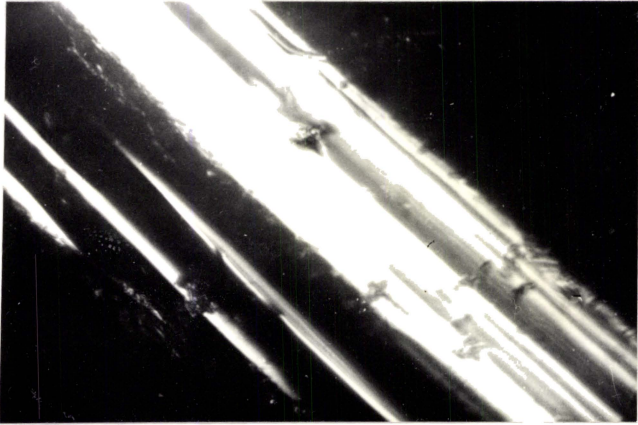


Fig. 6.37

(x150)



Fig. 6.38

(x125)

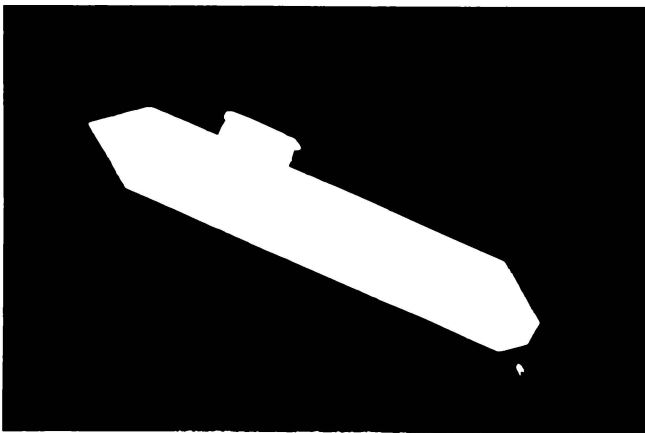


Fig. 6.39

(x80)

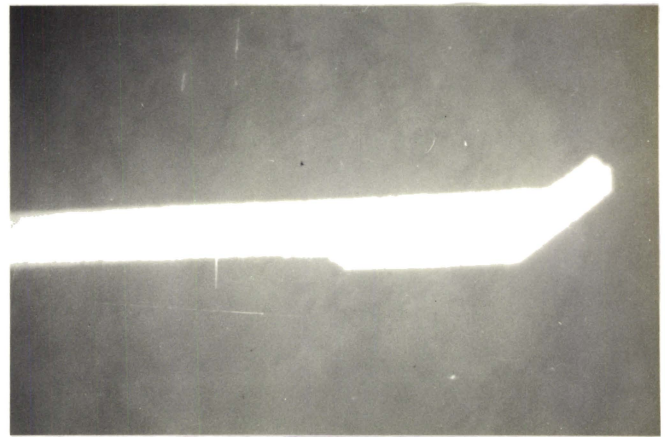


Fig. 6.40

(x 80)

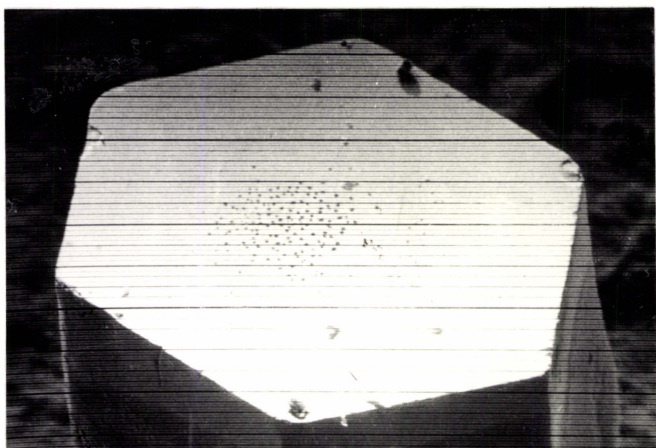
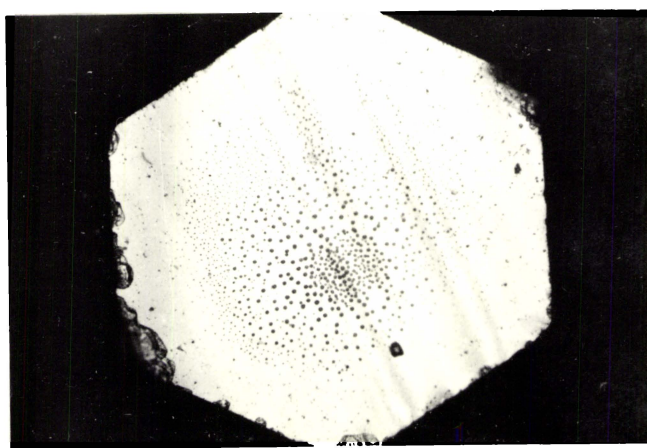


Fig. 6.41



(x180) Fig. 6.42(a)

(x180)

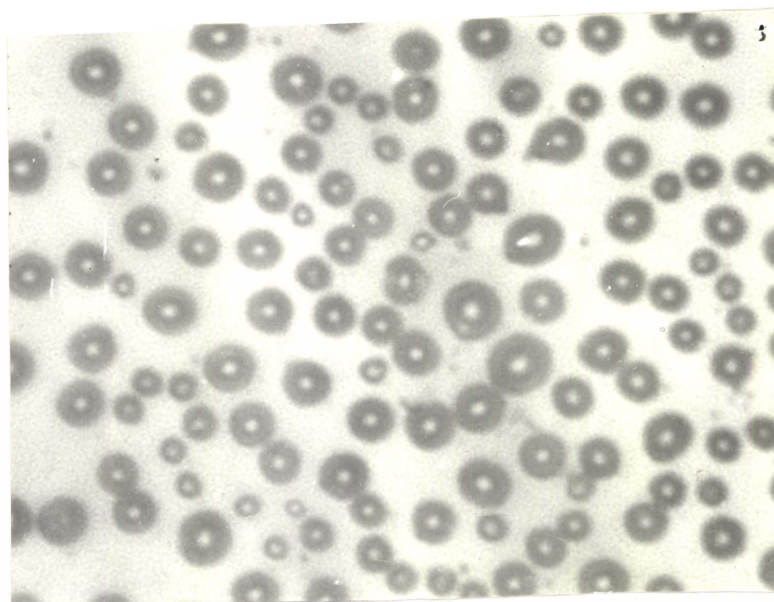


Fig. 6.42(b)

(x2000)

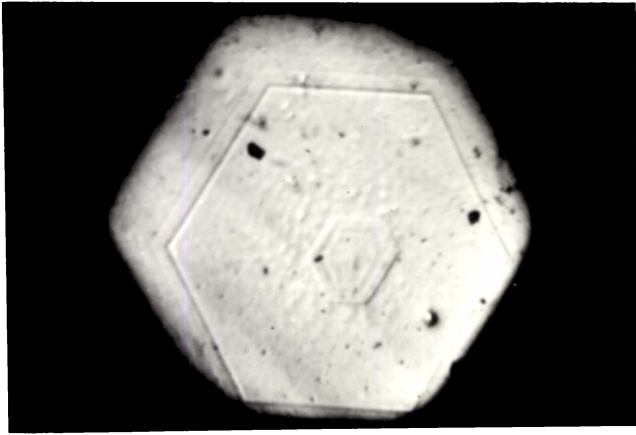
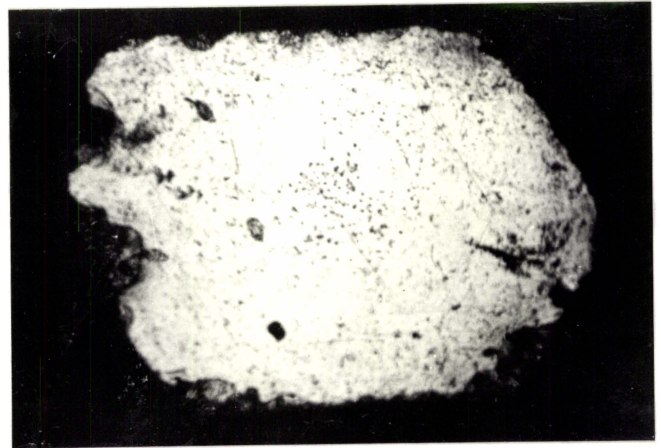


Fig. 6.42(c)



(x150) Fig. 6.43(a)

(x 33)

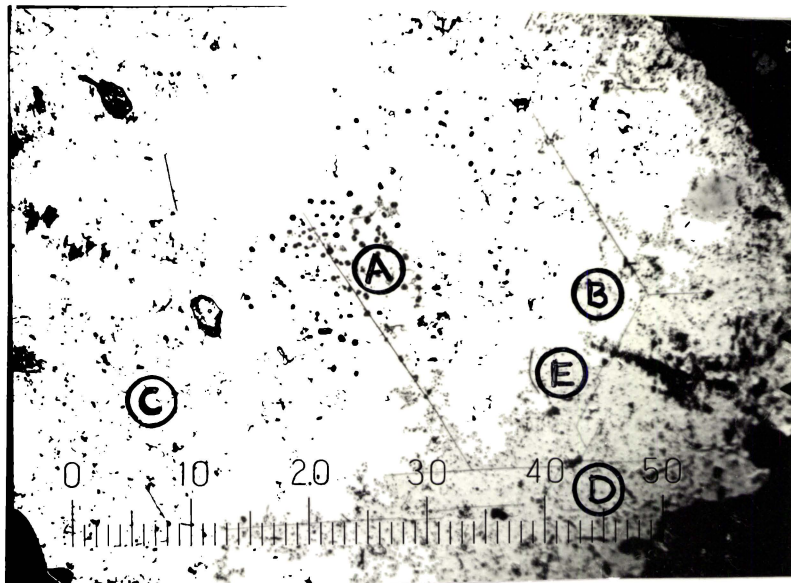


Fig. 6.43(b)

(x150)

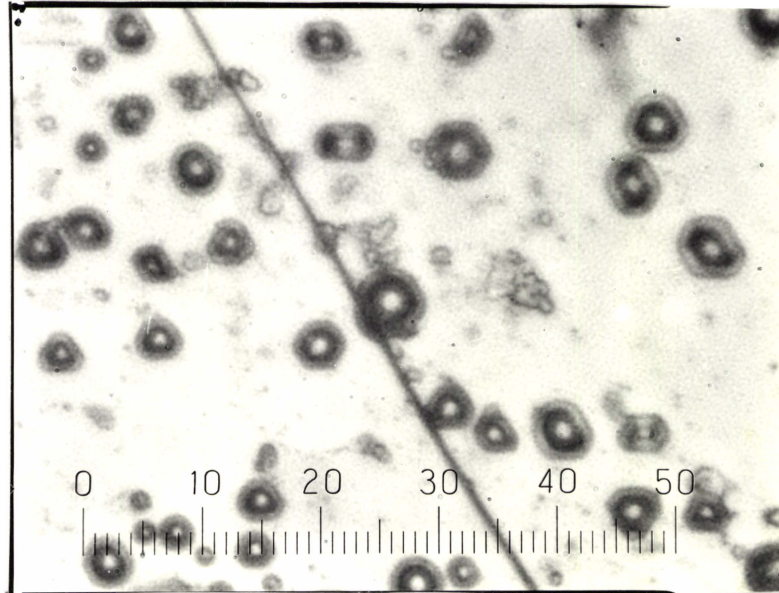


Fig. 6.43(c)

(x1500)

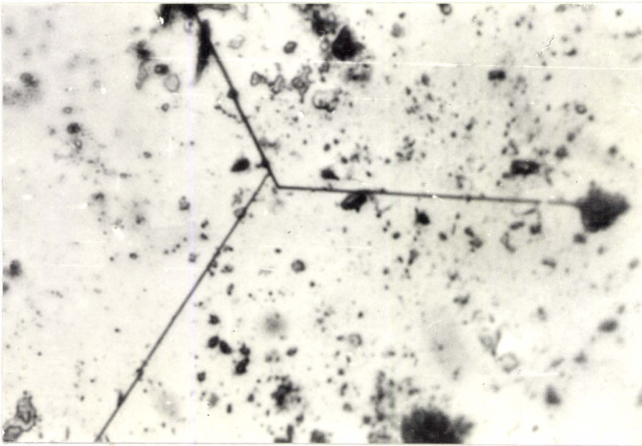


Fig. 6.43(d)

(x330)

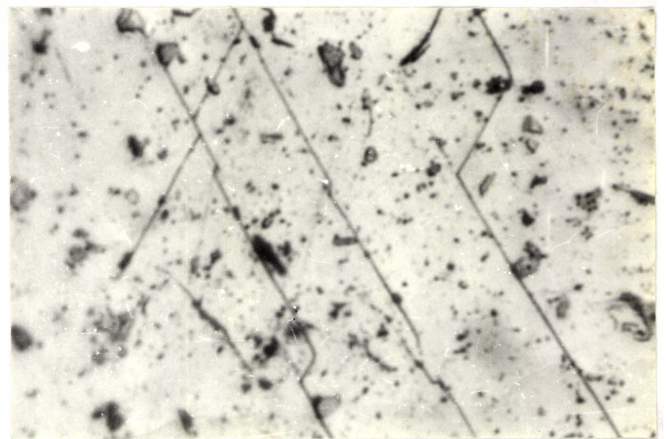


Fig. 6.43(e)

(x330)

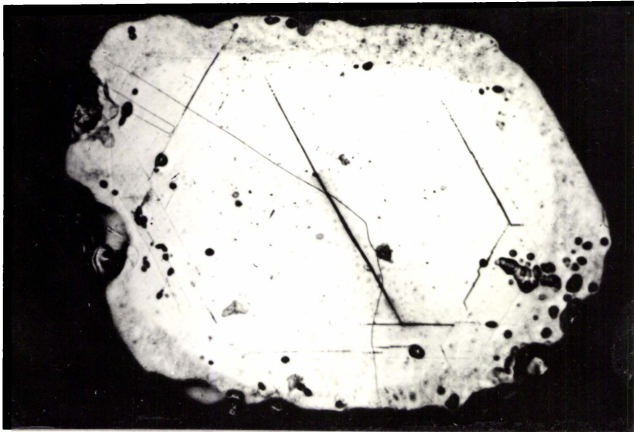


Fig. 6.44(a)

(x33)

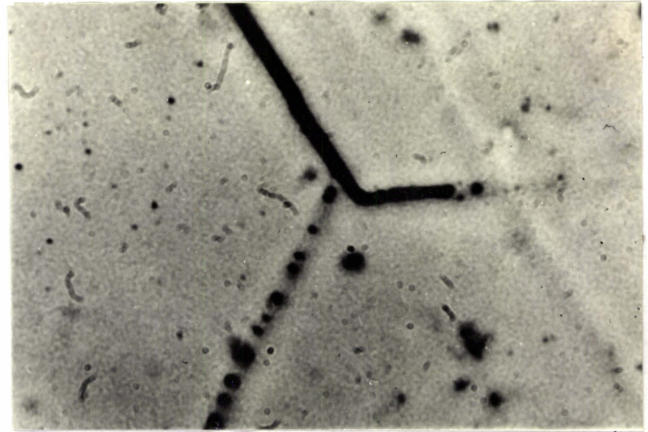


Fig. 6.44(b)

(x330)

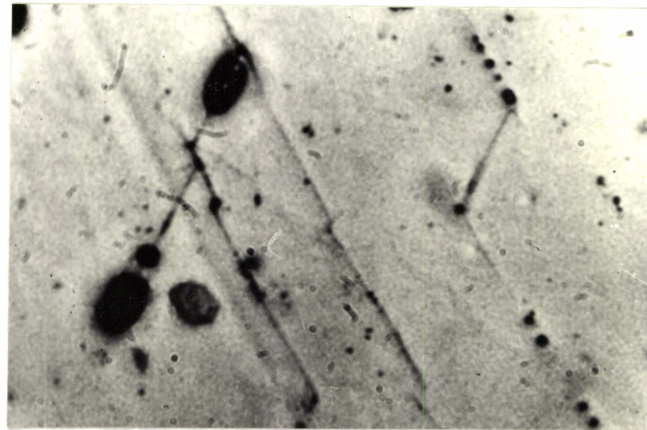


Fig. 6.44(c)

(x330)

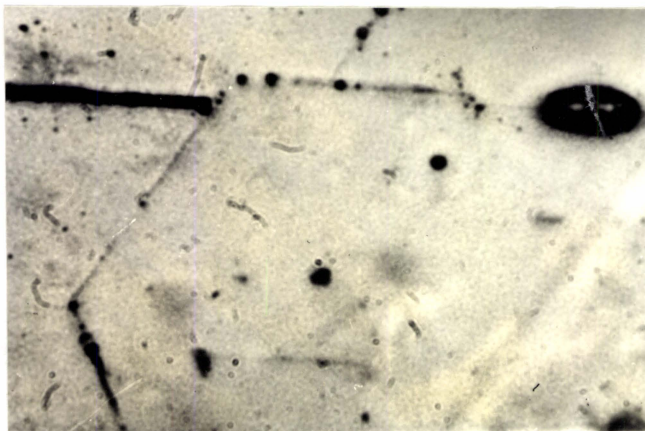
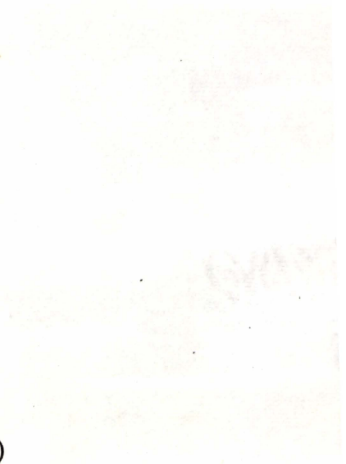


Fig. 6.44(d)

(x330)

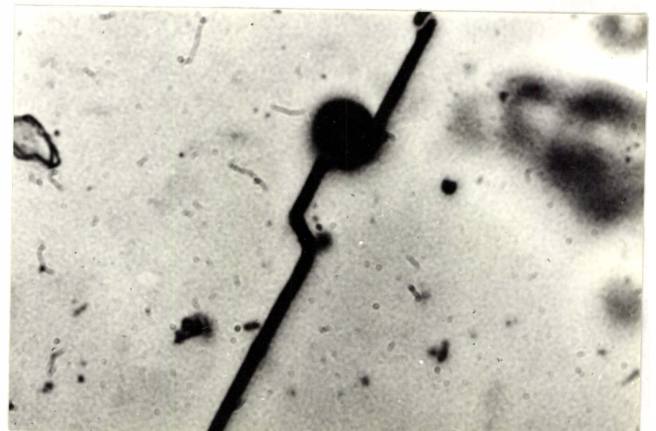


Fig. 6.44(e)

(x330)

6.6 REFERENCES

- [1] J.J.Loferski, *Phys. Rev.* 93 (1954) 707.
- [2] R.C.Keezer, C.H.Griffiths and J.P.Vernon, *J. Cryst. Growth* 3/4 (1968) 755.
- [3] I.Shih and C.H.Champness, in: *The Physics of Selenium and Tellurium* Eds. E.Gerlach and P.Grosse (New York, 1979) p.267.
- [4] N.V.Quang, I.Shih and C.H.Champness, *J. Cryst. Growth* 70 (1984) 529.
- [5] T.Shiosaki and A.Kawabata, *Japan J. Appl. Phys.* 10 (1971) 1329.
- [6] W.Beyer, H.Mell and J.Stuke, *Phys. Stat. Solidi (b)* 45 (1971) 153.
- [7] V.P.Bhatt and S.B.Trivedi, *J. Cryst. Growth* 44 (1978) 262.
- [8] S.B.Trivedi and V.P.Bhatt, *J. Cryst. Growth* 32 (1976) 227.

- [9] V.B.Bhatt and S.B.Trivedi, *Kristall Tech.* 13 (1978) 1435.
- [10] H.J.Goldsmid and R.W.Douglas, *J. Appl. Phys.* 5 (1954) 386.
- [11] D.R.Lovett, *Semimetals and Narrow-Band Gap Semiconductors* (London, 1977) p.181.
- [12] P.W.Lange, *Naturwissenschaften*, 27 (1939) 133.
- [13] M.H.Francombe, *Brit. J. Appl. Phys.* 9 (1958) 415.
- [14] J.R.Drabble and C.H.L.Goodman, *J. Phys. Chem. Solids*, 5 (1958) 142.
- [15] T.C.Harman, B.Paris, S.E.Miller and H.L.Goering, *J. Phys. Chem. Solids* 2 (1957) 181.
- [16] J.Black, E.M.Conwell, L.Seigle and C.W.Spencer, *J. Phys. Chem. Solids* 2 (1957) 240.
- [17] H.J.Goldsmid, *Proc. Phys. Soc.* 71 (1958) 633.

- [18] C.H.Champness and A.L.Kipling, *Canad. J. Phys.* **44** (1966) 769.
- [19] C.B.Satterthwaite and R.W.Ure, Jr. *Phys. Rev.* **108** (1957) 1164.
- [20] S.Shigetomi and S.Mori, *J. Phys. Soc. Jap.* **11** (1956) 915.
- [21] J.R.Drabble, R.D.Groves and R.Wolfe, *Proc. Phys. Soc.* **71** (1958) 431.
- [22] A.C.Yang and F.D.Shepherd, *J. Electrochem. Soc.* **108** (1961) 197.
- [23] R.A.Laudise, W.A.Sunder, R.L.Barns, R.J.Cava and T.Y.Kometani, *J. Cryst. Growth*, **94** (1989) 53.
- [24] D.Arivuoli, F.D.Gnanam and P.Ramasamy, *J. Mater. Sci. Lett.* **7** (1988) 711.
- [25] V.A.Petrusevich and V.M.Sergeeva, *Sov. Phys. Solid State*, **2** (1961) 2562.

- [26] P.G.Rustamov, Ya.N.Nasirov, M.A.Alidzhanov and Ya.N. Babaev, *Izv. Akad. Nauk SSSR, Neorgan Mat.* 13 (1977) 746.
- [27] D.B.Ananina, V.L.Bakumenko, G.G.Grushka and L.N.Kurbatov, *Sov. Phys. Semicond.* 10 (1976) 3.
- [28] A.Oginskas, A.Cesnys and L.P.Gal'chinetskii, *Lit. Fiz. Sbor.*, 20 (1980) 33.
- [29] A.I.Zaslavskii and V.M.Sergeeva, *Sov. Phys. Solid State*, 2 (1961) 2556.
- [30] A.I.Zaslavskii, N.F.Kartenko and I.Z.Karachentseva, *Sov. Phys. Solid State*, 13 (1972) 2152.
- [31] H.Inuzuka and S.Sugaike, *Proc. Japan Acad.* 30 (1954) 383.
- [32] J.C.Woolley and B.R.Pamplin, *J.Electrochem. Soc.* 108 (1961) 874.
- [33] D.Janowski, *Ann. Phys.* 23 (1969) 71.

- [34] A.S.Mamedov, K.P.Mamedov, G.Sh.Gasanov, S.B.Bagirov and G.M.Niftiev, *Izv. Akad. Nauk SSSR, Neorgan Mat.*, 13 (1977) 1987.
- [35] I.Yu.Verkelis, *Sov. Phys. Solid State*, 14 (1972) 1445.
- [36] C.Paorici, *J. Cryst. Growth*, 2 (1968) 324.
- [37] F.R.Nabarro and P.J.Jackson in: "Growth and Perfection of Crystals, Eds. R.H.Doremus, B.W.Roberts and D.Turnbull (Wiley, New York, 1958).
- [38] W.Guo, X.G.Ning, J.Zhu and H.Q.Ye, *J. Cryst. Growth* 106 (1990) 400.
- [39] M.Fujii, H.Iwanaga and N.Shibata, *J. Cryst. Growth* 99 (1990) 179.
- [40] A.Kuroyanagi, *Jpn. J. Appl. Phys. 1, Regul. Pap. Short Notes* 29 (1990) 1769.
- [41] S.Motojima, M.Hasegawa and T.Hattori, *J. Cryst. Growth* 87 (1988) 311.

- [42] H.Iwanaga, T.Yoshie, T.Yamaguchi and N.Shibata, J. Cryst. Growth 51 (1981) 438.
- [43] R.B.Sharma, J. Appl. Phys. 41 (1970) 1866.
- [44] G.Attolini, C.Paorici and P.Ramasamy, J. Cryst. Growth, 78 (1986) 181.
- [45] D.Arivuoli, F.D.Gnanam and P.Ramasamy, J. Mater. Sci. Lett. 5 (1986) 193.
- [46] D.Arivuoli, F.D.Gnanam and P.Ramasamy, J. Mater. Sci. 5 (1986) 959.
- [47] A.G.Kunjomana and E.Mathai, J. Cryst. Growth 92 (1988) 666.
- [48] A.G.Kunjomana and E.Mathai, Cryst. Res. Technol. (in press).
- [49] G.S.Baker, in: Growth and Perfection of Crystals, Eds. R.H.Doremus, B.W.Roberts and D.Turnbull (Wiley, New York, 1958).

- [50] A.G.Kunjomana and E.Mathai, Mater. Res. Bull 26 (1991) 1347.
- [51] A.G.Kunjomana and E.Mathai, J. Mater. Sci. Lett. 21 (1992) 613.
- [52] J.George, C.K.Valsalakumari, Cryst. Res. Technol. 21 (1986) 273.
- [53] D.Arivuoli, F.D.Gnanam and P.Ramasamy, J. Mater. Sci. 22 (1987) 981.
- [54] P.B.Hirsch., J. Silcox, R.E.Smallman and K.H.Westmacott, Philos. Mag. 3 (1958) 897.
- [55] A.Eikum and G.Thomas, J. Appl. Phys. 34 (1963) 3363.
- [56] X.G.Ning and H.Q.Ye, J. Phys. Condens. Matter, 2 (1990) 10223.
- [57] G.V.Tendeloo, T.Krekels and S.Amelinckx, Philos. Mag. Lett. 63 (1991) 189.
- [58] K.A.Jackson, Philos. Mag. 7 (1962) 1117.

- [59] D.Hull and D.J.Bacon, Introduction to Dislocations (Pergamon Press, New York, 1984).
- [60] P.Grigoriadis and J.Stoemenos, J. Mater. Sci. 13 (1978) 483.
- [61] P.Delavignette and S.Amelinckx, Philos. Mag. 6 (1961) 601.
- [62] A.G.Kunjomana and E.Mathai (Communicated).
- [63] I.Kovacs and L.Zsoldos, Dislocations and Plastic Deformation (Pergamon Press, New York, 1973).
- [64] F.C.Frank, Deformation and Flow of Solids (Springer Verlag, Berlin, 1956) p.73.
- [65] A.Fourdeux, A.Berghezan and W.W.Webb, J. Appl. Phys. 31 (1960) 918.

7

CHEMICAL AND THERMAL ETCHING STUDIES OF VAPOUR-GROWN
 $\text{Te}_{1-x}\text{Se}_x$, Bi_2Te_3 AND In_2Te_3 CRYSTALS

7.1 INTRODUCTION

Chemical etching studies of tellurium single crystals have been carried out by many authors. Chemical etchant to reveal dislocations on cleaved $(10\bar{1}0)$ faces of tellurium was first reported by Lovell et al. [1]. Blum [2] used concentrated nitric acid to etch the same face and found that it produced a large number of pits. He also developed an etchant composed of 49 gm H_3PO_4 , 1 c.c. conc. H_2SO_4 and 5 gm crystalline CrO_3 which produced isolated pits on the skull parallel to c-axis. Blakemore et al. [3,4] reported the formation of etch pits at dislocation sites on $(10\bar{1}0)$ cleavage faces of melt grown tellurium crystals by using hot concentrated sulphuric acid as the etchant. The pits had a very characteristic shape and were found to be asymmetric about the c-axis. Blakemore and Nomura [5] and Herrmann [6] observed two kinds of etch pits which were mirror images of each other. These were attributed to the dextro-and laevo-rotatory forms of tellurium. Koma et al. [7] have proposed a microscopic model for the formation of each pits and studied the shape of pits produced by hot sulphuric acid.

Etching experiments on the (0001) basal plane of tellurium crystals were also reported [8-10]. Azab et al

[11] tested the etchant consisting of 5 gm H_3PO_4 + 1 gm CrO_3 and reported triangular as well as hexagonal etch pits. Kalinski and Lehmann [12] found that hexagonal etch pits become triangular after prolonged etching in 200 gm H_3PO_4 + 3 gm CrO_3 at $160^\circ C$ for about 20 min. Later Shih and Champness [13] studied the basal plane etch pit orientation effect in tellurium crystals grown by the Czochralski method. They found that the etch pits on the (0001) surface facing the melt end are oriented differently with respect to the ingot prism faces from those on the (0001) surface facing the seed end.

A few workers have reported etchants for Se-Te alloy crystals. Trivedi and Bhatt [14] studied the etching on the prism faces of $Se_{90}Te_{10}$ whisker crystals grown from the vapour phase using 1 part conc. HNO_3 + 4 parts conc. H_2SO_4 as the etchant. The etchant produced well defined etch pits and they showed that the dislocation density was greatest near the root of a whisker and lower in the central part and near the tip. Later the same authors [15] have reported another etchant containing iodine in methanol to reveal the dislocation sites on the prism faces of $Se_{90}Te_{10}$ whisker crystals. Bhatt and Trivedi [16] also studied the etching of $(10\bar{1}2)$ cleavage plane of $Se_{90}Te_{10}$

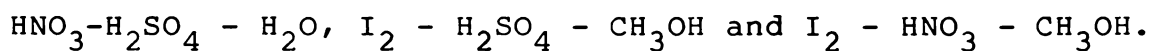
crystals grown from the melt using two etchants namely (1) 1 part conc. HNO_3 + 4 parts conc. H_2SO_4 and (2) Bromine in methanol + conc. HCl . They found that these etchants were capable of revealing dislocations intersecting the cleavage plane.

Weintroub and Ahmed [17] were carried out thermal etching on the $(10\bar{1}0)$, (0001) and $(11\bar{2}0)$ planes of tellurium crystals. They observed hexagonal pits on (0001) planes and rectangular pits on $(10\bar{1}0)$ and $(11\bar{2}0)$ planes. Azab et al [11] have observed hexagonal and long sided thermal pits on $(10\bar{1}0)$ planes. Bhatt and Trivedi [18] have done a systematic study of thermal etch pits on the $(10\bar{1}0)$ cleavage faces of tellurium crystals at various temperatures under a vacuum of the order of 10^{-3} Torr and suggested a simple model based on the crystal structure and bonding of the atoms to explain the shape of etch pits. Thermal etching studies on the prism faces of $\text{Se}_{90}\text{Te}_{10}$ whisker crystals grown from the vapour phase have been reported by Bhatt and Trivedi [15] and showed that thermal pits were not formed at dislocation sites but were due to impurities in the crystal.

Not much data is available in the literature on the chemical and thermal etching studies of Te-rich whiskers containing small concentrations of Se. Also no such studies were made on the as-grown faces of Bi_2Te_3 , α and β - In_2Te_3 whiskers grown from the vapour phase. Therefore it was intended to carry out a detailed study on the chemical and thermal etching characteristics of these whiskers. The results of these studies form the subject of this chapter.

7.2 EXPERIMENTAL

The whisker crystals grown by physical vapour deposition method were used for etching studies. The as-grown prism faces of $\text{Te}_{1-x}\text{Se}_x$ whiskers were etched in conc. H_2SO_4 at 120°C for about 3-4 min and the dislocation density for various concentrations of Se was determined. Etching of Bi_2Te_3 whiskers using a number of chemicals were tried and three etchants were developed:



Freshly grown whiskers with well developed plane faces were etched in these solutions. This was followed by washing the crystals in CH_3OH and finally drying in air. For each

etchant, the time of etching to produce good etch pits was obtained by trial and error. The etchant comprising 5 ml HNO_3 + 0.1 ml HF + 10 ml H_2O was found to be capable of revealing dislocations intersecting the prism faces of α and β - In_2Te_3 whiskers. Hence these whiskers were etched in this etchant under controlled etching conditions.

For thermal etching, freshly grown whiskers were etched under high vacuum ($\sim 10^{-5}$ Torr) using the vacuum system as described in Chapter 5. The etching was carried out at different temperatures and time.

The chemical and thermal etched crystal surfaces were examined under reflection mode using Carl Zeiss Jena and Union Versamet-2 metallographic microscopes.

7.3 RESULTS AND DISCUSSION

7.3.1 Chemical Etching studies

(a) $\text{Te}_{1-x}\text{Se}_x$ whiskers

The present investigation on $\text{Te}_{1-x}\text{Se}_x$ whiskers was undertaken with a view to study in detail the effect of addition of Se as impurity on the pit morphology and dislocation density.

When the crystals were etched in conc. H_2SO_4 at 120°C for 1 min. very small etch pits of irregular shape were observed. But after etching for 3 min, four-sided pits with asymmetric angles and sides were developed. So this was found to be the optimum condition for obtaining visible etch pits. The effect of increasing the temperature of the etchant on the etching characteristics was also tried. But the etch rates is found to be increased considerably. The distribution of four-sided etch pits on the prism face of a Te whisker etched at 120°C for 3 min. is shown in fig.7.1(a). One of the sides of the pit is parallel to the c-axis. A few flat bottomed pits are also seen. The point bottomed pits are slightly eccentric. The same face had been etched further for 1 min in conc. H_2SO_4 at the same temperature. That is for a total time of 4 min The pit size is increased as seen from fig.7.1(b). This indicates that the pits are formed at the dislocation sites. The etched region of a $\text{Te}_{0.98}\text{Se}_{0.02}$ whisker for 3 min is depicted in fig.7.2. Fig.7.3 is the photograph of the prism face of a $\text{Te}_{0.97}\text{Se}_{0.03}$ whisker after etching it for 3 min In fig.7.4, the etched prism face of a $\text{Te}_{0.94}\text{Se}_{0.06}$ whisker is shown. Here the etch pits are found to lose the sharpness of their edges. Fig.7.5 represents the etch patterns of a $\text{Te}_{0.92}\text{Se}_{0.08}$ crystal, where the

change in shape of the pits is quite clear. The morphology of etch pits has been changed markedly in the case of whiskers containing 10 at. % Se. Fig.7.6(a) shows the prism face of a $\text{Te}_{0.90}\text{Se}_{0.10}$ whisker after etching for 3 min. The sides of the pits become rounded and hence the pits developed have no well defined shape. Moreover it is seen that they are of different sizes. On sequential etching for 1 min, (Fig.7.6(b)) the pits become so large that they form clusters. The number and position of the pits remain practically the same. Fig.7.7 shows the variation of dislocation density as a function of Se concentrations.

In many cases, it has been found that successive etching of the same face neither produces new pits nor changes the orientation of earlier pits. On further etching, only the size is increased. Rows of pits are also formed along the slip lines (Fig.7.8). This indicates that pits are formed at the emergence points of dislocations. It is also interesting to note that, at different concentrations of Se, the dislocation density is found to be increasing where as the pit size is decreasing. The change in shape of the pits indicates that the dissolution directions change with the addition of Se [19].

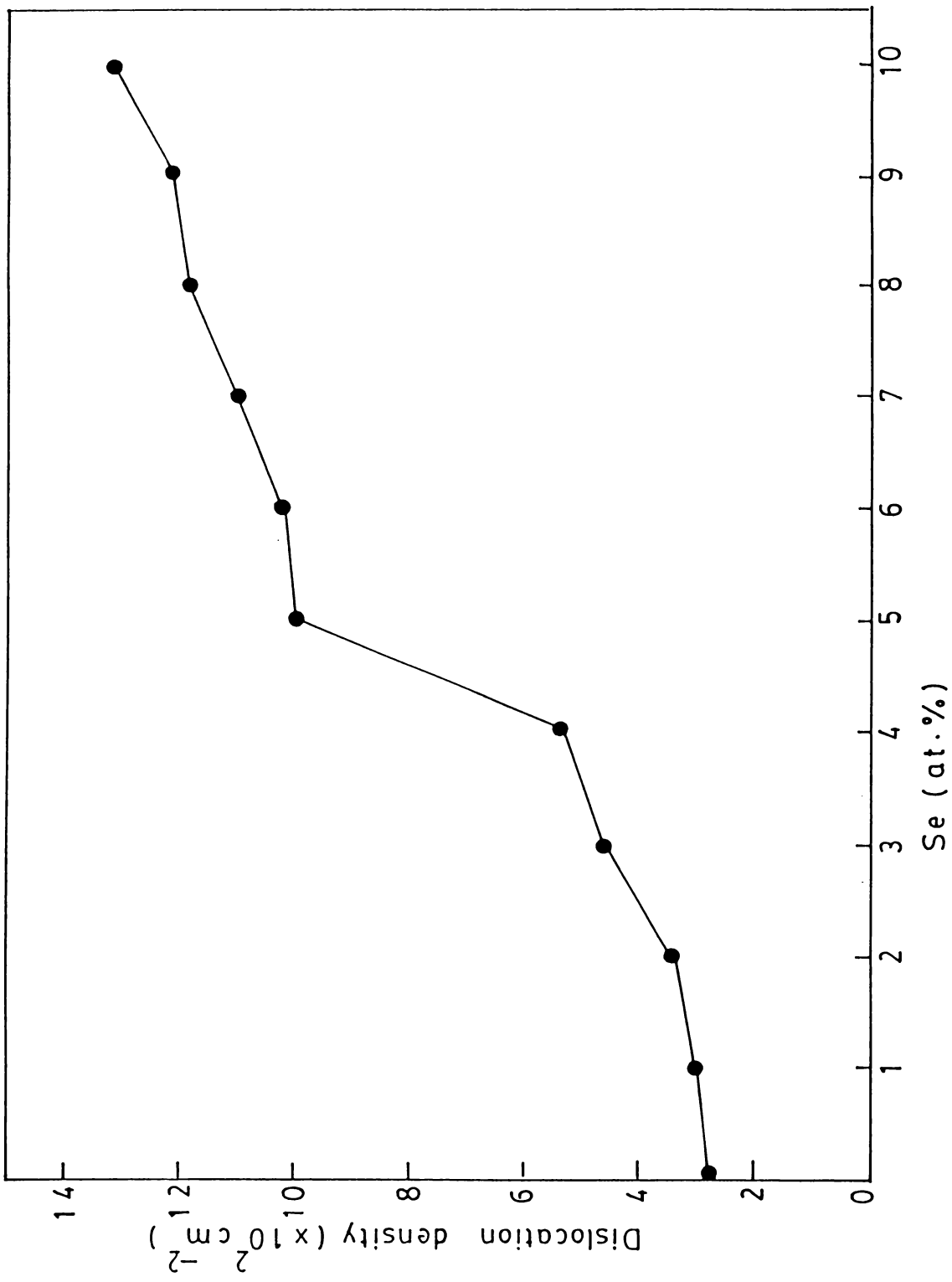


Fig. 7.7

(b) Bi₂Te₃ whiskers

During the present study various chemicals were tried to find out a suitable etchant for delineating the dislocations in Bi₂Te₃ whiskers. The dislocation studies using the different etchants are presented below:

Teramoto and Takayanagi [20] have employed the etchant composing 30% HNO₃ to obtain etch pits on the cleaved (0001) planes of melt-grown Bi₂Te₃ crystals. Sagar and Faust [21] used this etchant on the cleavage planes of Bi₂Te₃ crystals grown by horizontal zone levelling method. But they observed a black coating on the surface and so they could not establish the reliability of this etchant to produce pits corresponding to dislocation sites. In the present investigation, the suitability of this etchant was examined on the prism faces of Bi₂Te₃ whiskers which were grown from the vapour phase. The etching time was varied between 30 sec to 3 min. But only very small pits were formed which were not well defined and contrasting. Hence to produce etch pits on the prism faces, small amounts of conc. H₂SO₄ was added. It was found that the mixture containing 7 ml HNO₃ + 3 ml H₂SO₄ + 10 ml H₂O could reveal dislocation etch pits on the prism faces. Fig.7.9

shows the etched surface of a Bi_2Te_3 crystal for 10 sec. On etching for 2 min, well developed triangular etch pits were formed as shown in fig.7.10. At higher etching time, the crystal surface was corroded.

The second etchant used for revealing dislocation sites is composed of iodine, methanol and conc. H_2SO_4 . Some interesting results were obtained using this etchant. When the crystals were first etched in a solution containing iodine in methanol, no dislocation etch pits were formed on the prism face. But addition of conc. H_2SO_4 to iodine solution produced contrasting etch pits. The effect of varying the composition of etchant was studied on a number of samples and it has been found that well defined and visible etch pits are formed for a composition of 50 mg I_2 + 5 ml H_2SO_4 + 10 ml CH_3OH . Fig.7.11(a) shows the etched pattern of a prism face obtained after an etching time of 10 sec. The sides of the pit are curved. The higher magnification of the region marked A in Fig.7.11(a) is shown in fig.7.11(b). The etchant produced larger pits which retain their shapes on further etching. Figs.7.11(c) and 7.11(d) show the photographs of the same prism face at lower and higher magnifications respectively after successive etching. Rows of etch pits running parallel

to the c-axis are seen in fig.7.11(c) which indicates that they represent slip traces. Etch pits were also aligned in the form of low angle grain boundaries as shown in fig. 7.12. A typical four sided pit is seen with unequal sides. The tip of the whiskers was also etched (fig.7.13) where the terracing of pits can be seen.

The above results show that the etchant is capable of revealing the sites of emergence of dislocations [22].

In order to study the effect of etchant composition on the etching behaviour of Bi_2Te_3 whiskers, the amount of conc. H_2SO_4 has been slightly increased. Fig.7.14(a) shows the formation of terraced etch pits on the prism face of a typical whisker. This is due to the enhanced oxidising power of iodine in the presence of acidic medium. The composition of the etchant employed was 50 mg I_2 + 6 ml H_2SO_4 + 10 ml CH_3OH . Fig.7.14(b) shows the same surface at a higher magnification. Due to excess reaction, small circular shaped pits were also formed inside the bigger pits. When the iodine content is increased, keeping the other components in the same concentration, a number of randomly distributed pits were formed with different

sizes (Fig.7.15). The etch rate is increased considerably and the pit morphology is changed. Moreover, precipitation of iodine occurs on the surface after etching, in the form of irregular line markings.

The third etchant used in the present study is composed of iodine, methanol and conc. HNO_3 . The reliability of the etchant comprising 50 mg I_2 + 8 ml HNO_3 + 10 ml CH_3OH was examined in relation to the morphology of dislocation etch pits. When the crystals were etched in this solution for 10 sec, the surface was covered with a film formation. So further etching was carried out by adding more amounts of CH_3OH . Fig.7.16(a) shows the distribution of etch pits formed after etching in 50 mg I_2 + 8 ml HNO_3 + 20 ml CH_3OH for 20 sec. The pits are truncated and are oriented towards the edge of the prism face. On subsequent etching, these pits become flat bottomed (Fig.7.16(b)).

(c) In_2Te_3 whiskers

As no etchant has been reported so far for In_2Te_3 crystals many etchants with different reagents were tried. A new etchant capable of revealing the sites of emergence of dislocations on the prism faces of In_2Te_3

whiskers was developed. It was found that etching of the crystals in a solution of conc. HNO_3 and H_2O had no effect on the crystal surface. On adding small amounts of conc. HF to conc. HNO_3 and H_2O , it could produce etch pits on the prism face. The $\alpha\text{-In}_2\text{Te}_3$ whiskers were first immersed in a solution of 2 ml HNO_3 + 0.1 ml HF + 10 ml H_2O . No pits were formed even after etching for about 3 min. When the crystals were etched in a solution of 3 ml HNO_3 + 0.3 ml HF + 10 ml H_2O for 15 sec, etch pattern as shown in fig.7.17(a) is obtained. It is seen that quite a large surface of the whisker is devoid of pits which indicates the relative perfection of the grown whiskers. The pits [marked A and B in fig.7.17(a)] have different morphologies. In fig.7.17(b) the higher magnification of pit at B is shown. The bright feature seen inside the pit boundary is not formed at the geometrical centre of the pit. This indicates that inclined dislocations are intersecting the prism faces. Etching further for 10 sec produced circular point bottomed etch pits [Fig.7.17(c)]. From Figs.7.17(a) and 7.17(c), it is clearly seen that there is no increase in the number of pits but a one-to-one correspondence in the position of pits is observed. This indicates that the pits are formed at dislocation sites.

The above mentioned etchant could also produce dislocation pits on the prism plane of β - In_2Te_3 whiskers. Fig.7.18(a) shows the prism face of a β - In_2Te_3 whisker after etching in 3 ml HNO_3 + 0.3 ml HF + 10 ml H_2O for 15 sec. The pits have different morphology compared to those of α - In_2Te_3 . Circular shaped pits are seen and are aligned in the form of a closed structure. On successive etching these pits become shallower as shown in Fig.7.18(b). This indicates that the pits are formed mostly at the sites of intersection of shallow dislocations.

For the above etchant, the etch rate was found to be very fast. Therefore this can be also used as a polishing agent. No attempt was made to modify this etchant so as to obtain a desirable etch rate. The pit density of β - In_2Te_3 whiskers is more than that of α - In_2Te_3 whiskers.

7.3.2 Thermal Etching studies

Apart from chemical etching studies, particular attention has also been made to understand the thermal etching characteristics of $\text{Te}_{1-x}\text{Se}_x$, Bi_2Te_3 , and α and β - In_2Te_3 whiskers. A number of experiments were carried out on thermal etching of these whiskers at low and high vacuum conditions. It is found that as the order of vacuum increases, the temperature at which etching takes place can be conveniently

reduced. Since the etch rate also enhances at high vacuum, it also makes possible to give better results at lower etching time. In view of these facts, all the whiskers were etched under a vacuum of the order of 10^{-5} Torr.

(a) Te_{1-x}Se_x whiskers

Fig.7.19(a) shows the formation of thermal etch pits on the prism face of a Te whisker etched at 150°C for 10 min. The pits formed have nearly four or five sides with their longer side parallel to the c-axis. Some pits have tapering ends, whereas others have slightly rounded edges. A few shallow pits are also clearly visible in the photograph. On etching further for another 5 min, the pits were enlarged as shown in Fig.7.19(b). The edges of the pit lost their sharpness and changed into a curved nature. The shallow pits seen in Fig.7.19(a) become more deep and visible after successive etching. Fig.7.20(a) is the photograph of a Te_{0.97}Se_{0.03} whisker which had been etched for 10 min at the same temperature. In this case, most of the pits were first developed as shallow and grown larger with well developed sides after successive etching for 5 min. [Fig.7.20(b)]. Thermal etch grooves also developed clearly due to the increase in size of the etch pits. The etch

pattern of a $\text{Te}_{0.94}\text{Se}_{0.06}$ whisker after etching for 10 and 15 min is shown in Figs.7.21(a) and 7.21(b) respectively. Here some pits have six sides with their alternate sides parallel to each other. The size of the pits was increased, but their edges became rough on successive etching. At higher Se concentrations, thermal etch pit density is found to be increased markedly. Fig.7.22(a) is the photograph of an etched $\text{Te}_{0.90}\text{Se}_{0.10}$ whisker. Some pits are irregular shaped whereas some are well developed. Pits which are aligned along a line form etch grooves. In Fig.7.22(b) the higher magnification of pits is shown. The increase in the formation of small pits is due to higher concentrations of Se in the whiskers. Fig.7.22(c) shows the same region after successive etching for 5 min. All the pits were covered with some irregular markings and become roughened. The pit density was determined for various Se concentrations and the variation is plotted in Fig.7.23.

(b) Bi_2Te_3 whiskers

The thermal etching of Bi_2Te_3 whiskers has been performed by trial and error under different etching conditions. It was found that distinct etch pits could be obtained at 190°C for 15 min. Below this temperature no etch pits were observed even after etching for a longer time. Figs.7.24(a) and 7.24(b) show rows of etch pits on

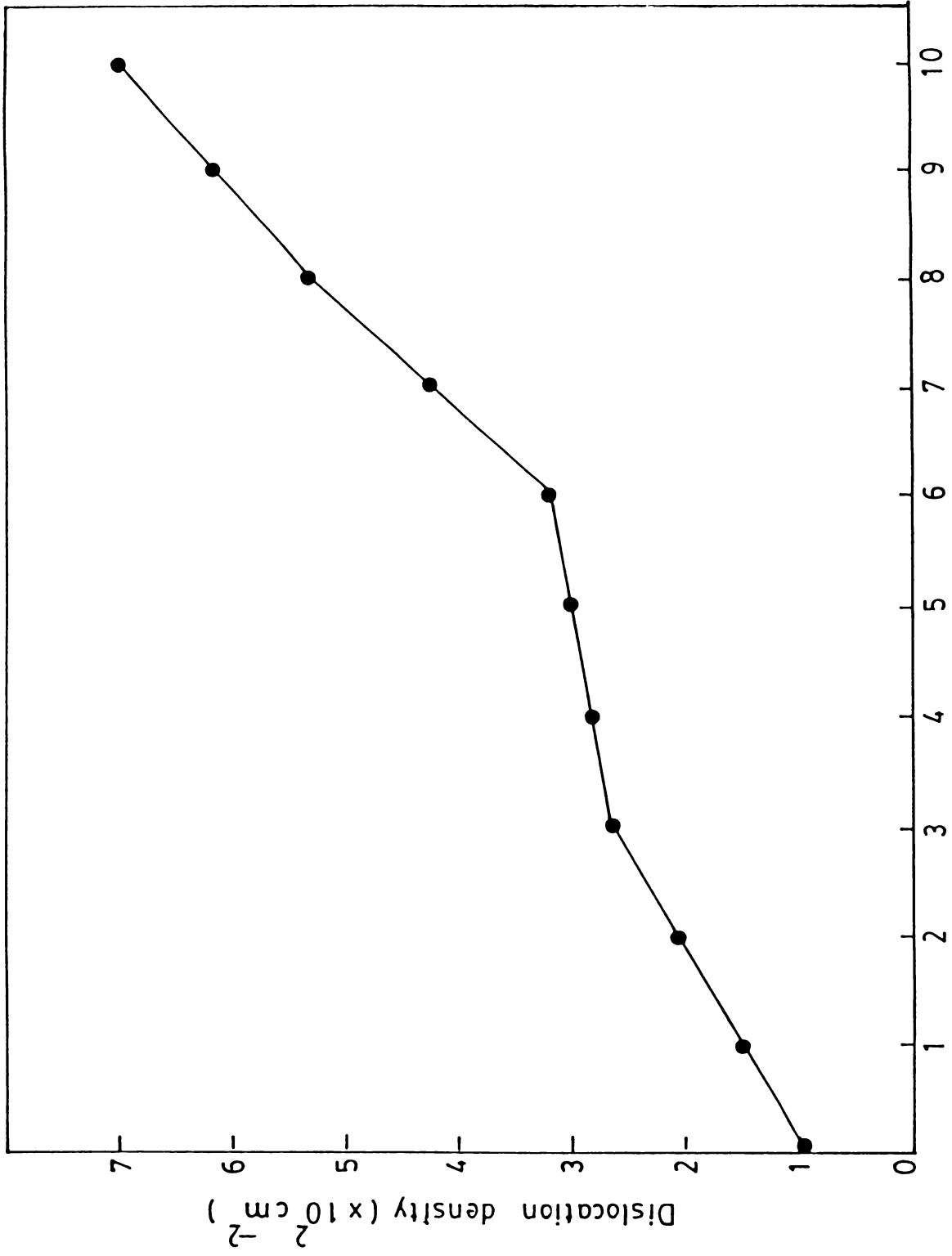


Fig. 7.23

the prism face of a crystal at lower and higher magnifications respectively. The pits that appeared have a rod like shape with rounded edges. They are almost symmetrical about the c-axis and their longer sides are parallel to the c-axis. On further etching for another 4 min, it is observed that the pits enlarged and diffused into each other leaving large complex pits as shown in Fig.7.24(c). The smaller etch pits seen in Fig.7.24(b) also grown larger. At temperature above 190°C, surface roughening is observed due to the onset of general evaporation. Fig.7.25 shows the photograph of the whisker surface after etching at 230°C for 5 min. It is seen that, evaporation of atoms occurs very fast in this surface.

(c) In₂Te₃ whiskers

The optimum condition for obtaining well defined thermal etch pits on the prism faces of α and β -In₂Te₃ whiskers was found after a systematic analysis. When the crystals with good plane prism faces were thermal etched at 180°C for 6 min, only a few irregular shaped etch pits were observed. On increasing the etching time to 10 min, well developed square and rectangular shaped etch pits were observed [Fig.7.26(a)]. Some of the pits have steps and kinks on their boundaries. It is also seen that thermal

etch grooves are nucleated from the edges and are propagated towards the center of the prism face. Etching the same face for 14 min resulted in the development of loop formation in and around the earlier pits [Fig.7.26(b)]. The morphology of etch pits at higher magnification [Fig.7.26(c)] clearly shows the loop structure.

The etching behaviour of β - In_2Te_3 whiskers was same as that of α - In_2Te_3 whiskers when etched under the same conditions. Figs.7.27(a) and 7.27(b) show the prism face of a β - In_2Te_3 whisker after thermal etching at 180°C for 10 and 14 min respectively. In this case, the number of etch pits was increased.

The thermal etching studies of $\text{Te}_{1-x}\text{Se}_x$, Bi_2Te_3 and α and β - In_2Te_3 whiskers showed an increase in the size of etch pits after successive etching. The persistence of etch pits upon longer etching time reveals that thermal etch pits are produced at dislocation sites.

Thermal etch pits are known to be formed by local sublimation of atoms from crystal surfaces. The importance of this method to reveal dislocations and to understand the mechanism responsible for etch-pit formation have been

the subject of many research papers [15,23,24]. The theory of evaporation mechanism is based on the terrace-ledge-kink (TLK) hypothesis of the crystal surface which gives a detailed consideration of kink nucleation and ledge motion [25].

It has been found during the present study that the edges of smooth prism faces were etched faster than the center of the face and hence more pits were found deeply in the regions nearby to the edge parts. The stepped regions of $\text{Te}_{1-x}\text{Se}_x$ whiskers were attacked very readily compared to the smooth prism faces. In the case of Bi_2Te_3 whiskers, long etch pits were formed only near the edges. Similar behaviour has been observed in In_2Te_3 whiskers where etch grooves were originated from the edges and are propagated towards the center of the face. Moreover, the pits formed have steps and kinks on their boundaries. This leads to the conclusion that the thermal etch pit formation of $\text{Te}_{1-x}\text{Se}_x$, Bi_2Te_3 , α and β - In_2Te_3 whiskers follows the TLK theory.

7.4 CONCLUSION

Chemical etching studies on the prism faces of $\text{Te}_{1-x}\text{Se}_x$ whiskers using H_2SO_4 etchant show that the dislocation density is increased with an increase in the

concentration of Se. The change in morphology of pits indicates that the dissolution directions change with the impurity concentrations.

The etchants developed for the etching of Bi_2Te_3 whiskers could produce dislocation etch pits on their prism faces. The morphology of etched pattern is different for all these etchants. The formation of terraced pits is due to the enhanced rate of dissolution on the crystal surfaces.

The etchant employed for α and $\beta\text{-In}_2\text{Te}_3$ whiskers is very reliable for revealing dislocations on their prism faces. The etchant produced shallow dislocation loops on the surface of $\beta\text{-In}_2\text{Te}_3$ whiskers.

The thermal etching studies of $\text{Te}_{1-x}\text{Se}_x$ whiskers showed an increase in the size of etch pits on successive etching. Array of thermal etch pits were formed along etch grooves which indicates that the pits are formed at dislocation sites. The dislocation density due to thermal etch pits increased with Se content.

In the case of Bi_2Te_3 whiskers, rod shaped pits are formed which grown larger on prolonged etching. The thermal etch pits on the prism faces of α and $\beta\text{-In}_2\text{Te}_3$ whiskers become doubly looped on successive etching.

7.5 FIGURE CAPTIONS

Fig.7.1(a) Chemical etch pattern on the prism face of a Te whisker produced after etching in conc. H_2SO_4 at 120°C for 3 min.

Fig.7.1(b) The same face after repeated etching.

Fig.7.2 Distribution of etch pits on the prism face of a $\text{Te}_{0.98}\text{Se}_{0.02}$ whisker.

Fig.7.3 Etch pits on the prism face of a $\text{Te}_{0.97}\text{Se}_{0.03}$ whisker.

Fig.7.4 Etched prism face of a $\text{Te}_{0.94}\text{Se}_{0.06}$ whisker.

Fig.7.5 Etch patterns on the prism face of a $\text{Te}_{0.92}\text{Se}_{0.08}$ whisker.

Fig.7.6(a) Etch patterns on the prism face of a $\text{Te}_{0.90}\text{Se}_{0.10}$ whisker.

Fig.7.6(b) The same face after etching.

Fig.7.7 Variation of chemical etch pit density as a function of Se concentration.

- Fig.7.8 Etch patterns on the prism face of a $\text{Te}_{0.95}\text{Se}_{0.05}$ whisker.
- Fig.7.9 Etch patterns produced on the prism face of a Bi_2Te_3 whisker by 7 ml HNO_3 + 3 ml H_2SO_4 + 10 ml H_2O after etching for 10 sec.
- Fig.7.10 The same face after repeated etching.
- Fig.7.11(a) Etch patterns produced on the prism face of a Bi_2Te_3 whisker by 50 mg I_2 + 5 ml H_2SO_4 + 10 ml CH_3OH after etching for 10 sec.
- Fig.7.11(b) Higher magnification of the region marked A in Fig.7.11(a)
- Fig.7.11(c) The face shown in 7.11(a) after etching for 20 sec.
- Fig.7.11(d) Higher magnification of the region marked A in Fig.7.11(c).
- Fig.7.12 Low angle grain boundaries observed on the prism face of a Bi_2Te_3 whisker.

Fig.7.13 The tip of a Bi_2Te_3 whisker after etching in 50 mg I_2 + 5 ml H_2SO_4 + 10 ml CH_3OH for 10 sec.

Fig.7.14(a) Formation of terraced etch pits on the prism face of a Bi_2Te_3 whisker after etching in 50 mg I_2 + 6 ml H_2SO_4 + 10 ml CH_3OH for 10 sec.

Fig.7.14(b) The same face at higher magnification.

Fig.7.15 Etch pits formed on the prism face of a Bi_2Te_3 whisker after etching in 100 mg I_2 + 5 ml H_2SO_4 + 10 ml CH_3OH for 10 sec.

Fig.7.16(a) Etch pits formed on the prism face of a Bi_2Te_3 whisker after etching in 50 mg I_2 + 8 ml HNO_3 + 20 ml CH_3OH for 20 sec.

Fig.7.16(b) The same face after successive etching for 30 sec.

Fig.7.17(a) Etch patterns formed on the prism of a $\alpha\text{-In}_2\text{Te}_3$ whisker after etching in 3 ml HNO_3 + 0.3 ml HF + 10 ml H_2O for 15 sec.

Fig.7.17(b) Higher magnification of the pit marked at B in Fig.7.17(a)

Fig.7.17(c) The face shown in Fig.7.17(a) after repeated etching.

Fig.7.18(a) Etch patterns formed on the prism face of a β - In_2Te_3 whisker after etching in 3 ml HNO_3 + 0.3 ml HF + 10 ml H_2O for 15 sec.

Fig.7.18(b) The same face after repeated etching.

Fig.7.19(a) Thermal etch patterns formed on the prism face of a Te whisker after etching at 150°C for 10 min.

Fig.7.19(b) The same face after repeated etching.

Fig.7.20(a) Thermal etch patterns formed on the prism face of a $\text{Te}_{0.97}\text{Se}_{0.03}$ whisker after etching at 150°C for 10 min.

Fig.7.20(b) The same face after repeated etching.

Fig.7.21(a) Thermal etch patterns formed on the prism face of $\text{Te}_{0.94}\text{Se}_{0.06}$ whisker after etching at 150°C for 10 min.

Fig.7.21(b) The same face after repeated etching.

Fig.7.22(a) Thermal etch patterns formed on the prism face of a $\text{Te}_{0.90}\text{Se}_{0.10}$ whisker, after etching at 150°C for 10 min.

Fig.7.22(b) Higher magnification of the pits shown in Fig.7.22(a).

Fig.7.22(c) The face shown in Fig.7.22(a) after repeated etching.

Fig.7.23 Variation of thermal etch pit density as a function of Se concentration.

Fig.7.24(a) Thermal etch patterns formed on the surface of a Bi_2Te_3 whisker after etching at 190°C for 15 min.

Fig.7.24(b) The same face at a higher magnification.

Fig.7.24(c) The face shown in 7.24(b) after repeated etching.

Fig.7.25 Prism face of a Bi_2Te_3 whisker after etching at 230°C for 5 min.

Fig.7.26(a) Thermal etch pattern formed on the surface of a α - In_2Te_3 whisker after etching at 180°C for 10 min.

Fig.7.26(b) The same face after repeated etching.

Fig.7.26(c) Higher magnification of the region shown in Fig.7.26(b).

Fig.7.27(a) Thermal etch pattern formed on the surface of a β - In_2Te_3 whisker after etching at 180°C for 10 min.

Fig.7.27(b) The same face after repeated etching.

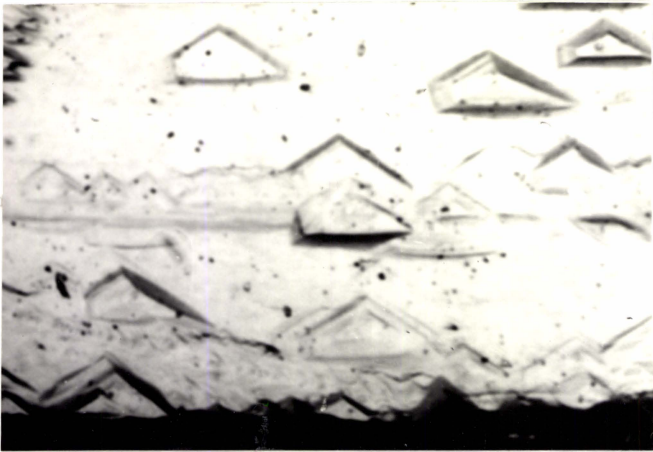


Fig. 7.1(a)

(x80)

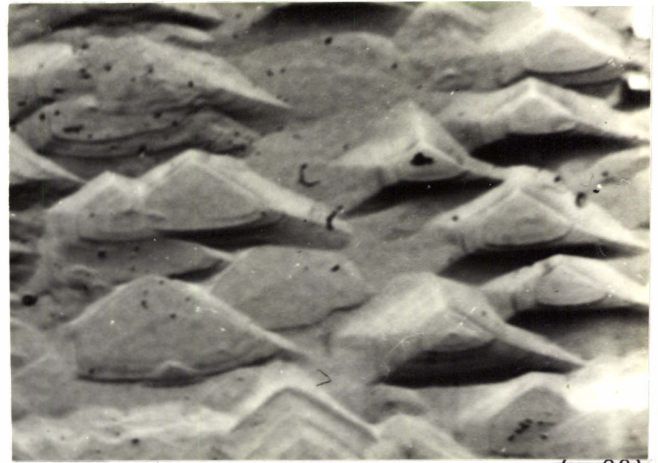


Fig. 7.1(b)

(x 80)

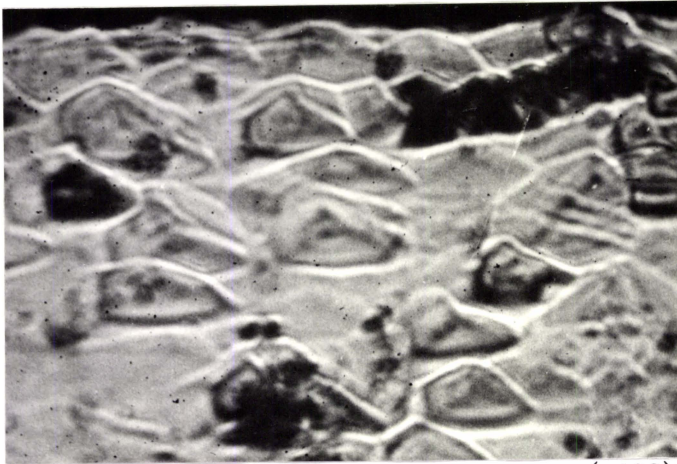


Fig. 7.2

(x100)

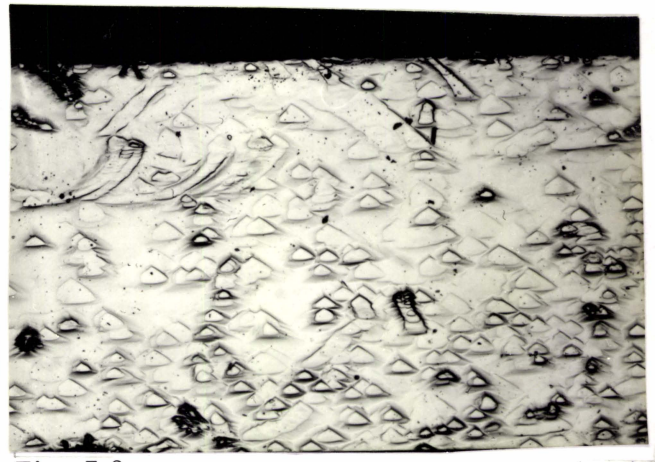


Fig. 7.3

(x90)

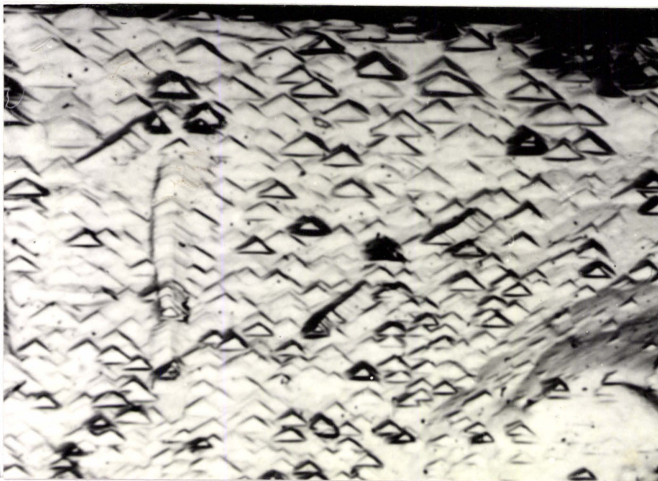


Fig. 7.4

(x100)

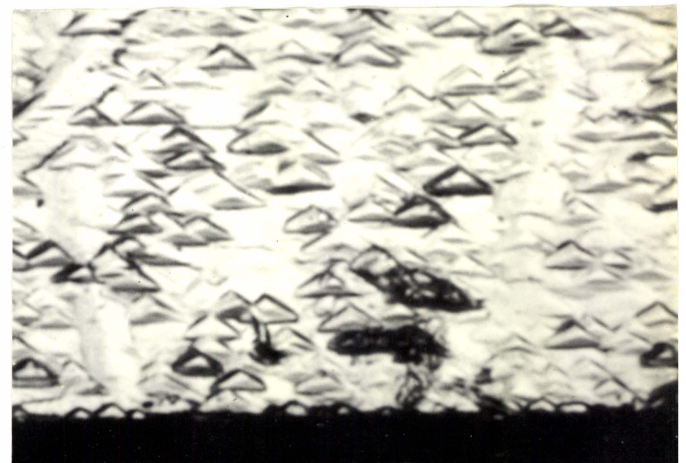


Fig. 7.5

(x110)

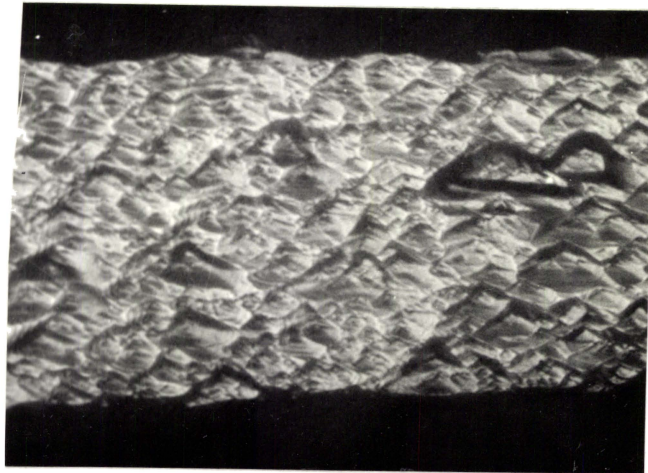


Fig. 7.6(a)

(x 110)

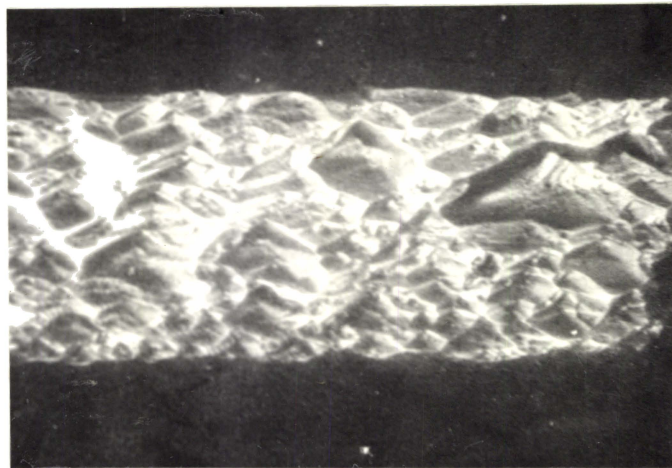


Fig. 7.6(b)

(x 100)

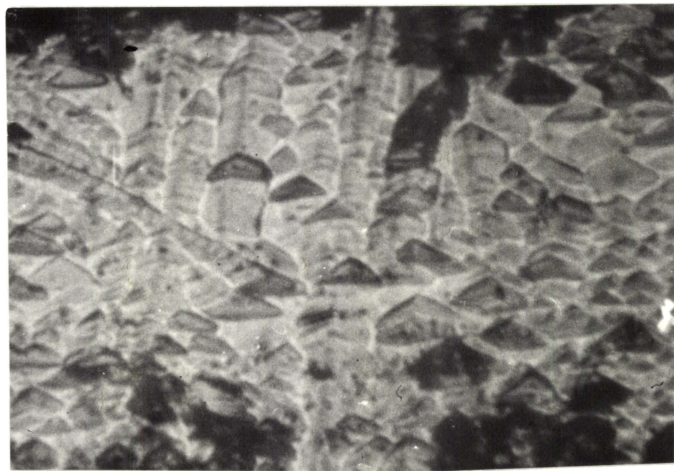


Fig. 7.8

(x80)

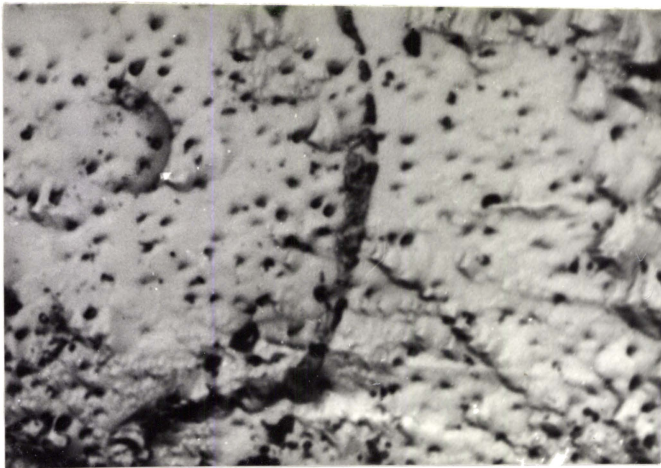


Fig. 7.9

(x33)

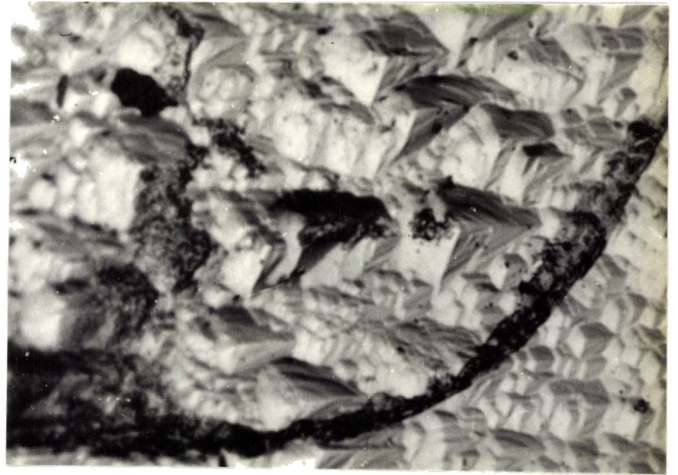


Fig. 7.10

(x 100)

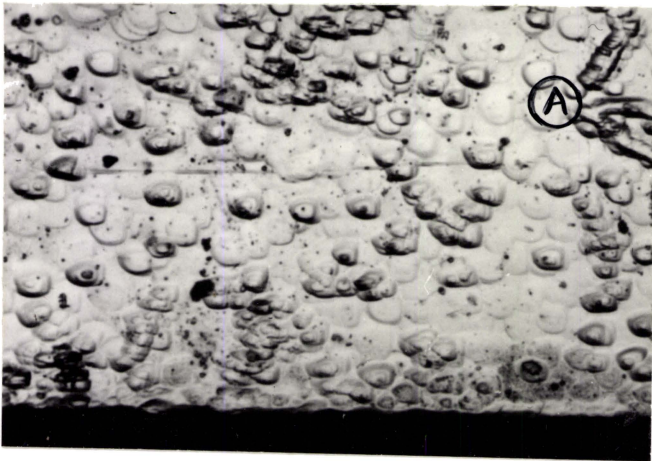


Fig. 7.11(a)

(x90)

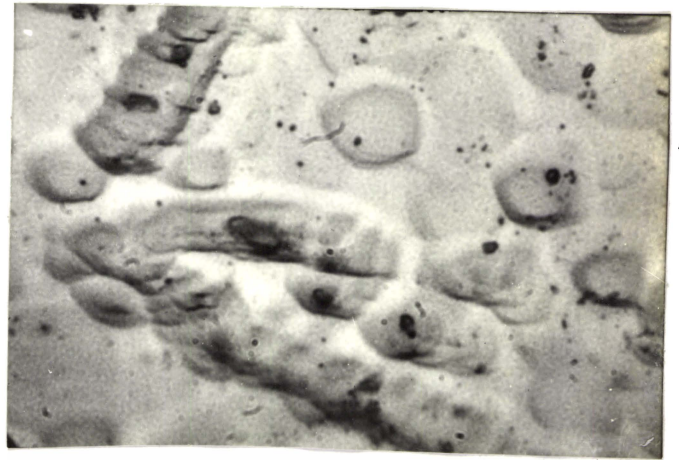


Fig. 7.11(b)

(x 200)



Fig. 7.11(c)

(x80)

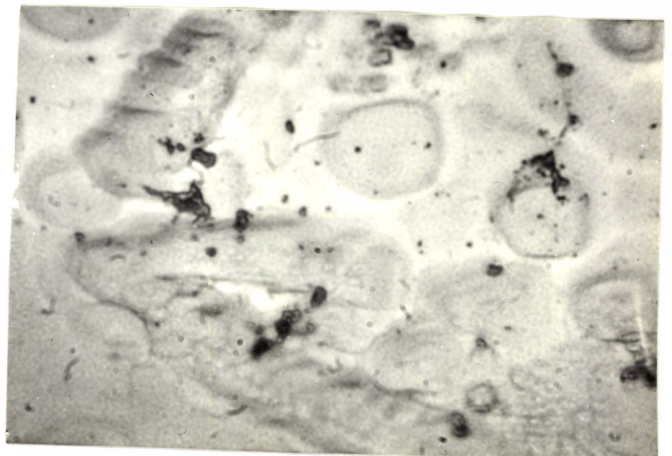


Fig. 7.11(d)

(x 200)

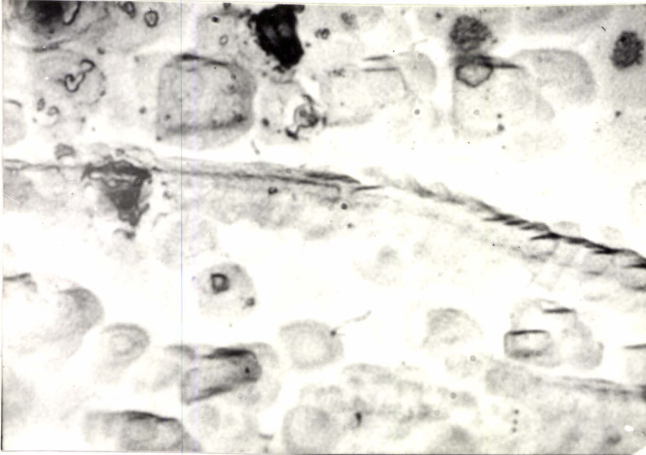


Fig. 7.12

(x200)

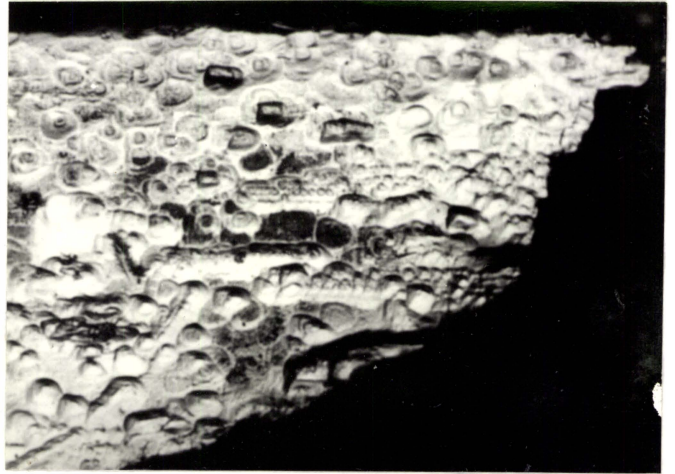
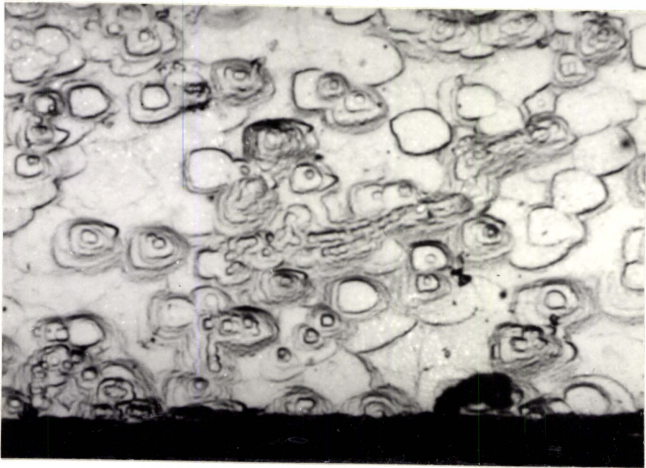


Fig. 7.13

(x80)



(Fig. 7.14(a)

(x80)

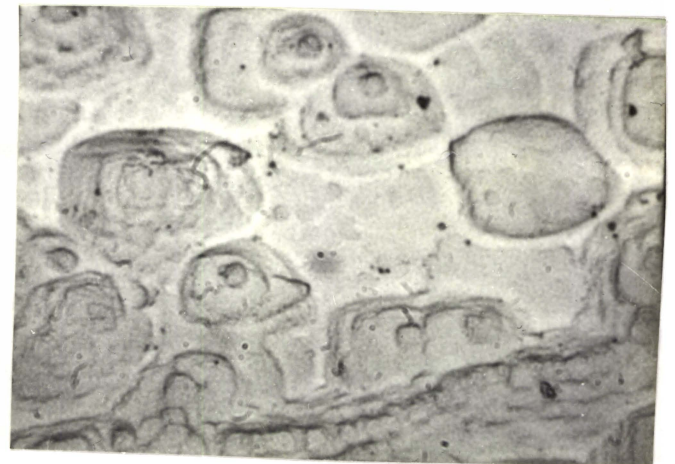


Fig. 7.14(b)

(x200)



Fig. 7.15

(x120)

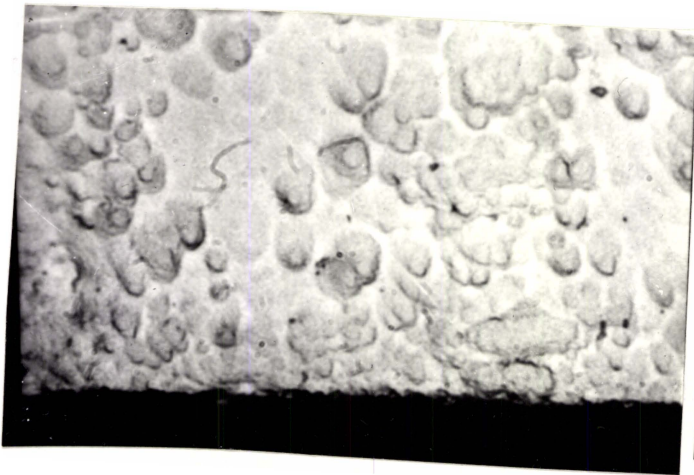
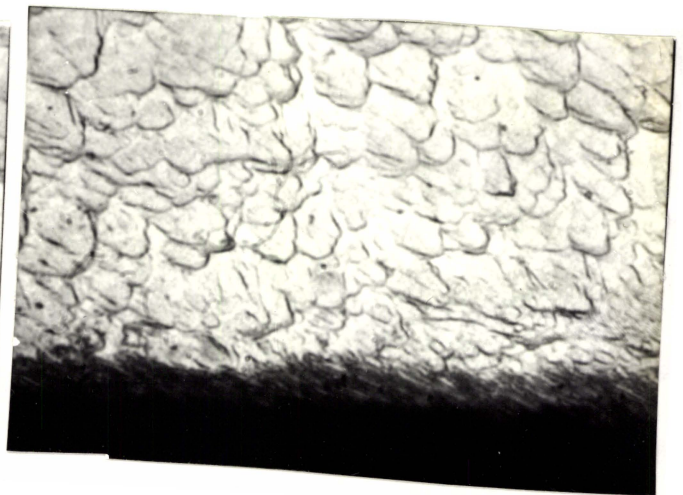


Fig. 7.16(a)



(x120) Fig. 7.16(b)

(x120)

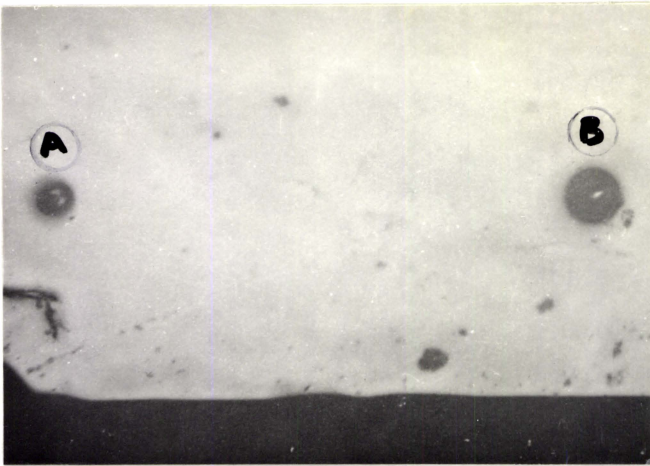
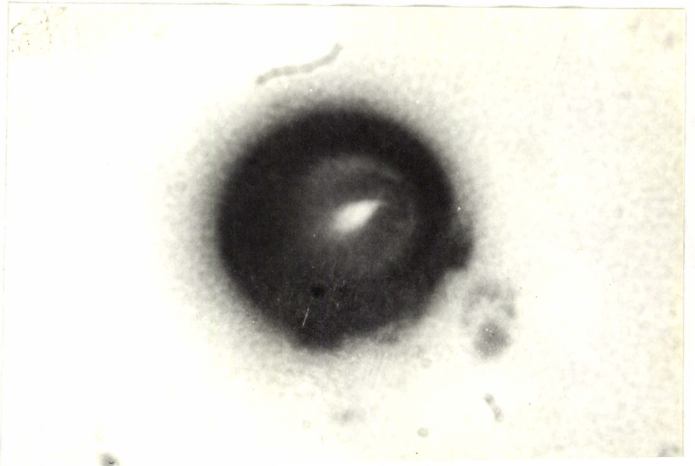


Fig. 7.17(a)

(x125) Fig. 7.17(b)



(x200)

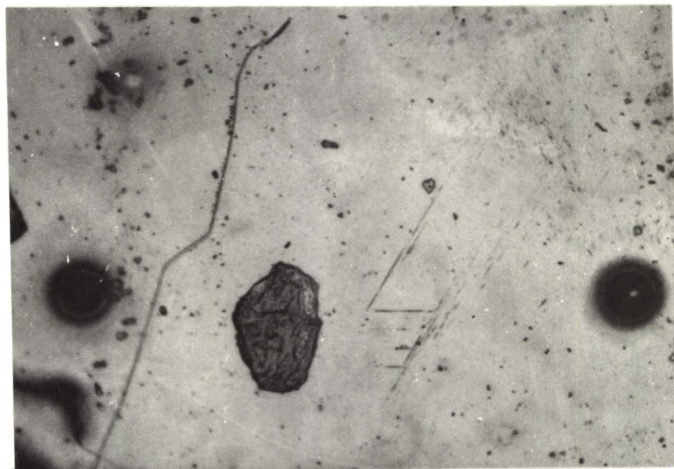


Fig. 7.17(c)

(x125)

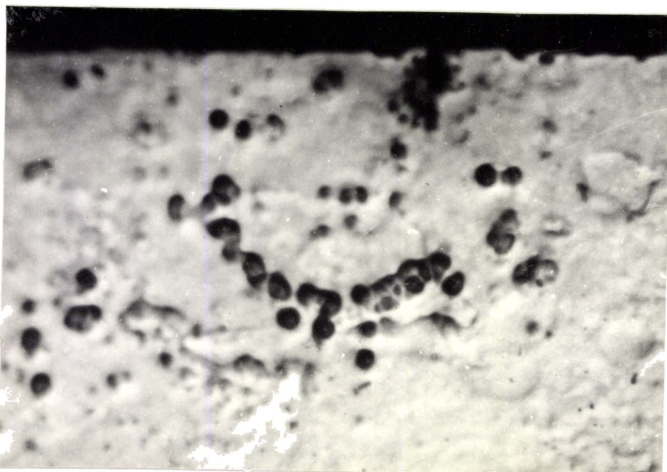
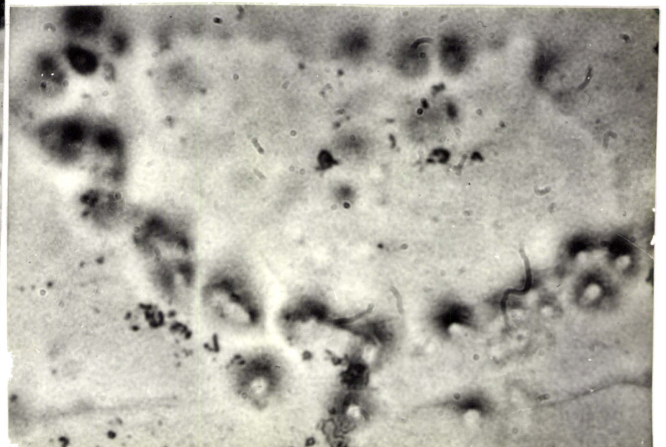


Fig. 7.18(a)

(x150) Fig. 7.18(b)



(x400)

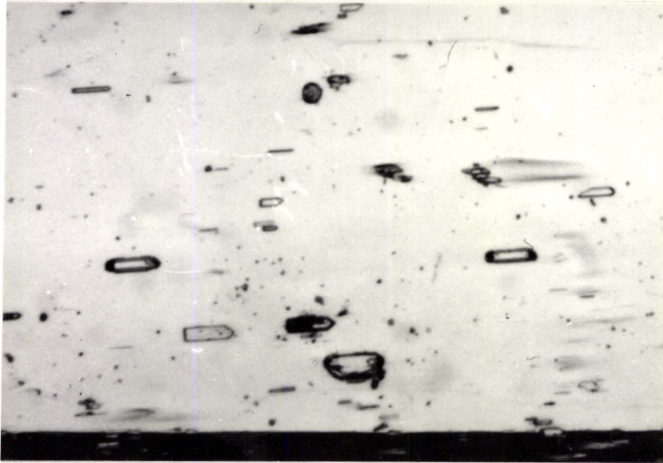


Fig. 7.19(a)

(x80)

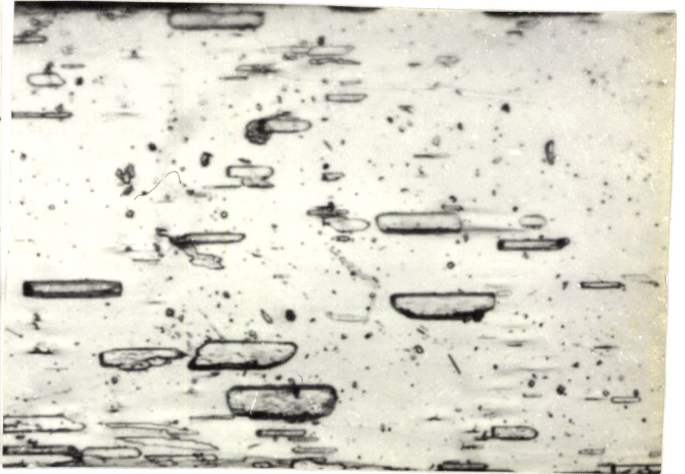


Fig. 7.19(b)

(x80)

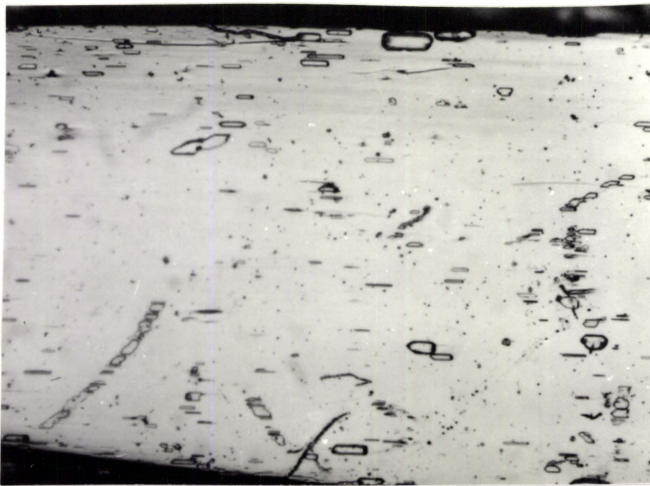


Fig. 7.20(a)

(x90)

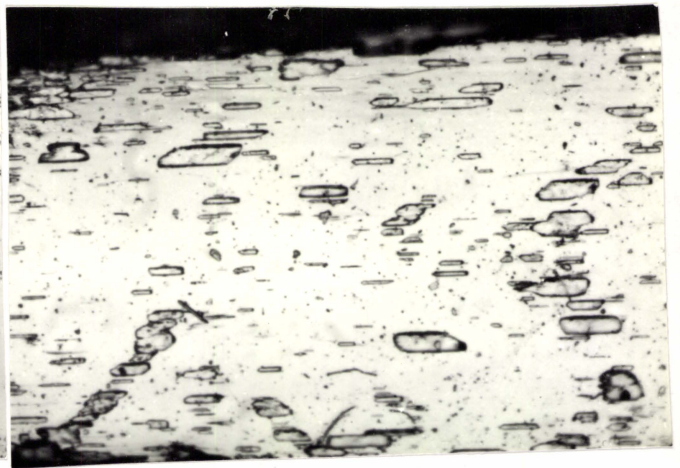


Fig. 7.20(b)

(x90)

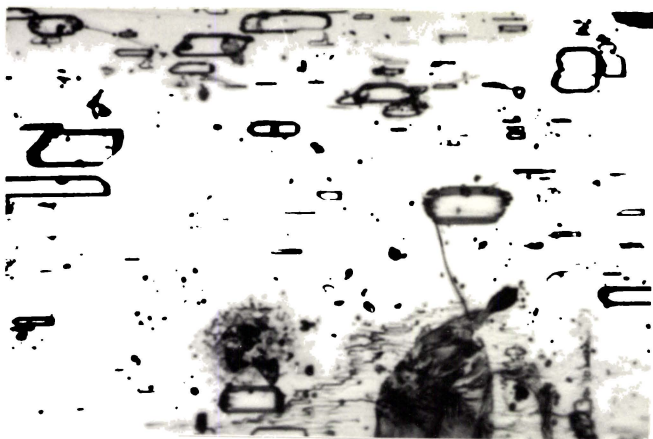
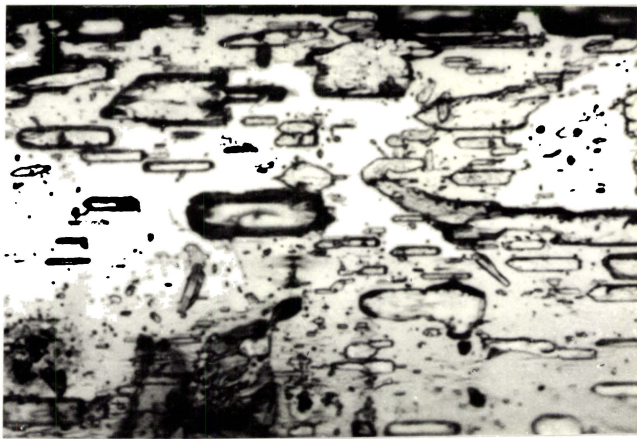


Fig. 7.21(a)



(x100) Fig. 7.21(b)

(x100)

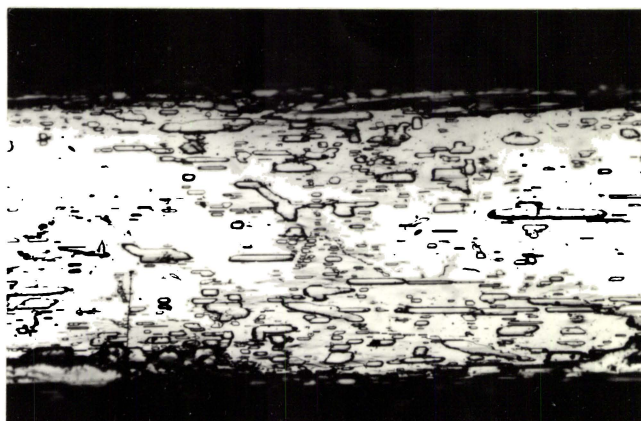


Fig. 7.22(a)

(x75)

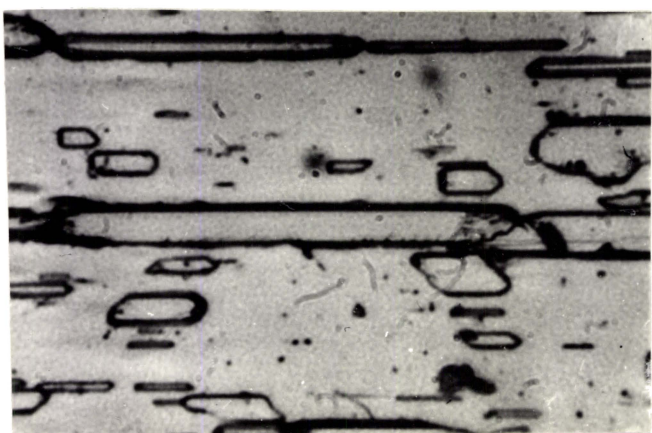
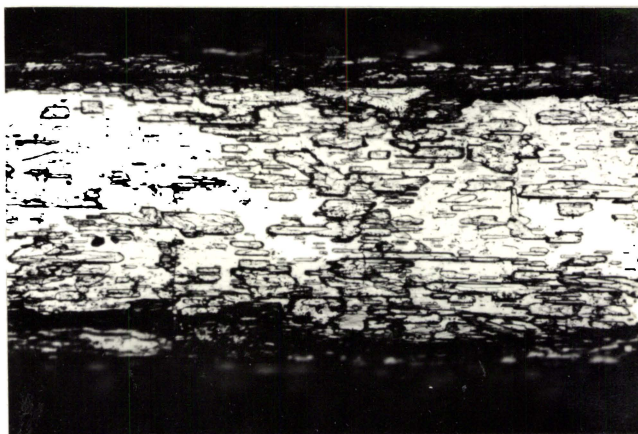


Fig. 7.22(b)



(x200) Fig.7.22(c)

(x 75)

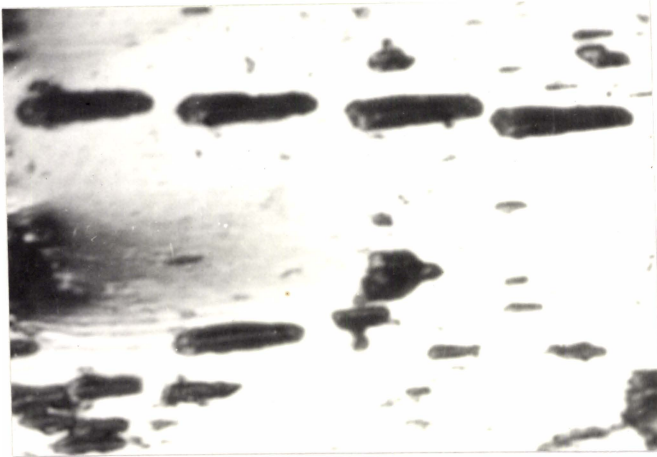


Fig. 7.24(a)

(x80)



Fig. 7.24(b)

(x200)

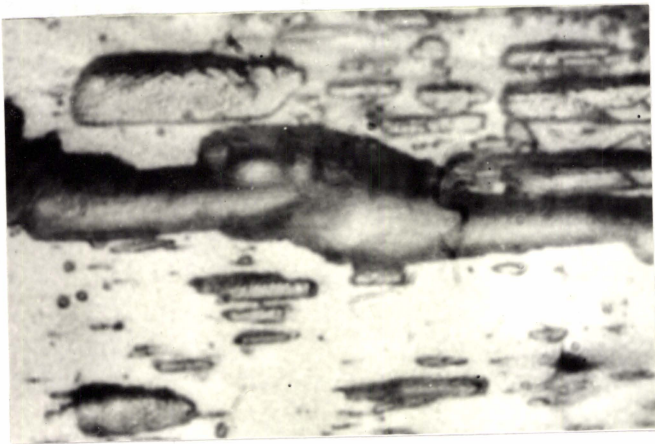


Fig. 7.24(c)

(x200)

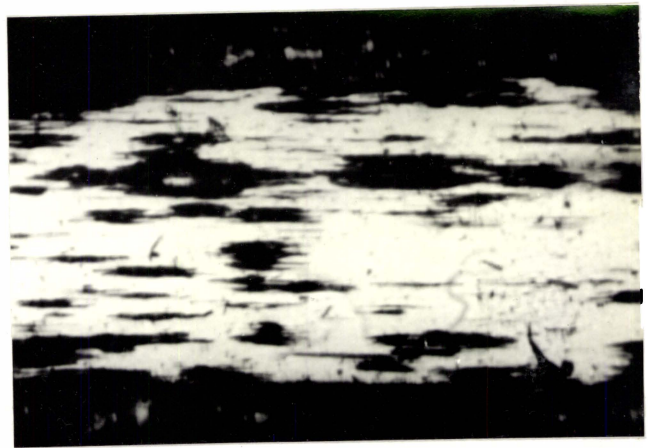


Fig. 7.25

(x 50)

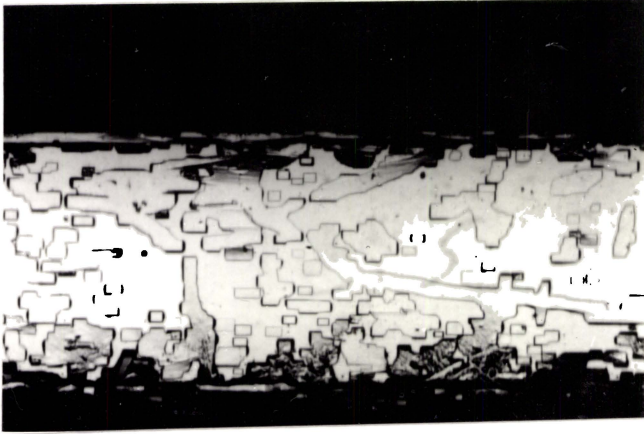
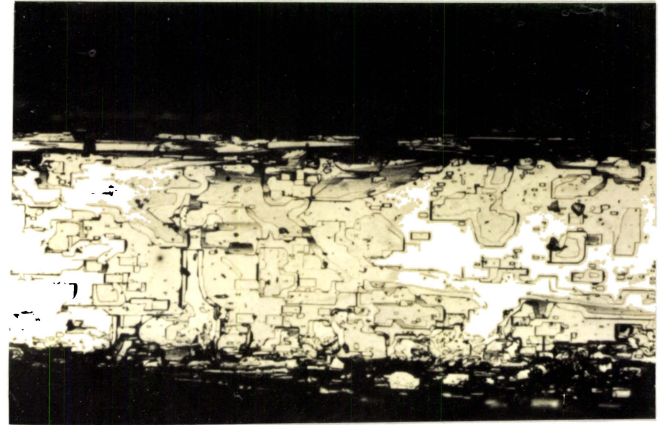


Fig. 7.26(a)



(x33) Fig.7.26(b)

(x33)

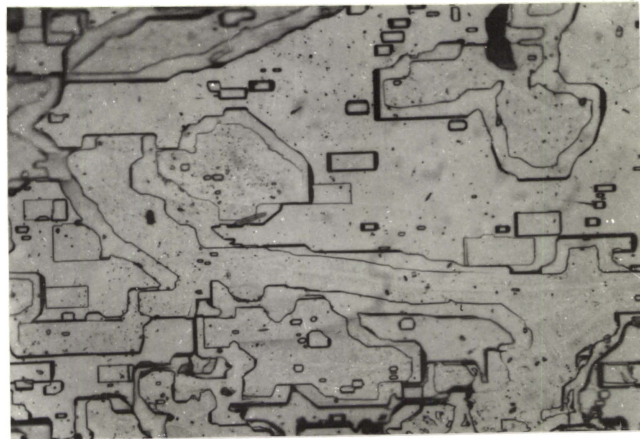


Fig. 7.26(c)

(x200)



Fig. 7.27(a)



(x100) Fig.7.27(b)

(x100)

7.6 REFERENCES

- [1] L.C. Lovell, J.H. Wernick and K.E. Benson, *Acta Metallurgica* 6 (1958) 716.
- [2] A.I. Blum, *Fiz. Tverdogo Tela* 2 (1960) 1666.
- [3] J.S. Blakemore, J.D. Heaps, K.C. Nomura and L.P. Beardsley, *Phys. Rev.* 117 (1960) 687.
- [4] J.S. Blakemore, J.W. Schultz and K.C. Nomura, *J. Appl. Phys.* 31 (1960) 226.
- [5] J.S. Blakemore and K.C. Nomura, *J. Appl. Phys.* 32 (1962) 745.
- [6] K. Herrmann, *Phys. Stat. Solidi* 1 (1961) 254.
- [7] A. Koma, E. Takimoto and S. Tanaka, *Phys. Stat. Solidi* 40 (1970) 239.
- [8] J. Di Persio, J.C. Doukhan and G. Saada, *Mater. Sci. Eng.* 4 (1969) 123.

- [9] S. Ahmed and S. Weintraub, *J. Cryst. Growth* **8** (1971) 299.
- [10] J.C. Doukhan and J.C. Farvacque, *Phys. Stat. Solidi(a)* **4** (1971) K1.
- [11] M.El - Azab, C.R. Mc. Laughlin and C.H.Champness, *J. Cryst. Growth* **28** (1975) 1.
- [12] Zb. Kalinski and G. Lehmann, *Kristall und Technik*, **11** (1976) 281.
- [13] I. Shih and C.H. Champness, *J. Cryst. Growth*, **56** (1982) 169.
- [14] S.B. Trivedi and V.P. Bhatt, *J. Cryst. Growth*, **32** (1976) 227.
- [15] V.P. Bhatt and S.B. Trivedi, *J. Cryst. Growth*, **37** (1977) 23.
- [16] V.P. Bhatt and S.B. Trivedi, *J. Cryst. Growth*, **49** (1980) 743.

- [17] S. Weintraub and S. Ahmed, *J. Cryst. Growth* **8** (1974) 299.

- [18] V.P. Bhatt and M.D. Trivedi, *Kristall und Technik* **15** (1980) 666.

- [19] A.G. Kunjomana and E. Mathai, *J. Cryst. Growth* **92** (1988) 666.

- [20] I. Teramoto and S. Takayanagi, *J. Appl. Phys.* **32** (1961) 119.

- [21] A. Sagar and J.W. Faust, Jr., *J. Appl. Phys.* **38** (1967) 482.

- [22] A.G. Kunjomana and E. Mathai (Communicated).

- [23] C.Y. Lou and G.A. Somorjai, *J. Appl. Phys.* **55** (1971) 4554.

- [24] M. Kitada, *J. Mater. Sci.* **15** (1980) 82.

- [25] J.P. Hirth and G.M. Pound, *J. Chem. Phys.* **26** (1957) 1216.

MICROINDENTATION ANALYSIS OF VAPOUR-GROWN
 $\text{Te}_{1-x}\text{Se}_x$, Bi_2Te_3 AND In_2Te_3 CRYSTALS

8.1 INTRODUCTION

Microindentation studies of Te-Se crystals have been done by a few workers. Boyarskaya et al. [1] studied the microhardness anisotropy of tellurium crystals grown by Bridgman method using the scratch method. They found that the hardness along the c-axis is lower than at right angles. But the microhardness measurements in Te-Se alloys were first studied by Lange and Regel [2] and the anomalies in the microhardness values with changing chemical composition of the material had been reported. Their results showed a minimum in the hardness value when doped with small amounts of Se additives. They interpreted this result by precision measurements of density / concentration relationship and observed a corresponding density minimum while doping with Se. The anisotropy of microhardness measurements was explained on the principle of the truncation of the chains of Te lattice [3]. However, no systematic investigation on the hardness anisotropy characteristics of $\text{Te}_{1-x}\text{Se}_x$ whiskers at compositions 0 to 10 at % Se has been made.

Arivuoli et al. [4] have reported the microhardness studies of V-VI group chalcogenides grown from vapour. But only a little information is available regarding the microhardness studies of Bi_2Te_3 whiskers. In the case of

In_2Te_3 whiskers, no data is reported in the literature in connection with their mechanical behaviour.

This chapter presents the microhardness studies on the prism faces of $\text{Te}_{1-x}\text{Se}_x$, Bi_2Te_3 , α and β - In_2Te_3 whiskers grown by physical vapour deposition (PVD) method. In the case of $\text{Te}_{1-x}\text{Se}_x$ whiskers, the variation of hardness with applied load was studied at different compositions of Se ($x = 0$ to 10 at %) additives. The work hardening exponent has also been computed for all samples and the results have been discussed.

8.2 EXPERIMENTAL

Whisker crystals of $\text{Te}_{1-x}\text{Se}_x$, Bi_2Te_3 , α and β - In_2Te_3 were grown by PVD method as already described in chapter 5. Crystals with good plane prism faces were chosen for microindentation studies. The measurements were made using a Hanemann microhardness tester (Model D32) fitted with a diamond pyramidal indenter attached to a metallurgical microscope (Epi typ II Carl-Zeiss, Jena). After proper mounting of the crystals on glass slides, the selected surfaces were indented for various loads ranging from 2.5 to 40 g. The time of indentation was kept at 15 sec throughout the work. Subsequent impressions were made after a time

lapse of 30 min to allow for any elastic recovery. Indentations were carried out in the low load region at different sites such that the distance between any two consecutive indentation marks is greater than three times the diagonal length. This was done to avoid any mutual influence of the indentations. All the measurements were made at room temperature. The length of the indentation diagonal was measured using the micrometer eyepiece of the microscope. Performing 10 trials of indentations for each loading, the mean value of the diagonal lengths was found. From these measurements, the values of microhardness H_v were computed as described in chapter 4.

8.3 RESULTS AND DISCUSSION

8.3.1 $Te_{1-x}Se_x$ whiskers

Figs.8.1 to 8.3 show the relation between microhardness H_v and load P for Te , $Te_{0.95}Se_{0.05}$ and $Te_{0.90}Se_{0.10}$ whiskers respectively. The inset shows the respective variation of $\log P$ with $\log d$. In all cases, it is seen that the value of hardness first increases, reaches a maximum and then decreases. The peak value is observed at 17.5 g load. The increase in hardness has been attributed to the effect of elastic recovery which results in the reduction of the diagonal length. The decrease in the

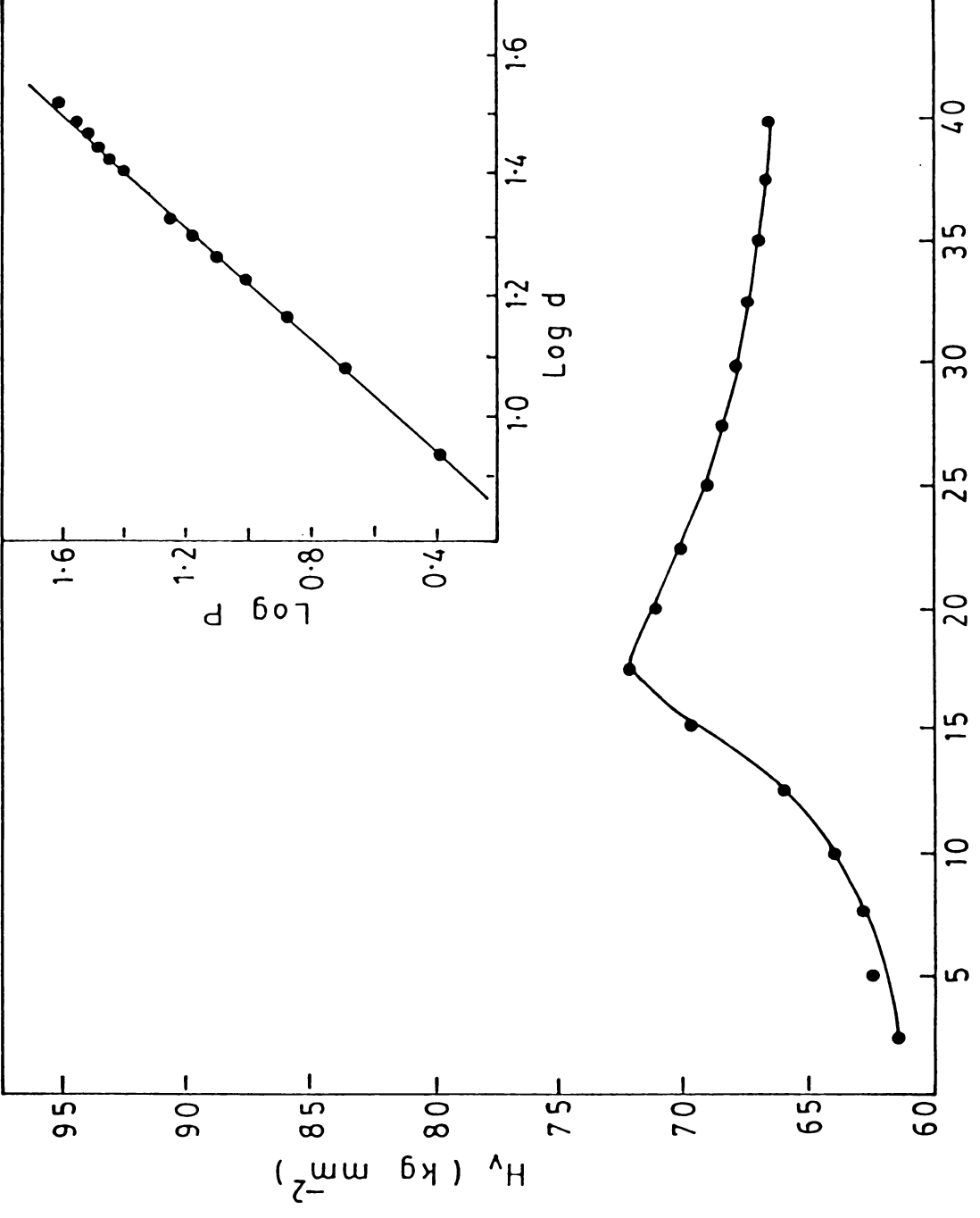


Fig. 8.1

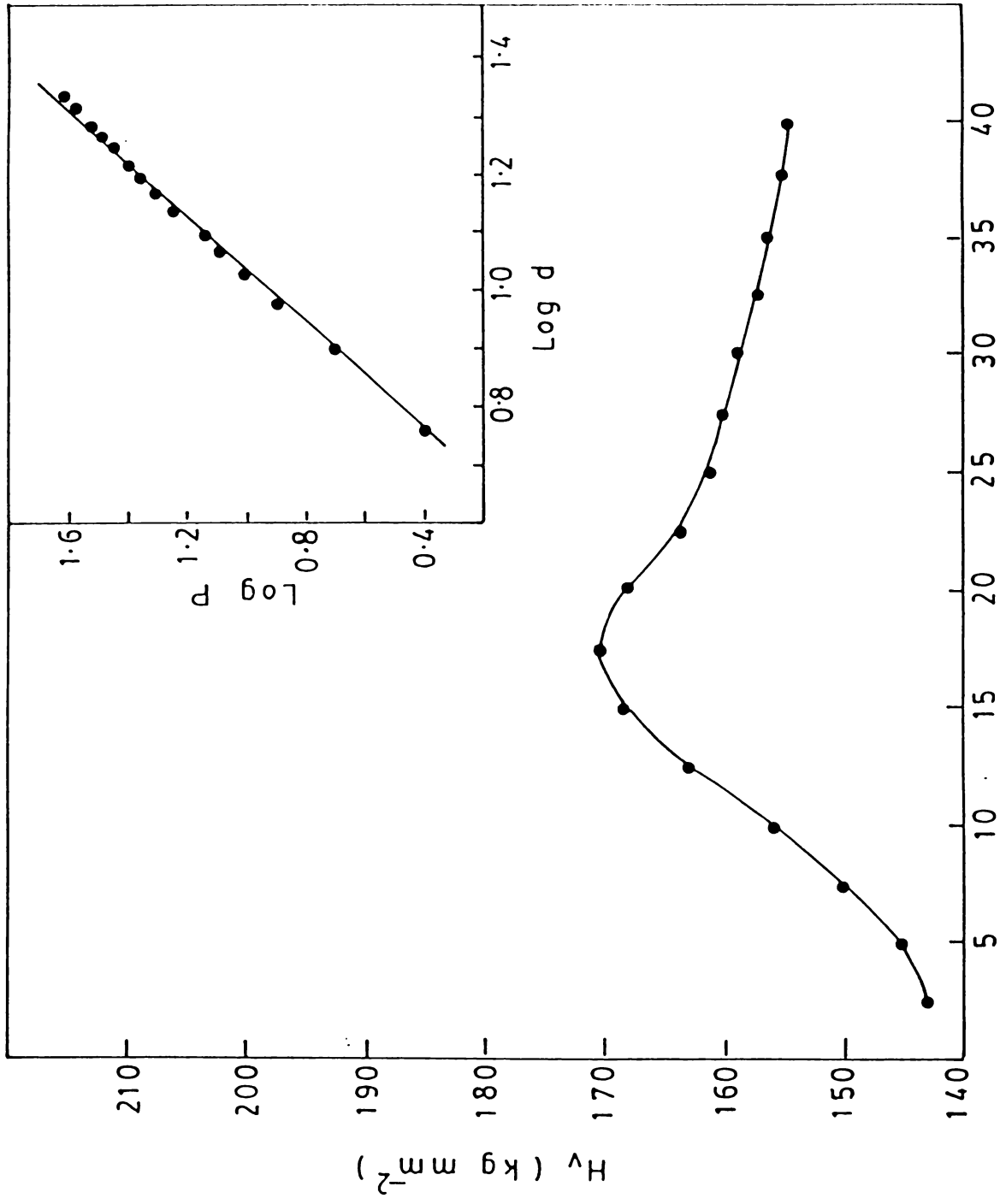


Fig. 8.2

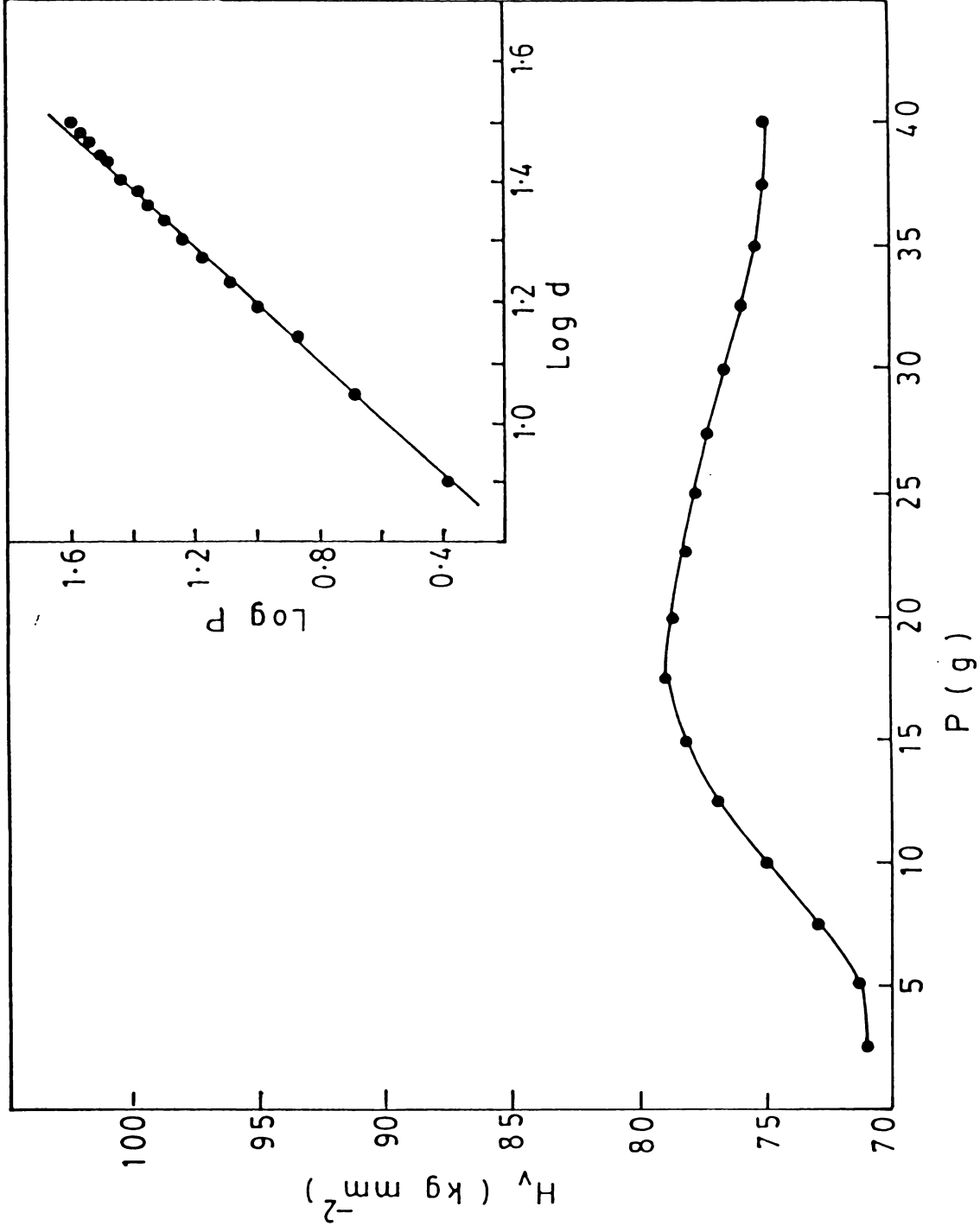


Fig. 8.3

hardness value at higher loads is associated with the slip mechanism, which arises due to the special nature of the structure and the character of the chemical bond in Te crystals. The tellurium lattice consists of spiral chains, each spiral having three atoms per turn. The chains lie parallel to one another with the corresponding atoms in each chain forming hexagonal nets. The bond between atoms on each chain is covalent whereas between the chains it is weak van der Waals forces. Due to the anisotropy in the atomic arrangement, on applying high stresses slip occurs along the spiral chains and hence hardness decreases due to deformation on the crystal surface.

The variation of microhardness with load can be represented by Meyer's equation,

$$P = ad^n \quad (8.1)$$

where P is the applied load, d is the diagonal length, a is the material constant and n is the Meyer index. The value of n represents the capacity for work hardening. The slope of inset figures gives the values of $n = 2.111$, 2.166 and 2.088 for Te, $\text{Te}_{0.95}\text{Se}_{0.05}$ and $\text{Te}_{0.90}\text{Se}_{0.10}$ whiskers respectively. According to Onitsch [5] the workhardening

coefficient n is greater than 2 when the hardness increases with increase of load and is less than 2 when the hardness decreases with load.

During the present investigations, some interesting results were obtained in relation to the change in anisotropy of the microhardness values with changing chemical composition of $\text{Te}_{1-x}\text{Se}_x$ whiskers. The composition dependence of the microhardness of $\text{Te}_{1-x}\text{Se}_x$ whiskers is depicted in Fig.8.4, whose behaviour resembles the typical hardness-composition curve for a binary solid solution system [6]. But the curve deviates from the ideal solid solution behaviour in the low x -region. Such deviations are attributed to the fact that distortion of tellurium lattice takes place as a result of doping tellurium with selenium. The fall in microhardness value is due to the loosening of the structure and the weakening of the bond between the structural units. At higher Se concentrations, the covalent bonds between the atoms in the chain are more saturated since the Te-Se bond is stronger than Te-Te bond and hence cause an increase in hardness value. The hardness anisotropy characteristics observed in the present study are seen to be similar to those reported by Lange and Regel [2,3].

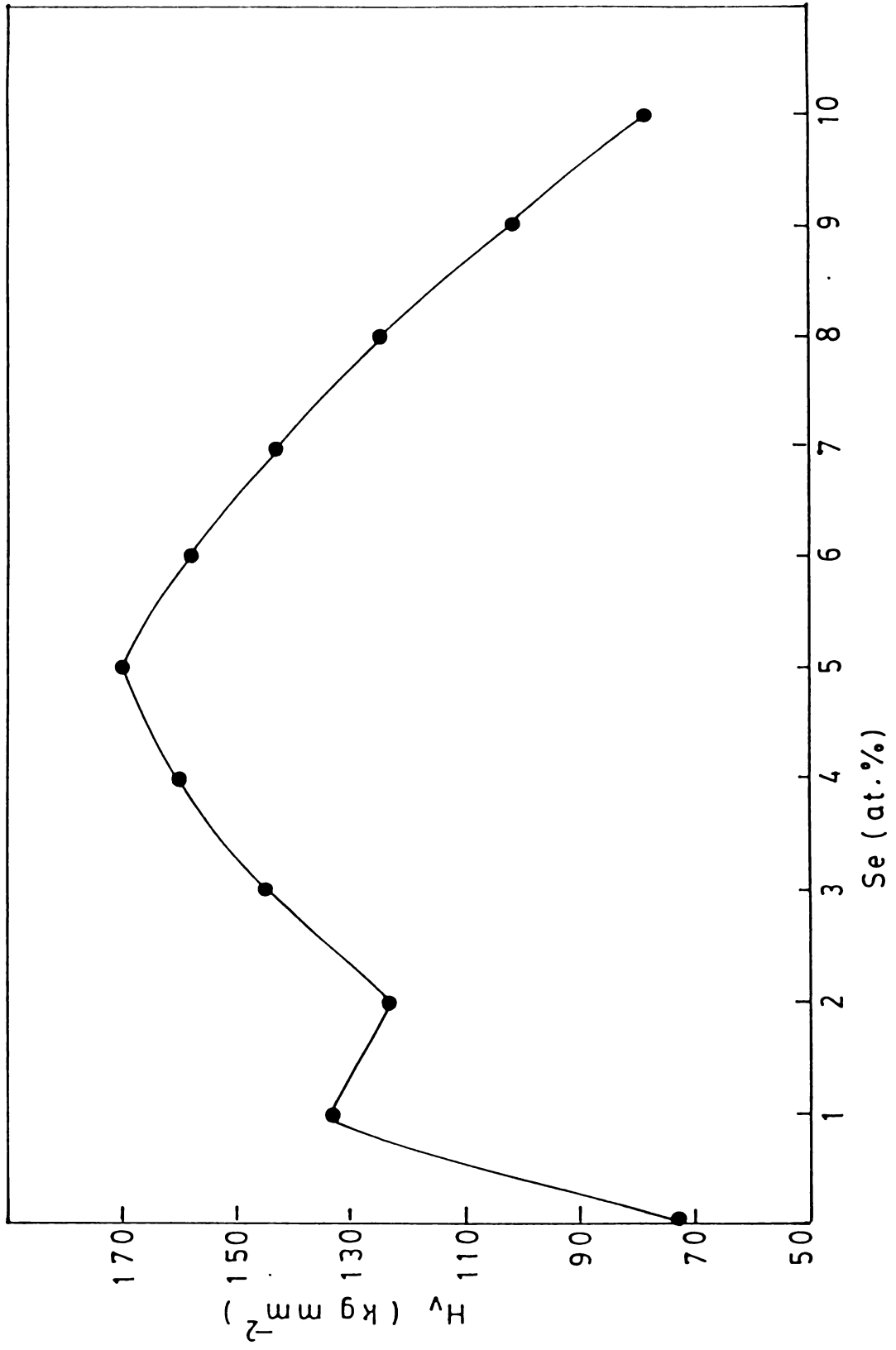


Fig. 8.4

8.3.2 Bi_2Te_3 whiskers

The hardness values of Bi_2Te_3 whiskers are found to increase with increase in load as seen from Fig.8.5. The indentation response to load is in accordance with Meyer's law. The graph of $\log P$ against $\log d$ is shown in the inset, which yields a straight line with slope $n = 2.5$. The work hardening exponent is higher when the indenter load is increased agreeing with the results of Onitsch [5].

In the present study, the increase of microhardness with load can be explained as follows. Bi_2Te_3 crystals have a peculiar layer structure [7]. The five layers form a more tightly bound sandwich and the structure results in inert and atomically smooth surfaces. Since the bonding between Bi-Te layers is predominantly covalent in character, the resistance to plastic flow is primarily determined by the increasing bond strength and the interactions between dislocations. The dislocations in the grown crystals offer a resistance to the fresh dislocations due to interaction which causes an increase in the hardness. The hardness values obtained for Bi_2Te_3 whiskers are found to be greater than that reported in [4].

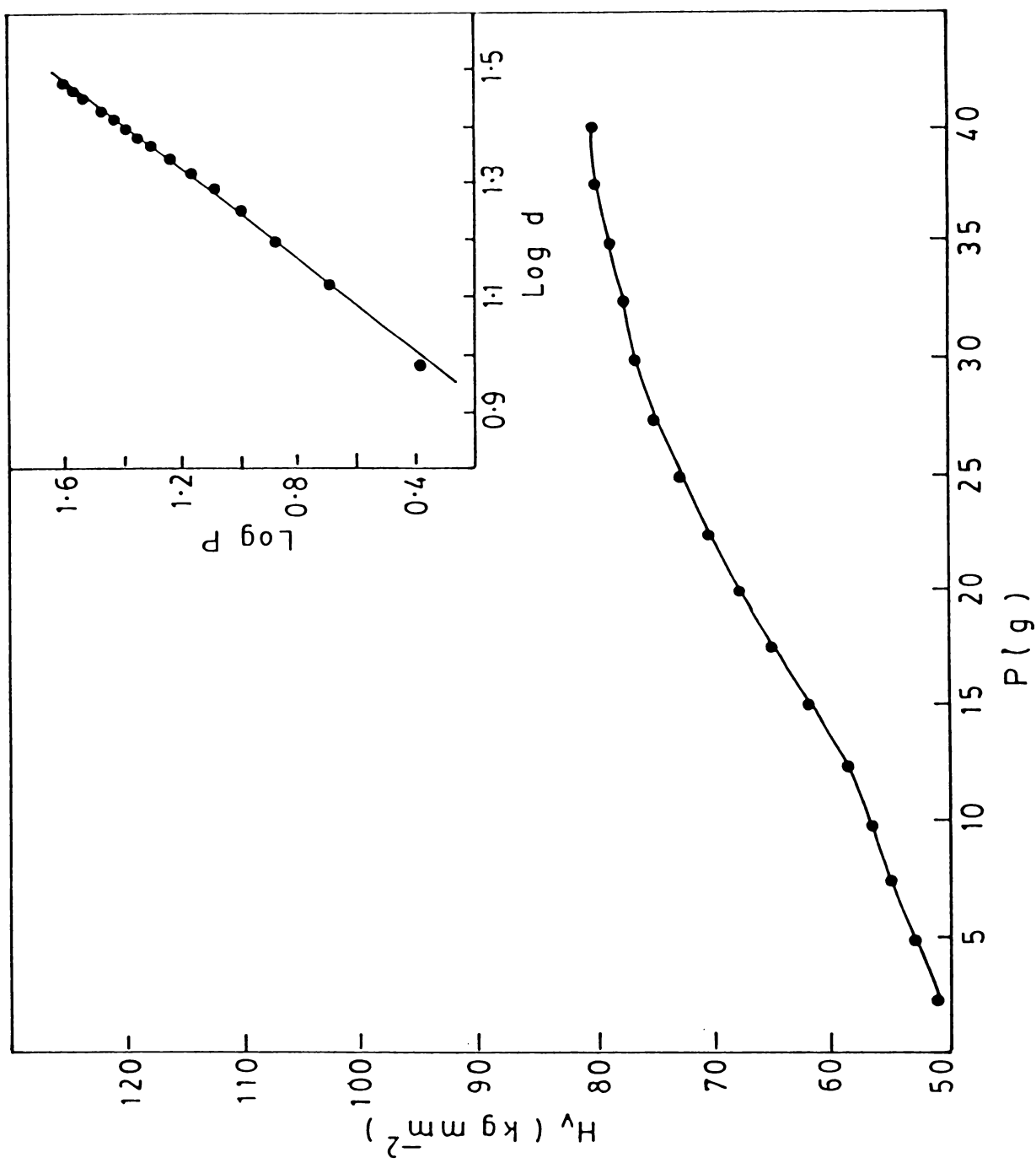


Fig. 8.5

8.3.3 In_2Te_3 whiskers

Fig.8.6 represents the variation of microhardness with applied load for $\alpha\text{-In}_2\text{Te}_3$ whiskers and the inset shows the corresponding $\log P$ versus $\log d$ plot. It is seen that the hardness first increases as the load increases, becomes a maximum, then slowly decreases and finally attains a constant value. This behaviour resembles the Grodzinski's general concept [8] of dependence of hardness on the applied load. Due to the application of mechanical stress by the indenter, dislocations are generated locally at the region of indentation and hence the microhardness increases initially with the increase of load. The small decrease in hardness from the peak value may be due to the deformation occurring by slip on the crystal surface. The rearrangement of dislocations and their mutual interactions increased with the increase in load and results to attain a constant value of hardness beyond a threshold load of 22.5 g [9].

During indentations on the prism faces of $\beta\text{-In}_2\text{Te}_3$ whiskers, some interesting radial crack patterns were observed (Fig.8.7). Radial cracks develop during indentation, due to the fact that the diamond point produces an inelastic deformation-induced flow stress. In the

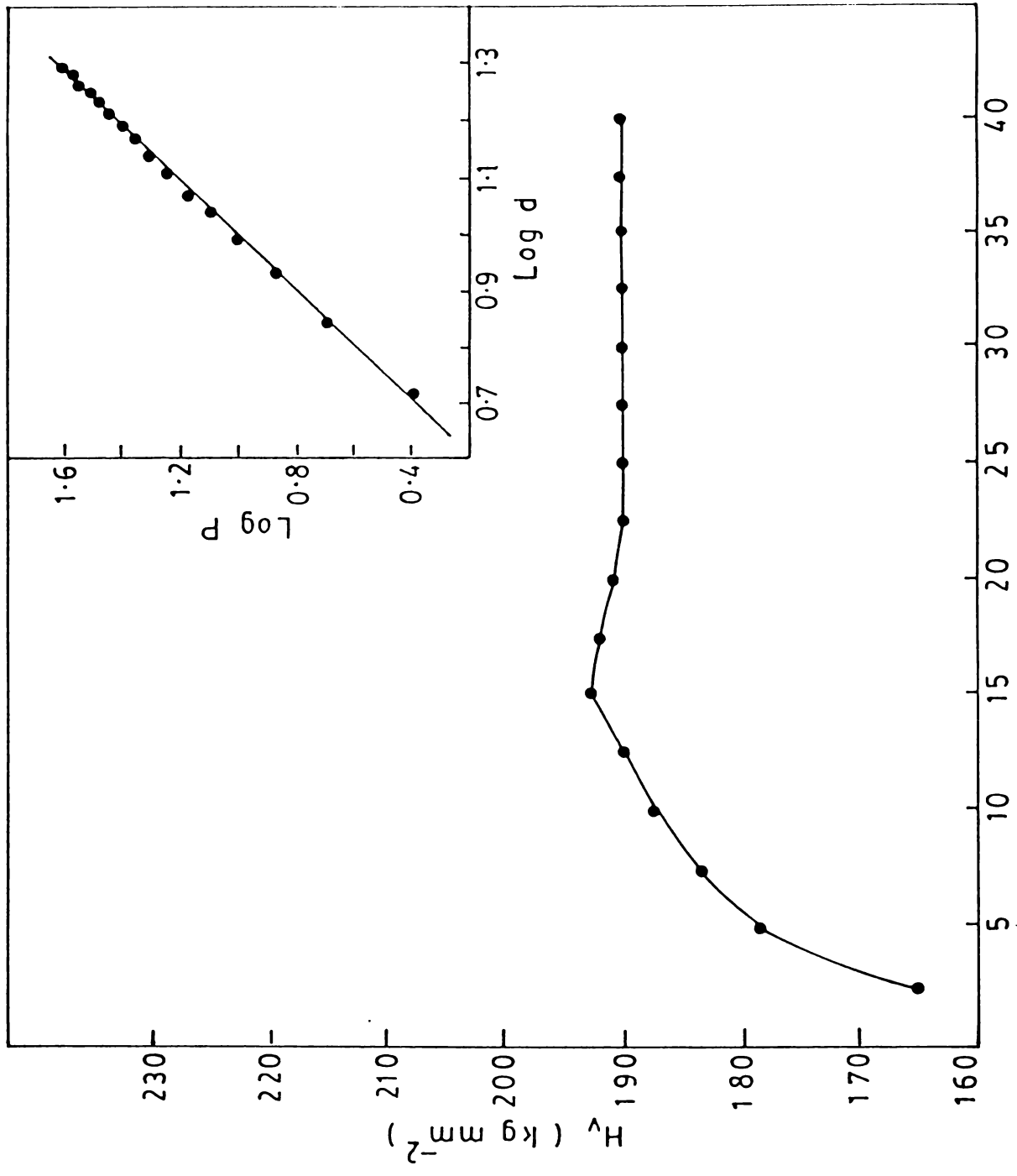


Fig. 8.6

present study, values of load upto 40 g were used, since the development of cracks does not seem to influence the deformation mechanics as long as the impression remains reasonably well-defined and the crack does not extend considerably compared with the impression diagonal [10]. The variation of hardness with load is shown in Fig.8.8. The inset of this figure shows the corresponding graph connecting $\log P$ and $\log d$. The special feature of the variation is that hardness attains a constant value after a steady increase. The major contribution to the increase in hardness with load is attributed to the high stress required for homogeneous nucleation of dislocations in the small dislocation-free region indented [11]. After a particular load, the hardness attains a constant value, due to a decrease in the resistance to the movement of the dislocations [12].

The hardness numbers obtained for α and β - In_2Te_3 whiskers are found to be in good agreement with those reported in [13]. The graphs of $\log P$ against $\log d$ yield straight lines with slope $n = 2.079$ and $n = 2.163$ for α and β - In_2Te_3 crystals respectively which proves the validity of the Meyer's relation (8.1).

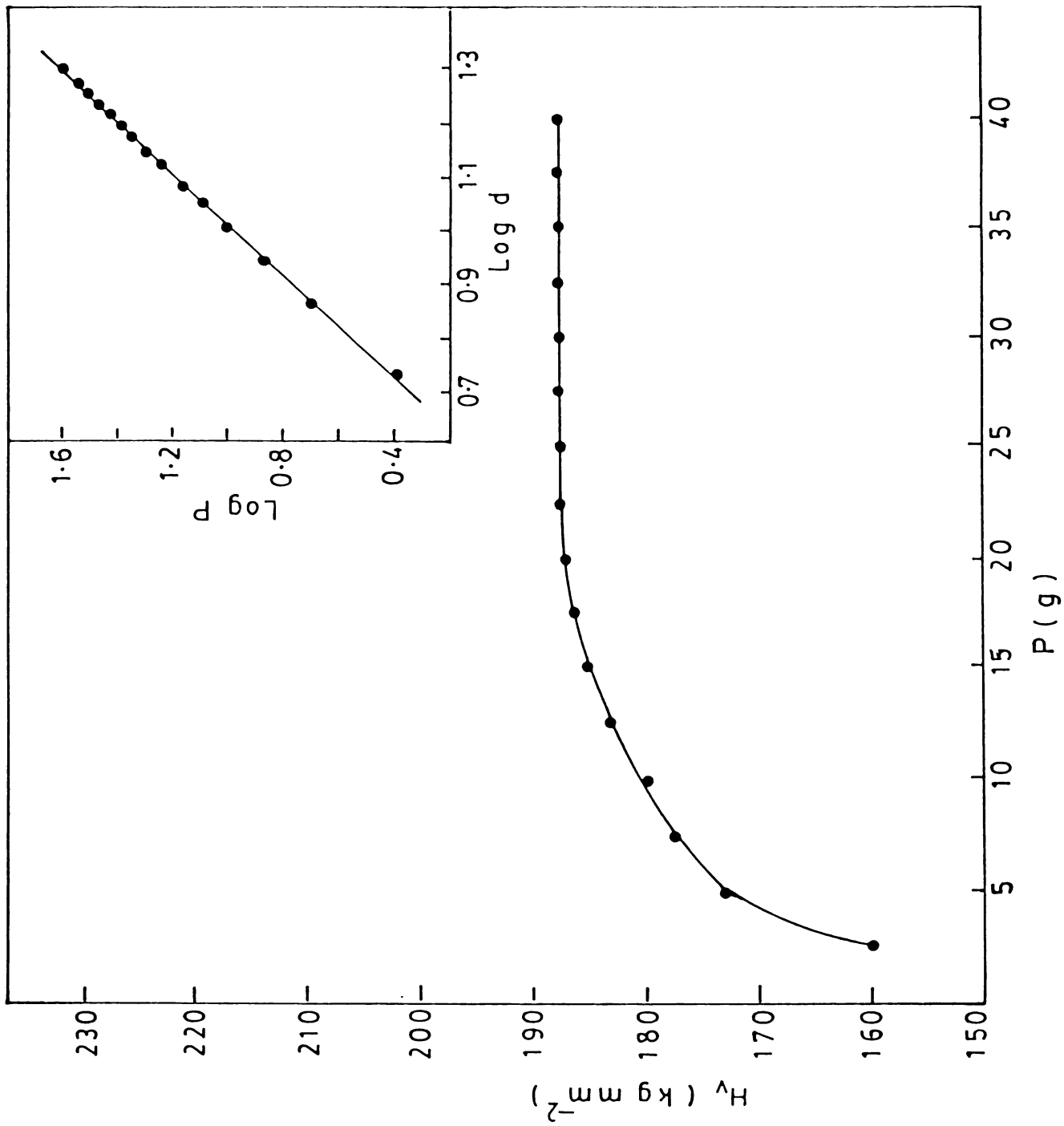


Fig. 8.8

8.4 CONCLUSION

For each composition ($x = 0$ to 10 at %) of $\text{Te}_{1-x}\text{Se}_x$ whiskers, the hardness number reaches a maximum at 17.5 g load. Further increase in load causes a slow decrease in the hardness value. The hardness-composition curve exhibits the typical behaviour of a binary solid-solution system. The deviation from the ideal solid solution behaviour in the low x region is due to the anisotropy caused in the tellurium lattice due to the addition of selenium. The microhardness of Bi_2Te_3 whiskers is found to increase with increase in load. In the case of $\alpha\text{-In}_2\text{Te}_3$ whiskers, the microhardness increases with load, becomes a maximum, slightly decreases and then attains a constant value. For $\beta\text{-In}_2\text{Te}_3$ whiskers microhardness is independent of load after a steady increase. The $\log P$ versus $\log d$ plots of the whiskers of all materials yield straight lines, satisfying the Meyer's relation.

8.5 FIGURE CAPTIONS

Fig.8.1 Variation of hardness with load for Te whiskers. The inset shows the plot of $\log P$ with $\log d$.

Fig.8.2 Variation of hardness with load for $\text{Te}_{0.95}\text{Se}_{0.05}$ whiskers. The inset shows the plot of $\log P$ with $\log d$.

Fig.8.3 Variation of hardness with load for $\text{Te}_{0.90}\text{Se}_{0.10}$ whiskers. The inset shows the plot of $\log P$ with $\log d$.

Fig.8.4 Hardness curve of $\text{Te}_{1-x}\text{Se}_x$ whiskers as a function of composition x (Load $P = 17.5$ g).

Fig.8.5 Variation of hardness with load for Bi_2Te_3 whiskers. The inset shows the plot of $\log P$ with $\log d$.

Fig.8.6 Variation of hardness with load for $\alpha\text{-In}_2\text{Te}_3$ whiskers. The inset shows the plot of $\log P$ with $\log d$.

Fig.8.7 Typical indentation mark and crack pattern on the prism face of $\beta\text{-In}_2\text{Te}_3$ whisker.

Fig.8.8 Variation of hardness with load for $\beta\text{-In}_2\text{Te}_3$ whiskers. The inset shows the plot of $\log P$ with $\log d$.

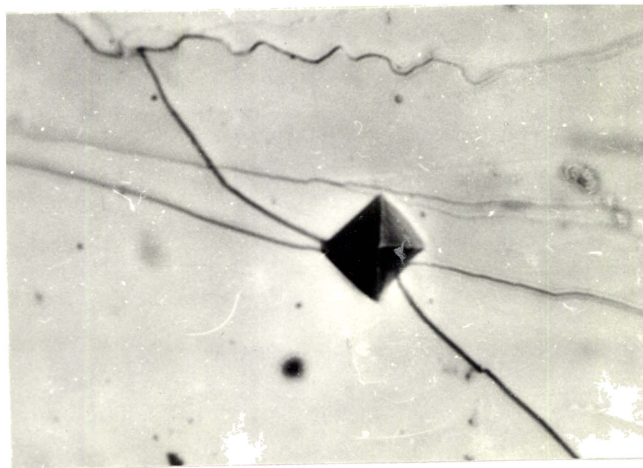


Fig. 8.7

8.6 REFERENCES

- [1] Yu . S.Boyarskaya, V.N.Lange and T.I.Lange, Soviet Research in New Semiconductor Materials, (Consultants Bureau, New York 1965).
- [2] V.N.Lange and A.R.Regel, Fiz. Tverd. Tela. 1 (1959) 562.
- [3] V.N.Lange and A.R.Regel, Fiz. Tverd. Tela. 1 (1959) 560.
- [4] D.Arivuoli, F.D.Gnanam and P.Ramasamy, J. Mater. Sci. Lett. 7 (1988) 711.
- [5] E.M.Onitsch, Mikroskopie, 2 (1947) 131.
- [6] R.K.Willardson and A.C.Beer, Semiconductors and semimetals, Vol.4,(Academic Press, New York 1968).
- [7] J.R.Drabble and C.H.L.Goodman, J. Phys. Chem. Solids 5 (1958) 142.
- [8] P.Grodzinski, Industr. Diam. Rev. 12 (1952) 209.

- [9] A.G.Kunjomana and E.Mathai, Mater. Res. Bull. 26 (1991) 1347.
- [10] A.Arora, D.B.Marshall and B.R.Lawn, J. Non-Cryst. Sol. 31 (1979) 415.
- [11] N.Gane and J.M.Cox, Philos. Mag. 22 (1970) 881.
- [12] A.G.Kunjomana and E.Mathai, J. Mater. Sci. Lett. 11 (1992) 613.
- [13] N.A.Goryuniva, Zh. Tekhn. Fiz. 27 (1957) 1408.

GROWTH AND FRACTOGRAPHIC STUDIES OF MELT-GROWN
 Bi_2Te_3 AND In_2Te_3 CRYSTALS

9.1 INTRODUCTION

Crystals of bismuth telluride are usually grown by melt methods [1-9]. Satterthwaite and Ure [5] have reported the growth of Bi_2Te_3 crystals using a vertical crystal furnace. The growth of large crystals of Bi_2Te_3 by zone melting method has been described by Shigetomi and Mori [6] and Drabble et al. [7]. Yang and Shepherd [8] have grown Bi_2Te_3 single crystals by the Czochralski method at pull rates of 0.2 to 20 cm/h. Also Laudise et al. [9] have used Czochralski method for the growth of doped single crystals of Bi_2Te_3 . They performed the growth both in H_2 and inert atmosphere with a seed rotation speed of 30 rpm and a pull rate of 12 mm/h. One of the most striking features of layered type Bi_2Te_3 crystals is the existence of easy cleavage along the (0001) basal planes. Since the cleavage plane of Bi_2Te_3 crystals is easy to glide, some deformation may accompany the cleavage step formation process. Amelinckx and Delavignette [10,11] have observed extensive dislocation patterns in thin foils of Bi_2Te_3 by transmission electron microscopy. But none of the earlier reported workers has done the fractographic analysis of cleavage steps in Bi_2Te_3 crystals.

Indium telluride crystals exist in two forms: a low temperature α -form and a high temperature β -form [12].

These crystals have been grown by many researchers [13-18]. Inuzuka and Sugaike [13] have grown In_2Te_3 crystals in sealed silica crucibles using Lawson's double furnace technique and showed that the crystals have a perfect cleavage along (111) planes. Woolley and Pamplin [14] have prepared In_2Te_3 using the directional freezing technique. Janowski [15] has designed a Czochralski technique crystal puller for the use of growing α and β - In_2Te_3 and obtained needle shaped crystals. Zaslavskii et al. [16] have also prepared In_2Te_3 crystals from stoichiometric amounts of high purity indium and tellurium. Mamedov et al. [17] have obtained α - In_2Te_3 samples using synthesised charge. Using the chemical gas transport method, Verkelis [18] has grown β - In_2Te_3 single crystals in the form of pyramids, prisms and needles bounded by (111) planes. However, the study of cleavage patterns formed on the fracture surfaces of In_2Te_3 crystals has not been reported so far.

In this chapter the growth of Bi_2Te_3 and α and β - In_2Te_3 crystals by horizontal zone levelling (HZL) method is described. The structure and lattice parameter of these crystals have been investigated by X-ray analysis. DSC studies have been performed in In_2Te_3 crystals to identify the phase transition temperature. Fractographic analysis of

cleavage steps present on the cleavage surfaces in these crystals has also been done and is presented here.

9.2 EXPERIMENTAL

The compounds were prepared from high purity elements of bismuth (99.999%), indium (99.999%) and tellurium (99.999%) by vacuum fusion in quartz ampoules as described in chapter 6. A horizontal gradient furnace discussed earlier (chapter 5) was used for growing crystals in the present investigation. The growth of Bi_2Te_3 was carried out by keeping the ampoule with a temperature of 700°C at the hotter end and 600°C at the cooler end for about 72 h. For In_2Te_3 , the hotter end was kept at 750°C and the cooler end at 650°C . In the case of $\alpha\text{-In}_2\text{Te}_3$, the ampoule was slowly cooled to room temperature. But in the case of $\beta\text{-In}_2\text{Te}_3$, the ampoule was cooled to about 480°C and then quenched to ice temperature. X-ray diffraction studies were carried out with $\text{CuK}\alpha$ radiation. It has been found that good stoichiometric crystals of Bi_2Te_3 , $\alpha\text{-In}_2\text{Te}_3$ and $\beta\text{-In}_2\text{Te}_3$ are obtained under the present growth conditions. Differential scanning calorimetric data have been taken on

In_2Te_3 crystals at a scanning rate of $5^\circ\text{C}/\text{min}$ during heating using a Perkin-Elmer delta series differential scanning calorimeter model DSC-7.

The crystals obtained were carefully cleaved at liquid nitrogen temperature and the cleaved surfaces were observed in reflection using a Union Versamet-2 metallurgical microscope.

9.3 RESULTS AND DISCUSSION

9.3.1 Bi_2Te_3 Crystals

Fig.9.1 shows the X-ray diffractogram of a typical bismuth telluride crystal. The standard values of the X-ray powder data along with the data obtained in the present case [19] are given in Table 9.1. The calculated values of the rhombohedral unit cell parameters are $a_R = 10.473 \text{ \AA}$ and $\alpha_R = 24^\circ 9'44''$ which are found to be in good agreement with Francombe's result [20].

The propagation of cleavage cracks in a wide range of solids has been the subject of a number of previous investigations [21-23]. Because cleavage surfaces are never atomically smooth, it is important to understand their

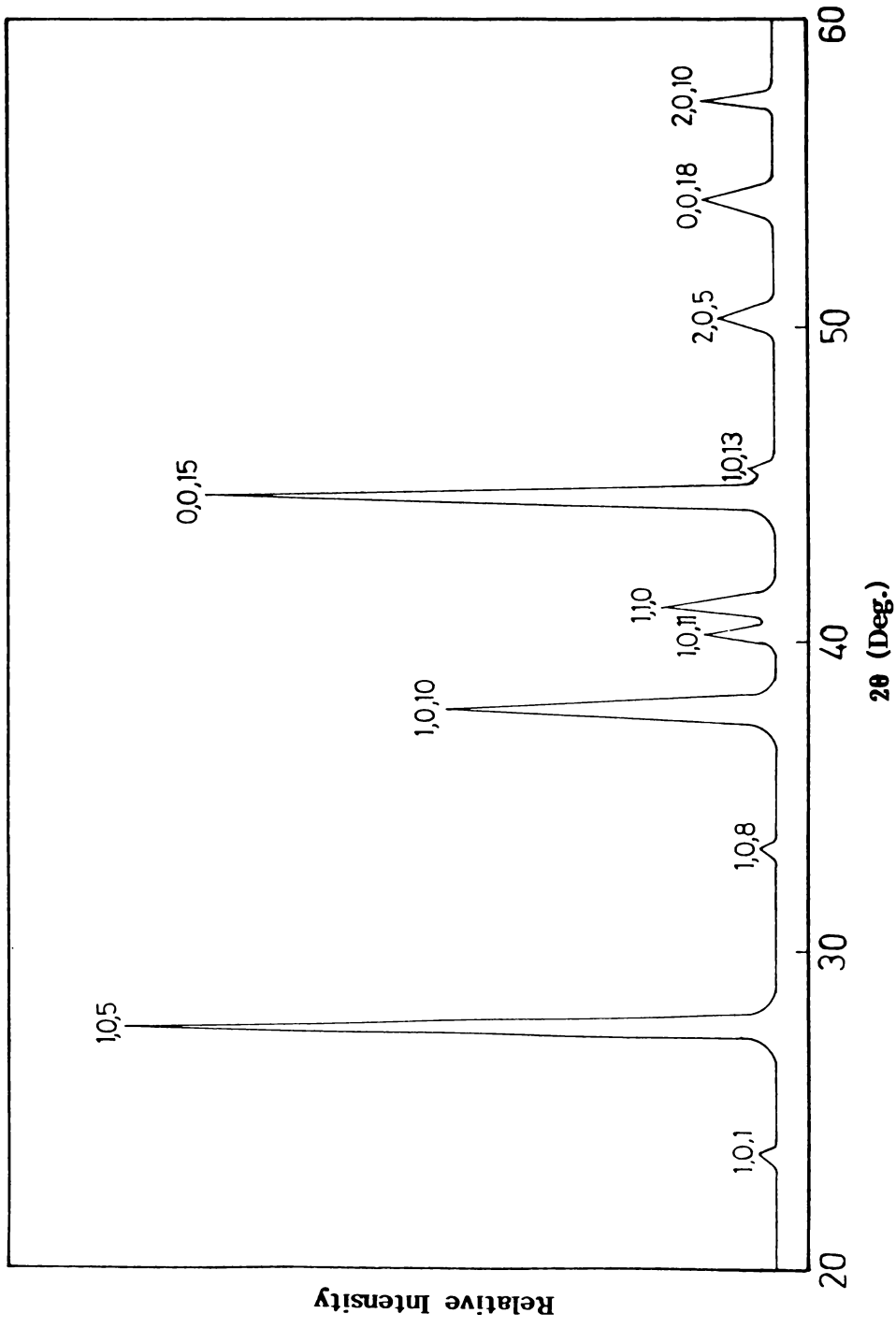


Fig. 9.1

Table 9.1 X-ray diffraction data for bismuth telluride crystal

hkl*	Standard pattern		Grown crystal	
	$d, \text{\AA}$	I/I_0	$d, \text{\AA}$	I/I_0
1,0,1	3.780	8	3.770	8
1,0,5	3.220	100	3.220	100
1,0,8	2.694	5	2.690	7
1,0,10	2.378	55	2.374	53
1,0,11	2.237	11	2.232	15
1,1,0	2.191	35	2.191	22
0,0,15	2.032	40	2.030	88
1,0,13	1.995	6	1.993	9
2,0,5	1.810	20	1.810	13
0,0,18	1.694	5	1.693	16
2,0,10	1.610	16	1.610	16

* The hkl indices are referred to the hexagonal structure cell.

irregularities. In actuality, they present a system of steps very nearly parallel to the cleavage direction. These steps converge to form higher steps or rivers. Such a typical river pattern observed on the (0001) face of a Bi_2Te_3 crystal is shown in Fig.9.2. It is formed due to the forest of dislocations which pierce the cleavage plane [24]. The crack propagation through grain boundary is clearly seen in the figure. The height of the river pattern is found to increase with distance from the grain boundary. Cleavage steps formed characteristic river patterns nucleating from different parts of the same surface and crossing at different boundaries are shown in Fig.9.3.

Interesting features relating to fracture produced by twins were sometimes observed (Figs.9.4(a) and 9.4(b)). Fracture occurs as soon as twins with a thickness larger than a few microns stop within the crystal. This is due to the fact that the concentration of the applied stress produced on the edge of the twin by the piling up of twinning dislocations is sufficient to separate the crystal along the cleavage plane. The twin pattern shown in Fig.9.4(a) is very similar to that given in [25].

Dislocation patterns were also observed due to the deformation produced during cleavage of the samples.

Fig.9.5 depicts network of dislocations formed on a cleavage face. Similar result was reported by Amelinckx and Delavignette [10,11] in thin foils of Bi_2Te_3 prepared by repeated cleavage. They suggested that hexagonal grid-like patterns could be revealed in the plane of observation since the main glide plane coincides with the cleavage plane.

9.3.2 In_2Te_3 Crystals

Figs.9.6(a) and 9.6(b) ^{show} the X-ray powder diffractometer traces of α and β - In_2Te_3 crystals. The unit cell parameter of α - In_2Te_3 crystals is found to be $a = 18.455 \text{ \AA}$ and that of β - In_2Te_3 crystals is $a_0 = 6.161 \text{ \AA}$ [26]. The results obtained (Tables 9.2 and 9.3) are found to be in good agreement with that reported earlier [17,18] for α and β -phases respectively. Fig.9.7 shows the DSC spectrum recorded for In_2Te_3 samples in the temperature range 400 to 500°C with a scanning rate of 5°C/min. The spectrum shows a variation in the heat flow indicative of the occurrence of phase transition at 458.279°C.

The topography of the surface layer of some ingots of In_2Te_3 was observed to be of dendritic relief as a result of solidification process. When the melt was cooled slowly, the type of structure as shown in Fig.9.8 as obtained. The

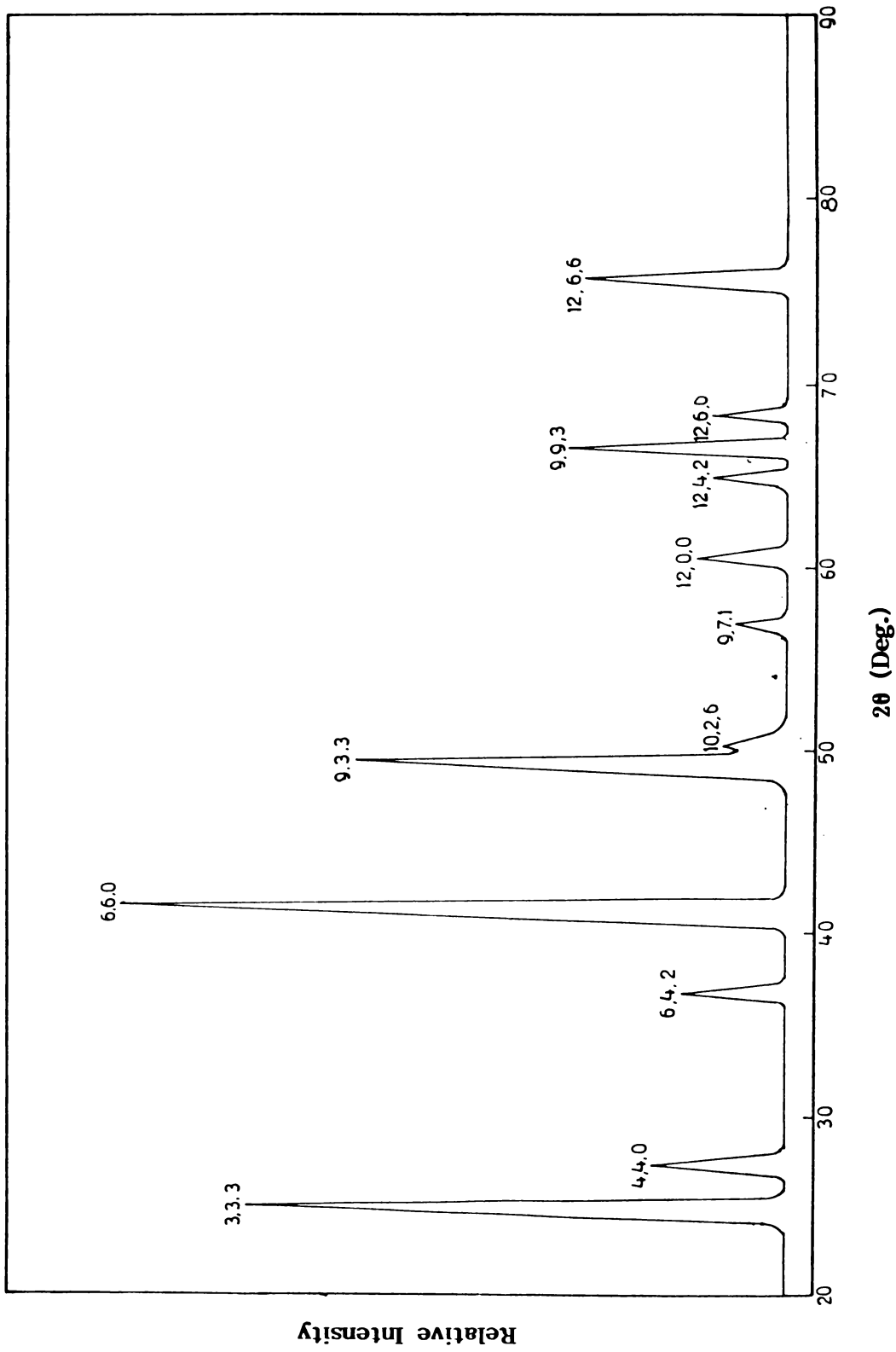


Fig. 9.6(a)

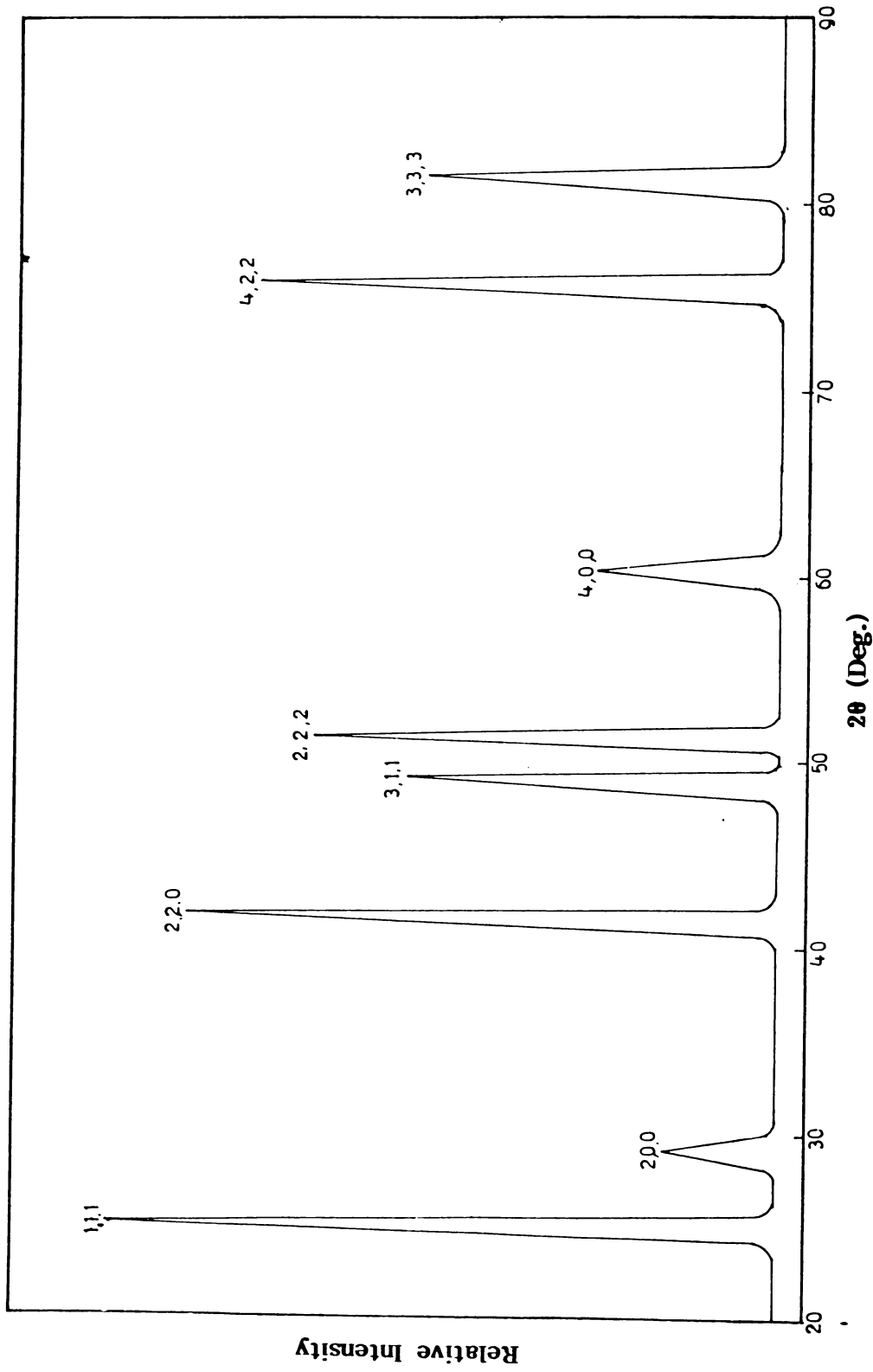


Fig. 9.6(b)

Table 9.2 X-ray diffraction data for α -In₂Te₃ crystal

Bragg angle, θ (deg.)	Calculated d_o , (Å)	Reported [17], d_o (Å)	I/I _o	hkl
12.53	3.553	3.552	82	3,3,3
13.65	3.266	3.264	23	4,4,0
18.30	2.455	2.460	19	6,4,2
20.80	2.170	2.176	100	6,6,0
24.70	1.844	1.854	67	9,3,3
25.10	1.817	1.808	13	10,2,6
28.55	1.613	1.611	11	9,7,1
30.20	1.532	1.539	17	12,0,0
32.50	1.434	1.439	15	12,4,2
33.25	1.405	1.410	35	9,9,3
34.15	1.373	1.375	14	12,6,0
37.90	1.255	1.255	33	12,6,6

Table 9.3 X-ray diffraction data for β -In₂Te₃ crystal

Bragg angle θ (deg.)	Calculated $d, (\text{\AA})$	Reported [18], d (\AA)	I/I ₀	hkl
12.55	3.547	3.548	100	1,1,1
14.55	3.068	3.069	20	2,0,0
20.75	2.176	2.178	89	2,2,0
24.50	1.858	1.857	57	3,1,1
25.65	1.780	1.779	70	2,2,2
30.05	1.539	1.539	30	4,0,0
37.80	1.257	1.259	79	4,2,2
40.58	1.185	1.186	55	3,3,3

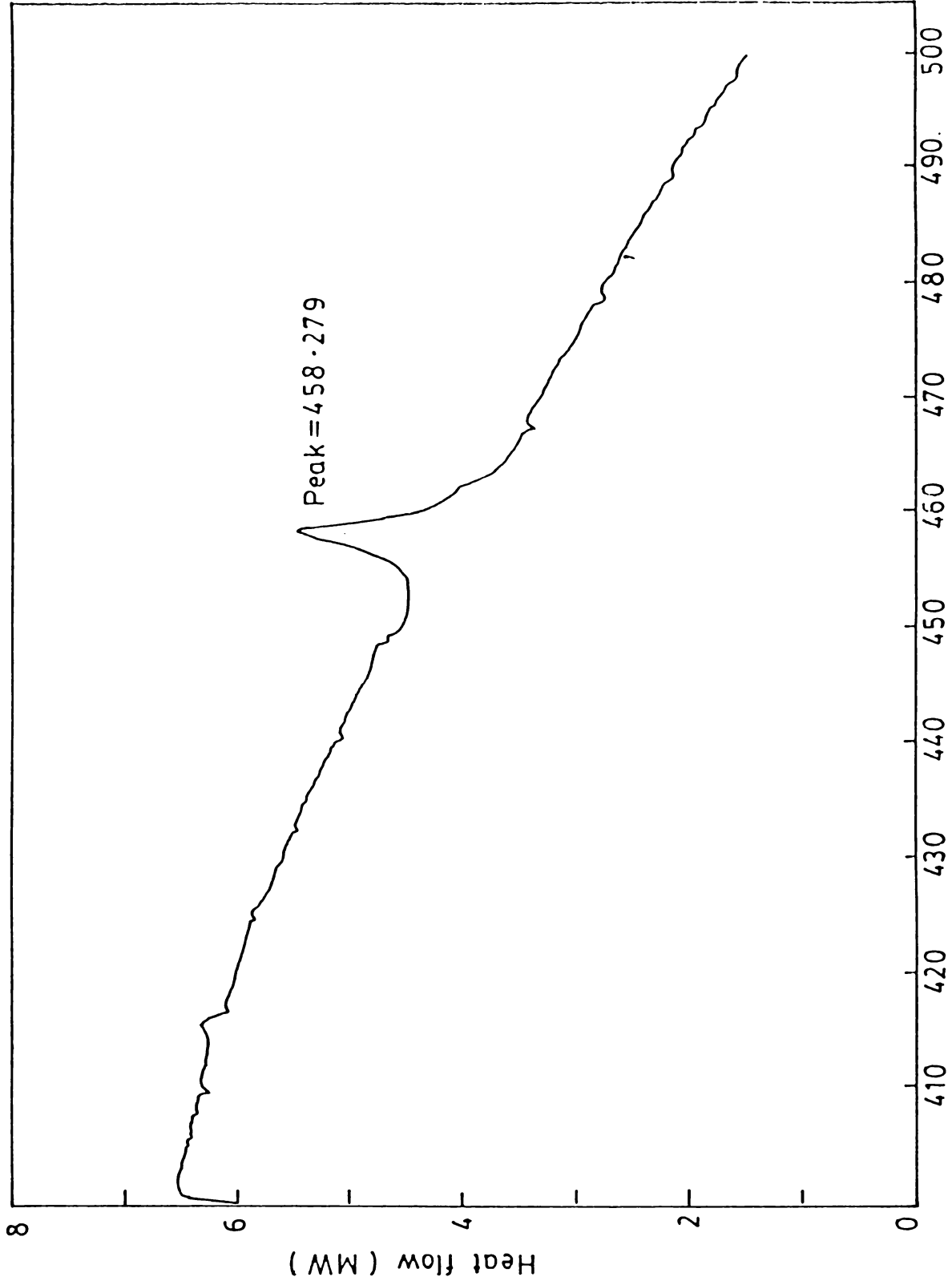


Fig. 9.7

change in supercooling conditions during growth are responsible for this. An explanation for the crystallographic features of dendritic growth is given in detail by Chalmers [27].

The (111) cleavage plane of In_2Te_3 crystals showed characteristic patterns of cleavage steps. In Fig.9.9 parallel cleavage steps terminating at different points of the surface of $\alpha\text{-In}_2\text{Te}_3$ crystals are shown. Kaufman and Forty [21] have reported such type of features on the cleavage surface of silicon. Fig.9.10 shows a large step formed by the combination of much smaller parallel elementary steps. This is attributed to the fact that when a cleavage crack crosses sub-boundaries, it takes a large density of elementary steps, resulting from the crossing of the parallel dislocations of the boundary. From the figure, it is seen that the steps are converging to form rivers at the tip of the crack. The formation of transverse step-like features within a cleavage step is shown in Fig.9.11. These are generated by the fracture on the (111) plane of $\alpha\text{-In}_2\text{Te}_3$ crystals.

The fractographic studies on the cleavage plane of $\beta\text{-In}_2\text{Te}_3$ crystals showed patterns which strongly resemble

the lamellar structure (Fig.9.12). Fig.9.13 shows a zone where different grains with cleavage lines oriented in different directions meet.

9.4 CONCLUSION

Single crystals of Bi_2Te_3 and α and β - In_2Te_3 have been grown by HZL method. X-ray diffraction studies show that Bi_2Te_3 crystals have the rhombohedral unit cell parameters as $a_R = 10.473 \text{ \AA}$ and $\alpha_R = 24^\circ 9' 44''$. The lattice constant of α - In_2Te_3 crystals is found to be $a = 18.455 \text{ \AA}$ and that of β - In_2Te_3 crystals is $a_0 = 6.161 \text{ \AA}$. Fractographic analysis of the crystals is useful to study the imperfection structures. Cleavage faces of all crystals show river patterns, twin formation, dislocation networks, parallel cleavage steps and lamellar structures.

9.5 FIGURE CAPTIONS

- Fig.9.1 X-ray powder diffraction pattern of Bi_2Te_3 crystal.
- Fig.9.2 A river pattern observed on the cleavage face of Bi_2Te_3 crystal.
- Fig.9.3 Rivers crossing at different boundaries on the cleavage face of Bi_2Te_3 crystal.
- Figs.9.4(a) and 9.4(b) Micrographs showing twin patterns on the cleavage face of Bi_2Te_3 crystal.
- Fig.9.5 A cleavage surface of Bi_2Te_3 crystal containing hexagonal network of dislocations.
- Fig.9.6(a) X-ray powder diffraction pattern of $\alpha\text{-In}_2\text{Te}_3$ crystal.
- Fig.9.6(b) X-ray powder diffraction pattern of $\beta\text{-In}_2\text{Te}_3$ crystal.
- Fig.9.7 DSC spectrum of In_2Te_3 sample.

- Fig.9.8 Surface dendrites of In_2Te_3 crystal.
- Fig.9.9 A typical cleavage surface of $\alpha\text{-In}_2\text{Te}_3$ crystal.
- Fig.9.10 Mircograph of a region where parallel elementary steps have combined to form one larger step of $\alpha\text{-In}_2\text{Te}_3$ crystal.
- Fig.9.11 Transverse step like features within a cleavage step of $\alpha\text{-In}_2\text{Te}_3$ crystal.
- Fig.9.12 A cleavage surface of $\beta\text{-In}_2\text{Te}_3$ crystal showing the lamellar structure.
- Fig.9.13 Different grains on a cleavage face of $\beta\text{-In}_2\text{Te}_3$ crystal.



Fig. 9.2

(x150)

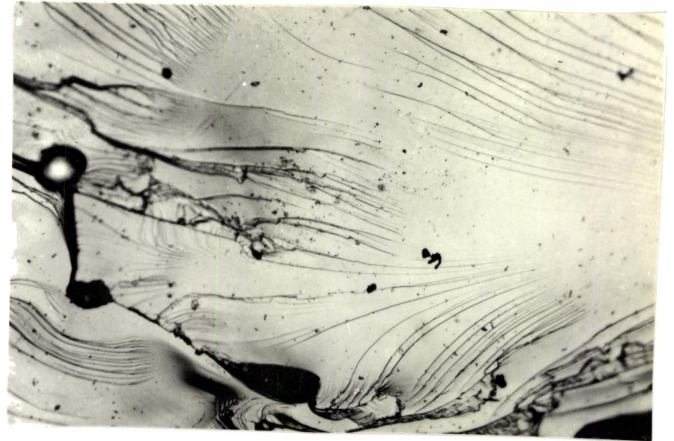


Fig. 9.3

(x 80)

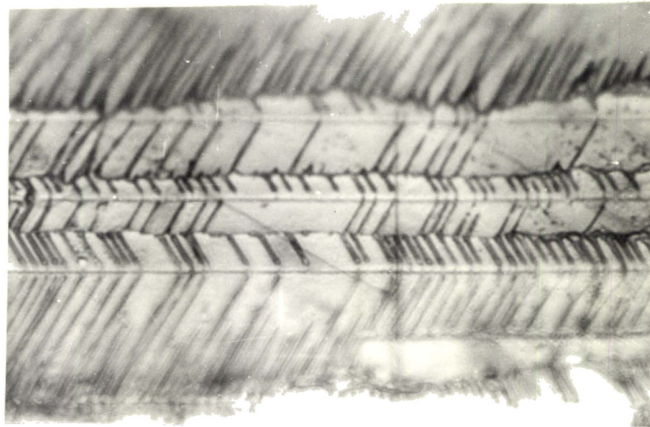


Fig. 9.4(a)

(x160)

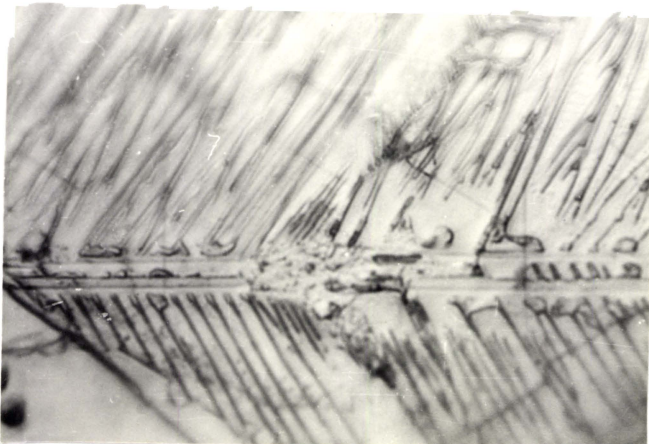


Fig. 9.4(b)

(x160)

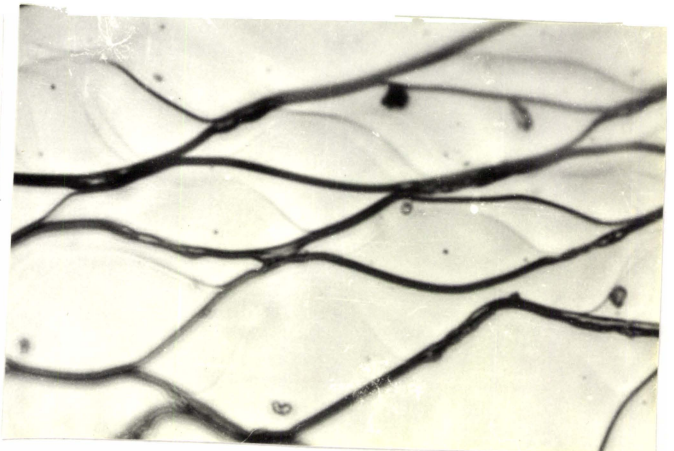


Fig. 9.5

(x 330)

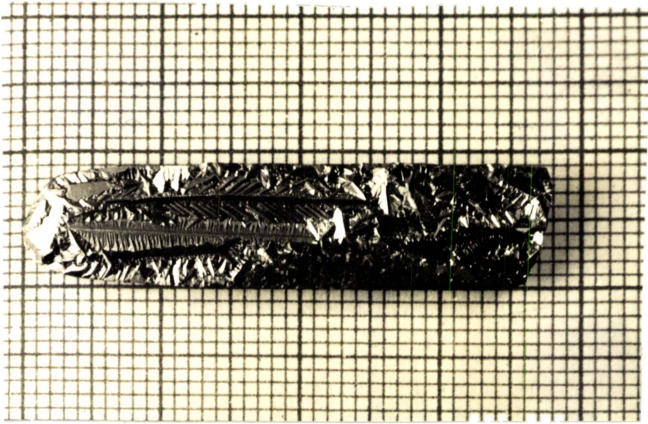


Fig. 9.8

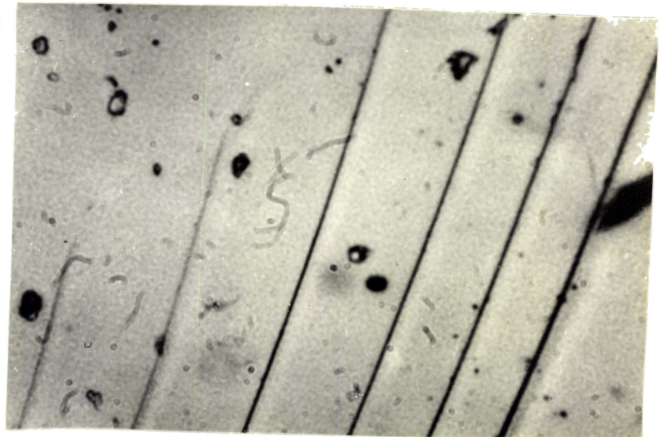


Fig. 9.9

(x330)

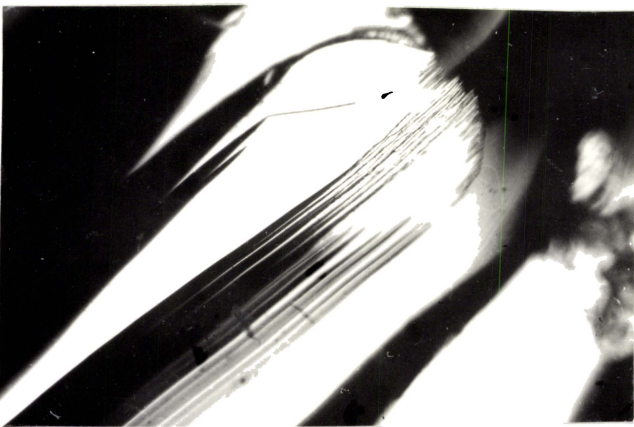


Fig. 9.10



(x125) Fig. 9.11

(x100)

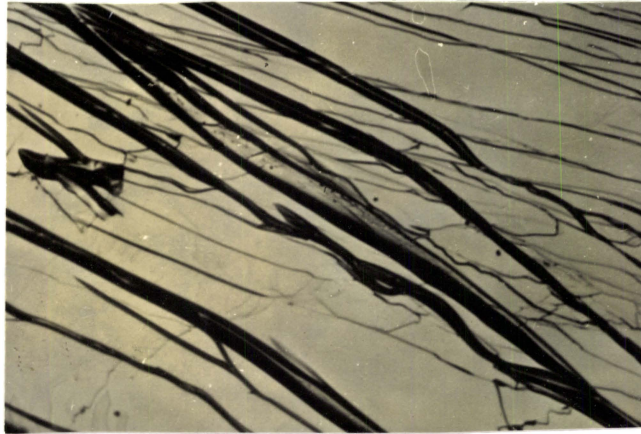


Fig. 9.12

(x 100)



Fig. 9.13

(x 100)

9.6 REFERENCES

- [1] T.C.Harman, B.Paris, S.E.Miller and H.L.Goering, J. Phys. Chem. Solids. 2 (1957) 181.

- [2] J.Black, E.M.Conwell, L.Seigle and C.W.Spencer, J. Phys. Chem. Solids. 2 (1957) 240.

- [3] H.J.Goldsmid, Proc. Phys. Soc. 71 (1958) 633.

- [4] C.H.Champness and A.L.Kipling, Canad. J. Phys. 44 (1966) 769.

- [5] C.B.Satterthwaite and R.W.Ure, Jr., Phys. Rev. 108 (1957) 1164.

- [6] S.Shigetomi and S.Mori, J. Phys. Soc. Jap. 11 (1956) 915.

- [7] J.R.Drabble, R.D.Groves and R.Wolfe, Proc. Phys. Soc. 71 (1958) 430.

- [8] A.C.Yang and F.D.Shepherd, J. Electrochem. Soc. 108 (1961) 197.

- [9] R.A.Laudise, W.A.Sunder, R.L.Barns, R.J.Cava and T.Y.Kometani, *J. Cryst. Growth*, **94** (1989) 53.
- [10] S.Amelinckx and P.Delavignette, *Nature*, **27** (1960) 603.
- [11] P.Delavignette and S.Amelinckx, *Philos. Mag.* **5** (8th series) (1960) 729.
- [12] A.I.Zaslavskii and V.M.Sergeeva, *Sov. Phys. Solid State*, **2** (1961) 2556.
- [13] H.Inuzuka and S.Sugaike, *Proc. Japan Acad.* **30** (1954) 383.
- [14] J.C.Woolley and B.R.Pamplin, *J. Electrochem. Soc.* **108** (1961) 874.
- [15] D.Janowski, *Ann. Phys.* **23** (1969) 71.
- [16] A.I.Zaslavskii, V.M.Sergeeva and I.A.Smirnov, *Sov. Phys. Solid State*, **2** (1961) 2565.
- [17] A.S.Mamedov, K.P.Mamedov, G.Sh.Gasanov, S.B.Bagirov and G.M.Niftiev, *Izv. Akad. Nauk SSSR, Neorgan, Mat.*, **13** (1977) 1987.

- [18] I.Yu Verkelis, *Sov. Phys. Solid State*, **14** (1972) 1445.
- [19] A.G.Kunjomana and E.Mathai, *J. Mater. Sci.* **26** (1991) 6171.
- [20] M.H.Francombe, *Brit. J. Appl. Phys.* **9** (1958) 415.
- [21] M.J.Kaufman and A.J.Forty, *J. Mater. Sci.* **21** (1986) 3167.
- [22] J.Y.Lee and K.N.Subramanian, *J. Mater. Sci.* **18** (1983) 1765.
- [23] K.J.Mathai, Ph.D. Thesis, Sardar Patel University (1970).
- [24] F.C.Fisher, *Acta. Met.* **2** (1954) 9.
- [25] J.Friedel, 'Dislocations' (Addison-Wesley, London 1967).
- [26] A.G.Kunjomana and E.Mathai (Communicated).
- [27] B.Chalmers, *Principles of Solidification*, (John-Wiley and Sons, New York 1967).

DISLOCATION STUDIES OF MELT-GROWN
 Bi_2Te_3 AND In_2Te_3 CRYSTALS

10.1 INTRODUCTION

Dislocation studies on the (0001) cleavage planes of bismuth telluride crystals by etching technique have been reported by various groups. Etching experiments on iodine doped Bi_2Te_3 crystals were studied by Drabble et al. [1]. They reported triangular and hexagonal etch pits on the cleavage surfaces using a dilute solution of HCl , HNO_3 and H_2O as the etchant. Teramoto and Takayanagi [2] observed hexagonal etch pits with alternating long and short sides on the cleavage surfaces of Bi_2Te_3 not doped with iodine. The etchants used for this study were 30% HNO_3 and a solution composed of two parts HNO_3 , one part HCl and six parts H_2O . They also produced triangular etch pits using the etchant consisting of 10 ml HNO_3 , 10 ml HCl , 40 ml H_2O and 1 g iodine. The pits had an eccentric shape. Sagar and Faust [3-6] also studied dislocations in Bi_2Te_3 by etching techniques. They reported [3] the formation of perfect triangular and hexagonal etch pits of different sizes, etch grooves and networks of dislocations using the etchant consisting of a solution of bromine in methanol. From the observation of etched surfaces they suggested that bending of the dislocations within the crystal is responsible for some of the flat bottomed pits and the pits of different sizes. The structural perfection of single

crystals of Bi_2Te_3 has been carried out by Vasil'eva et al. [7] using selective etching and X-ray diffraction techniques. They found that the basal planes are less perfect and reported the value of dislocation density to be equal to $(0.5-1) \cdot 10^5 \text{ cm}^{-2}$. In all these studies, there is no information about the morphology of etched surfaces relating to terracing and bunch formation of etch pits.

Plastic deformation of crystals is usually associated with the movement and multiplication of dislocations. But only a few results are available regarding the movement and multiplication of dislocations in Bi_2Te_3 crystals. Amelinckx and Delavignette [8-9] have applied transmission electron microscopic technique to study dislocations in thin foils of Bi_2Te_3 crystals prepared by repeated cleavage. Since the c-plane is simultaneously the easy glide and cleavage plane, they observed the presence of extensive dislocation patterns in the c-plane of the foils. They also observed extensive movement of dislocations in the c-plane giving rise either to elimination of dislocations or to the formation of networks by heating the samples in the electron beam. But they reported that they were not able to observe any evidence of Frank-Read sources in the foils. Using the etch-pit technique, Sagar et al.

[6] observed concentric dislocation loops and multiturn spirals on the basal planes in heat treated and quenched Bi_2Te_3 crystals grown by horizontal zone levelling from a non-stoichiometric tellurium-rich melt. They haven't mentioned the precise concentrations of the etchant consisting of bromine in methanol for the formation of such loops. The exact mechanism responsible for the formation of dislocation loops in Bi_2Te_3 crystals has not, however, been clearly established.

Plastic deformation plays a still more important role in fracture and surface damage of crystals prepared by cleavage operations. At places with weakened bonds, cracks arise whose development leads to fracture. No work has been reported in the literature regarding the investigation on cracks formed on the cleavage surfaces of Bi_2Te_3 crystals. It is therefore of interest to study the development of cracks on the (0001) cleavage plane of Bi_2Te_3 crystals by etching method.

The dislocation etch studies on the cleavage faces of α and β - In_2Te_3 crystals have not been reported so far.

This chapter contain the dislocation studies on the cleavage faces of Bi_2Te_3 and α and β - In_2Te_3 crystals

grown by horizontal zone levelling method. The formation of terraced etch pits on the (0001) face of Bi_2Te_3 crystals have been investigated by employing different etchants. The direct observation of regenerative multiplication of dislocations by Frank-Read sources on the (0001) face of Bi_2Te_3 crystals has been reported for the first time. New etchants have been developed to investigate the nature and distribution of dislocations on the cleavage faces of α and β - In_2Te_3 crystals. The formation of cracks on the cleavage faces of Bi_2Te_3 and α and β - In_2Te_3 crystals has also been studied by a new etchant. On the basis of microscopic observations, the possible mechanism responsible for the nucleation and development of microcracks has been suggested and is reported here.

10.2 EXPERIMENTAL

The crystals were grown by the horizontal zone levelling method as described in chapter 5. The crystals were carefully cleaved at liquid nitrogen temperature and were thoroughly cleaned for etching studies. Etching of Bi_2Te_3 crystals was done at room temperature in various etchants: $\text{HNO}_3\text{-H}_2\text{O}$, $\text{HNO}_3\text{-H}_2\text{SO}_4\text{-H}_2\text{O}$, $\text{HNO}_3\text{-HF-H}_2\text{O}$, $\text{I}_2\text{-H}_2\text{SO}_4\text{-CH}_3\text{OH}$ and $\text{I}_2\text{-HNO}_3\text{-CH}_3\text{OH}$. The effect of etching time and concentration of particular etchant components on the shape

of etch pits was examined. A stock solution of bromine in methanol (10% by volume) was found to be capable of revealing dislocation spirals and loops due to Frank-Read sources in Bi_2Te_3 crystals. The etchant $\text{HNO}_3\text{-HF-CH}_3\text{COOH}$ system was found to be very reliable for the revelation of cracks. The dislocation studies of α and β - In_2Te_3 crystals were also done as in the case of Bi_2Te_3 crystals using the etchants, $\text{HNO}_3\text{-HF}$, $\text{HNO}_3\text{-HF-H}_2\text{O}$ and $\text{HNO}_3\text{-CH}_3\text{COOH-HF}$. The etched surfaces were observed under reflection using metallographic microscopes (Union Versamet-2 and Carl Zeiss, Jena).

10.3 RESULTS AND DISCUSSION

10.3.1 Bi_2Te_3 Crystals

(a) Investigation on the Morphology of Etch Pits

The revelation and morphology of dislocation etch pits on the (0001) plane of Bi_2Te_3 crystals have been investigated in relation to the nature and concentration of components in various etchants i.e., $\text{HNO}_3\text{-H}_2\text{O}$, $\text{HNO}_3\text{-H}_2\text{SO}_4\text{-H}_2\text{O}$, $\text{HNO}_3\text{-HF-H}_2\text{O}$, $\text{I}_2\text{-H}_2\text{SO}_4\text{-CH}_3\text{OH}$ and $\text{I}_2\text{-HNO}_3\text{-CH}_3\text{OH}$. The results obtained are reported as below:

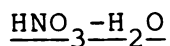
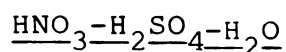


Fig.10.1 shows a photograph of the etch pattern formed at dislocation sites on the (0001) cleavage face of

a Bi_2Te_3 crystal etched in 3 ml HNO_3 + 10 ml H_2O for 5 sec. It is seen that the etch pits are arranged in parallel rows from the cleavage steps on the surface. When the etching of crystals was carried out on another crystal for 10 sec, well defined etch pits were produced (Fig.10.2). The pits were uniform in size and had hexagonal shape. Some of the pits were flat bottomed. These results agreed with the earlier findings by Teramoto and Takayanagi [2]. But their etchant didn't show much contrast and terracing as obtained in the present case. It was found that the pits formed exhibited many phenomena associated with dislocation etch pits. For example, on prolonged etching, the pits were grown larger, retaining their shape. Etch grooves were also revealed on the surface, (Fig.10.3) whose ends were marked with shorter sides of hexagonal etch pits. The orientation of the pits lying on and near the edges of these grooves is similar to that of individual pits lying in the same plane. The fact that the etch pits are preferentially formed on the sides and at the termination points of the etch grooves strongly suggested that the etching can reveal the sites of the dislocation.



The addition of H_2SO_4 to $\text{HNO}_3-\text{H}_2\text{O}$ system leads to an increase in etch rate and hence the etch pits formed are

terraced on a macroscopic scale. The pits have a crystallographic orientation at a lower concentrations of H_2SO_4 but at higher concentrations, a macroscopic build up of steps distributed evenly across the surface were observed resulting into bunch formation.

On etching the crystals in 3 ml HNO_3 + 0.1 ml H_2SO_4 + 10 ml H_2O solution for 10 sec, the pits started losing their hexagonal symmetry and showed a tendency to rounding off (Fig.10.4). The change in the morphology of dislocation etch pits due to the addition of 0.1 ml H_2SO_4 is quite clear from comparing Figs.10.2 and 10.4. At relatively higher concentrations of H_2SO_4 , the sides of the pit were almost rounded and showed more terracing. Figs.10.5(a) and 10.5(b) depict the formation of conical shaped etch pits after etching for 10 sec. in 3 ml HNO_3 + 0.3 ml H_2SO_4 + 10 ml H_2O . In point bottomed pits the bottom of the pit is not at its geometrical centre which reveals that the pits were formed at inclined dislocations. In Fig.10.6 the formation of terraced etch pits along with etch grooves is shown. Due to high etch rate, the ledges of neighbouring etch pits were combined together to form macroledges. When 0.4 ml H_2SO_4 was added to 3 ml HNO_3 + 10 ml H_2O , the etch rate was so high that bunches were

developed at the dissolution steps generated by the dislocations. Fig.10.7 represents a cluster of point bottomed etch pits due to the fast reaction of the crystal surface in 3 ml HNO_3 + 0.4 ml H_2SO_4 + 10 ml H_2O after 10 sec etching. In Fig.10.8 a typical bunch formation is shown, where the steps were piled up one after another on a low angle grain boundary. Bunches were also formed with high density of etch pits (Figs.10.9(a) and 10.9(b)) after 10 sec. etching in 3 ml HNO_3 + 0.6 ml H_2SO_4 + 10 ml H_2O . Etching of the crystals at a still higher acid concentrations leads to the formation of etch pits as shown in Fig.10.10. The etchant composition employed was 3 ml HNO_3 + 0.9 ml H_2SO_4 + 10 ml H_2O and etching time was 5 sec. The irregular markings seen inside the pits were formed due to the fast dissolution reactions. Above this acid concentration, surface roughening due to corrosion occurred within 2 sec (Fig.10.11). In all the studies mentioned above it has been observed that with a change in the concentration of H_2SO_4 in the etchant system HNO_3 - H_2O , the morphology of dislocation etch pits was changed.

During the present study, attempt has also been made to understand the change in morphology of etch pits by changing the concentration of HNO_3 , keeping the H_2SO_4 concentration as constant. At low concentrations of HNO_3 ,

small circular etch pits were formed, whereas at high concentrations, terraced circular etch pits were formed. Fig.10.12 shows the etch-pit pattern produced by the etchant 0.2 ml HNO_3 + 0.5 ml H_2SO_4 + 10 ml H_2O after 10 sec. In Fig.10.13, circular etch pits aligned on opposite sides of an etch groove are seen which indicates that the pits were formed at dislocation sites. In this case the pits were formed by 0.4 ml HNO_3 + 0.5 ml H_2SO_4 + 10 ml H_2O for 10 sec. Fig.10.14 is the morphology of an etched surface produced after etching in 0.6 ml HNO_3 + 0.5 ml H_2SO_4 + 10 ml H_2O for 10 sec. When the concentration of HNO_3 was increased, the increased dissolution at dislocations caused terraced etch pits (Fig.10.15). The morphology change has been attributed to the difference in the rate of removal of atomic layers from the dislocation sites at low and high acid concentrations and directional dissolution. The geometry of etch pits clearly reveals that they are at the dislocation sites intersecting the crystal surface.

HNO_3 -HF- H_2O

It has been found that HF increases the etch rate more rapidly than H_2SO_4 . The etched surfaces of the crystals after etching in 3 ml HNO_3 + 0.1 ml HF + 10 ml H_2O for 10 sec produced macroedges as shown in Fig.10.16. It is seen that the pits are terraced and the etched surface

revealed dissolution layers. The increased nucleation and motion of kinks due to an enhanced etch rate is responsible for this type of morphology. Similar results were reported by Desai et al. [10] on the (111) face of CaF_2 by etching in HCl vapour at room temperature. When the concentration of HF is increased, etch pits were observed in the form of a macroscopic bunching of dissolution steps. Fig.10.17 shows such pattern produced by 3 ml HNO_3 + 0.2 ml HF + 10 ml H_2O after etching for 10 sec. At higher concentrations of HF, the surface is overetched and the pits lose their circular morphology (Fig.10.18). Cabrera and Coleman [11] have explained the formation of macroscopic steps in terms of the processes occurring between steps of monoatomic height. If two steps happen to meet as a result of encountering an imperfection of the crystal, or due to an instability of the equidistant step spacing, they will have a tendency to join together, since steps on surfaces neighbouring a singular face have an attractive interaction. More monoatomic steps join this combined step and form a macroscopic step. Mullins and Hirth [12] also found that in some cases one step may overtake the preceding one and form a double-height step.

The formation and development of bunches and terraced etch pits on the (0001) face of Bi_2Te_3 crystals

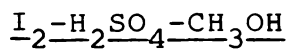
may be explained by the kinematic theory of step motion [12]. As the etch rate is high at high reactant concentrations the train of steps is unstable against disturbances in their motion. Since the velocity of individual steps is also higher, fast steps collide with the whole group to develop a visible macroscopic bunch. In the present case, since the etch rate was very high even for an etching time of 10 sec, bunches were developed not only on the surface, but also at the dissolution steps generated by the dislocations. The increased dissolution at dislocations also caused terracing of etch pits.

According to the kinematic theory, the interpretation of the terracing of etch pits is based on the presumption that the etching surface is misoriented with respect to the crystallographic face. The misorientation determines the step density. The larger the inclination of a dislocation with respect to the surface, the greater the step density. In this condition, terraced etch pits are formed. This mechanism is operative in the present case, where the dislocations are inclined to the surface.

A detailed investigation of the etching on the (0001) faces of Bi_2Te_3 crystals has also been made in the

•

present study using two newly developed etchants i.e., $I_2-H_2SO_4-CH_3OH$ and $I_2-HNO_3-CH_3OH$. In these etchants, the role of I_2 is to oxidise the crystals, while the reagents H_2SO_4 and HNO_3 help to dissolve the oxides formed during the dissolution process. The third component CH_3OH serves as a medium for the reaction. The influence of the concentration of particular etchant components on etching and on the shape of the crystal surface was examined.



When the Bi_2Te_3 crystals were etched in the I_2-CH_3OH solution, dislocation etch pits were not observed on the surfaces. This is possibly due to the deposition of insoluble oxide layers on them which will passivate dissolution. However, well defined and contrasting etch pits were readily formed by the addition of small amounts of H_2SO_4 . Fig.10.19 depicts the distribution of etch pits produced using a mixture of 1 g I_2 + 0.5 ml H_2SO_4 + 10 ml CH_3OH for 10 sec. Flat bottomed and shallow triangular etch pits were observed. On further etching for an additional 10 sec, the pit geometry is found to be distorted due to high etch rate. In order to slow down the etching reaction, the concentration of CH_3OH has been increased, so that the etchant of composition 1 g I_2 + 0.5

ml H_2SO_4 + 20 ml CH_3OH was found to be capable of revealing dislocations on the cleavage face. When the crystals were immersed in this particular composition for 30 sec, deep triangular etch pits were prevailed all over the surface (Fig.10.20(a)). So this was found to be the optimum condition for obtaining visible etch pits. Fig.10.20(b) represents the distribution of etch patterns on the same region after etching for 60 sec. It can be seen from Figs.10.20(a) and 10.20(b) that the pit size become larger, while the number and position of pits remain practically the same. This shows that the pits are formed at the sites of emergence of dislocations. The difference in pit size at different sites on the same surface (Figs.10.19, 10.20(a) and 10.20(b)) may be attributed to the different strengths of dislocation and the inclination of dislocation lines with the surface. From the above studies, it is found that acidification of etching medium is essential for the etch-pit formation.

On increasing the concentration of iodine in the etchant, the etch rates have been increased markedly. Figs.10.21(a) and 10.21(b) show the photographs of the etch pattern produced by 2 g I_2 + 0.5 ml H_2SO_4 + 20 ml CH_3OH for 30 sec. at lower and higher magnifications respectively.

The distribution of row of etch pits from either sides of the cleavage step indicates that this etchant reveals dislocation sites in Bi_2Te_3 crystals. The change in morphology of etch pits due to the addition of iodine is quite clear from Fig.10.21(b).

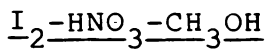


Fig.10.22(a) shows a (0001) surface etched in 1 g I_2 + 10 ml HNO_3 + 10 ml CH_3OH for 3 min. The higher magnification of the region marked A in Fig.10.22(a) is shown in Fig.10.22(b). In Figs.10.22(c) and 10.22(d) the same surface after successive etching for 5 min is shown at lower and higher magnifications respectively. It is seen from Figs.10.22(b) and 10.22(d) that the etch groove in the area indicated B in Fig.10.22(b) has grown larger and joined to the arms of the intersecting etch grooves. Fig.10.23 shows the formation of a row of triangular etch pits inside one of the etch grooves. Etch grooves were also developed from cleavage cracks (Fig.10.24). When the iodine content is increased in the etchant, well developed etch pits were observed. Fig.10.25(a) shows the morphology of etch pits observed after etching in 3 g I_2 + 10 ml HNO_3 + 10 ml CH_3OH for 2 min. The pits were formed with different sizes and shapes on the same surface. Some of

the pits has straight sides while others have curved sides. It is also seen that some pits were aligned in the form of a loop structure. The higher magnification of such pits (marked A in Fig.10.25(a)) is shown in Fig.10.25(b) where the loop structure is clearly visible. The peculiar morphology of etch pits obtained in the present case is associated with the etchant composition. The etch pits observed by Teramoto and Takayanagi [2] using the etchant containing 10 ml HNO_3 , 10 ml HCl , 40 ml H_2O and 1 g I_2 have almost equal sizes and the steps of the inner pits were parallel to the corresponding sides of the outer pits. But in the present case, the etch pattern is entirely different. The innermost pits are situated at different positions on the outer pits. On prolonged etching the etch pits have grown larger so that they combined with each other to attain the loop structure as shown in Fig.10.25(c). It is seen from this figure that the curved edge of the pits become straight and steps were formed on their sides. In Fig.10.26(a) a typical four sided etch pit is shown, which has a black dot in the centre. The dot become larger in size and developed into a triangular etch pit after prolonged etching (Fig.10.26(b)). The straight sides of the pit become changed and acquired the geometry as shown in Fig.10.26(b). Since the triangular pit did not

vanish on successive etching, it seems that, it is formed at dislocation sites on the crystal surface.

(b) Investigation on multiplication of dislocations due to Frank-Read sources

Br-CH₃OH

The multiplication of dislocations is of importance to the plasticity of crystals. Frank and Read [13] proposed the classical multiplication mechanism in which a dislocation, anchored at each end, expands in its slip plane. This was first observed by Dash [14] in silicon samples plastically deformed at 1000°C, using infrared transmission microscopy. During the present study, special attention has been paid to understand the movement and multiplication of dislocation, by employing bromine in methanol as etchant. Dislocation spirals and loops due to Frank-Read sources have been observed on the basal plane. This section describes the report of such observations.

When the cleavage faces of the crystals were etched in 5 ml of 10% bromine in methanol by volume for 30 sec, small shallow pits of undefined shape and prismatic loops were observed. Further etching of the crystal for a

total time of 1 min. resulted in the development of spirals and closed loop patterns. Etching for longer times made the crystal surface corroded. So this composition of etchant and etching time was found to be the optimum condition for obtaining visible multiturn dislocation spirals and loops. This can be seen from the optical micrographs (Figs.10.27 to 10.37). From these figures, it is fairly clear that the multiplication mechanism [13] is responsible for the present observations. According to this slip mechanism, the most suitable explanation for the large amount of slip occurring on a single slip plane can be obtained by a process of expansion and subdivision due to simple motion of dislocation [15].

Although the origin of the loops is not completely understood, the reason for their occurrence has to be sought in the stoichiometry of Bi_2Te_3 . This point of view is based on the fact that similar types of closed loops do not occur in the Te-rich Bi_2Te_3 crystals of Sagar et al. [6]. They have observed spirals and concentric loops only in the heat treated and quenched Bi_2Te_3 samples grown from the non-stoichiometric Te-rich melt. When these samples were heated at 500°C for a few days in vacuum, there may be a possibility of the removal of excess Te atoms, thus

rendering these samples nearer to stoichiometry. This supports the present observation of ideal Frank-Read dislocation mill on the basal plane of stoichiometric Bi_2Te_3 crystals without any heat treatment. Moreover, the different shaped pyramidal pit formation in the Te-rich samples [3,6] is not at all found in the present case. Hence this implies that, deviations from the stoichiometric proportions of the constituent elements may have an important effect on the dislocation pattern of Bi_2Te_3 .

An example of Frank-Read spiral due to a section of dislocation that lies in the (0001) slip plane and leaves that plane at a point in the interior of the crystal is shown in Fig.10.27.

The various events in the development of Frank-Read sources are quite clear from Figs.10.28-10.31. In this case the dislocation line connects two interior points on the two arms of L-shaped dislocation. The pinning of these anchor points may be due to other dislocation intersections. When this dislocation leaves the slip plane at these points under the action of shear stress it will bow out as stress increases and the expanding loops double back on itself. Thus a large kidney shaped loop will be

observed (Fig.10.28). It is seen that the length of dislocation line is $\simeq 10^{-3}$ cm. This is in agreement with the value ($\lambda \simeq 10^{-3}$ cm) corresponding to the experimental elastic limit, which is the order of magnitude of the Frank network [16]. The very same type of behaviour has been observed in silicon using decoration technique [17]. Fig. 10.29 shows the two parts of slipped area, which have almost doubled back on itself. Finally the sections of dislocation join and annihilate one another (Fig.10.30). This occurs because the two segments moving in opposite directions under the same stress have the same burgers vector but opposite line sense. Further formation of closed loops of dislocation and their expansion is as shown in Fig. 10.31. Fig.10.32 depicts the expansion of a single closed loop with two emerging points of circular dislocation sites. These Frank-Read sources can also be considered as two oppositely winding spirals joined together.

Many other interesting observations of dislocation loops were revealed on the basal plane of Bi_2Te_3 . Fig. 10.33 represents the expansion of closed loops from multiple dislocation sources of various orientations lying in the same plane. This implies that the neighbouring

parts of the same crystal plane have undergone slip in different directions. Further, it is also observed that the various sections of dislocation have been bulged in different proportions. This may be due to the fact that the stress required for the expansion of each pair of unlike dislocation sources is not the same. Fig.10.34 illustrates the unequal spiralling of the two pivot points of dislocation. The lack of stable pinning of anchor points and the interference from other dislocations can result in the formation of slightly asymmetric closed loops. Dislocation loops expanding around two Frank-Read sources (A and B) oriented face to face and sweeping out the whole plane are depicted in Fig.10.35. Fig.10.36 represents a dislocation spiral resulting from the operation of more than one pair of sources. Fig.10.37 is an example of a single closed loop formed by the successive interaction between three Frank-Read sources. The individual nature of the central part of the sources could not be resolved in this photograph.

In many cases, the successive arms of the loops originating from different dislocations are observed to join with each other. This can be explained only if the heights of the different series of steps are the same, i.e.,

the dislocations are of the same strength. The dislocations spirals and loops observed on the basal plane of Bi_2Te_3 are due to Frank-Read dislocation multiplication mechanism and the shape of these are shown to be in accordance with the theory [18]. The internal stresses produced in this sample may be related to the constraining of neighbouring regions due to the thermal gradient. The stoichiometry of Bi_2Te_3 is of primary importance for the occurrence of dislocation loops. The dislocation density is found to be $\sim 10^3 \text{ cm}^{-2}$.

(c) Investigation on cracks formed by cleavage process

HNO_3 - CH_3COOH - HF

Crystal surfaces prepared by cleavage operations often lead to damaged surfaces. The etching of cleaved samples provides a simple method for investigating the nature and distribution of defects in the damaged layer. Since cleavage of Bi_2Te_3 crystals takes place between two tellurium layers and the bonds are also weakest there, some damage was produced depending on the care taken during the cleavage process. Hence it was thought useful to make a study on the effect of deformation on the cleavage surface by etching method.

Fig.10.38 shows the nucleation of cracks on a (0001) face of Bi_2Te_3 crystal after 10 sec etching in 6 ml HNO_3 + 1 ml CH_3COOH + 1 ml HF solution. This is the optimum condition for revealing cracks on the surfaces. Dark etch pits were formed near the edges and on other parts of the same surface, which represents the dislocations introduced at the sites of cracks. Fig.10.39 depicts the formation of well developed cracks propagating parallel to the edge of the cleavage face. From Figs.10.38 and 10.39 it is seen that the surface microstructure is enriched with alternate bright and dark regions in between the crack channels. This occurs because the dislocations approach each other forming a dark area in the slip plane.

Dislocations created in the form of closed loops were also observed as shown in Fig.10.40. In Fig.10.41, the cracks revealed on cleavage steps are shown. No deep cracks were formed on the neighbouring parts of the surface, which indicates that the passage of crack around the cleavage step did not produce new dislocations in the crystal. When the crystal is highly plastic, plastic zones may be formed at the crack tip. The propagation of such a crack was often retarded by the large number of dislocations near the tip and hence the crack tip rounds off.

This is shown in Fig.10.42. The shape of these cracks is in agreement with the structure of cracks described in [19]. The depth of cracks ranges from 50 to 100 μm .

Crack nucleation in crystals has been studied by several workers [20-22]. Sangwal and Arora [22] investigated the nature and depth of surface damage of mechanically abraded surfaces of MgO crystals and revealed surface cracks by chemical etching on the (111) faces. In the present study the nucleation and development of cracks may be explained as follows.

The basic mechanism of growth of a crack is the input of dislocations to it. When the crystal is subjected to mechanical stress, a dislocation source is generated on it. The stress applied to the sample tends to deform it gradually. In the course of deformation, the dislocations move along the slip plane as long as they are not pinned by any obstacles. Obstacles capable of slowing down whole groups of dislocations may be sessile dislocations, dislocation dipoles (pairs of parallel, dislocations with opposite Burgers Vector) low--misorientation--angle block boundaries, grain boundaries and other defects. The generation of dislocations was increased under the effect

of increasing stress and thus caused an increased in dislocation density in the slip planes. When the stress is raised above a particular level, the dislocations interact with each other very closely and a stress concentration arises in different regions of the surface. Further increase in the applied stress leads to the growth of well developed cracks. Similar scheme of crack nucleation was proposed by Mott [23]. According to this scheme a crack nucleates in front of a dislocation pile up and develops in the plane with maximum normal stress.

10.3.2 In_2Te_3 Crystals

(a) Investigation on the morphology of etch pits

Various chemical etchants were tried to delineate dislocations in In_2Te_3 crystals. Finally two etchants: $\text{HNO}_3\text{-HF}$ and $\text{HNO}_3\text{-HF-H}_2\text{O}$ were selected to study the morphology of etch patterns.

$\text{HNO}_3\text{-HF}$

Fig.10.43(a) depicts the etched surface of $\alpha\text{-In}_2\text{Te}_3$ crystal after etching it in 3 ml HNO_3 + 0.5 ml HF for 10 sec. Fig.10.43(b) shows the higher magnified view of the etch pit marked B in Fig.10.43(a). After repeated etching for 20 sec, a one-to-one correspondence in the

position of pits was observed (Fig.10.43(c)). Moreover, there was no increase in the number of pits. The above observations strongly suggested that the etch pits were produced at the emergence points of dislocations.

The etching of β - In_2Te_3 crystals was carried out in the same etchant for 10 sec and the resulting pattern is as shown in Fig.10.44(a). The etch pits exhibited different morphologies like A-type, B-type and C-type pits as indicated in the figure. Figs.10.44(b) and 10.44(c) show the morphology of A-type and B-type pits at higher magnifications. On successive etching (Fig.10.45(a)) both pits came close together due to the increase in their size and acquired the morphologies as shown in Figs.10.45(b) and 10.45(c). The outer layers of the pit become flattened whereas the interior parts become deepened. The increased size and depth of the pits may be due to a larger Burgers vector. The C-type pits seen in Figs.10.44(a) developed further on successive etching, whereas the smaller etch pits vanished, which indicates that they were formed due to the segregation of impurities. Fig.10.46 depicts a typical etch pit formed by etching in 3 ml HNO_3 + 0.6 ml HF for 10 sec. The change in morphology of etch pits is quite clear.

From the above observations, it is clear that the etchant is capable of revealing dislocations [24]. Of the various factors, the morphology of etch pits observed in the present case is sensitive to the nature and composition of the etchant, etching conditions, nature of the crystal face to be etched, character of dislocation lines running into the body of a crystal as well as on the precipitation of impurities along dislocation lines and at random sites in the crystal.

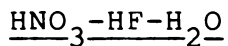


Fig.10.47(a) shows the morphology of etch pits on the cleavage_{face} of $\alpha\text{-In}_2\text{Te}_3$ crystal produced by the etchant 7 ml HNO_3 + 0.1 ml HF + 3 ml H_2O for 15 sec. Three types of etch pits were observed on the same face: (1) Etch pits exhibiting circular pattern in the centre (marked A in Fig.10.47(a)). (2) Etch pits having an elongated pattern in the centre (Marked B in Fig.10.47(a)) and (3) Etch pits having a tail (marked C in Fig.10.47(a)). Pits of type A and B persisted and got enlarged on prolonged etching. Hence they may be formed at the sites of emergence of dislocations on the crystal faces. The difference in orientation of bright feature in the center of pits A and B indicates that the dislocations are inclined at different

angles at both sites. In the C-type pits (Fig.10.47(b)) the tail disappeared on subsequent etching. These pits may be formed at sites where the impurities had segregated or where the dislocations had moved away by abrupt bending. In Fig.10.48 a peculiar morphology of etch pits was observed, when the crystals were etched in 7 ml HNO_3 + 0.2 ml HF + 3 ml H_2O for 15 sec. Both pits were distributed along a line and developed continuously upon etching.

On etching $\beta\text{-In}_2\text{Te}_3$ crystals in 7 ml HNO_3 + 0.1 ml HF + 3 ml H_2O , spiral type distribution of etch pits were obtained as shown in Fig.10.49. In addition, etch grooves were also observed as shown in Fig.10.50.

The morphology of etch patterns observed on the (111) faces of In_2Te_3 crystals are similar to those reported on the (111) faces of InSb crystals [25].

(b) Investigation on cracks formed by cleavage process

$\text{HNO}_3\text{-CH}_3\text{COOH-HF}$

The dislocation etchant 6 ml HNO_3 + 1 ml CH_3COOH + 1 ml HF employed for the revelation of microcracks on the cleavage faces of Bi_2Te_3 crystals was found to be reliable

for the same studies in In_2Te_3 crystals. Since the cleavage of In_2Te_3 crystals didn't cause much damage, only a few crack patterns were observed on their cleavage faces.

In Figs.10.51(a) and 10.51(b) the formation of a long crack on the cleavage face of $\alpha\text{-In}_2\text{Te}_3$ crystal is shown at lower and higher magnifications respectively. The cracks formed along the cleavage steps of a $\beta\text{-In}_2\text{Te}_3$ crystal is depicted in Fig.10.52. It is found that a large area of the surface was free of dislocations which indicates that only a small amount of deformation was produced during the cleavage process.

10.4 CONCLUSION

The morphology of dislocation etch pits on the (0001) plane of Bi_2Te_3 crystals has been studied using different etchants like $\text{HNO}_3\text{-H}_2\text{O}$, $\text{HNO}_3\text{-H}_2\text{SO}_4\text{-H}_2\text{O}$, $\text{HNO}_3\text{-HF-H}_2\text{O}$, $\text{I}_2\text{-H}_2\text{SO}_4\text{-CH}_3\text{OH}$ and $\text{I}_2\text{-HNO}_3\text{-CH}_3\text{OH}$. The terracing and bunching of etch pits were studied by changing the concentration of acids. Dislocation spirals and loops due to Frank-Read sources have been observed on the basal plane by using bromine in methanol as the etchant. The density of dislocations intersecting the (0001) face of Bi_2Te_3

crystals is found to be $\sim 10^3 \text{ cm}^{-2}$. The etchant consisting of 6 ml HNO_3 , 1 ml CH_3COOH and 1 ml HF is found to be capable of revealing cracks on the (0001) faces. It is also reliable for detecting cracks in α and β - In_2Te_3 crystals. HNO_3 -HF and HNO_3 -HF- H_2O are reliable etchants for the observation of dislocation etch pits in α and β - In_2Te_3 crystals.

10.5 FIGURE CAPTIONS

Fig.10.1 Etch pit patterns produced on the (0001) face of a Bi_2Te_3 crystal by 3 ml HNO_3 + 10 ml H_2O after 5 sec.

Fig.10.2 Etch pits produced on the (0001) face of a Bi_2Te_3 crystal by 3 ml HNO_3 + 10 ml H_2O after 10 sec. (Marker: 1 div. = $10\mu\text{m}$).

Fig.10.3 Etch pits accompanied by etch grooves on the (0001) face of a Bi_2Te_3 crystal by 3 ml HNO_3 + 10 ml H_2O after 10 sec.

Fig.10.4 Etch pits produced on the (0001) face of a Bi_2Te_3 crystal by 3 ml HNO_3 + 0.1 ml H_2SO_4 + 10 ml H_2O after 10 sec. (Marker: 1 div = $10\mu\text{m}$.)

Figs.10.5(a) and 10.5(b) Etch pits produced on the (0001) face of a Bi_2Te_3 crystal by 3 ml HNO_3 + 0.3 ml H_2SO_4 + 10 ml H_2O after 10 sec at lower and higher magnifications respectively.

Fig.10.6 Formation of terraced etch pits along with etch grooves on the (0001) face of a Bi_2Te_3 whisker by etching in 3 ml HNO_3 + 0.3 ml H_2SO_4 + 10 ml H_2O after 10 sec.

- Fig.10.7 A cluster of point bottomed etch pits formed on the (0001) face of a Bi_2Te_3 crystal by 3 ml HNO_3 + 0.4 ml H_2SO_4 + 10 ml H_2O after 10 sec.
- Fig.10.8 Bunch formation on the (0001) face of Bi_2Te_3 crystal after etching in 3 ml HNO_3 + 0.4 ml H_2SO_4 + 10 ml H_2O for 10 sec.
- Figs.10.9(a) Bunches observed on the (0001) face of a and 10.9(b) Bi_2Te_3 crystal etched in 3 ml HNO_3 + 0.6 ml H_2SO_4 + 10 ml H_2O after 10 sec.
- Fig.10.10 Etch pits produced on the (0001) face of a Bi_2Te_3 crystal after etching for 5 sec in 3 ml HNO_3 + 0.9 ml H_2SO_4 + 10 ml H_2O (Marker: 1 div. = 5 μm).
- Fig.10.11 Etch pits formed on the (0001) face of Bi_2Te_3 crystal due to high etch rates after etching in 3 ml HNO_3 + 1 ml H_2SO_4 + 10 ml H_2O for 2 sec.
- Fig.10.12 Etch patterns produced on the (0001) face of a Bi_2Te_3 crystal by 0.2 ml HNO_3 + 0.5 ml H_2SO_4 + 10 ml H_2O after etching for 10 sec. (Marker: 1 div. = 10 μm).

- Fig.10.13 Etch pits formed on the (0001) face of a Bi_2Te_3 crystal by etching in 0.4 ml HNO_3 + 0.5 ml H_2SO_4 + 10 ml H_2O for 10 sec. (Marker: 1 div. = 10 μm).
- Fig.10.14 Morphology of etch pits formed on the (0001) face of a Bi_2Te_3 crystal by 0.6 ml HNO_3 + 0.5 ml H_2SO_4 + 10 ml H_2O after etching for 10 sec. (Marker 1 div. = 10 μm).
- Fig.10.15 Formation of terraced etchpit patterns on the (0001) face of a Bi_2Te_3 crystal after etching in 0.8 ml HNO_3 + 0.5 ml H_2SO_4 + 10 ml H_2O for 10 sec.
- Fig.10.16 Etch pit pattern formed on the (0001) face of a Bi_2Te_3 crystal after etching in 3 ml HNO_3 + 0.1 ml HF + 10 ml H_2O for 10 sec. (Marker: 1 div. = 5 μm).
- Fig.10.17 Bunching of etchpits observed on the (0001) face of a Bi_2Te_3 crystal after etching in 3 ml HNO_3 + 0.2 ml HF + 10 ml H_2O for 10 sec.
- Fig.10.18 Etchpits produced on the (0001) face of a Bi_2Te_3 crystal by 3 ml HNO_3 + 0.3 ml HF + 10 ml H_2O for 10 sec.

Fig.10.19 Etch pit pattern on the (0001) face of Bi_2Te_3 crystal after etching for 10 sec. in 1 g I_2 + 0.5 ml H_2SO_4 + 10 ml CH_3OH (Marker 1 div. = 10 μm).

Fig.10.20(a) Formation of etch pits on the (0001) face of a Bi_2Te_3 crystal by 1 g I_2 + 0.5 ml H_2SO_4 + 20 ml CH_3OH solution after etching for 30 sec. (Marker 1 div = 10 μm)

Fig.10.20(b) The same area after prolonged etching (Marker 1 div = 10 μm).

Fig.10.21(a) Morphology of etch pits on the (0001) face produced by etching in the 2 g I_2 + 0.5 ml H_2SO_4 + 20 ml CH_3OH solution for 30 sec.

Fig.10.21(b) Higher magnification of the pits in 10.21(a) (Marker 1 div = 10 μm).

Fig.10.22(a) The etch grooves on the (0001) face of a Bi_2Te_3 crystal produced by etching in 1 g I_2 + 10 ml HNO_3 + 10 ml CH_3OH for 3 min.

Fig.10.22(b) Higher magnification of the region marked A in Fig.10.22(a).

Fig.10.22(c) The area shown in Fig.10.22(a) after successive etching.

Fig.10.22(d) Higher magnification of the region marked A in Fig.10.22(c).

Fig.10.23 Formation of a row of triangular etch pits inside one of the etch grooves.

Fig.10.24 Etch grooves developed from the cleavage cracks on the (0001) surface of Bi_2Te_3 crystal.

Fig.10.25(a) Morphology of etch pits produced after etching in 3 g I_2 + 10 ml HNO_3 + 10 ml CH_3OH for 2 min. (Marker 1 div = 10 μm).

Fig.10.25(b) Higher magnification of the region marked A in Fig.10.25(a).

Fig.10.25(c) The distribution of etch pits shown in Fig.10.25(a) after prolonged etching. (Marker 1 div = 10 μm).

Fig.10.26(a) Etch patterns produced by 3 g I_2 + 10 ml HNO_3 + 10 ml CH_3OH solution after etching for 3 min.

- Fig.10.26(b) The same face after prolonged etching.
- Fig.10.27 A circular spiral originating from a single dislocation.
- Fig.10.28 Configuration of dislocations resulting from the operation of a Frank-Read source of the double ended type (Marker: 1 div = 5 μm).
- Fig.10.29 Formation of an unstable dislocation loop where the two segments have almost joined.
- Fig.10.30 Mutual annihilation of two dislocations of opposite sense.
- Fig.10.31 Formation of closed loops from a pair of unlike dislocations.
- Fig.10.32 Emergence points of two dislocations inside a single closed loop.
- Fig.10.33 A group of interacting dislocation spirals and loops.
- Fig.10.34 Unequal movement of two dislocations.

Fig.10.35 Expanding loops from two Frank-Read sources (A and B) of opposite sign.

Fig.10.36 An expanding spiral spreading from multiple sources.

Fig.10.37 A single closed loop formed by the interaction between three Frank-Read sources.

Fig.10.38 Nucleation of microcracks on a (0001) face of a Bi_2Te_3 crystal produced after 10 sec. etching in 6 ml HNO_3 + 1 ml CH_3COOH + 1 ml HF solution.

Fig.10.39 Propagation of cracks parallel to the edge of the (0001) face of a Bi_2Te_3 crystal.

Fig.10.40 Nucleation of dislocations in the form of closed loops.

Fig.10.41 Revelation of cracks on the cleavage steps of a (0001) face of Bi_2Te_3 crystal.

Fig.10.42 Rounding of crack tips on a (0001) face of Bi_2Te_3 crystals.

Fig.10.43(a) Distribution of etch pits produced on cleavage face of a α - In_2Te_3 crystal by etching in 3 ml HNO_3 + 0.5 ml HF for 10 sec.

Fig.10.43(b) Higher magnified view of the pit marked B in Fig.10.43(a).

Fig.10.43(c) The face shown in Fig.10.43(a) after repeated etching.

Fig.10.44(a) Etch pattern formed on the cleavage face of β - In_2Te_3 crystal after etching in 3 ml HNO_3 + 0.5 ml HF for 10 sec.

Figs.10.44(b) Higher magnified view of the A-type and B-type and 10.44(c) pits shown in Fig.10.44(a).

Fig.10.45(a) Successive etching of the face shown in Fig.10.44(a).

Figs.10.45(b) Higher magnified view of the A-type and B-type and 10.45(c) pits shown in Fig.10.45(a) respectively.

Fig.10.46 Morphology of a typical etch pit formed by etching in 3 ml HNO_3 + 0.6 ml HF for 10 sec.

Fig.10.47(a) Etch patterns produced on the cleavage face of a α - In_2Te_3 crystal by etching in 7 ml HNO_3 0.1 ml HF + 3 ml H_2O for 15 sec.

Fig.10.47(b) Higher magnification of the pit marked C in Fig.10.47(a).

Fig.10.48 Etchpits on the cleavage face of α - In_2Te_3 crystal by etching in 7 ml HNO_3 + 0.2 ml HF + 3 ml H_2O for 15 sec.

Fig.10.49 Distribution of etch pits on the cleavage faces of a β - In_2Te_3 crystal after etching in 7 ml HNO_3 + 0.1 ml HF + 3 ml H_2O for 15 sec.

Fig.10.50 Etch grooves observed on the cleavage face of β - In_2Te_3 crystal.

Figs.10.51(a) and 10.51(b) Formation of a crack on the cleavage face of a α - In_2Te_3 crystal at lower and higher magnifications respectively.

Fig.10.52 Cracks formed along the cleavage of a β - In_2Te_3 crystal.



Fig. 10.1

(x33)

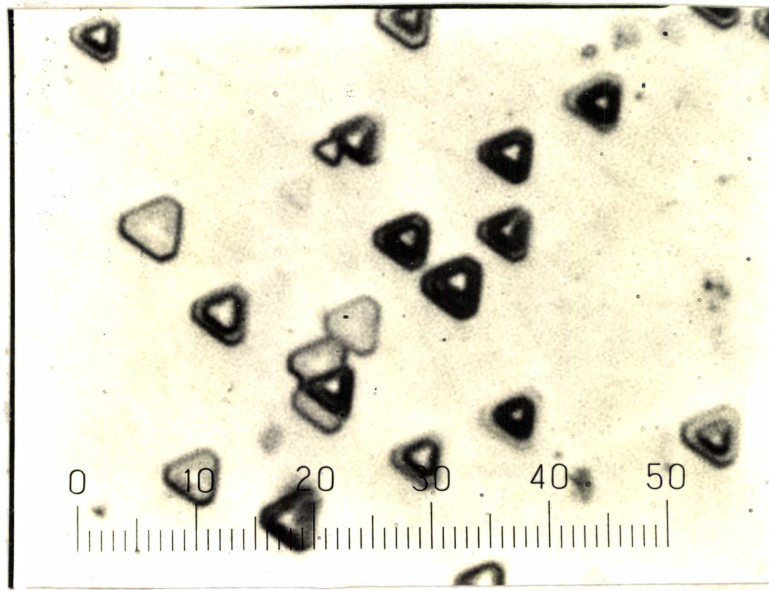


Fig. 10.2

(x150)

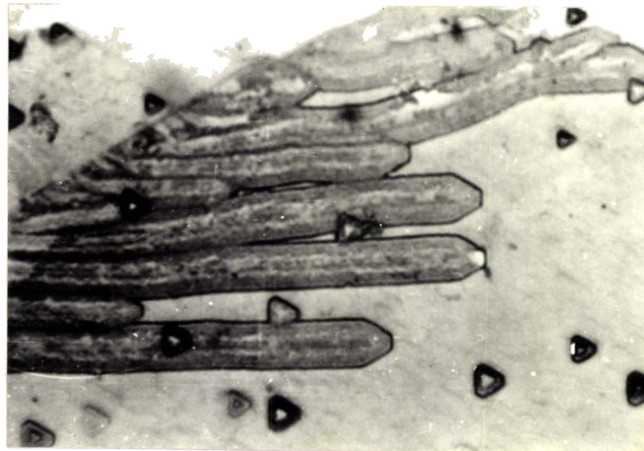


Fig. 10.3

(x80)

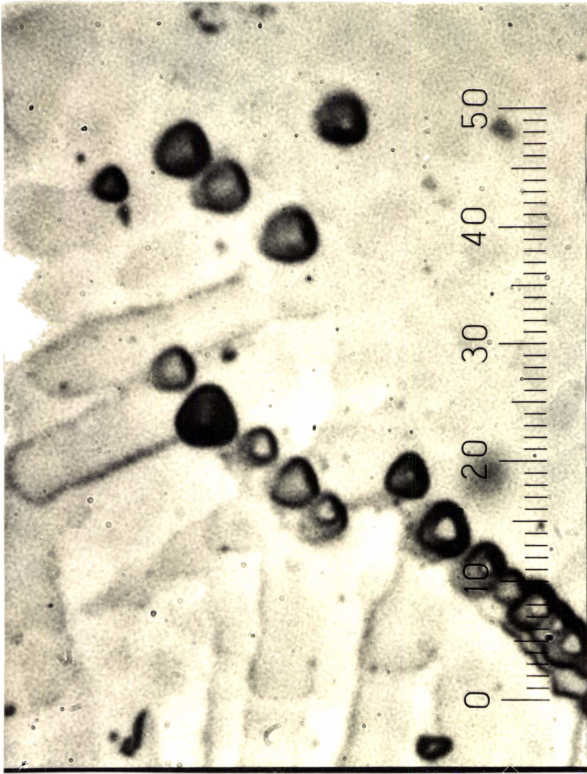


Fig. 10.4

(x150)



Fig. 10.5(a)

(x160)

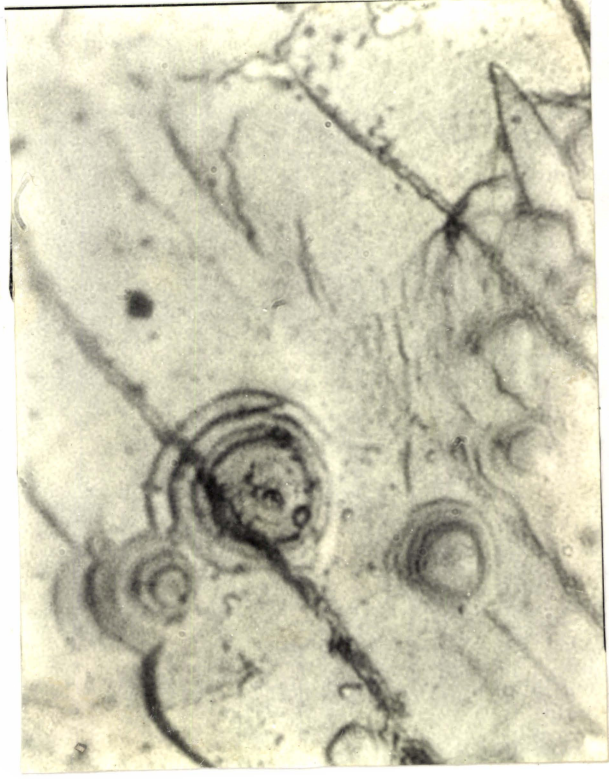


Fig. 10.6

(x150)

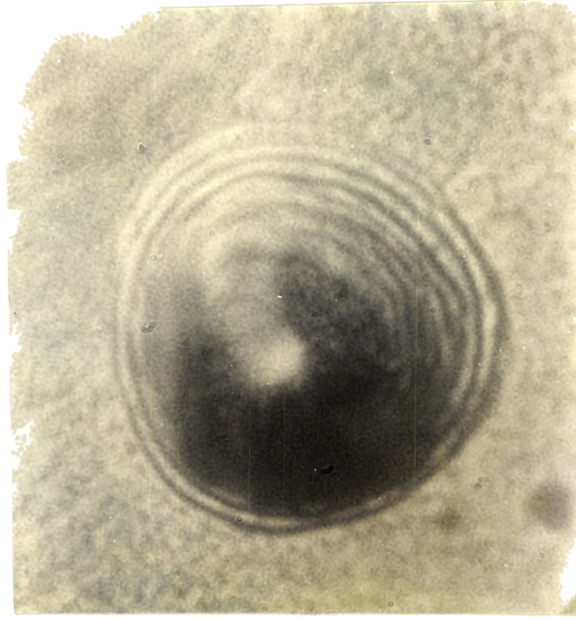


Fig. 10.5(b)

(x400)



Fig. 10.7

(x125)

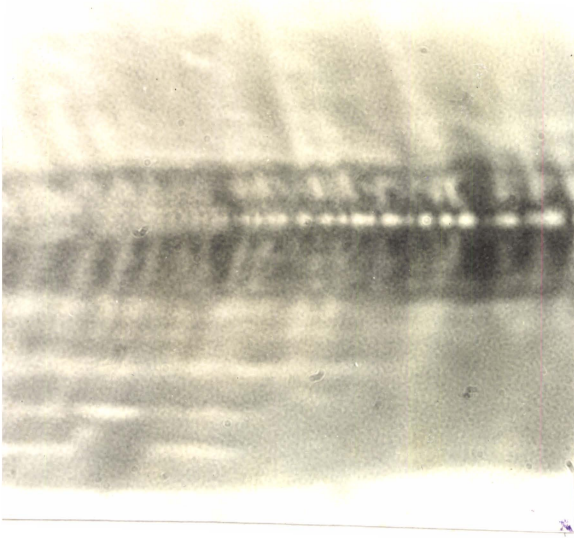


Fig. 10.8

(x500)

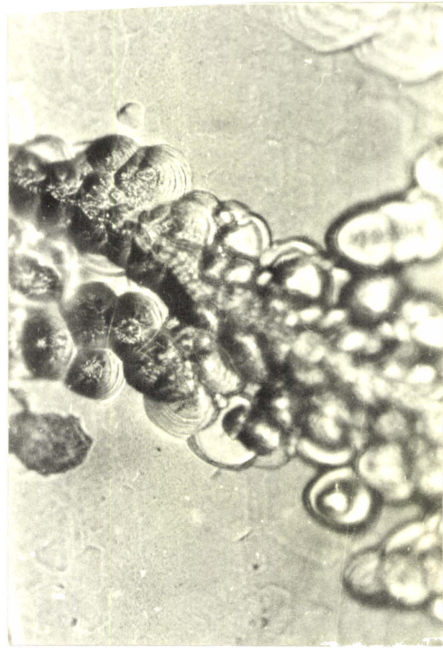


Fig. 10.9(a)

(x100)



Fig. 10.9 (b)

(x200)

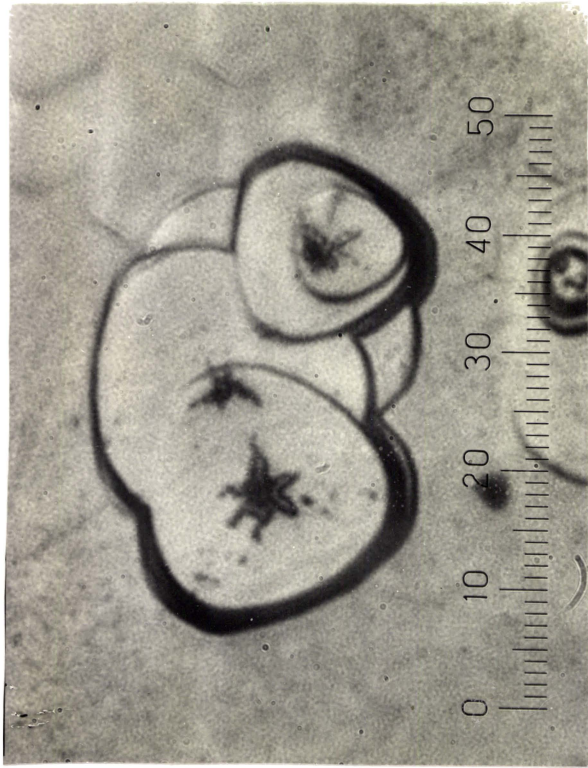


Fig. 10.10 (x350)

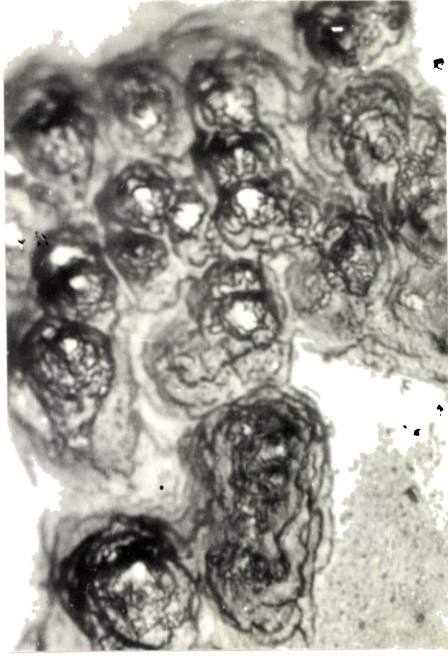


Fig. 10.11 (x80)

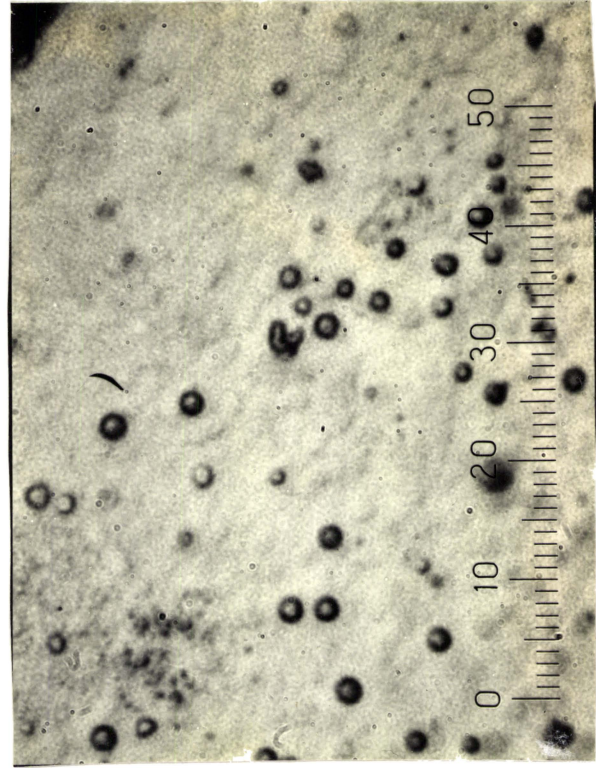


Fig. 10.12 (x150)

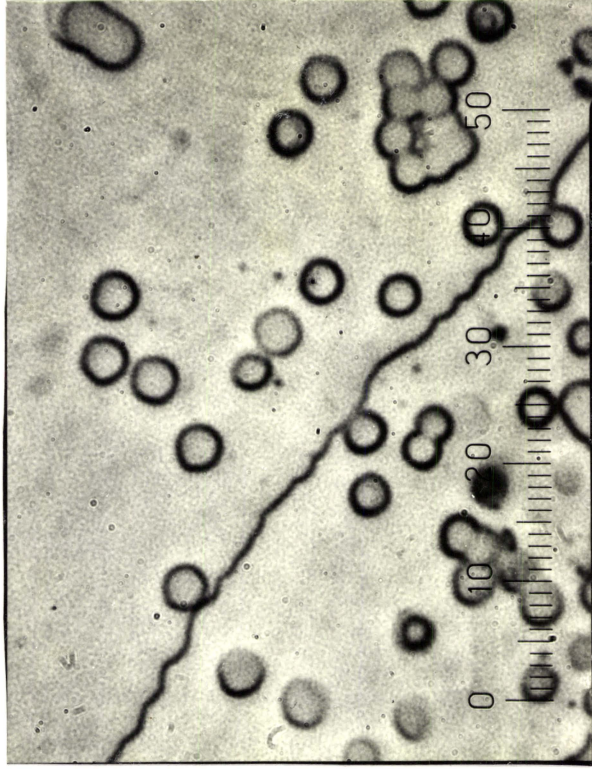


Fig. 10.13 (x150)

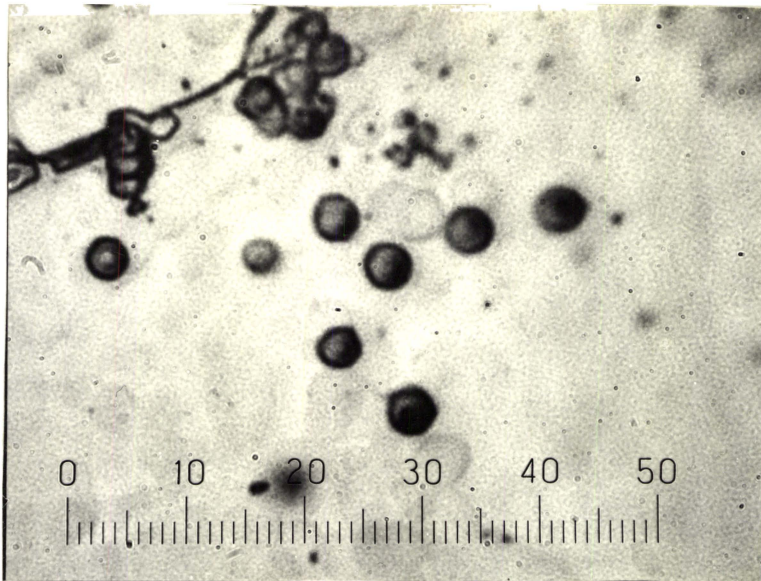


Fig. 10.14 (x150)

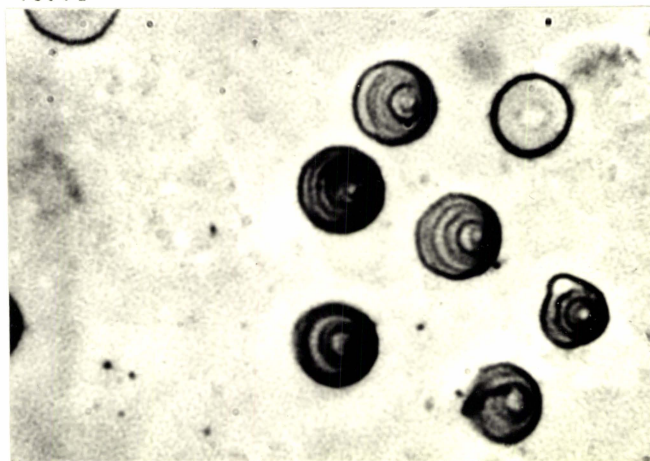


Fig. 10.15 (x200)

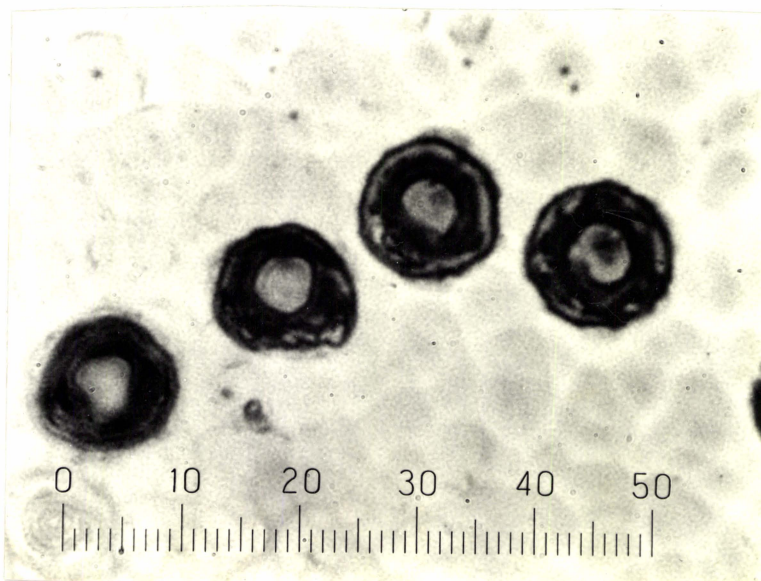


Fig. 10.16 (x350)

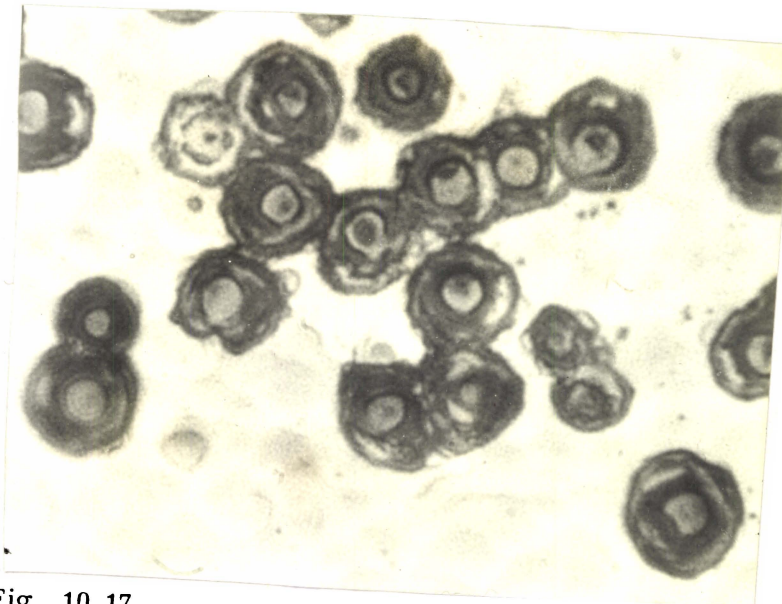


Fig. 10.17

(x200)

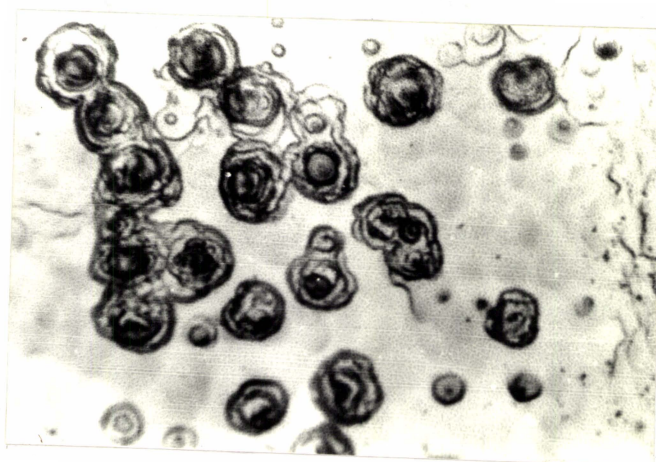


Fig. 10.18

(x80)

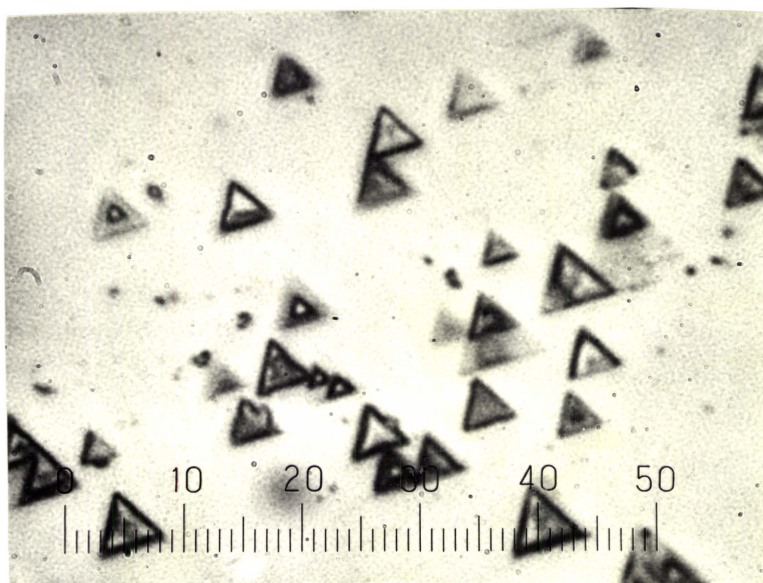
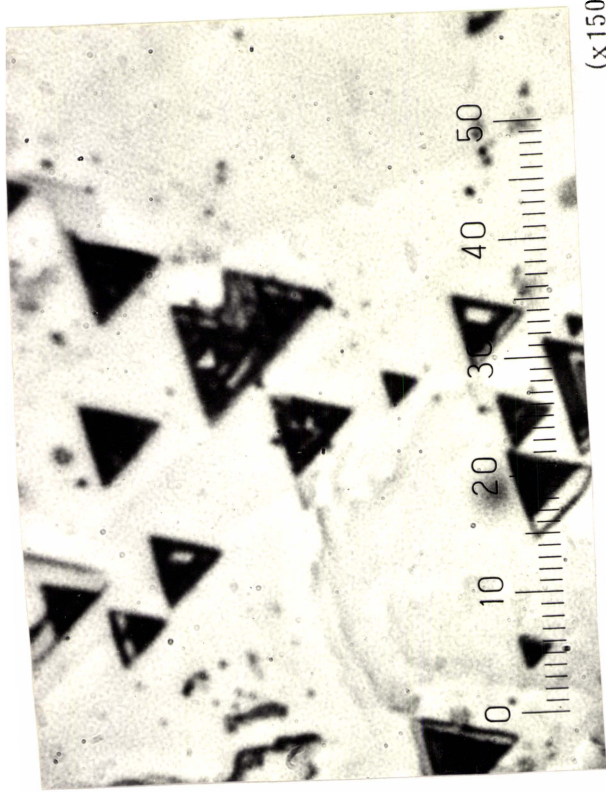


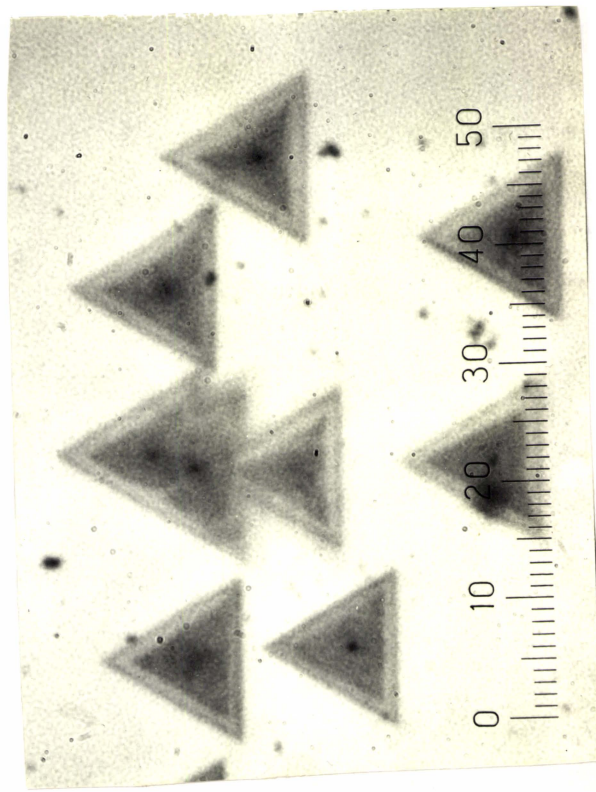
Fig. 10.19

(x150)



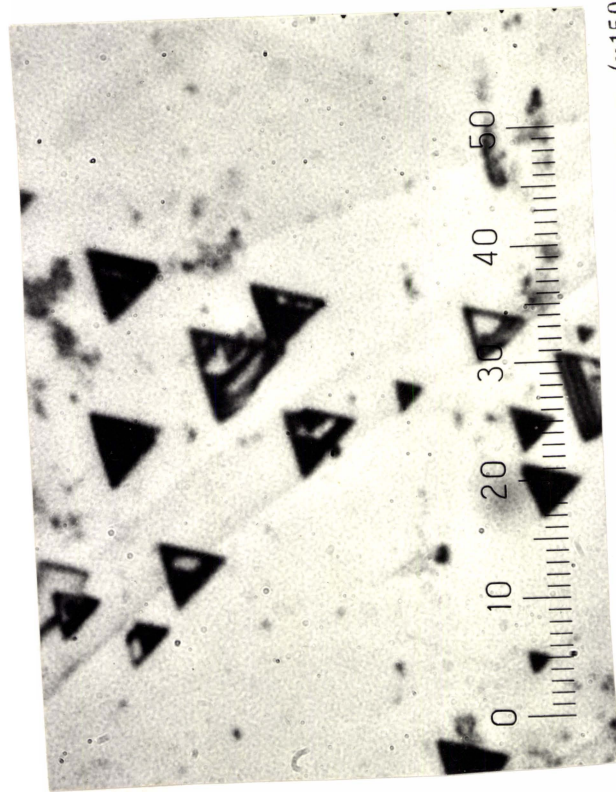
(x150)

Fig. 10.20(b)



(x150)

Fig. 10.21(b)



(x150)

Fig. 10.20(a)



(x 33)

Fig. 10.21(a)



Fig. 10.22(a)

(x50)



Fig. 10.22(c)

(x50)

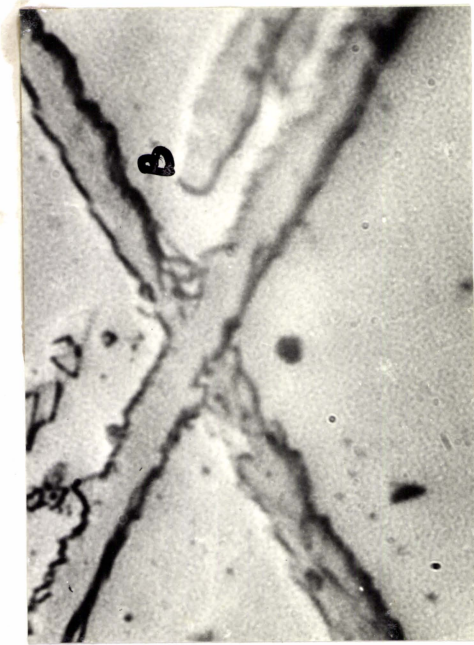


Fig. 10.22(b)

(x400)

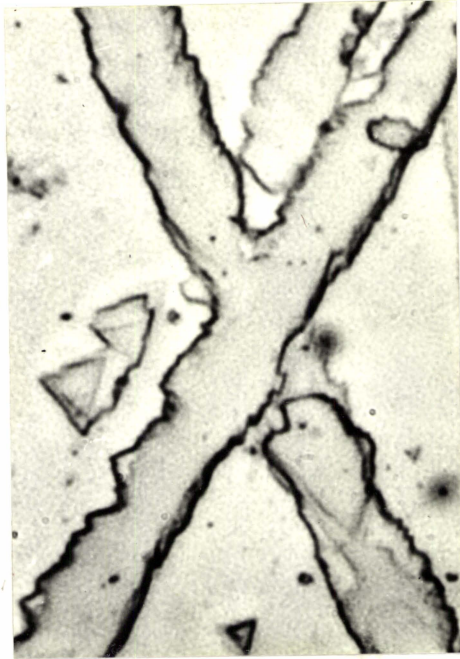


Fig. 10.22(d)

(x400)

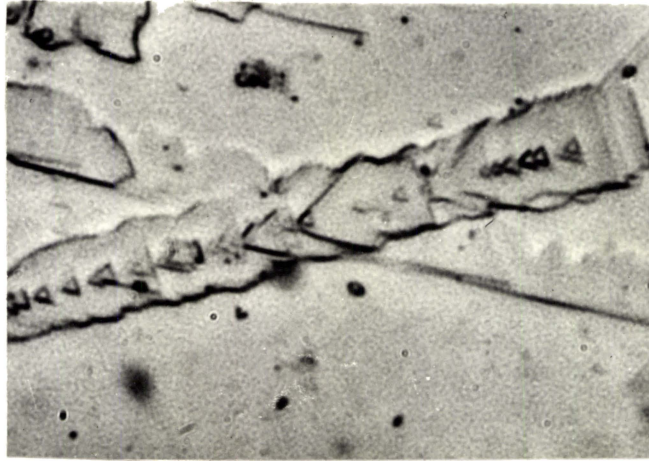


Fig. 10.23

(x200)

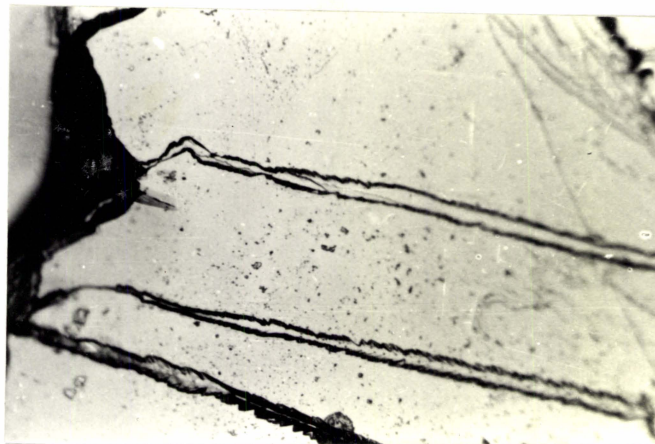


Fig. 10.24

(x 66)

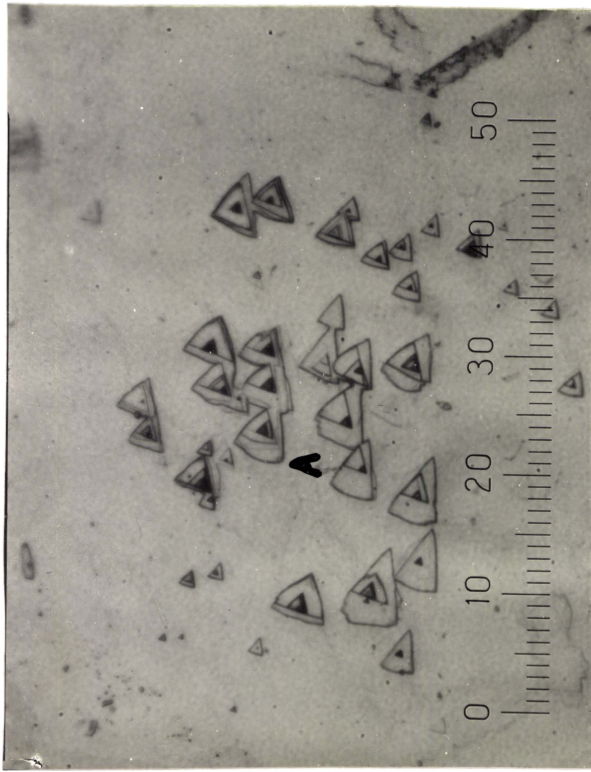
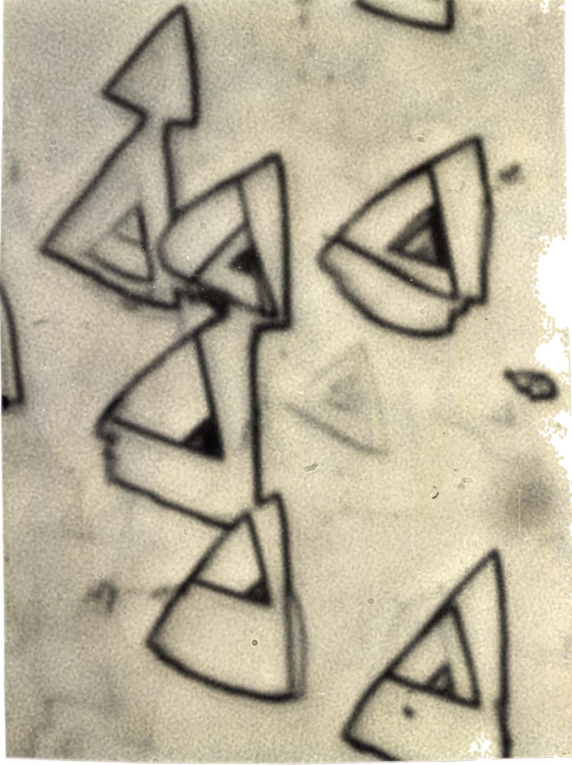


Fig. 10.25(a)



(x150) Fig. 10.25(b)

(x500)

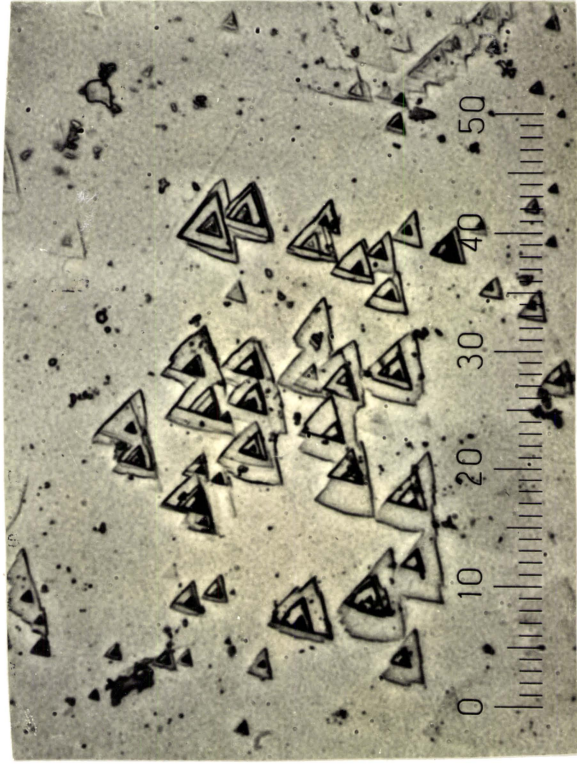


Fig. 10.25(c)

(x150)

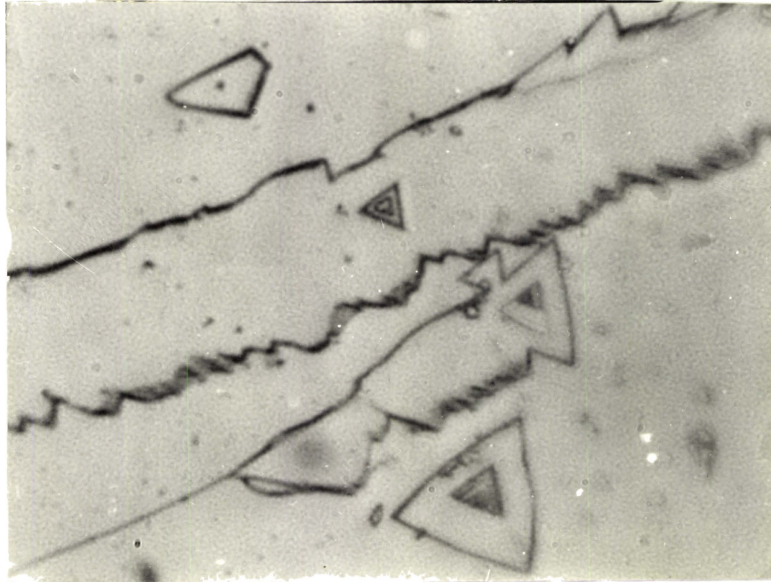


Fig. 10.26(a)

(x400)

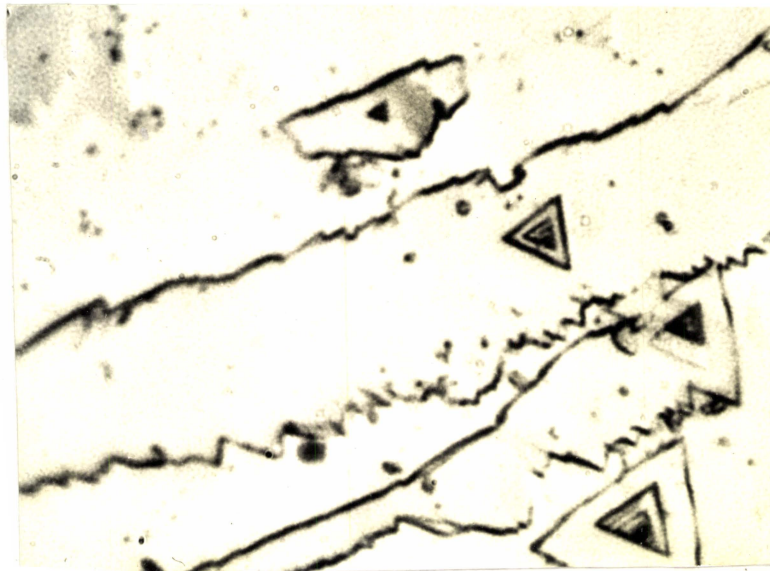


Fig. 10.26(b)

(x400)

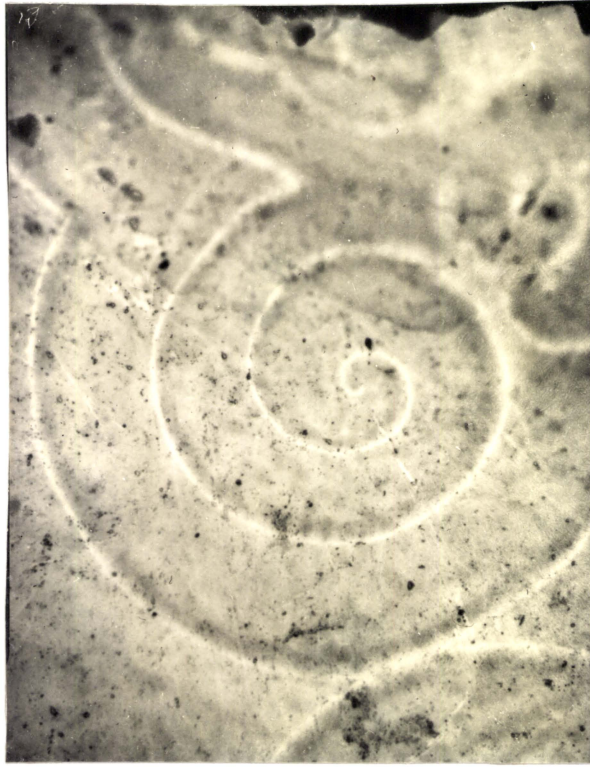


Fig. 10.27

(x470)

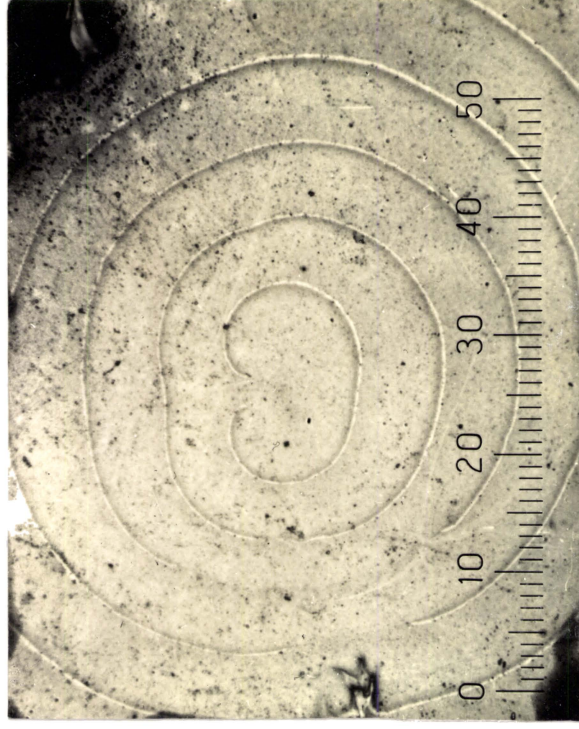


Fig. 10.28

(x350)

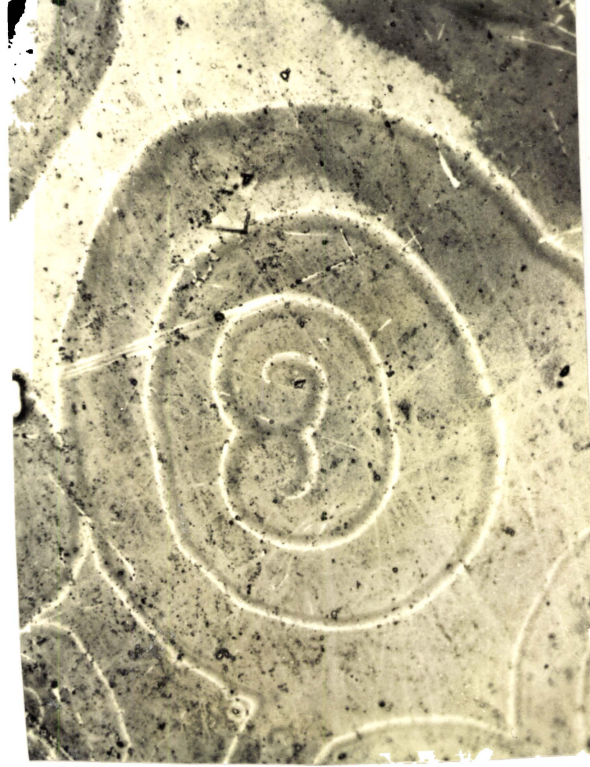


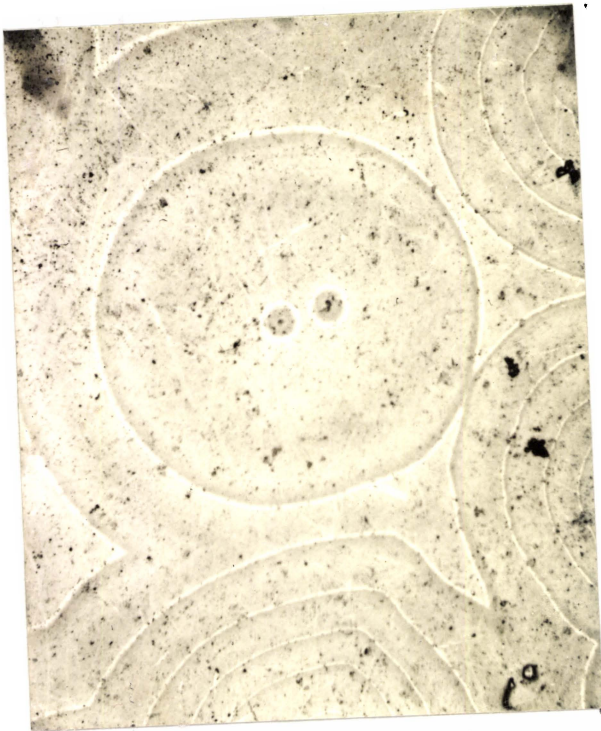
Fig. 10.29

(x350)



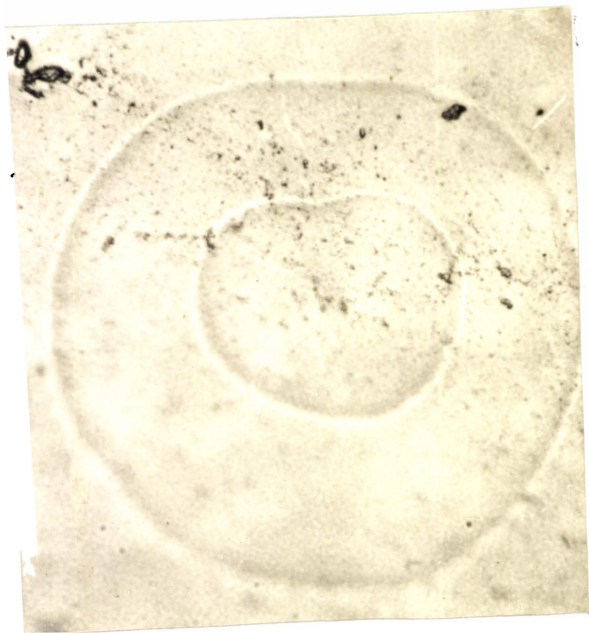
Fig. 10.30

(x200)



(x170)

Fig. 10.32



(x490)

Fig. 10.31



(x150)

Fig. 10.33

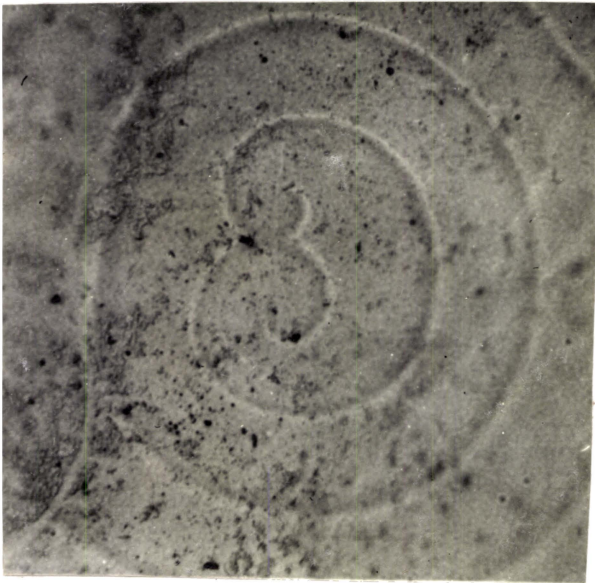


Fig. 10.34

(x490)

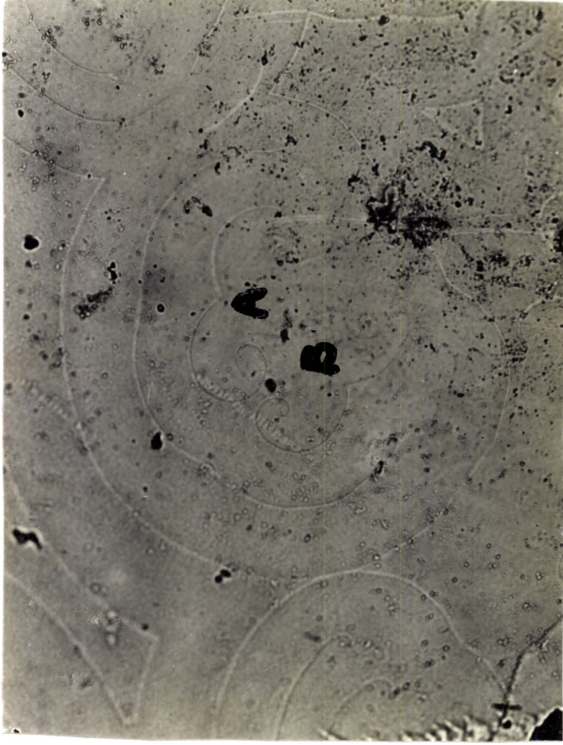


Fig. 10.35

(x290)



Fig. 10.36

(x500)

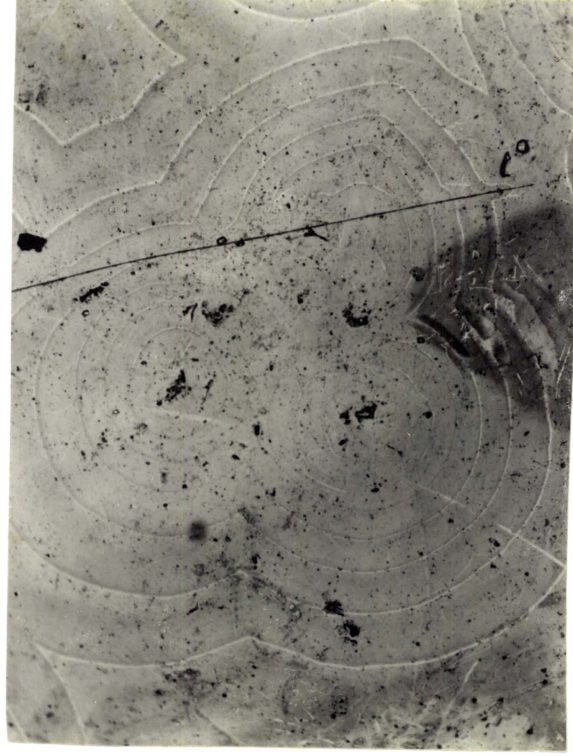


Fig. 10.37

(x120)

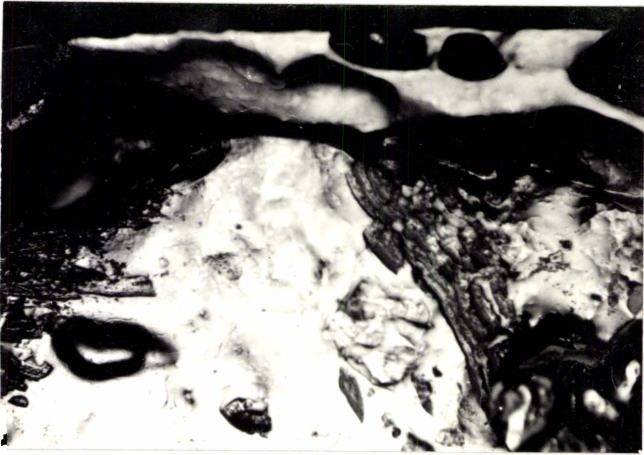
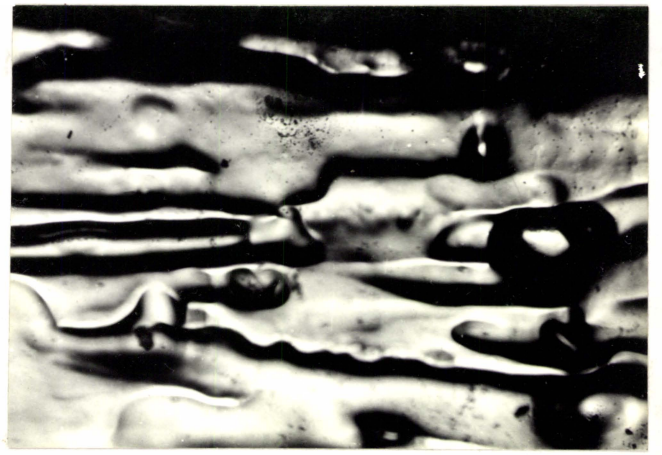


Fig. 10.38

(x150)



(x150)



Fig. 10.40

(x150)

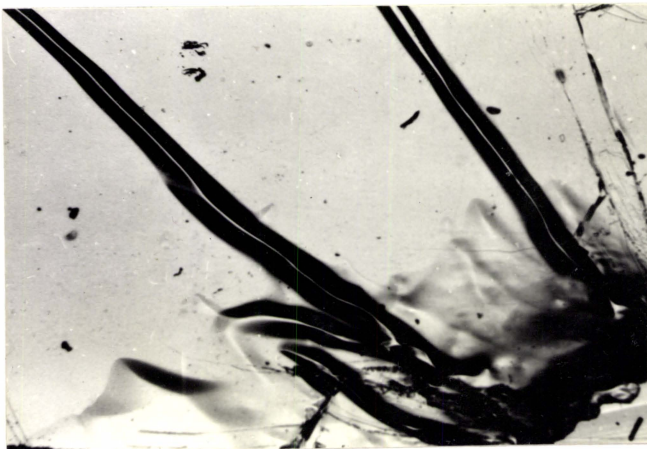
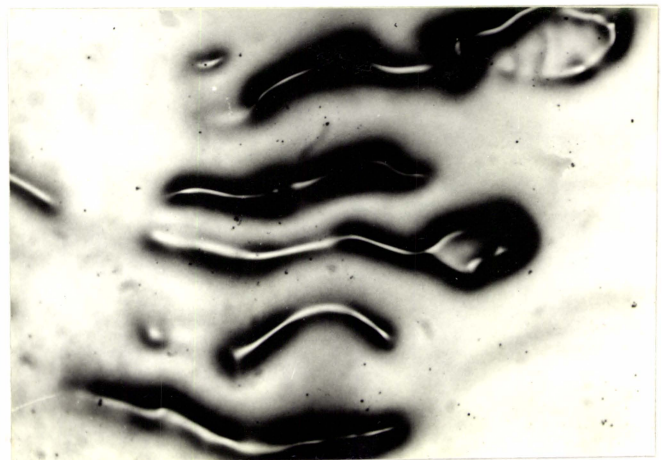


Fig. 10.41

(x150)



(x150)

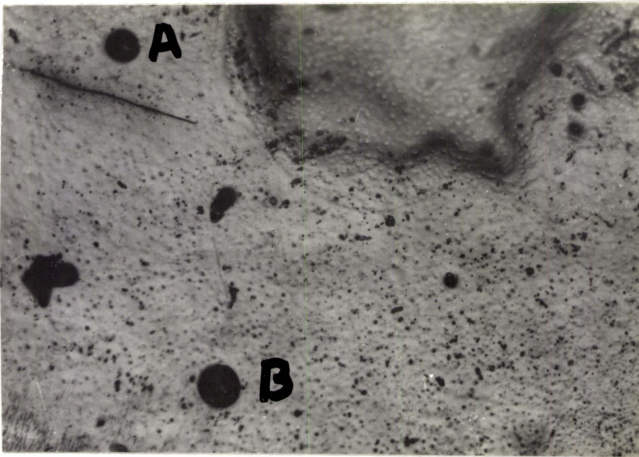


Fig. 10.43(a)

(x150)

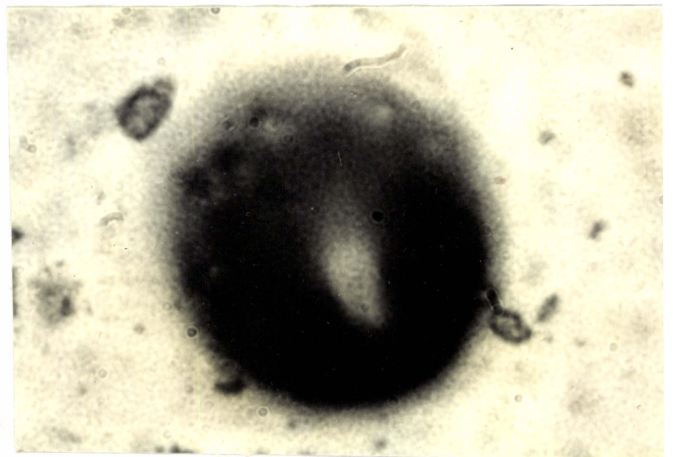


Fig. 10.43(b)

(x800)

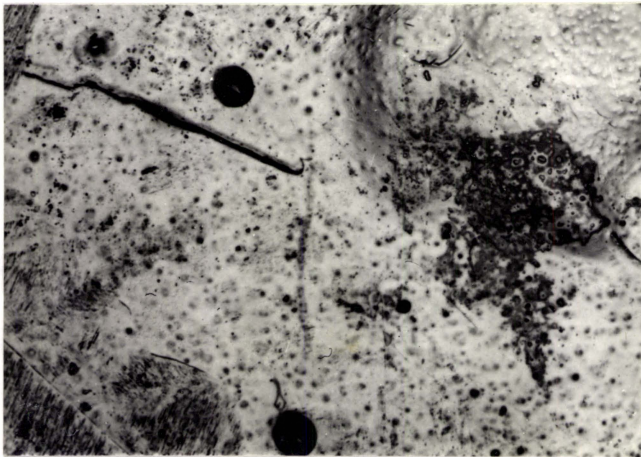


Fig. 10.43(c)

(x150)

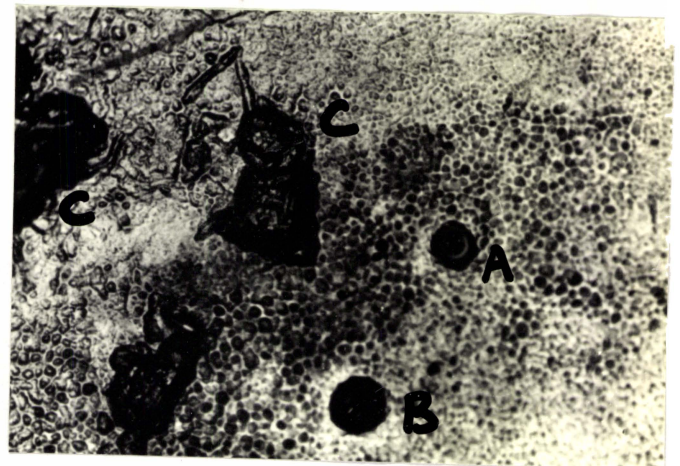


Fig. 10.44(a)

(x160)

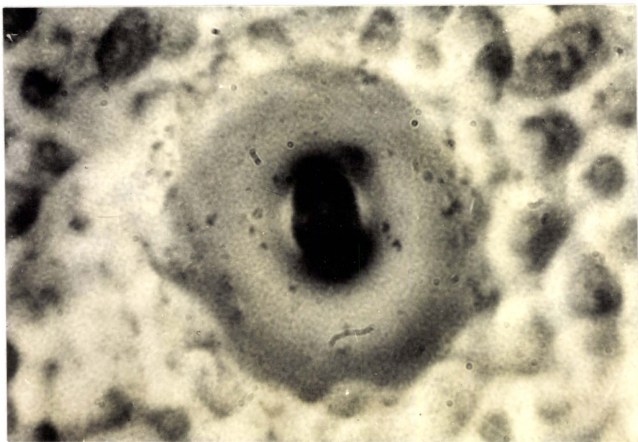


Fig. 10.44(b)

(x800)

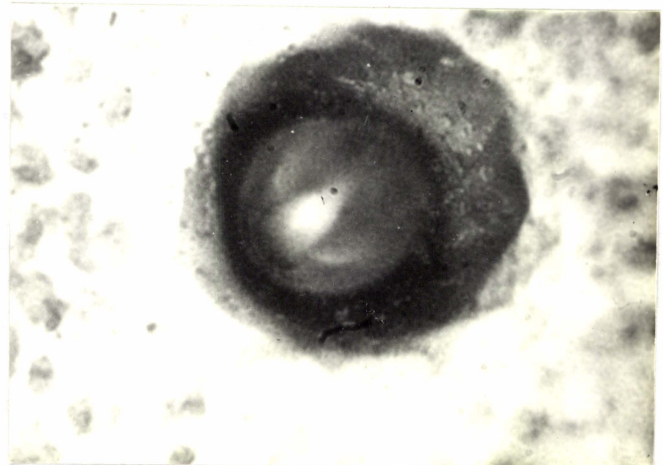


Fig. 10.44(c)

(x800)

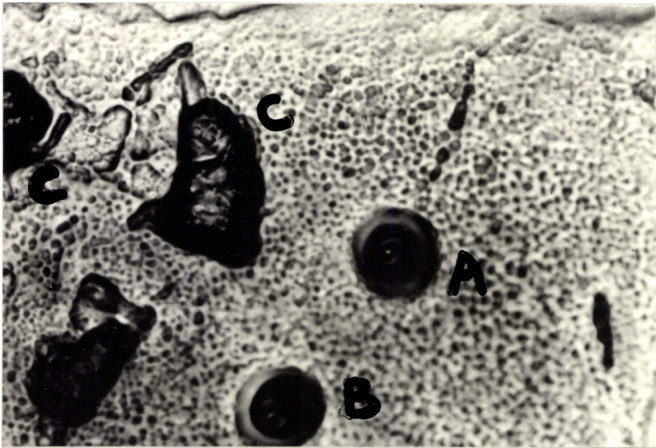


Fig. 10.45(a)

(x160)

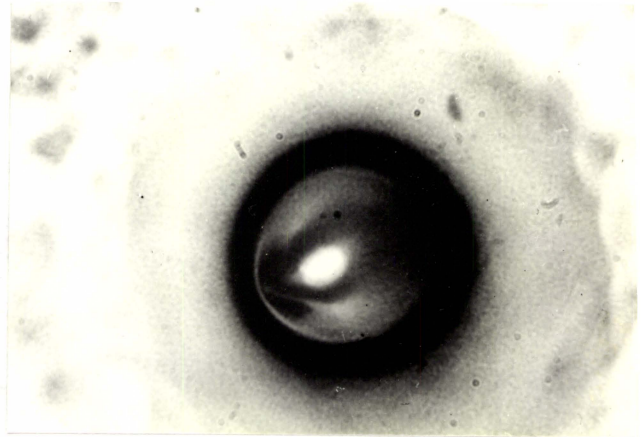


Fig. 10.45(b)

(x800)

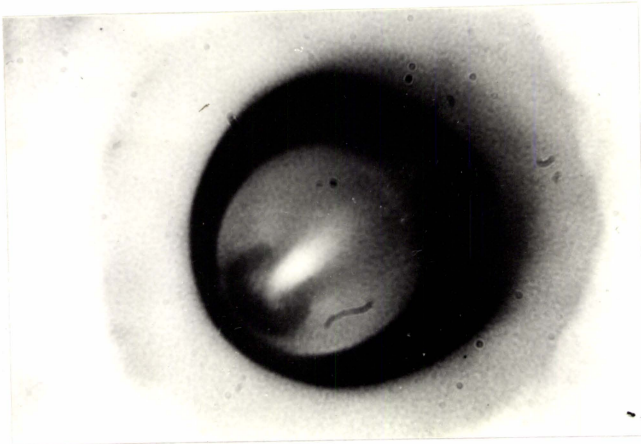
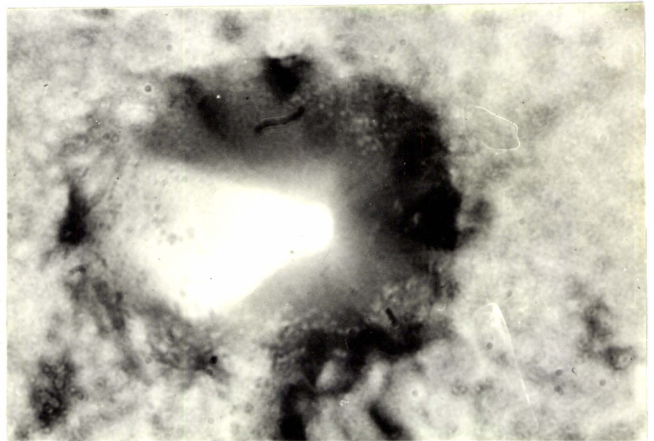


Fig. 10.45(c)

(x800) Fig. 10.46



(x800)

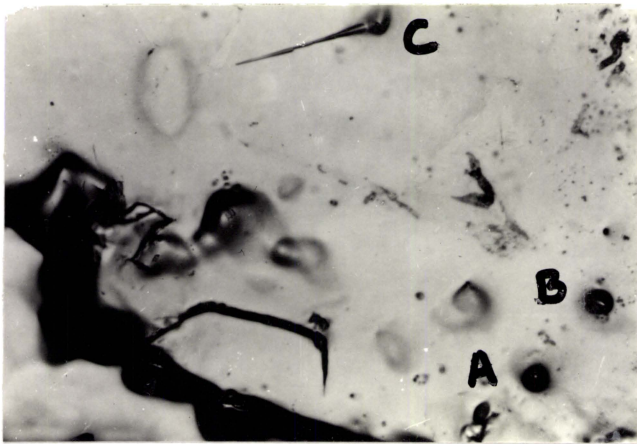


Fig. 10.47(a)

(x150)

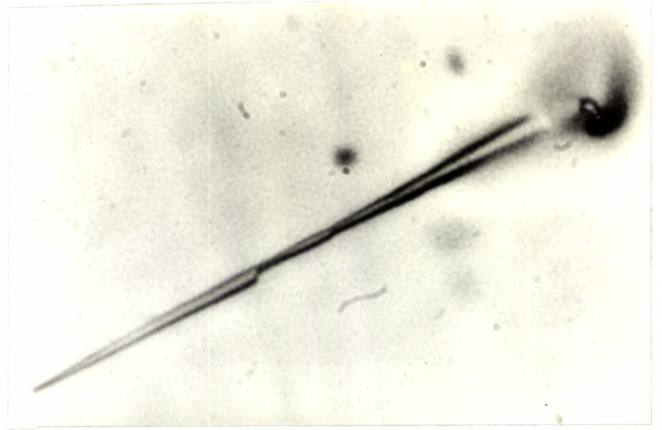


Fig. 10.47(b)

(x330)

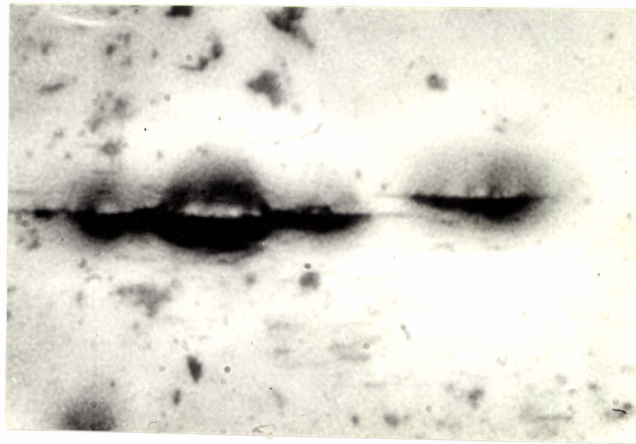


Fig. 10.48

(x200)

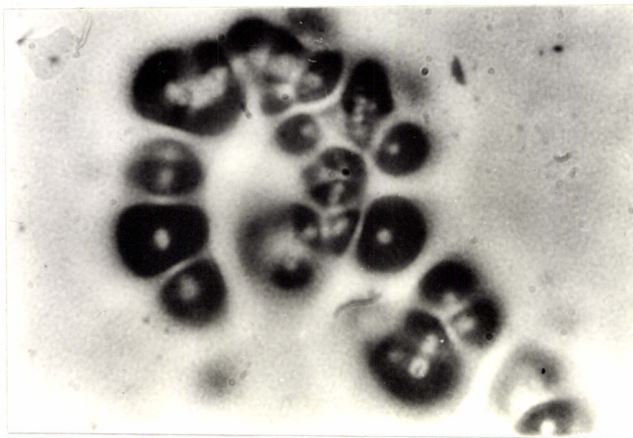


Fig. 10.49

(x125)

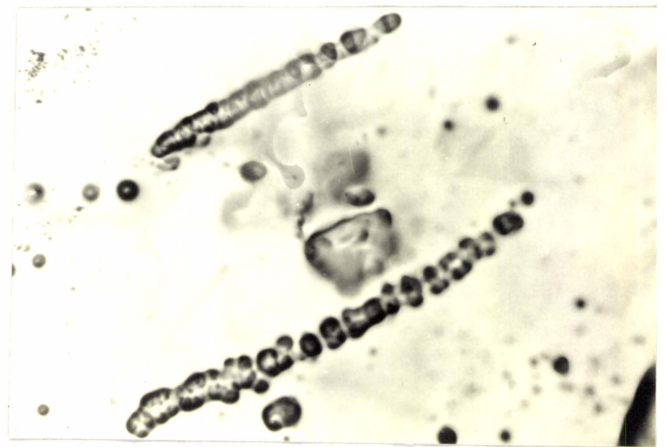


Fig. 10.50

(x33)

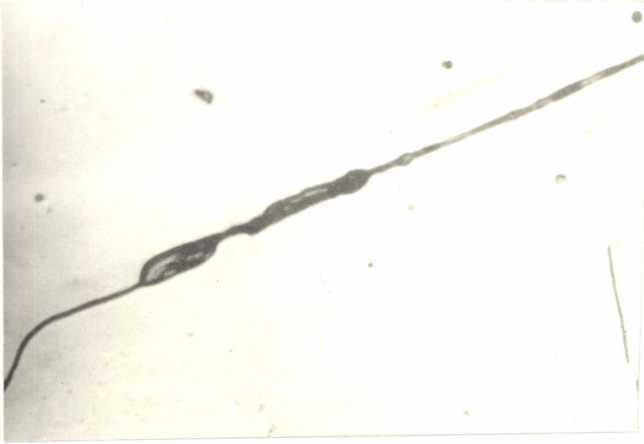


Fig. 10.51(a)

(x100)

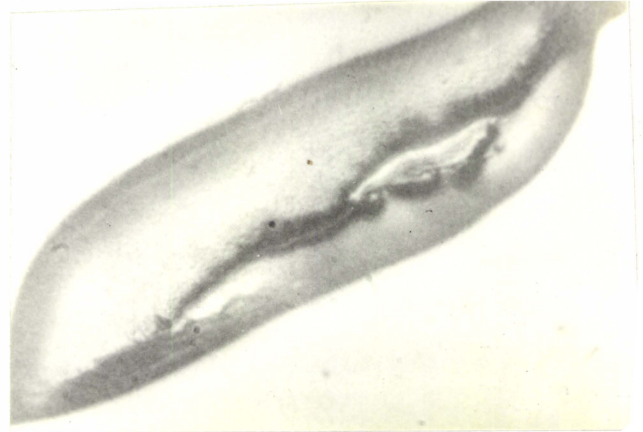


Fig. 10.51(b)

(x1000)

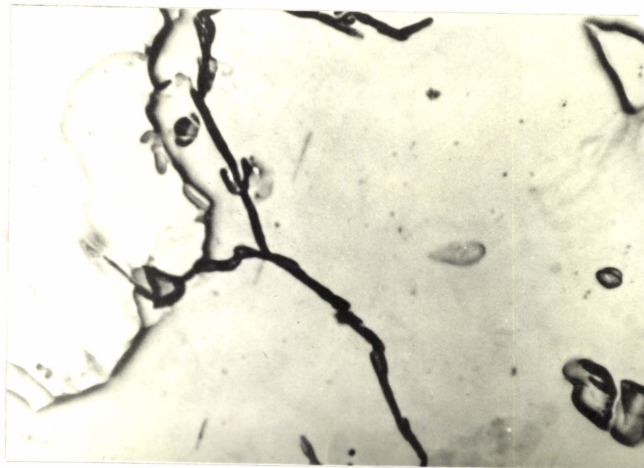


Fig. 10.52

(x100)

10.6 REFERENCES

- [1] J.R.Drabble, R.D.Groves and R.Wolfe, Proc. Phys. Soc., 71 (1958) 430.

- [2] I.Teramoto and S.Takayanagi, J. Appl. Phys. 32 (1961) 119.

- [3] A.Sagar and J.W.Faust.Jr., J. Appl. Phys. 38 (1967) 482.

- [4] A.Sagar and J.W.Faust. Jr., J. Appl. Phys. 38 (1967) 2240.

- [5] A.Sagar and J.W.Faust. Jr., J. Appl. Phys. 38 (1967) 2410.

- [6] A.Sagar and J.W.Faust.Jr., Phys. Lett. 23 (1966) 406.

- [7] N.D.Vasil'eva, A.N.Dubrovina, G.A.Kulikova, M.E.Rezniskii and M.I.Tsy-pin. Inorg. Mater. 14 (1978) 1116.

- [8] S.Amelinckx and P.Delavignette, Nature, 185 (1960) 603.

- [9] P.Delavignette and S.Amelinckx, Philos. Mag. 5 (8th series) (1960) 729.

- [10] C.C.Desai, K.Sangwal and V.John, *Krist & Tech.* 12 (1977) 1269.
- [11] N.Cabrera and R.V.Coleman, in: "The art and science of growing crystals", ed. J.J.Gilman (Wiley, New York, 1963).
- [12] K.Sangwal, *Etching of Crystals--Theory, Experiment and Application* (North Holland, New York, 1987).
- [13] F.C.Frank and W.T.Read.Jr., *Phys. Rev.* 79 (1950) 722.
- [14] W.C.Dash, *J. Appl. Phys.* 27 (1956) 1193.
- [15] W.T.Read Jr., *Dislocations in Crystals* (Mc Graw Hill, New York, 1953).
- [16] J.Friedel, *Dislocations* (Addison-Wesley, London, 1967) p.218.
- [17] W.C.Dash in: *Dislocations and Mechanical Properties of Crystals*, ed. J. Fisher (Wiley, New York, 1957), p.51.
- [18] A.G.Kunjomana and E.Mathai, *J. Mater. Sci.* 26 (1991) 6171.

- [19] L.A.Shuvalov, *Modern Crystallography IV* (Springer-Verlag, Heidelberg, 1988).
- [20] T.Foecke and W.W.Gerberich, *Scr. Metall. Mater.* 24 (1990) 553.
- [21] U.Messerschmidt, V.Schmidt, T.Imura, Y.Nishino and H.Saka, *Mater. Sci. & Eng.* 68 (1984) p.L1.
- [22] K.Sangwal and S.K.Arora, *J. Phys. D* 12 (1979) 645.
- [23] N.F.Mott, *J. Phys. Soc. Japan* 13 (1955) 650.
- [24] A.G.Kunjomana and E.Mathai (communicated).
- [25] H.C.Gatos and M.C.Lavine, in: *Progress in semiconductors, Vol.9*, eds. A.F.Gibson and R.E.Burgess (Heywood, London) p.1.

MICROINDENTATION ANALYSIS OF MELT-GROWN
 Bi_2Te_3 AND In_2Te_3 CRYSTALS

11.1 INTRODUCTION

Tsy-pin et al. [1] studied the mechanical properties of monocrystalline Bi_2Te_3 and reported that P-type Bi_2Te_3 crystals are less strong than solid solutions based on it. Leonov and Chunarev [2] carried out measurements of the overall microhardness of oriented eutectics $\text{Te-Bi}_2\text{Te}_3$ and $\text{Te-Sb}_2\text{Te}_3$ and the minimum period of the distribution of their constituent phases. They have also reported [3] the interrelation of microhardness and electrical conductivity of these eutectic systems. The influence of second phase of deformation and recrystallization of Bi_2Te_3 based alloys was carried out by Dubrovina et al. [4]. Arivuoli et al. [5] have reported the microhardness studies of Bi_2Te_3 crystals grown from vapour.

Goryuniva [6] has first investigated the microhardness of semiconducting materials with the zinc blende structure. They determined the hardness numbers with loads between 10 and 50 g and estimated the hardness of In_2Te_3 to be equal to 180 kg/mm^2 for a load of 20 g.

Not much data has been seen reported on the mechanical behaviour of Bi_2Te_3 , α and β - In_2Te_3 crystals grown by

horizontal zone-levelling (HZL) method. So it was thought useful to make a microindentation analysis to study the hardness, toughness and brittleness of these crystals. The work hardening exponent n has been determined from the dependence of hardness on applied load. Attempts have also been made to understand the nature of crack system developed around the indented impressions.

11.2 EXPERIMENTAL

The crystals used in the present investigation were grown by the HZL method. Freshly cleaved crystals with highly reflecting (0001) cleavage planes of Bi_2Te_3 and (111) planes of In_2Te_3 crystals ($\sim 10 \times 3 \times 2$ mm) were selected for indentation purposes. The samples were mounted on to glass slides with the cleaved face parallel to the slide surface. The indentation study was performed at room temperature using a microhardness tester as described in chapter 5. All investigations have been done in the load range 2.5 to 50 g, above which intensive cracks were observed. For each sample, several trials of indentations with each loading were carried out. Since the area of the impression did not bear any observable dependence on loading time for the constant load used, the time of indentation employed was

15 sec for all subsequent trials. The indentation-induced crack patterns around the indented impressions were viewed under the microscope. The microhardness H_V was calculated as described in chapter 4. Fracture toughness K_C has been calculated from the observed crack lengths. The values of brittleness B_r were determined using Lawn and Marshall's [7] proposal that brittleness is equal to hardness divided by toughness. Chemical etching technique was employed with the etchant comprising 6 ml HNO_3 , 1 ml CH_3COOH and 1 ml HF to delineate the development of cracks formed under different loads.

11.3 RESULTS AND DISCUSSION

11.3.1 Bi_2Te_3 crystals

The microhardness on the (0001) cleavage plane of Bi_2Te_3 crystals strongly depends on plastic deformation and their greater tendency towards crack formation and easy cleavage. So during the present investigations, special attention has been made to understand these characteristics while measuring the microhardness. Fig.11.1 shows the dependence of microhardness on load for Bi_2Te_3 crystals, where a sudden decrease is observed at increasing loads. This is due to the fact that the cleavage plane of Bi_2Te_3

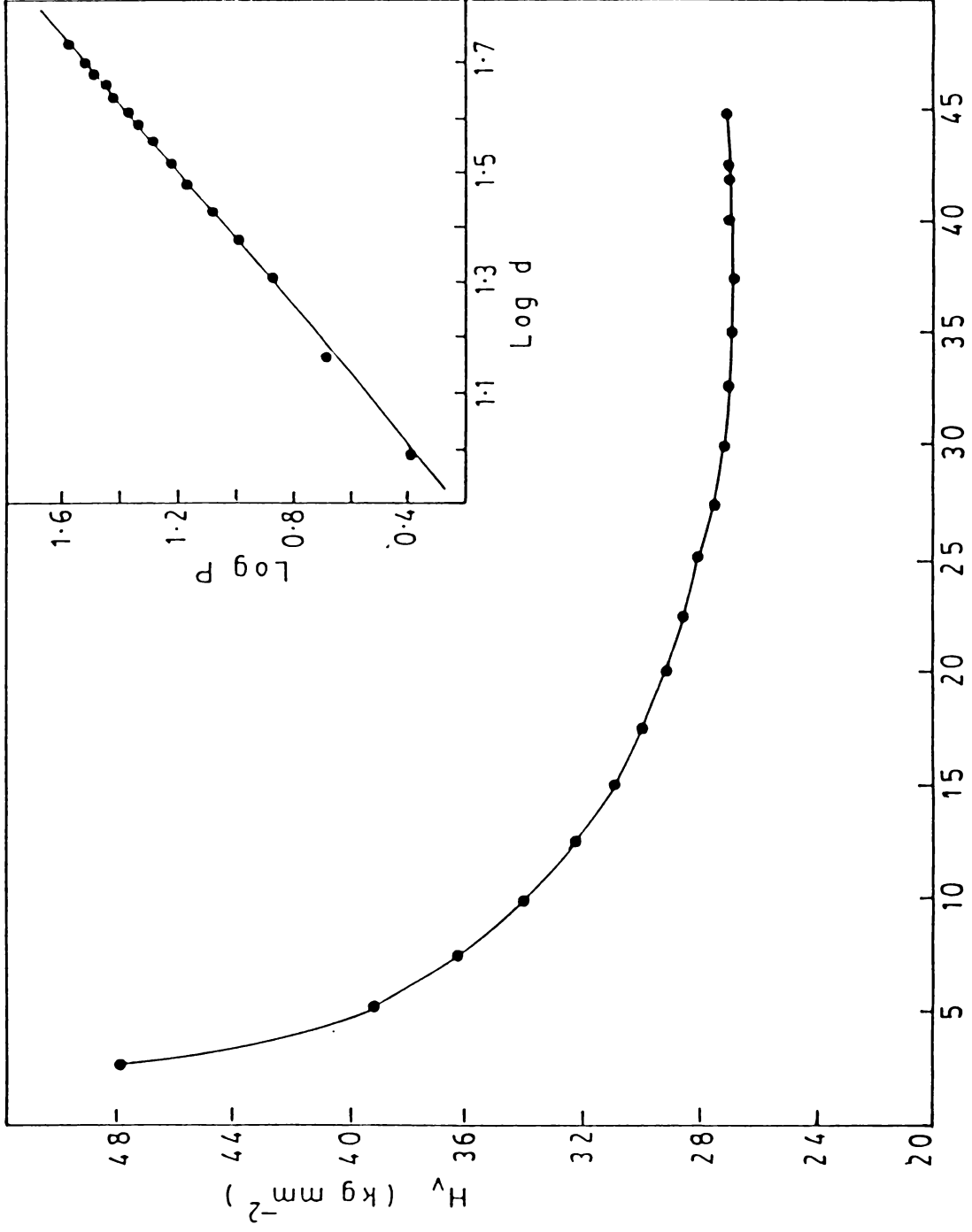


Fig. 11.1

crystals is consisting of weakly bonded Te layers, which have a substantially large bond length equal to 3.74 Å [8]. As this bond is primarily of the van der Waals kind, the cleavage plane is easy to glide and hence it will slip during indentation process. Indentation produces plastic deformation which must be accompanied by movement and multiplication of dislocations. Hence as the load is increased, the amount of plastic strain is also increased, which in turn reduces the microhardness values. The average value of hardness is 0.305 GPa. On comparing this result with that obtained for Bi_2Te_3 whiskers it is found that the hardness of melt grown Bi_2Te_3 crystals is less than that of Bi_2Te_3 whiskers. The inset of Fig.11.1 represents the plot of $\log P$ versus $\log d$ whose slope (n) is found to be equal to 1.656. This supports the concept of Onitsch [9] who reported that the value of n is less than 2 when the hardness decreases with load.

The cracks which form around a sharp indentation have been the subject of many investigations [10-12]. These studies allowed the cracks to be viewed not as a cause of perturbation of hardness measurements, but as a new possibility for toughness determination. In Bi_2Te_3 crystals

cracks were propagated from the corners of the indented impressions at increasing loads. Loads beyond 50 g were not used for the evaluation of toughness as chipping of the material occurred above this load. The mean value of toughness is $0.106 \text{ MPa m}^{\frac{1}{2}}$ and the brittleness of Bi_2Te_3 is $2.877 \mu\text{m}^{-\frac{1}{2}}$.

The deformation pattern around the indentation marks on the crystals was detected by chemical etching technique, from which the crack system can be easily observed. In the present study, the etchant comprising 6 ml HNO_3 + 1 ml CH_3COOH + 1 ml HF (previously employed to investigate cracks formed by cleavage process) is found to be very reliable to understand the deformation formed during the indentation process. Some interesting results were obtained by employing this etchant on the indented samples at different loads. Fig.11.2(a) shows the micrographs of Vickers indentations made in Bi_2Te_3 crystals at increasing loads. The indentation mark at the site A is for 5 g and that at B is for 10 g. The same surface after etching for 10 sec is shown in Fig.11.2(b). At 5 g load, rosette patterns were formed on the indentation mark, while at the load of 10 g, extensive cracks were formed. From these features, the

effect of surface damage produced by subjecting to different loads can be clearly seen. Figs.11.3 to 11.5 represent the indentation marks at loads 7.5, 15 and 20 g respectively after etching for 10 sec. In this case also, it can be found that at low loads, less deformation was produced due to indentation, whereas at higher loads, lateral and interior cracks were revealed which indicates that higher deformations were produced. On etching, the damaged surface layers were removed very fast from the marks at higher loads. From these observations it is clear that the etchant employed in the present study is very reliable to reveal the surface damage extending on the surface due to cracks caused by indentation.

11.3.2 In_2Te_3 crystals

The variation of hardness with load on the (111) cleavage faces of α and β - In_2Te_3 crystals is shown in Figs.11.6 and 11.7 respectively. The inset shows the log P versus log d plot for these crystals. The average value of hardness of α - In_2Te_3 crystals is 1.509 GPa and that of β - In_2Te_3 crystals is 1.470 GPa. The values are found to be less than that obtained for α and β - In_2Te_3 whisker crystals. This is due to the fact that, on the cleavage faces of

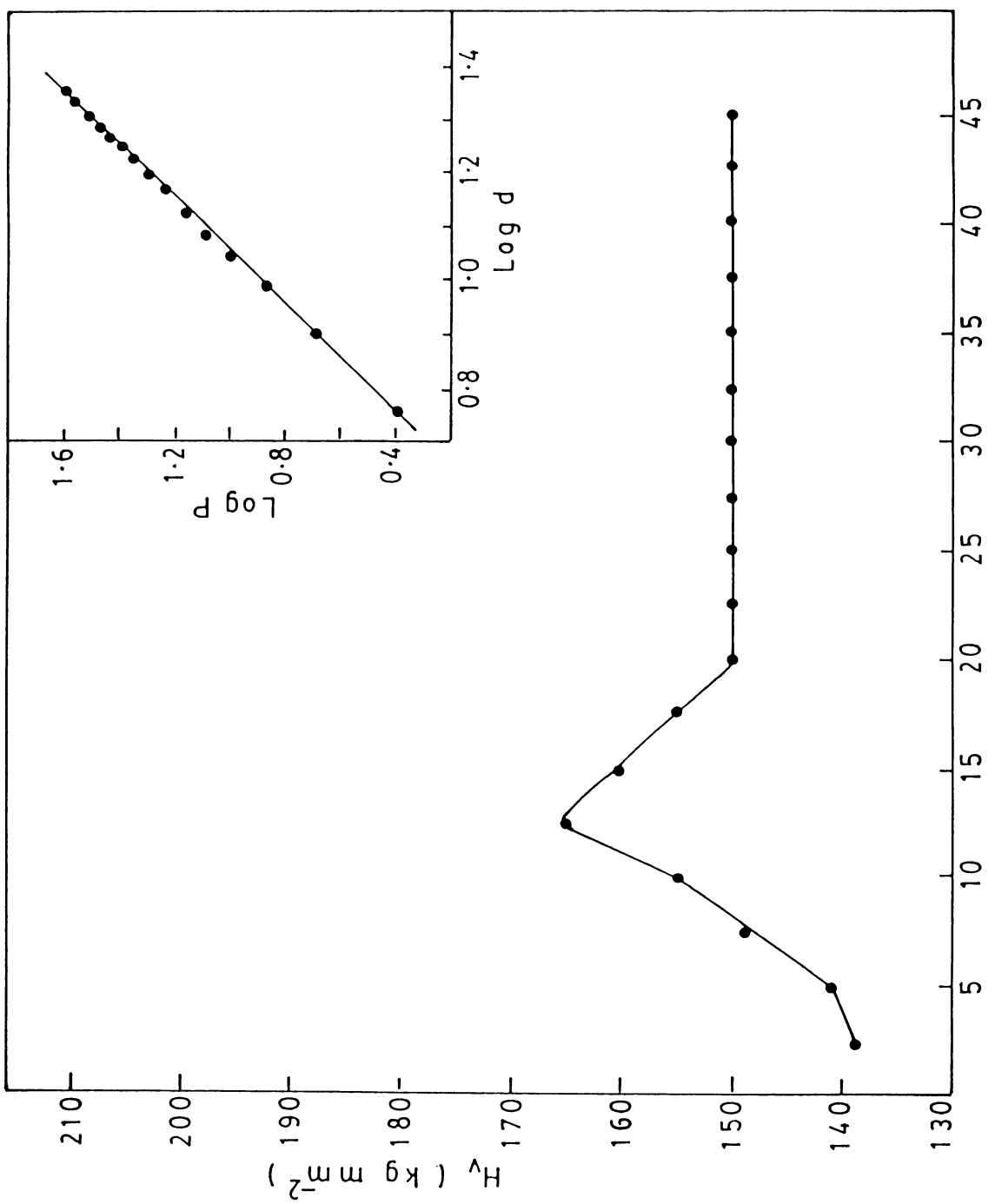


Fig. 11.6

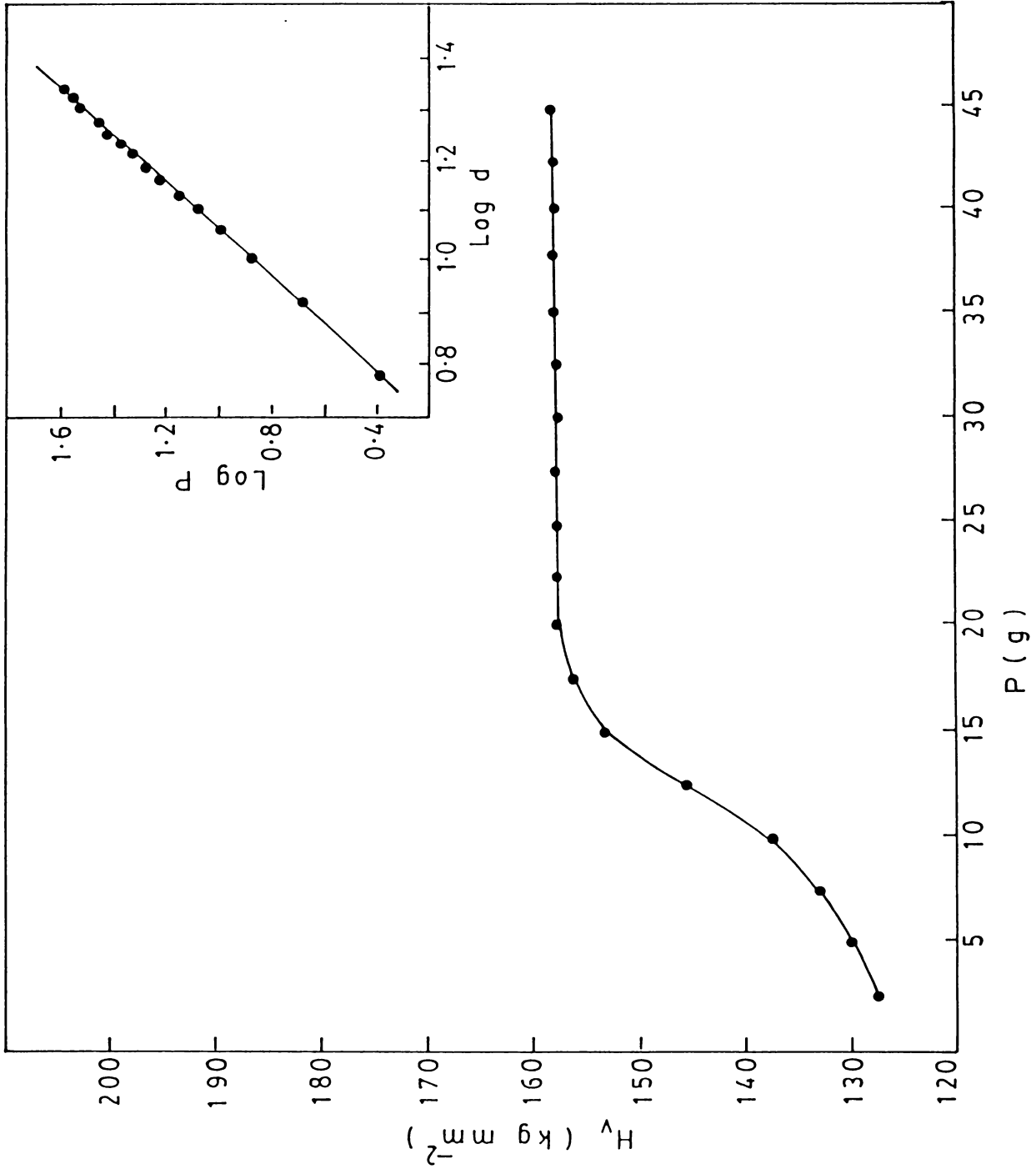


Fig. 11.7

In_2Te_3 crystals, as a load sufficient to cause plastic deformation is first applied, atomic planes which are suitably oriented will slip more readily than that of whiskers. The hardness numbers obtained are fairly in good agreement with those reported in [6]. The values of work hardening exponent for α and β - In_2Te_3 crystals are found to be 2.083 and 2.174 respectively.

In In_2Te_3 crystals, no cracks were formed upto a load of 12.5 g. On increasing the loads, distinct radial cracks appeared. Figs.11.8 and 11.9 are the micrographs of α and β - In_2Te_3 crystals showing the cracks induced by the indentation for a load of 30 g. It is seen that for β - In_2Te_3 crystals, the cracks propagated through a long distance. Also the cracks are not extended deep into the crystal. The absence of any bulk median cracks on the surface of these crystals indicate the low damage of the surface. The average values of toughness of α and β - In_2Te_3 crystals are found to be $0.437 \text{ MPa m}^{\frac{1}{2}}$ and $0.366 \text{ MPa m}^{\frac{1}{2}}$ respectively. The brittleness values of α and β - In_2Te_3 crystals are $3.453 \mu\text{m}^{-\frac{1}{2}}$ and $4.016 \mu\text{m}^{-\frac{1}{2}}$ respectively [13].

11.4 CONCLUSION

Microhardness studies on the cleavage plane of Bi_2Te_3 crystals showed decrease in the hardness values at

increasing loads. This is due to the existence of weak bond between Te-Te layers in the cleavage plane. The value of work hardening exponent is equal to 1.656. The deformation produced on the surface by indentation is revealed by etching technique. The hardness of In_2Te_3 crystals are found to vary with load. The work hardening exponent calculated from the $\log P$ versus $\log d$ plot for α and β - In_2Te_3 crystals is equal to 2.083 and 2.174 respectively. Radial cracks are formed around the indentation marks at higher loads.

Hardness, toughness and brittleness values of Bi_2Te_3 crystals are found to be 0.305 GPa, $0.106 \text{ MPa m}^{\frac{1}{2}}$ and $2.877 \mu\text{m}^{-\frac{1}{2}}$; that of α - In_2Te_3 crystals are 1.509 GPa, $0.437 \text{ MPa m}^{\frac{1}{2}}$ and $3.453 \mu\text{m}^{-\frac{1}{2}}$ and that of β - In_2Te_3 crystals are 1.470 GPa, $0.366 \text{ MPa m}^{\frac{1}{2}}$ and $4.016 \mu\text{m}^{-\frac{1}{2}}$ respectively. The hardness values obtained for the cleaved surfaces are less than that of whiskers.

11.5 FIGURE CAPTIONS

Fig.11.1 Variation of hardness with load for Bi_2Te_3 crystals. The inset shows the plot of $\log P$ with $\log d$.

Fig.11.2(a) Indentation marks on a cleavage face of Bi_2Te_3 crystals at two different loads, 5 g (A) and 10 g (B).

Fig.11.2(b) The same face after etching.

Fig.11.3 Etch figure of the indentation mark on a cleavage face of Bi_2Te_3 crystals at 7.5 g load.

Fig.11.4 Etch figure of the indentation mark on a cleavage face of Bi_2Te_3 crystals at 15 g load.

Fig.11.5 Etch figure of the indentation mark on a cleavage face of Bi_2Te_3 crystals at 20 g load.

Fig.11.6 Variation of hardness with load for $\alpha\text{-In}_2\text{Te}_3$ crystals. The inset shows the plot of $\log P$ with $\log d$.

Fig.11.7 Variation of hardness with load for β - In_2Te_3 crystals. The inset shows the plot of $\log P$ with $\log d$.

Fig.11.8 Indentation mark at 30 g load showing crack patterns on a cleavage face of α - In_2Te_3 crystals.

Fig.11.9 Indentation mark at 30 g load showing crack patterns on a cleavage face of β - In_2Te_3 crystals.

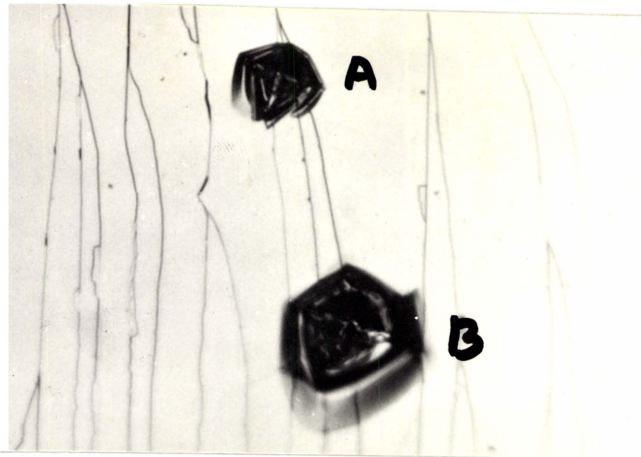


Fig. 11.2(a)

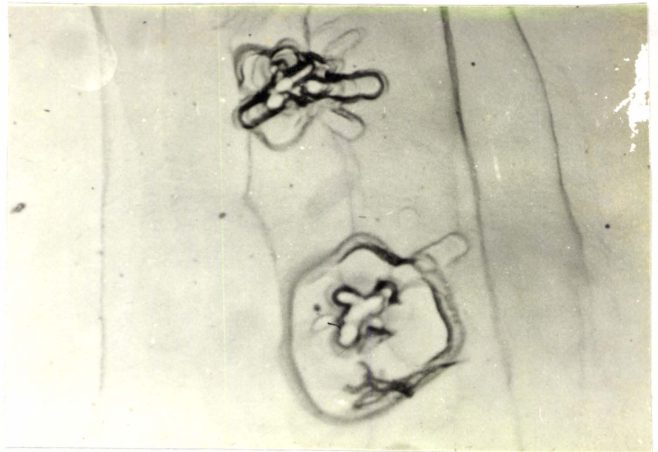


Fig. 11.2(b)



Fig. 11.3

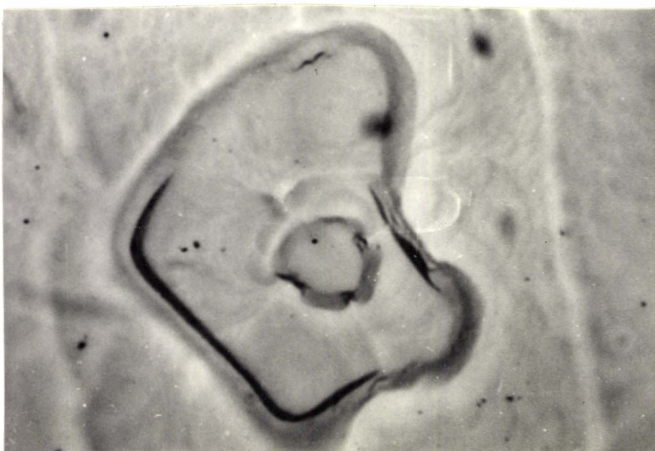


Fig. 11.4

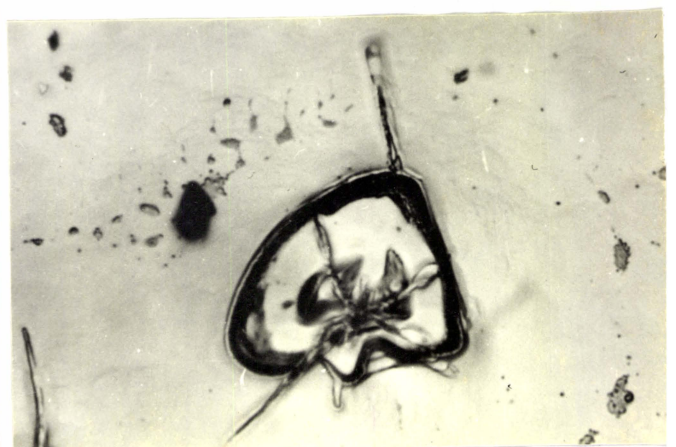


Fig. 11.5

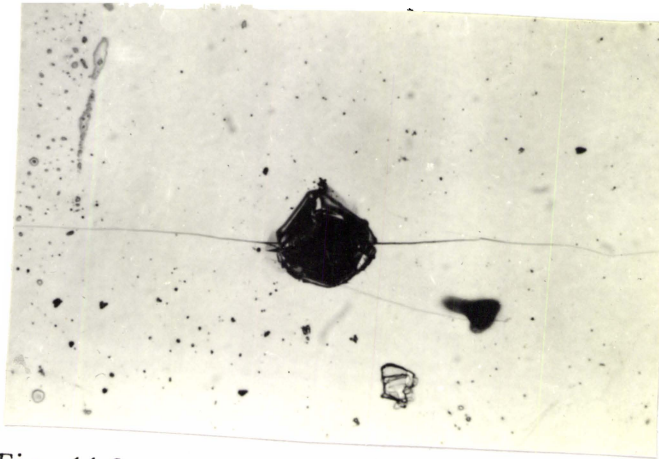


Fig. 11.8

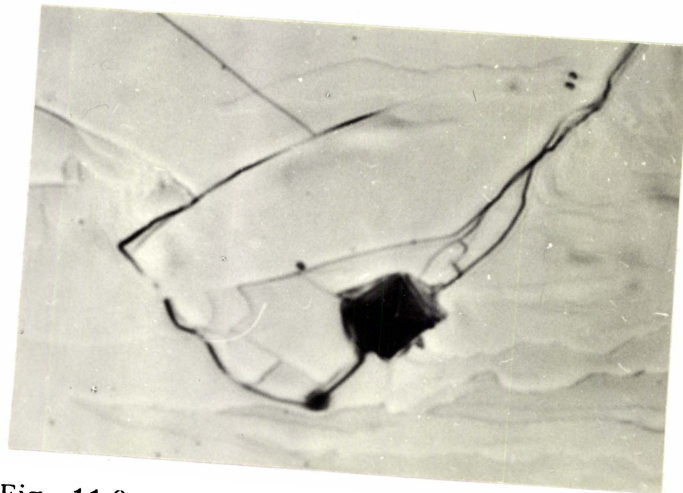


Fig. 11.9

11.6 REFERENCES

- [1] M.I.Tsy-pin, A.A.Chipzhenko, G.A.Kulikova, L.M.Ostrovskaya, A.N.Dubrovina and L.E.Kvyatkovskii, *Inorg. Mater.* 9 (1973) 1112.
- [2] V.V.Leonov and E.N.Chunarev, *Fiz. Met. & Melloved* 46 (1978) 156.
- [3] V.V.Leonov and E.N.Chunarev, *Inorg. Mater.* 18 (1982) 324.
- [4] A.N.Dubrovina, L.A.Leont'eva, G.A.Drozdova, A.I.Kazakov and V.S.Smirnov, *Inorg. Mater.* 17 (1981) 403.
- [5] D.Arivuoli, F.D.Gnanam and P.Ramasamy, *J. Mater. Sci. Lett.* 7 (1988) 711.
- [6] N.A.Goryunova, *Zh. Tekhn. Fiz.* 27 (1957) 1408.
- [7] B.R.Lawn and D.B.Marshall, *J.Amer. Ceram. Soc.* 62 (1978) 347.
- [8] J.R.Drabble and C.H.L.Goodman, *J. Phys. Chem. Solids* 5 (1958) 142.

- [9] E.M.Onitsch, Mikroskopie 2 (1947) 131.
- [10] B.R.Lawn and E.R.Fuller, J. Mater. Sci. 10 (1975) 2016.
- [11] A.G.Evans and E.A.Charles, J. Amer. Ceram. Soc. 59 (1976) 371.
- [12] B.R.Lawn, A.G.Evans and D.B.Marshall, J. Amer. Ceram. Soc. 63 (1980) 574.
- [13] A.G.Kunjomana and E.Mathai (communicated).

ELECTRICAL CONDUCTIVITY STUDIES OF MELT-GROWN
 Bi_2Te_3 AND In_2Te_3 CRYSTALS

12.1 INTRODUCTION

Electrical conductivity studies have provided valuable information regarding the motion of charge carriers in various materials [1-4]. It can also yield sufficient knowledge of the defect levels as well as the band gap in solids.

This chapter deals with the basic theory of electrical conduction and the study of conductivity of Bi_2Te_3 and In_2Te_3 crystals. Special attention has been given to analyse the dependence of annealing temperature on the conductivity of $\beta\text{-In}_2\text{Te}_3$ crystals. The values of activation energy of charge carriers are also estimated.

12.2 MECHANISM OF ELECTRICAL CONDUCTION IN SEMICONDUCTORS

The term semiconductor implies that it is a material having an electrical conductivity intermediate between that of metals and insulators. Metallic conductivity is typically between 10^6 and $10^4 \Omega^{-1}\text{cm}^{-1}$, while for insulators the conductivity is less than $10^{-10} \Omega^{-1}\text{cm}^{-1}$. Some solids with conductivities between 10^4 and $10^{-10} \Omega^{-1}\text{cm}^{-1}$ are classified as semiconductors. The semi-conducting properties are brought up by thermal excitation, impurities, lattice defects etc. Semiconductors in which

conductivity is controlled by valence electrons are known as intrinsic semiconductors and those in which conductivity is controlled by impurities are called extrinsic semiconductors.

Electrical conduction in an ideal semiconductor consists of motion of electrons in the conduction band under the influence of an electric field and holes in the valence band. Thus the basic idea of electrical conduction in a semiconductor is that the electrons occupying donor levels (or holes occupying acceptor levels) may contribute to the electrical conductivity in a manner other than the usual process of thermal excitation followed by band conduction.

The transport of carriers under the influence of an applied electric field produces a current I

The resistivity ρ of the material is defined as a proportionality constant between the electric field intensity E and the current density J

$$E = \rho J \quad (12.1)$$

The conductivity σ is the reciprocal of resistivity ρ

$$J = \sigma E \quad (12.2)$$

The current density can be expressed by

$$J = env_d \quad (12.3)$$

where n is the carrier density, e is the carrier charge and v_d is the drift velocity.

Substituting $v_d = \mu E$ into (12.3), equating (12.3) and (12.2) and solving for conductivity leads to

$$\sigma = e\mu n \quad (12.4)$$

The electron conductivity σ_n and hole conductivity σ_p can be expressed as

$$\sigma_n = e_n \mu_n n \quad (12.5)$$

and

$$\sigma_p = e_p \mu_p p \quad (12.6)$$

The total conductivity of the semiconductor must be expressed by

$$\sigma_s = \sigma_n + \sigma_p = e_n \mu_n n + e_p \mu_p p \quad (12.7)$$

Often either n or p dominates and one of the terms on the right hand side of the equation (12.7) may be neglected [5].

The temperature dependence of the conductivity of semiconductors is one of the most striking characteristics of their properties. The conduction mechanism can be determined by measuring the variation of current in a semiconductor with temperature. The conductivity of a semiconductor depends on two factors such as the number of current carriers per unit volume and the mobility of carriers through the substance under an applied electric field. As the temperature is increased from absolute zero, the electrons in the defect level get excited to the conduction band (or to the valence band in the case of holes) and contribute to conduction. This process continues until all the defect levels are exhausted. The conductivity may decrease with further increase of temperature due to the decrease in mobility of the charge carriers. At still higher temperatures, the electrons are excited from the valence band to the conduction band and yield to intrinsic conduction.

The variation of conductivity with temperature can be given by

$$\sigma = \sigma_0 \exp \frac{-\epsilon}{2kT} \text{ (Intrinsic conduction)} \quad (12.8)$$

and

$$\sigma = \sigma_0 \exp \frac{-\epsilon}{kT} \text{ (Extrinsic conduction)} \quad (12.9)$$

where σ_0 is a constant, k is Boltzmann constant, T the absolute temperature and ϵ is the activation energy of charge carriers.

The exponential increase in conductivity with temperature is simply associated with the activation energy required for the thermal motion of charge carriers. The value of the activation energy for the donor level can be determined from the slope of the (σ - T) curve. The slope of the intrinsic region of this curve represents the activation energy required for an electron to go from the valence band to the conduction band and this must be equal to the band gap of the material.

12.3 EXPERIMENTAL

The crystals were grown by HZL method as already described in Chapter 5. β - In_2Te_3 crystals were annealed in vacuum for 30 min at temperatures 323 and 343 K. Samples of typical sizes $5 \times 5 \times 2 \text{ mm}^3$ with their cleavage faces coated with silver paint were kept in the sample holder and the measurements were made in an evacuated metallic chamber as discussed in Chapter 5. The conductivity measurements

were carried out by applying a steady voltage of 9 V across the crystal and the resulting current was measured using an electrometer. During the measurements, the temperature of the crystal was controlled by the current applied to the heater from a stabilized voltage source. Temperature of the sample was measured using a chromel-alumel thermocouple kept close to the sample. Details of the sample holder and the chamber used for the conductivity studies have been already described in Chapter 5. The thickness of the crystals used in this study was measured using a micrometer.

12.4 RESULTS AND DISCUSSION

12.4.1 Bi_2Te_3 crystals

The electrical conductivity of Bi_2Te_3 crystals as a function of temperature is measured to determine the energy gap of this material. Fig.12.1 shows the temperature dependence of the conductivity. It is found that the material is extrinsic in the temperature region 166-333K. The decrease in conductivity with increase in temperature from 166 to 333K is due to the decrease in the mobility as the temperature increases [6]. Above 333K, conductivity increases with temperature and this is typical of an intrinsic conduction. The slope of the intrinsic region

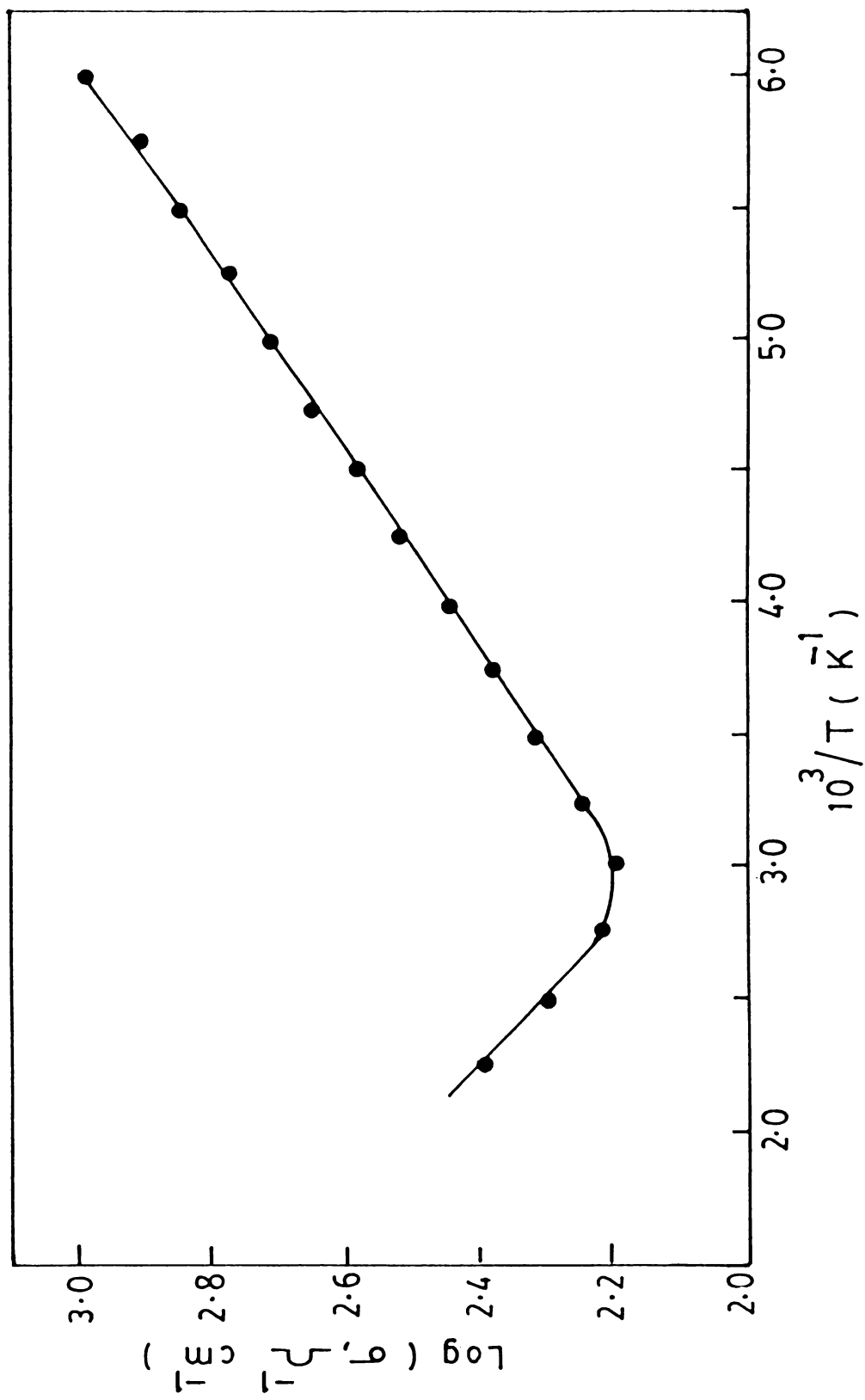


Fig. 12.1

gives an energy gap of 0.158 eV and this value is in good agreement with that reported in [7-9].

12.4.2 In_2Te_3 crystals

Figs.12.2 and 12.3 show the variation of electrical conductivity as a function of $10^3/T$ for α and β - In_2Te_3 crystals respectively. This type of behaviour has been reported by Dmitriev et al. [10]. The effect of annealing at different temperatures on the electrical conductivity of β - In_2Te_3 crystals is also shown in Fig.12.3. It is seen that for In_2Te_3 crystals, the conductivity first rises slowly in the temperature range 100-250K and thereafter it increases sharply upto 333K. The process of conduction in the 100-250K temperature region is indicative of the release of charge carriers from the shallow acceptor levels and the abrupt increase in conduction of the samples above 250K is attributed to the fact that the number of carriers from the next deep acceptor levels are considerably increased as the temperature is increased.

From the figures it is clear that the conductivity of β - In_2Te_3 crystals is found to be higher than that of α - In_2Te_3 crystals. This is due to the increase in the concentration of lattice vacancies in the disordered

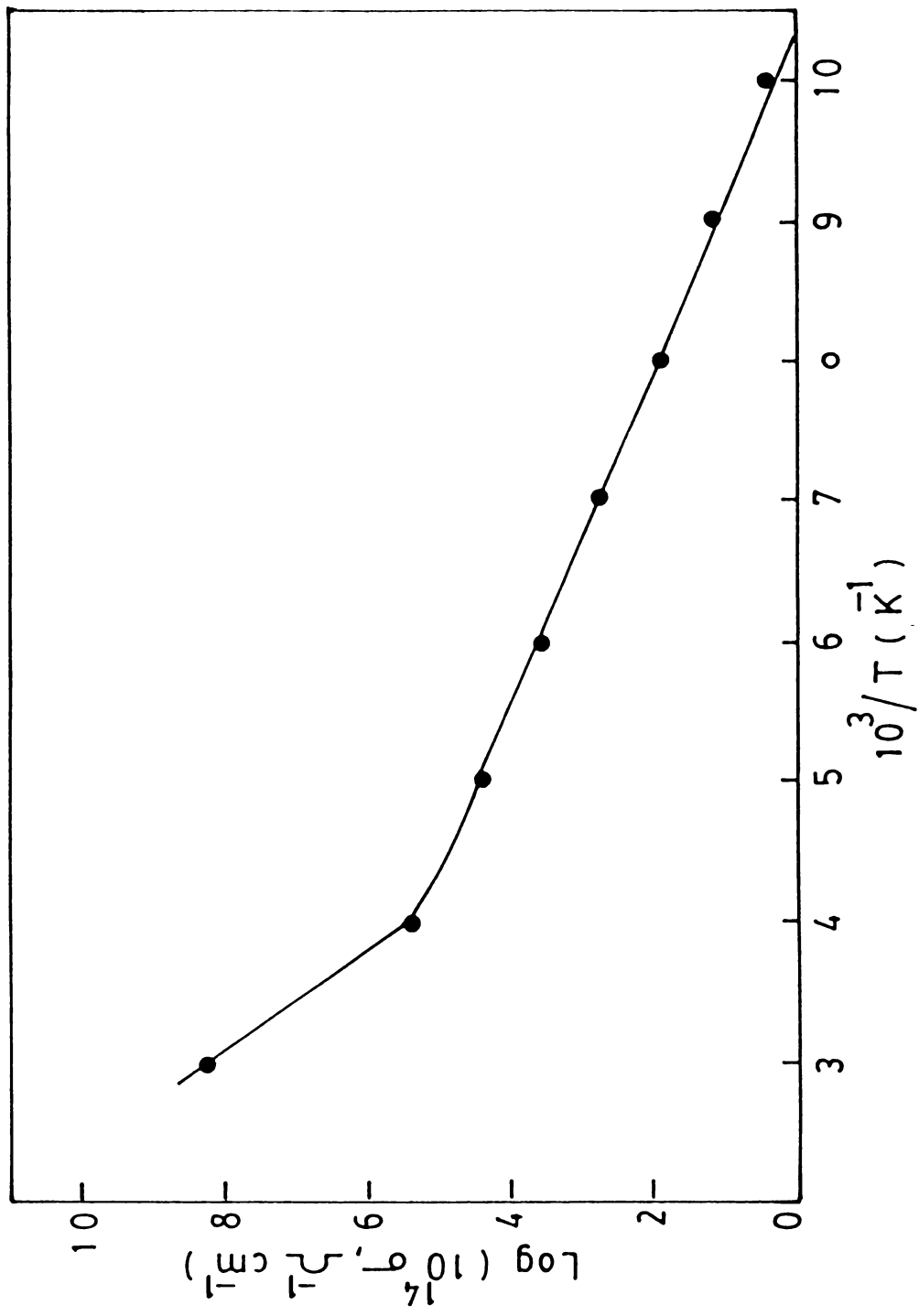


Fig. 12.2

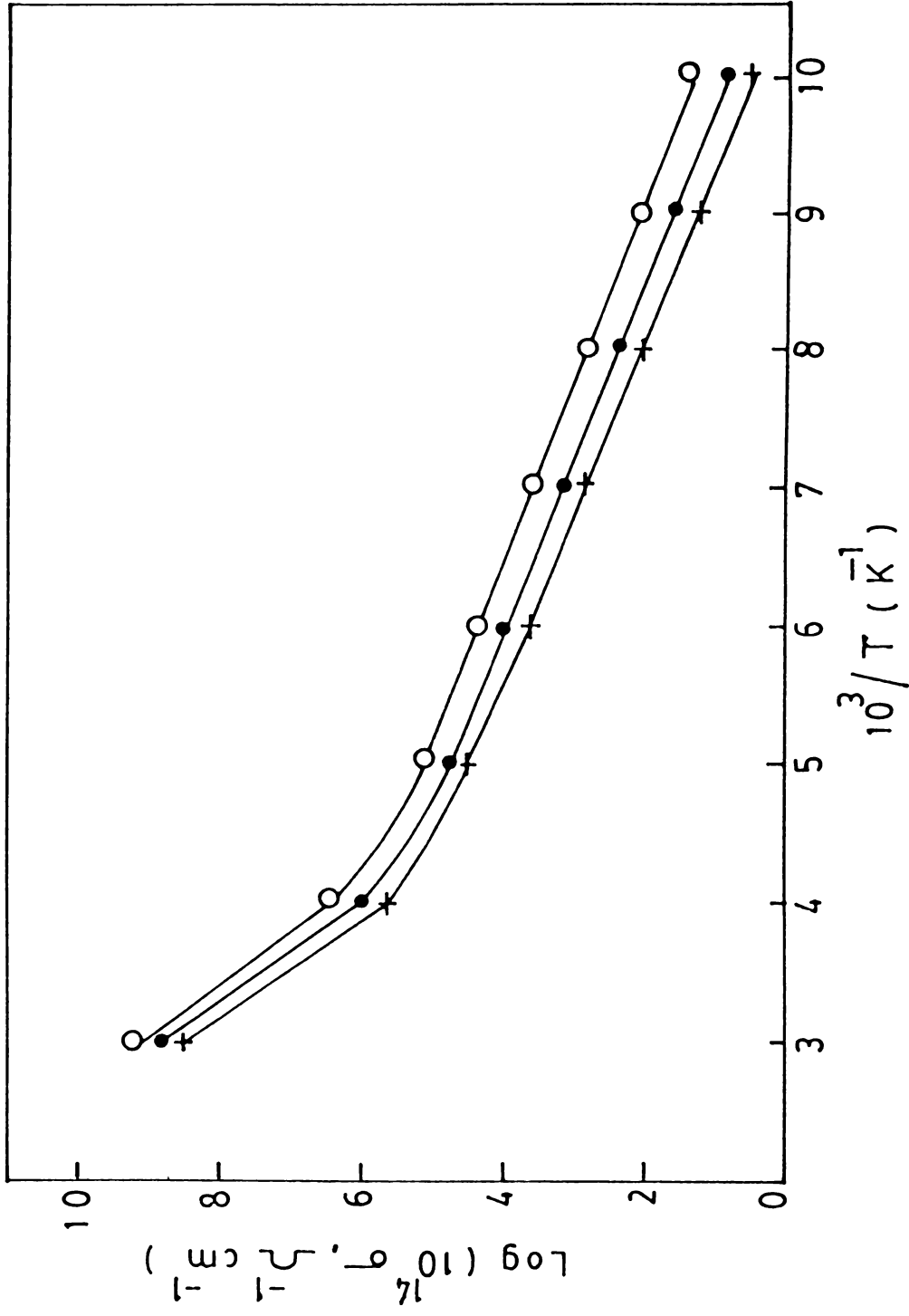


Fig. 12.3

material. The effect of annealing on the conductivity of β - In_2Te_3 crystals is also performed and the result obtained is presented in Fig.12.4. It should be noted that annealing at 323K resulted in a low value of conductivity and this may be explained on the basis that annealing reduces the number of defects present in the crystal. But annealing of the samples at 343K increased the value of conductivity due to the creation of defects and the increase in carrier concentration [11].

Table 12.1 shows the values of electrical conductivity of In_2Te_3 crystals at 100, 303 and 333K. It is also clear from this table that the conductivity of β - In_2Te_3 crystals responds sensitively to the changes in the annealing temperature. In Table 12.2 the values of activation energy calculated for all samples are listed. The results are found to be in good agreement with that obtained by Sen and Bose [12]. Since the electrical conductivity of these samples is governed mainly by the hole concentrations, the values obtained here correspond to the activation energy of the acceptor levels.

12.5 CONCLUSION

The energy gap of Bi_2Te_3 crystals determined from the slope of the intrinsic region of $\log\sigma$ vs. $10^3/T$ plot

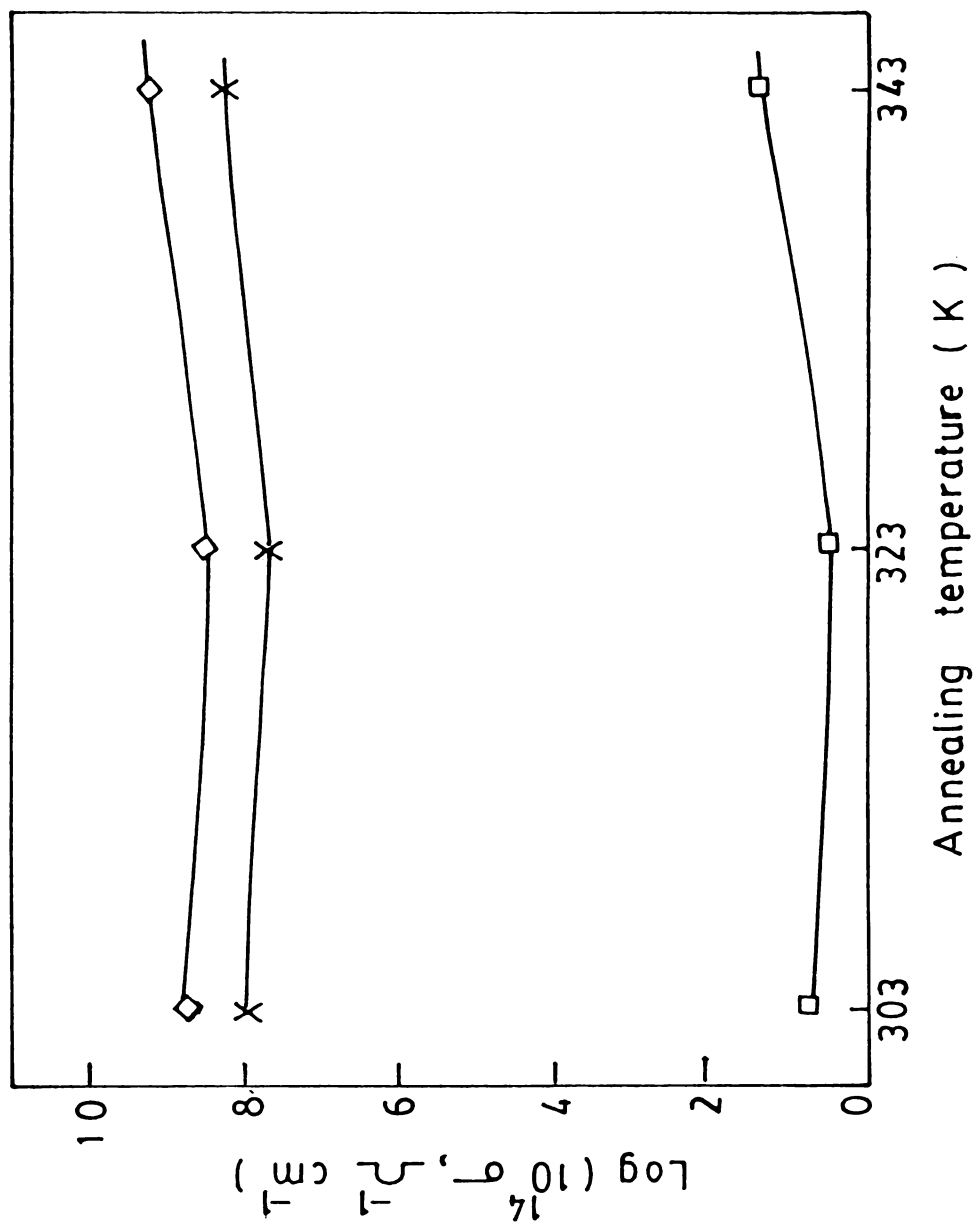


Fig. 12.4

Table 12.1 The values of electrical conductivity σ of In_2Te_3 crystals

Sample	σ at 100 K $\Omega^{-1}\text{cm}^{-1}$	σ at 303 K $\Omega^{-1}\text{cm}^{-1}$	σ at 333 K $\Omega^{-1}\text{cm}^{-1}$
$\alpha\text{-In}_2\text{Te}_3$	2.511×10^{-14}	2.512×10^{-7}	1.584×10^{-6}

$\beta\text{-In}_2\text{Te}_3$			
303 K (Unannealed)	6.310×10^{-14}	10^{-6}	6.313×10^{-6}
323 K (Annealed)	3.162×10^{-14}	5.012×10^{-7}	3.160×10^{-6}
343 K (Annealed)	2.512×10^{-13}	1.580×10^{-6}	1.585×10^{-5}

Table 12.2 The values of activation energy at different temperature ranges in In_2Te_3 crystals

Sample	Activation energy in the temperature range at	
	100-250 K eV	250-333 K eV
$\alpha\text{-In}_2\text{Te}_3$	0.1656	0.5860

$\beta\text{-In}_2\text{Te}_3$		
303 K (Unannealed)	0.1589	0.5564
323 K (Annealed)	0.1622	0.5660
343 K (Annealed)	0.1490	0.5464

is 0.158 eV. The conductivity of β - In_2Te_3 crystals is found to be higher than that of α - In_2Te_3 crystals. Annealing of β - In_2Te_3 crystals at 323K decreases the conductivity whereas annealing at 343K increases the value of conductivity.

12.6 FIGURE CAPTIONS

Fig.12.1 Variation of electrical conductivity with reciprocal absolute temperature for Bi_2Te_3 crystals.

Fig.12.2 Variation of electrical conductivity with reciprocal absolute temperature for $\alpha\text{-In}_2\text{Te}_3$ crystals.

Fig.12.3 Variation of electrical conductivity with reciprocal absolute temperature for $\beta\text{-In}_2\text{Te}_3$ crystals. (\bullet) 303 K (Unannealed), (+) 323 K (Annealed) and (o) 343 K (Annealed).

Fig.12.4 Plot of $\log \sigma$ against annealing temperature for $\beta\text{-In}_2\text{Te}_3$ crystals at different temperatures. (\square) 100 K, (X) 303 K and (\diamond) 333 K.

12.7 REFERENCES

- [1] L.I. Isaenko, I.F. Kanaev, V.K. Malinovskii and V.I. Tyurikov, *Sov. Phys. Solid State* **30** (1988) 199.

- [2] C.C. Desai and M.S.V. Ramana, *Cryst. Res. Technol.* **22** (1987) 809.

- [3] J.J. Vuillemin, A. Khellaf and J.E. Johnston, *Solid State Commun.* **76** (1990) 229.

- [4] H.S. Lee, I.H. Oh, J.J. Lee, J.H. Ro and D.I. Lee, *New Phys. (Korean Phys. Soc.)*, **30** (1990) 431.

- [5] N.B. Hannay, *Semiconductors*, (Reinhold Publishing Corp., New York, 1960).

- [6] A.G. Kunjomana and E. Mathai (Communicated).

- [7] T.C. Harman, B. Paris, S.E. Miller and H.L. Goering, *J. Phys. Chem. Solids* **2** (1957) 181.

- [8] J. Black, E.M. Conwell, L. Seigle and C.W. Spencer, *J. Phys. Chem. Solids* **2** (1957) 240..

- [9] C.H. Champness and A.L. Kipling, Canad J. Phys. 44 (1966) 769.
- [10] Yu. N. Dmitriev, V.N. Kulik, L.P. Galchinetskii and V.M. Koshkin, Sov. Phys. Solid State 17 (1976) 2396.
- [11] A.G. Kunjomana and E. Mathai (Communicated).
- [12] S. Sen and D.N. Bose, Solid State Commun. 50 (1984) 39.

